Aerodynamic loads on a wind turbine rotor in axial motion

by

Lene Eliassen

Thesis submitted in fulfillment of
the requirement
PHILOSOPHIAE DOCTOR
(PhD)

University of
Stavanger

Faculty of Science and Technology
Department of Mechanical and Structural Engineering
and Materials Science
2015

Universitetet i Stavanger
N-4036 Stavanger
NORWAY
www.uis.no

ISBN: 978-82-7644-593-0
ISSN: 1890-1387
Doktorgradavhandling nr: 245

Acknowledgement

This thesis is submitted in partial fulfillments of the requirements for the degree of Doctor of Philosophy (PhD) at the University of Stavanger (UiS), Norway. The research has been part of the Norwegian Centre for Offshore Wind Energy (NORCOWE).

Foremost I would like to express my gratitude and thanks to my supervisors, Prof. Jasna Bogunović Jakobsen, Adj. Prof. Finn Gunnar Nielsen and Prof. Jonas Snæbjörnsson. Specifically, I would like to thank Prof. Jakobsen for her ongoing support and motivation, and Adj. Prof. Nielsen for guiding when I was stuck. Also a special thanks to Assoc. Prof. Michael Muskulus, who introduced me to vortex theory and GPU's.

I am grateful to all of my colleagues at UiS and in NORCOWE for interesting discussions, for answering my questions and for broadening my mind. In particular I would like to mention my fellow PhD students Siri M. Kalvig, Heidi Christiansen, Etienne Cheynet, Ole-Erik Endrerud, Mika Buxhuku and Arunyoti Sarkar. I would also mention Charlotte Obhrai, Tanja Bergby and Samindi Samarakoon and others. It has been a pleasure working at the department.

Special thanks to all my friends for making my years in Stavanger memorable. You are too many to be named here. Thanks to family and friends for support over the years. A special thanks to my brother who managed to retrieve files from my crashed hard-drive.

Lene Eliassen

Abstract

This study investigates the unsteady aerodynamics of attached flow on a two-dimensional airfoil. The unsteady aerodynamics introduces aerodynamic damping of the offshore wind turbine structure and is thus important for the turbine structural integrity. This includes an impact on the fatigue damage of the structure and, consequently, an effect on the total cost of energy.

Unsteady aerodynamics can be studied using a variety of methods. In this thesis, a panel vortex method was developed to estimate the aerodynamic forces. This method is based on potential theory, which can't account for the viscosity in the fluid. Consequently, dynamic stall, which is an important unsteady aerodynamic effect, can not be modeled, and we are limited to attached flow conditions.

Despite this limitation, the vortex method is in some situation the preferred option when investigating unsteady aerodynamics. The vortex method has the advantage of considering the wake history in the estimation of the aerodynamic forces. Using the panel vortex method developed in this study, one is not dependent on look-up tables since the aerodynamic loads are calculated by direct modelling of flow conditions on an airfoil of a given geometry. However, the computational time of the vortex method is long and is therefore often not used.

There is a possibility to reduce the computational time of the vortex method. By using a graphic processing unit, it is demonstrated how the computational time can be reduced for a two-dimensional panel vortex code. A significant reduction in computational time can be achieved for the simulation, depending on the number of vortex elements in the analysis. For a low amount of vortex elements, the computation is faster on a central processing unit, CPU.

The panel vortex method is used to investigate the motion induced aerodynamic loads on an offshore wind turbine. Studying the flow conditions on an airfoil oscillating in plunge motion at frequencies similar to the eigenfrequencies for a floating spar type wind turbine, the aerodynamic damping for eigenmodes represented is estimated. Including the neighbouring airfoils and their wakes in the analysis has a relatively large effect on the estimated aerodynamic damping. The aerodynamic damping is reduced when the period of the oscillating airfoil is equal to the time

it takes for one airfoil to travel from its original position to the neighbouring airfoil's original position. One example where this can occur is if the eigenfrequency of the tower is equal to the blade passing frequency. This effect has previously been studied by other researchers, but mostly for helicopter rotors.

The change in the wind-structure interaction effects is studied with regards to the fatigue damage of the tower using a single degree of freedom model. Comparing the fatigue damage results using different computational methods to estimate the aerodynamic forces can be useful when evaluating the effect of the aerodynamic model chosen on the cost. This study only focuses on one unsteady plunging motion, and is therefore limited. It is found that the unsteady aerodynamic models that are most commonly used may overestimate the damping, and thus estimate a too low fatigue damage. This will have a negative impact on the cost if the wind turbine fails.

Abbreviations

BEM Beam Element Momentum.

CENER National Renewable Energy Centre (Spain).

CFD Computational Fluid Dynamics.

COB Center of Buoyancy.

COG Center of Gravity.

CPU Central Processing Unit.

DLL Dynamic Link Library.

DNV Det Norske Veritas.

DOF Degree of Freedom.

DONG Danish Oil and Natural Gas Energy (Denmark).

DS Dynamic Stall.

FEM Finite Element Method.

GDW Generalized Dynamic Wake.

GH Garrard Hassan & Partners Limited.

GPU Graphics Processor Unit.

IWES Frauenhofer Institute for Wind Energy and Energy System Technology.

MBS Multibody Simulation.

ME Morison Equation.

MEXICO Measurements and Experiments in Controlled Conditions.

NORCOWE Norwegian Centre for Offshore Wind Energy.

NOWITECH Norwegian Research Center for Offshore Wind Technology.

NREL National Renewable Energy Laboratory (USA).

OC3 Offshore Code Comparison collaborative.

OC4 Offshore Code Comparison Collaborative Continuation.

RHS Right Hand Side.

RPM Rotations per Minute.

SWE Endowes Chair of Wind Energy of Universität Stuttgart (Germany).

SWL Still Water Level.

TSR Tip Speed Ratio.

UD User Defined.

Nomenclature

Term	Description	Units
Latin letters		
A_d	Rotor disc area	$[m^2]$
A_w	Area in the wake	$[m^2]$
A_{in}	Area in the inlet	$[m^2]$
$B_{k,j}$	Influence from source elements at panel k at the collocation point (x_j, y_j)	
C	Curve around the surface S	
$C'(k)$	Loewy's transfer function	
$C(k)$	Theodorsen's transfer function	

Term	Description	Units
C_D	Aerodynamic drag coefficient	
C_L	Aerodynamic lift coefficient	
C_M	Aerodynamic moment coefficient	
C_a	Aerodynamic damping	[kg/s]
C_p	Power coefficient	
C_{L0}	Lift coefficient for the mean angle of attack, α_0	
C_{LC}	Circulatory part of the lift coefficient	
C_ϵ	Curve around the surface, S_ϵ	
$C_{a,2D}$	Two dimensional aerodynamic damping at an airfoil section	[kg/ms]
$C_{k,j}$	Influence from doublet element at panel k at collocation point (x_j, y_j)	
C_{sdof}	Damping of a SDOF	[kg/s]
D	Aerodynamic drag force	[N]
$F(k)$	Real part of Theodorsen's transfer function, $C(k)$	
F_N	The force normal to a given surface	[N]
F_T	Tangential force	[N]
F_p	Prandtl's tip loss correction factor	
G	Green's function	
$G(k)$	Imaginary part of Theodorsen's transfer function, $C(k)$	
$H(\omega)$	Frequency response function	
KE	Kinetic energy	[Nm]
K_a	Aerodynamic stiffness	[kg/s^2]
$K_{a,2D}$	Two dimensional aerodynamic stiffness	[kg/m^2]

Term	Description	Units
K_{sdof}	Stiffness of a single degree of freedom system	[kg/s^2]
L	Aerodynamic lift force	[N]
L_C	Circulatory lift force	[N]
L_{NC}	Non-circulatory component of the lift force	[N]
L_∞	Steady state aerodynamic lift	[N]
M	Aerodynamic moment	[Nm]
M_0	Aerodynamic moment about the leading edge of the airfoil	[Nm]
M_1	Mass moment of inertia in pitch	[kgm]
M_a	Aerodynamic added mass	[kg]
M_i	Modal mass, or mass moment of inertia	[kg]/[kg m^2]
$M_{a,2D}$	Two dimensional aerodynamic added mass at an airfoil section	[kg/m]
M_{sdof}	Mass of a single degree of freedom system	[kg]
M_{va}	Virtual aerodynamic mass	[kg]
M_{yNC}	Non-circulatory aerodynamic moment	[Nm]
N_i	Expected number of cycles to fatigue failure at a given stress range, $\Delta\sigma_i$, see Eq 6.46	
P	Mechanical power	[W]
P_{avail}	Available aerodynamic power	[W]
Q_∞	Total free flow velocity	[m/s]
R	Radius of the rotor	[m]
S	Surface area, bounded by the curve C	[m^2]

Term	Description	Units
S_c	Distance between airfoils in a cascade	[m]
S_f	Responsen spectra	[m^2/Hz]
S_j	Ocean wave spectra	[m^2/Hz]
S_u	Wind spectra	[m^2/s^2/Hz]
S_ϵ	Small suface with singularity, bounded by the curve C_ϵ	[m^2]
T	Thrust force	[N]
T_{cas}	Time it takes to travel one cascade spacing, $T_{cas} = U_x S_c$	[s]
T_{osc}	Osciallating period of the rotor	[s]
U_X	Velocity along the X-axis	[m/s]
U_Y	Velocity along the Y-axis	[m/s]
U_d	Wind velocity at rotor disc	[m/s]
U_w	Wind velocity in the far wake	[m/s]
U_∞	Free stream wind speed	[m/s]
$U_{i,b}$	Induced velocity of the vortex element at the airfoil surfcae	[m/s]
$U_{i,w}$	Induced velocity of the vortex element in the wake	[m/s]
U_{rot}	Rotational velocity of the wind turbine airfoil	[m/s]
W	Relative wind velocity	[m/s]
W_∞	Free flow in y-direction	[m/s]
$\bar{h}$	Amplitude of the oscillating plunging motion	[m]
$\ddot{h}_{1/2}$	Acceleration of the plunge at midfoil	[m/s^2]
a	Axial induction factor	
a'	Rotational induction factor	

Term	Description	Units
a_n	The nth element in Cauchy's convergence test, see Eq 4.89	
a_t	Location of rotational center for Theodorsen's function	
$a_{i,k}$	The element in linear cascade, where i is the blade or wake, and k_c is the element number in the series	
c	Chord length of an airfoil	[m]
f_p	Prandtl's tip loss function	
h	Translation, or plunges, of the thin airfoil	[m]
k	Reduced frequency	
k_c	Cascade number, related to number of airfoils in a cascade, $k_c = n_{bl}/2-1$	
k_p	Peak number, used in cascade simulation. See Eq 4.101	
l_w	Number of wake elements shed from the trailing edge	
l_{ca}	Slope of the trend line used ot compute the aerodynamic damping	[kg/ms]
m_{nac}	Mass of the nacelle	[kg]
m_{sub}	Mass of the substructure	[kg]
m_{tow}	Mass of tower	[kg]
n_{bl}	Number of airfoils in cascade	
p	Aerodynamic pressure	[N/m^2]
p_∞	Pressure in the free flow	[N/m^2]
q_r	Radial velocity in polar coordinates	[m/s]
q_θ	Azimuthal velocity in polar coordinates	[rad/s]
r	Resultant displacement	[m]

Term	Description	Units
s_{dt}	Dimensionless time-step, see Eq 5.38	
t_{cm}	Cascade spacing between vortices in z-plane	[m]
u_d	Induced velocity, due to a doublet element, in x-direction	[m/s]
u_s	Induced velocity, due to a source element, in x-direction	[m/s]
v_a	Velocity normal to the surface of a thin plate	[m/s]
v_d	Induced velocity, due to a doublet element, in y-direction	[m/s]
v_g	Gust velocity	[m/s]
v_i	Axial induced velocity	[m/s]
v_s	Induced velocity, due to a source element, in y-direction	[m/s]
v_∞	Velocity of a vertical uniform stream	[m/s]
w	Tangential induced velocity	[m/s]
$w_{3/4}$	Downwash at 3/4 chord	[m/s]
x_g	Distance to vortex element from collocation point, x_{cp}, in x-direction	[m]
x_{cp}	Collocation point	
y_a	Instantaneous small displacement of the chord line	[m]
y_g	Distance to vortex element from collocation point, x_{cp}, in y-direction	[m]
z_{nac}	Distance from pitch rotational center to nacelle	[m]
Greek letters		
Γ	Circulation	[m^2/s]

Term	Description	Units
Γ_b	Strength of a point vortex element located on a blade	[m^2/s]
Γ_{W_n}	Strength of a point vortex element in wake element n	[m^2/s]
$\Gamma_{w,l}$	Circulation strength of wake particle l	[m^2/s]
Ω	Rotational speed of the wind turbine rotor	[rad/s]
Ψ	Stream function	
α	Angle of attack	[rad]
α_0	Mean angle of attack	[rad]
α_r	Angle of rotation about a point	[rad]
$\dot{\beta}_f$	Velocity of the blade flapping angle	[rad/s]
$\dot{\eta}_{xp}$	The predifined values used to describe the velocity of the rotor as input to AeroDyn	[m/s]
ϵ_w	Convergence limit for wake elements in the cascade	
ϵ_{bl}	Convergence limit for the airfoils in the cascade	
η	Surface of the airfoil	[m]
η_x	Axial motion of the wind turbine rotor, see Eq 6.6	[m]
γ	Strength of distributed vortex elements	
λ_R	Tip speed ratio	
λ_r	Local tip speed ratio	
μ	Strength of a doublet element	
μ_{cm}	Radial coordinate in cascade Z plane	
ω	Angular frequency	[rad/s]

Term	Description	Units
ω_e	Angular eigenfrequency	[rad/s]
ω_x	Angular velocity about x	[rad/s]
ω_y	Angular velocity about y	[rad/s]
ω_z	Angular velocity about z	[rad/s]
ϕ	Flow angle	[rad]
ϕ^*	Velocity potential of the flow field	[m^2/s]
ϕ_i^*	The inner velocity potential, see Eq 5.12	[m^2/s]
ϕ_C	Phase of Theodorsen's transfer function, C(k)	
ϕ_d	Velocity due to a doublet element	[m^2/s]
ϕ_i	Inidicial function	
ϕ_m	Mode shape	
ϕ_s	Velocity potential due to a source element	[m^2/s]
ϕ_w	Wagner's function	
ϕ_∞	Velocity potential of the free flow	[m^2/s]
ϕ_{cm}	Azimuth coordinate in cascade Z plane	[rad]
ψ_k	Küssner's function	
ρ	Air density	[kg/m^3]
σ	Strength of source element	
θ	Angle from vortex element to a point, see Figure 5.2	[rad]
θ	Twist of the airfoil	[rad]
ζ	Aerodynamic damping ratio	
Vectors		
$\vec{V}$	Velocity vector	[m/s]

Term	Description	Units
$\vec{\zeta}$	Vorticity vector	
$d\vec{S}$	A unit vector normal to the surface, S	
$\vec{q}$	Flow field	[m/s]
$\vec{q}_\phi$	Solenoidal component of the flow field	[m/s]
$\vec{q}_\xi$	Rotational component of the flow field	[m/s]
$\vec{x}$	Evaluated point	
$\vec{x}_0$	Singular vortex element	

Contents

Chapter 1

Introduction

1.1 Background

For thousands of years, humans have taken advantage of the energy in offshore wind. One of the oldest examples are the sailboats constructed by the people of Mesopotamia five thousand years ago. These simple sailboats have since been replaced in modern times with boats designed with a better understanding of hydro- and aerodynamics. Nowadays, however, the term offshore wind energy is mostly related to the wind turbines located offshore. By locating the wind turbine offshore, far from populated areas, the visual and noise impacts are reduced.

The first offshore wind turbine farm was erected in 1991, in sheltered and shallow waters outside Denmark. The park was named Vindeby, and consisted of 11 Bonus 450 kW wind turbines [1]. In the beginning, most wind farms were installed near the shoreline and in shallow waters, but current trends place wind turbines further from the coast and in deeper waters [2]. Figure 1.1 illustrates the average distance to shore and water depth of the offshore wind farms. The London Array Phase One, which was installed in 2013, consists of 175 wind turbines and has a production capacity of 630 MW. It is located more than 20 km off the British coast, in water depths of 25 m [3].

As wind turbines increase in size to harvest more energy, and at the same time are located further from the coast in areas with more wind, the wind turbine operators are faced with increasing costs [5]. To make the offshore wind industry viable these costs will need to be reduced. Some of the challenges wind farm operators face are installation methods, logistics issues and new foundations structures. Some of these issues are being

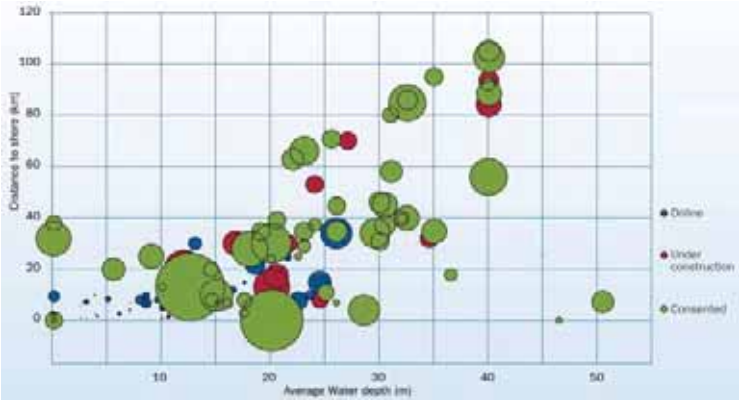

Figure 1.1: Average distance to shore and water depth of offshore wind farms [4] where the area of the circles are proportional to the total capacity of the wind farm.

investigated by the Offshore Wind Accelerator [6].

The challenges related to new foundations relate to the soil condition, water depth and installation method. The monopile, which is currently the most common foundation for offshore wind turbines, is piled into the ground. The tower is connected to the pile via a transition piece. As the water depth increases, more steel is required to maintain the stiffness of the structure. Other types of fixed foundations, such as jackets, may prove to be more cost efficient in deeper water.

Innovative concepts, such as the floating wind turbine Hywind [7], may also be a cost effective solution for the deeper waters. These solutions involve increasingly complex structures and a need for load analyses. Such analyses are needed to study the structural response and to certify the structure. It is also necessary to make an estimate of the loads on the wind turbine during the design phase of a new wind turbine. This requires a fully integrated analysis of the offshore wind turbine structure, including the hydrodynamic loads, aerodynamic loads, the control system, the soil model and the structural model. If the analysis tool overestimates fatigue damage, or extreme loads, the price of the structure may be too high for the wind turbine operator to invest in it. The consequence of an underestimated load is however even larger, and can lead to fracture of the wind turbines or other failures that may reduce their operational life times.

Aerodynamic damping is among the parameters governing the struc-

tural response, which are most properly assessed during an integrated analysis of an offshore wind turbine. For example, for an offshore wind turbine the wave loads can excite tower top response. When the wind turbine tower top is moving into the wind, this is felt as an increase in windspeed at the rotor. The aerodynamic forces will then act as a damper and reduce the response of the tower top motion. This is referred to as aerodynamic damping. It is of interest for fatigue calculations to estimate the magnitude of the aerodynamic damping for the key eigen-modes of the wind turbine tower, as well as how accurately the aerodynamic damping is estimated in the commonly used analysis tools.

Different methods can be used to calculate the aerodynamic forces on a wind turbine. The Beam Element Momentum (BEM) method is commonly used for integrated analyses of offshore wind turbines due to its low computational time. The downside is that the method is based on stationary conditions and two-dimensional airfoil data. Correctional functions are applied to include three dimensional effects and unsteady aerodynamics. These corrections have been developed combining both flow measurement and analytical functions.

However, the BEM method is not an optimal solution for estimating the aerodynamic forces on a wind turbine accurately. Other methods such as fully resolved Computational Fluid Dynamics (CFD) will give a more correct estimate of the loads. However, the time spent finding the aerodynamic forces is too long for it to be commonly used in integrated analyses of wind turbines.

As mentioned previously, another issue with BEM is that it is based on steady momentum theory. Thus, the BEM method must be corrected for the often unsteady aerodynamic conditions that a wind turbine operate in. Unsteady aerodynamics occurs when the change in flow velocity is too fast to establish a steady condition. The unsteady aerodynamics can be a result of blade motion, a turbulent wind field, or the blade passing the tower. The unsteadiness is normally measured using the reduced frequency, k, which is the ratio between the frequency of the flow and a characteristic length relative to the flow velocity. The relationship for a wind turbine airfoil is defined as:

$$k = \omega c/2V$$

where ω is the angular frequency of the disturbance in the flow, c is the chord length of the airfoil and V is the average flow velocity. Leishman

[8] claims that only if $k < 0.01$, can the flow be assumed steady or quasi-steady.

One unsteady aerodynamic phenomena is dynamic stall. At dynamic stall the flow separates, and one get large increase in aerodynamic loads. Modern wind turbines are normally designed to avoid this situation. However, there is unsteady aerodynamics in attached flow conditions, which has an effect on the dynamic response of the wind turbine.

In BEM methods, the unsteady aerodynamics are normally corrected for. A variety of models can be applied, e.g. Stig Øye's method or Beddoes-Leishman model. Little research has been done to investigate the performance of the unsteady aerodynamic models that are included in the BEM codes on the response of a wind turbine. This is especially interesting for offshore wind turbines, where the hydrodynamic loads will increase the response of the tower top. There is a need to investigate the semi-empirical correction models implemented in BEM codes, and compare them to aerodynamic methods that include the unsteadiness in the solution, such as vortex methods.

1.2 Previous Research

In a review of wind turbine aerodynamics from 1993, Hansen & Butterfield [9] claim that the area of dynamic load analysis is probably the analytical discipline with the greatest potential for turbine reliability improvement and cost reduction. Over the next 20 years, a lot of work was put into improving the simulation codes.

One approach chosen to improve and verify wind turbine aerodynamic codes was to conduct experiments, and compare the predicted values to the measured values. In May 2000, one of the largest experiments conducted on wind turbines in a wind tunnel was completed in the NASA-Ames wind tunnel [10]. The wind turbine itself measured 10 m in diameter, and the working section of the wind tunnel is 24.3 m x 36.6 m. A blind comparison between the code predictions and the measurements showed a large scatter. Even at conditions that were assumed easy to predict, the power predictions ranged from 25 % to 175 % of the measured turbine power [10].

In Europe, a successor of the NASA-Ames wind tunnel test was performed in the German-Dutch wind tunnel. The diameter of the wind turbine was 4.5 m, and the test section in the wind tunnel was 9.5 m x 9.5 m. The measurements were performed as a part of the EU project Measure-

ments and Experiments in Controlled Conditions (MEXICO), and the testing programme was completed in 2006 [11]. The difference between the two projects was that MEXICO measured the flow field around the rotor plane and the blade loads simultaneously, while the NASA experiment concentrated on loads. Over a period of three years, the results from the MEXICO measurements were evaluated and compared to values predicted by various simulations tools in the project MexNext. One of the major achievements from the MEXICO project was an improved understanding of the 3D flow field around a wind turbine and in the near wake [11]. Work is still ongoing to investigate the large amount of data retrieved in both the NASA-Ames tunnel and the MEXICO project. An ongoing project, Mexnext-II, also includes some new measurements on the MEXICO rotor [12].

The interest in wake modelling and power prediction was also triggered in Norway. As a part of the joint research programs Norwegian Centre for Offshore Wind Energy (NORCOWE) and Norwegian Research Center for Offshore Wind Technology (NOWITECH), wind tunnel experiments investigating the performance and wake development for a model wind turbine were conducted in 2011. The rotor diameter of the test turbine was 0.9 m and the wind tunnel had a cross-section of 1.8 m x 2.7 m. The blind comparison following the experiments again illustrated the large spread in prediction of the measured power output. The eight participants in the comparison used in total 11 different simulation methods, and uncertainty in the power production was $\pm 10\%$ [13].

Several aerodynamic tools are utilized to estimate the forces in wind tunnel experiments. The methods used to estimate the aerodynamic loads in the wind tunnels includes the BEM method, the vortex method and CFD method [13, 11, 10].

For the design of wind turbines, standards recommend a fully integrated analysis of the wind turbine [14, 15]. Especially for fatigue, an extensive amount of analysis is required. Thus, an important factor for analysing the aerodynamic forces is computational time. A fully resolved CFD computation has a very long computational time, compared to the BEM and vortex method [8]. Consequently, the BEM and vortex methods are commonly used for estimating the aerodynamic loads on an offshore wind turbine design.

Due to the low computational time of BEM method, it is the most common to be implemented in the integrated analysis softwares for offshore wind turbines. A few examples of softwares using BEM as the

aerodynamic model are FAST, HAWC2, Bladed and Flex5 [16]. The BEM method uses the momentum balance of neighbouring annuli of the rotor disc and a blade element representation of the sectional aerodynamics [17]. However, this method has some drawbacks and limitations. It is based on a two-dimensional representation of the airfoils, although three dimensional effects must be accounted for [8]. In addition, the method is based on steady momentum theory, thus the unsteady aerodynamics must be corrected for.

The vortical wake system behind the wind turbine, which is a major source of the three-dimensional nature of the airloads over the disc, cannot be modelled correctly by the BEM codes [8]. This is not an issue in the vortex models because the vortical wake is included as an inherent part of the solution. By including the vortical wake, a better estimate of the unsteady aerodynamics is achieved. Thus a three dimensional vortex model includes both three dimensional effects, unsteady aerodynamics and yawed conditions.

The vortex codes are not as commonly used as the BEM codes. The main drawback for vortex codes is the long computational time, even though it is faster than CFD methods. A few softwares use the vortex methods to predict the aerodynamic loads on a wind turbine, among these are GENUVP (NTUA) [18], AWSM (ECN) [19] and RotorFlow (ECN) [20]. These are all developed at different research institutions specified in the brackets behind their names.

The vortex code can estimate the aerodynamic load in various ways. The blades in AWSM are modelled using a vortex lifting line model [19], while in GENUVP the blades are modelled as thin lifting surfaces [18]. In RotorFlow the flow field along a wind turbine blade is modelled using a panel method flow solver [20]. The lifting line in AWSM is fastest of the three, but the disadvantage is that stall modelling is available. In GENUVP a double wake concept, where the vorticity is shed not only from the trailing edge of the airfoil, but also from the leading edge, enables a simplified stall model. A more advanced technique is used in RotorFlow to model the stall. The flow field in the thin boundary layer near the surface of the wind turbine blade is solved using an integral boundary layer solver.

Other codes often used to study aerodynamic loads, which are not specifically developed for wind turbine simulations, are XFOIL [21] and AVL [22]. XFOIL is a two-dimensional panel vortex code for simulation of steady aerodynamic loads, while AVL is a three dimensional code,

specialized for aerodynamic and flight dynamic analysis of rigid aircraft [22]. Both AVL and XFOIL are developed by Marc Drela and are open source programs.

The main reason for the long computational time is solving the velocities, which is a highly parallel problem. The velocities are estimated using the vortex strengths, which is known for all vortex elements prior to the velocity calculations. Consequently, the different velocities can be computed at once, without waiting for the other velocities to be computed, and is therefore a highly parallel problem. On a computer with more than one core processor, computation of the velocities at the different points can thus be computed in parallel. However, the number of cores in a laptop is limited, and the reduction in computational time is not sufficient to make it comparable with the computational speed of BEM method.

In general, new computational tools will reduce the computational time in the future. More specific, the Graphics Processor Unit (GPU), which is used to accelerate the creation of images and are commonly found in personal computers and workstations, can be used to reduce the computational time of vortex codes. The highly parallel structure of a GPU make it more effective than a general-purpose Central Processing Unit (CPU).

Even though it may be possible to reduce the long computational for vortex codes, another issue is that it is based on potential flow theory. As a consequence, the separation of flow on the airfoil, which gives the dynamic stall effect, can't be modeled. However, there are methods to include this in the vortex codes, but these require more computational time and are often based on empirical theory.

With the vortex code the unsteady aerodynamics is a part of the solution, since the vortical wake is included in the estimation of the aerodynamic loads. The unsteady aerodynamics is due to the induced velocity from the vorticity contained in the shed wake and the induced velocity from the trailing wake. Thus, in BEM codes the unsteady aerodynamics is normally implemented in two steps, one that solves the shed wake and one that solves the trailing wake [8]. The shed wake is the wake shed from the trailing edge, and the trailing wake is shed at the tip of the blade. The shed wake can thus be referred to as the inner problem, while the trailing edge is the outer problem.

The outer problem, in BEM codes, can be modeled using a dynamic inflow model. The inner problem relates to unsteady airfoil dynamics,

which is often related to the dynamic stall of an airfoil. Dynamic stall is related to the detachment of the flow. Previously, especially for stall controlled wind turbines, the dynamic stall received a lot of attention. For example, Øye developed a dynamic stall model, which takes into account the separation at the trailing edge [23]. Currently, large wind turbines currently pitch the blade to control the flow through the rotor and avoid stall conditions. Thus, modern wind turbines operate often in attached flow conditions, which is well predicted by potential theory that the vortex method is based on. A vortex code can therefore be valuable for estimating the aerodynamic loads on modern wind turbines.

The Beddoes-Leishman model is implemented in BEM codes to correct for the unsteady aerodynamics [24]. It corrects for both leading and trailing edge separation, as well as incompressibility effects and unsteady effects for attached flow [25]. For the unsteady attached flow at the airfoil, the method applied in the Beddoes-Leishman model is based on the classic theories for unsteady aerodynamics for attached flow. The most known results are developed by Theodorsen [26], Wagner [27] and Küssner [28]. They are all based on a thin two-dimensional airfoil, incompressible flow and potential flow theory.

The unsteady aerodynamics will influence the dynamics of the wind turbine. For the edgewise vibrations of the blade, the unsteady aerodynamic effects increase the damping [29]. This is however not true for the aerodynamic damping of the modes in the fore-aft direction. A low aerodynamic damping will to a lesser degree limit the response, and increase fatigue damage. Differences in the unsteady aerodynamic model can therefore give differences in the estimated response of a wind turbine.

1.3 Motivation

To improve the cost effectiveness of offshore wind turbines, an accurate dynamic analysis should be performed. Currently, the most common method used in estimating the aerodynamic loads for a wind turbine is the BEM method. This is a method based on a steady momentum condition, and the unsteadiness is included through semi-empirical functions. This study aims to investigate how the time-dependent aerodynamic loads affect a wind turbine structure using both a numerical fluid solver, based on potential flow theory, and an aero-elastic wind turbine code using the BEM method.

1.4 Objective

There are several methods to compute the aerodynamic loads on a wind turbine rotor. As mentioned earlier, the most common method is the BEM method. The advantage of the BEM method is that it has a short computational time. The disadvantage is that BEM is based on steady momentum theory combined with a quasi-static model of two-dimensional airfoils. Since a wind turbine rotor is subjected to unsteady flow, and the flow is three-dimensional, these assumptions are wrong and must be corrected for. Adjustments are normally made to the BEM method to include the effects of unsteady aerodynamics and 3D flow by including semi-empirical functions. Direct numerical simulation methods, such as CFD and vortex methods, can model the unsteady and three dimensional effect. However, these methods are normally not used for engineering analysis due to the long computational time. With the advance of new computational techniques that can reduce their computational time, direct numerical simulation methods, such as the vortex method, to compute the aerodynamic forces should be revisited.

The vortex-based simulations have the advantage of being more closely related to physical laws compared to the BEM method. The vorticity in the wake is taken into consideration when computing the aerodynamic forces on the blade, which will give accurate predictions of unsteady aerodynamic forces. The downside of the vortex method has always been the long computational time of the simulations. As the computational tools have evolved, the speed of computational tools has increased. One of these advances, the GPU, originally developed for the computer gaming industry, can be utilized to reduce the computational cost for highly parallel methods. This study demonstrates that the GPU can significantly reduce the computational cost for high number of panel elements for a panel vortex method.

Furthermore, a two-dimensional vortex code based on potential flow theory can be used to investigate the wind-structure interaction of an offshore wind turbine structure. The excited motion of the wind turbine can be reduced by aerodynamic damping, especially the fore-aft motion of the wind turbine tower can be highly damped. With a decrease in the excited motion, the fatigue life of a wind turbine increases. A correct estimation of response and fatigue therefore requires a good understanding of the aerodynamic damping. One additional effect not taken into account by the current BEM calculations is the effect of the wakes from other blades.

A wind turbine blade is affected by the wake shed by the neighbouring blades, and its own returning wake due to the rotational motion of the rotor. It is shown how this can reduce the aerodynamic damping and have an impact on the fatigue of the wind turbine substructure.

1.5 Thesis Outline

This thesis is an investigation of the analysis tools used for calculating the aerodynamics of an offshore wind turbine. A panel vortex method is developed and application is shown using the structural characteristics of a floating wind turbine. This section gives an outline of the chapters in the thesis.

A general background for the basics of wind turbines is given in Chapter 2, and a more detailed description of the rotor aerodynamics is presented in Chapter 3. This study focuses especially on the analysis tool and aerodynamic loads, thus the state-of-the-art of the present analysis tool for wind turbines is presented here as well.

The background of the vortex theory is explained in Chapter 4. Results indicate that a GPU can be used to reduce the computational speed of the vortex method. A direct numerical simulation tool, based on vortex theory, is developed as a part of the study. Chapter 4 describes the details of the numerical code. It is limited to potential, two dimensional flow theory.

The method is used to study the wind-structure interaction in Chapter 6. Results from the analysis are compared to current BEM models, and are used to investigate the aerodynamical behaviour of the loads for a floating wind turbine in platform pitch mode and the first elastic bending mode of the tower. A simple estimate of fatigue damage of the first elastic tower bending mode illustrates that the fatigue damage can be twice as large as estimated when the neighbouring wakes are not included in the model. However, this is only during specific operational conditions.

Chapter 7 summarizes the conclusions and gives an outlook on the further development of offshore wind turbine analysis codes and offshore wind turbine standards.

Chapter 2

Basics of Offshore Wind Turbine Design

2.1 Introduction

A study of offshore wind turbines is highly multidisciplinary. Aerodynamic loads will act on the wind turbine blade and create torque on the shaft of the wind turbine that creates mechanical energy. A generator is used to turn the mechanical energy into electrical energy. A control system is used to control the energy output and the loads on the wind turbine. Some other factors that contribute to the loads are gravity, waves, current and more. All these elements should be included to give a correct simulation result.

The present study focuses on horizontal axis wind turbines with three blades, as these are the most common wind turbines [30]. The study concentrates on aerodynamics, turbulence and fatigue, and this chapter will give a broader overview of the offshore wind turbine; first some history about the offshore wind industry, then aerodynamics, some basic control theory, offshore wind turbine foundations and basic mechanics.

2.2 History

The offshore wind energy is growing from demonstration projects, and maturing into a modern industry. In the 1970's, during the economic crisis, one was looking at offshore wind as a new way to produce energy. People didn't want to be dependent on the oil harvested by other countries

anymore and wanted to create the energy by themselves [31].

It took 20 years before the first offshore wind farm was constructed. In 1991 the first offshore wind farm, Vindeby, was commissioned [31]. Vindeby is located in sheltered waters off the coast of Denmark, and in the years that followed more wind farms were erected in the sea outside Denmark, Sweden and Netherlands.

Vindeby is located close to shore, only 1.8 km from shore, and at relatively shallow water depth, 2 m - 4 m. The foundations used are gravity based, and the turbine capacity is 0.45 MW. The rotor diameter is 35 m, and a total of 11 wind turbines is installed. The first modern wind farm was Horns Rev. Horns Rev 1 is located 18 km from the western Danish coast, which is not very sheltered. It has a total capacity of 160 MW, and consists of 80 wind turbines. The foundations are monopiles, and the rotor diameter is 80 m.

At the start of 2013, there are more than 1600 offshore wind turbines, with a capacity of almost 5 GW in Europe. Europe has 90 % of the capacity world-wide. In 2012 the capacity was increased with 33 %, 1.2 GW was installed [2]. By 2020 it is projected that 10 000 structures will be installed, producing 40 GW installed power. The oil and gas industry built 700 structures world wide in the last 80 years, so 10 000 structures for the wind energy industry in less than 10 years is a challenge. The wind turbine structures must be based on mass production.

2.3 General Terminology

A wind turbine consists of a topside structure, which is the machinery, and a support structure. The topside structure consists of blades, hub and nacelle, and the support structure consists of a tower, substructure and foundation. The wind turbine nacelle can be rotated around the tower axis, this is referred to as yawing of the rotor. The blades can also be rotated, this is called pitching of the blades. The terminology may vary in the literature, but this is the terminology as used by Germanischer Lloyd [32] and is illustrated in Figure 2.1.

When designing a structure it is important to investigate that its eigenmodes are excited by external forces only to a limiting degree. The elastic eigenmodes of a wind turbine will vary according to the design. For bottom fixed wind turbines, the fore-aft and side-to-side elastic tower bending modes have typically the two lowest eigenfrequencies. The flap motion of the blades will generally follow. However, the drivetrain tor-

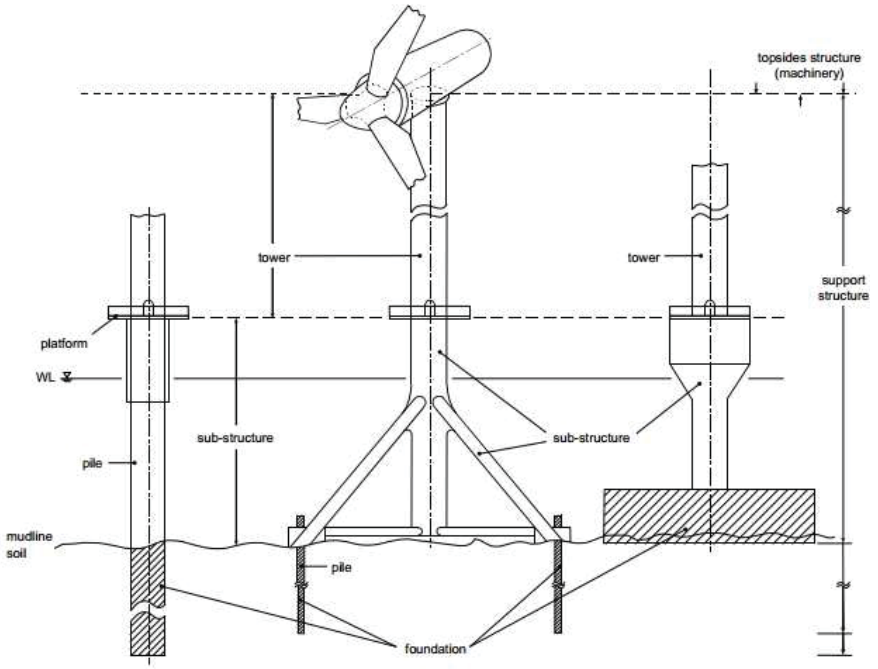

Figure 2.1: Definition of offshore wind turbine sections from Germanischer Lloyd [32].

sion may be somewhere in between the tower and blade-flapping modes. This is very dependent on the drivetrain used. Eigenfrequencies for the first four elastic modes are shown in Table 2.1 for a monopile with a 5 MW wind turbine. A floating wind turbine has six additional rigid body Degree of Freedom (DOF) shown in Figure 2.2. The translational DOFs are surge, sway and heave and the rotational DOFs are roll, pitch and yaw.

2.4 Aerodynamics

A more detailed study of the aerodynamics will be given later, the following section is an introduction only. The wind turbine blades have similarities to the wings of an airplane. The shape of the cross-section is similar, and the pressure difference on the upper relative to the lower surface will create a lift force. The lift force will lift the airplane off the

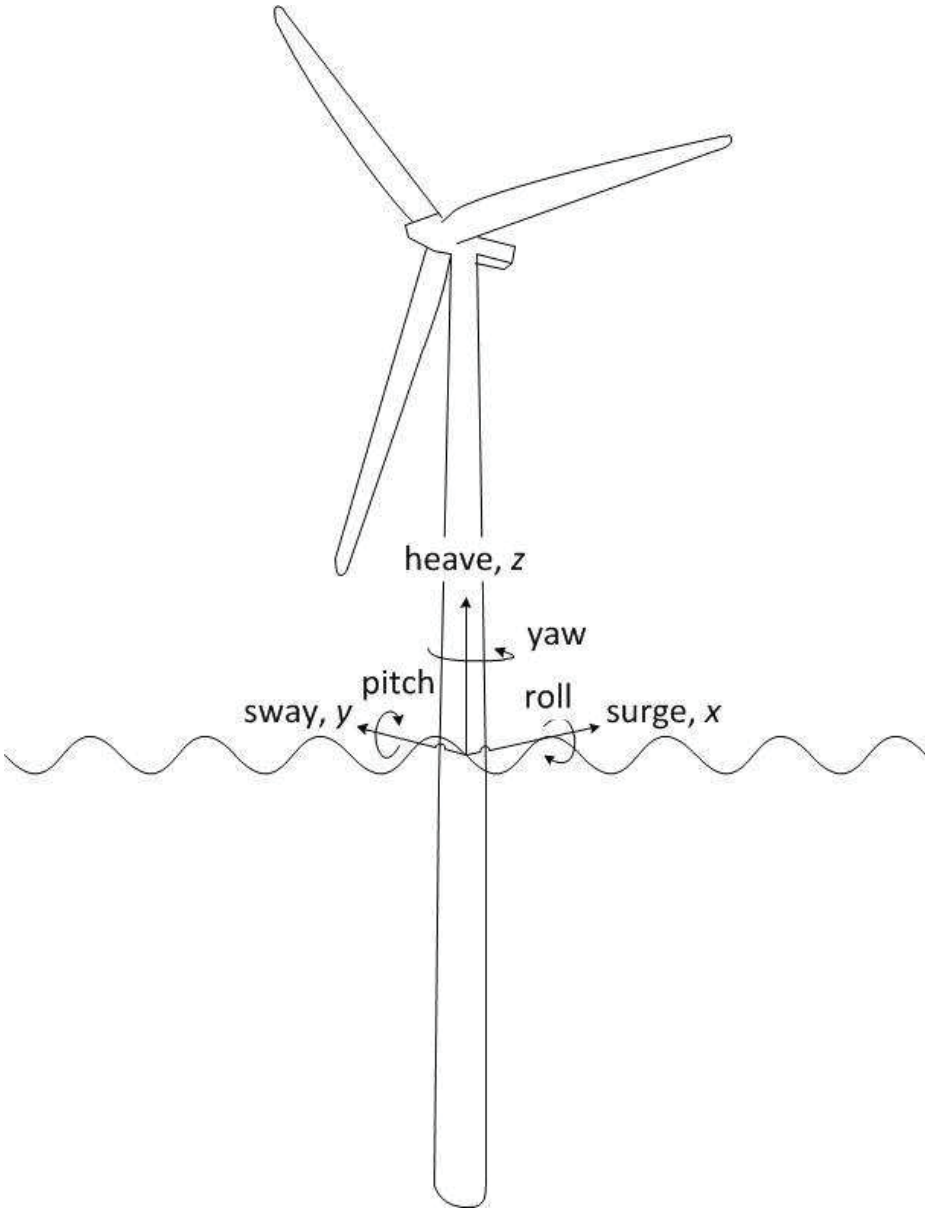

Figure 2.2: Illustration of the OC3 Hywind and its extra rigid degrees of freedom.

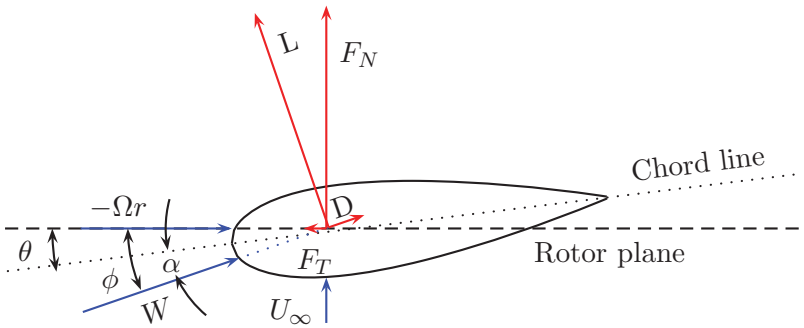

Figure 2.3: The resulting forces on a wind turbine airfoil. 3D effects and induced velocities are not included in this illustration.

ground, and it is primarily the lift component in the rotor plane that make the blades rotate on a wind turbine.

The lift force, L, is perpendicular to the direction of the relative velocity of the incoming wind. The force in the direction of the wind is the drag force, D. The forces are illustrated in Figure 2.3. As seen in the illustration, the lift and the drag force can be decomposed into a normal and a tangential force, F_N and F_T. The tangential force is the force that rotate the blades so that power is produced by the wind turbine.

The angles of the relative wind velocity, shown in Figure 2.3, are important for the loads on the wind turbine. The angle of attack, α, is the angle between the relative wind speed and the chord line of the airfoil. The twist of the airfoil, θ, is the angle between the chord line of the airfoil and the rotor plane. The angle between the relative wind speed and the rotor plane is the flow angle, ϕ. The angles may be changed by actively pitching the blade. This will help controlling the lift force on the blade.

The relative wind velocity, W, consists of the apparent tangential air velocity, Ωr, and the incoming wind speed, U_∞. The tangential velocity is directed opposite of the rotational direction of the wind turbine and Ω is the rotational speed of the wind turbine. Since the rotational speed increases along the span of the blade, the tangential air velocity will vary accordingly. The tangential velocity speed will increase along the blade from the root to the tip. The direction and strength of the relative air velocity, W, will also vary, and the flow angle, ϕ, is decreased from root

to tip if the free stream wind velocity, U_∞ is constant. In order to keep a preferred angle of attack, α, the twist of the blade is often reduced as one moves from root to tip.

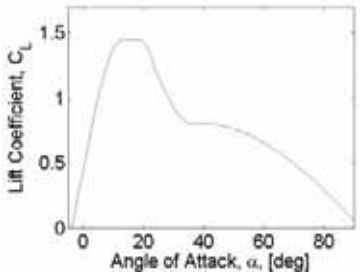

Figure 2.4: An illustration of the lift coefficient for an airfoil at different angles of attack.

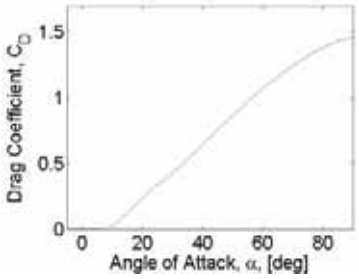

Figure 2.5: An illustration of the drag coefficient for an airfoil at different angles of attack.

The coefficients for lift, drag and moment forces, for two dimensional wing profiles, can be found as tabulated information. The value of the coefficients will vary with the angle of attack. The lift coefficient will typically show an increase with increasing angle of attack for low values of angles of attack, as shown in Figure 2.4. The lift will typically reach a peak, and after this the lift will decrease. This is referred to as the stall limit. The reason for this drop is that the suction at the upper surface of the airfoil drops, as a result of flow separation at higher angles of attack. The flow around an airfoil during attached flow condition and at stall conditions is illustrated in Figure 2.6.

The graphs in Figure 2.4 and 2.5 are valid for stationary flow. The dynamic of the lift and drag forces will be investigated in more details in a later chapter. The drag coefficient is almost zero at low angles of attack, and will have a slow increase as the angle of attack increases, until stall occurs.

2.5 Wind Turbine Control

The objective of the wind turbine control is to optimize the lifetime cost of energy. The lifetime cost of energy is dependent on the investment

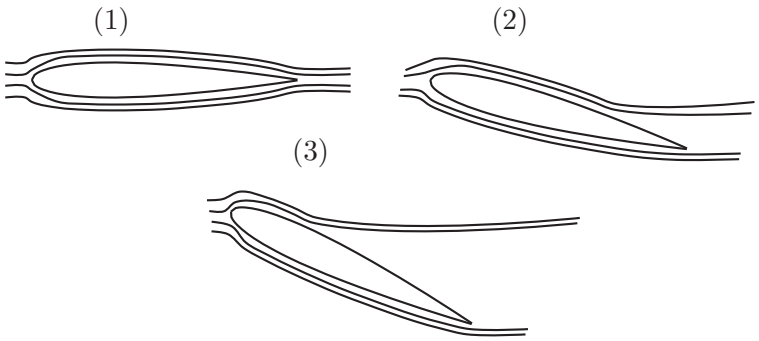

Figure 2.6: A sketch of an airfoil and flowlines during attached flow (1), as the stall limit is been reached (2) and a fully stalled blade (3)

in the wind turbine, the operational cost and the energy captured by the wind turbine. The wind turbine control can reduce the loads, which results in a longer lifetime and less maintenance. This will reduce the investment and operational cost. The power output can be optimized by using the controller to harvest more of the wind energy. However, one can't optimize for both maximizing power output and reducing loads at the same time, so different strategies have to be used for different scenarios.

The strategies for the power control will vary according to the wind speed, and this is illustrated in Figure 2.7. The bold line is the power curve. At wind speeds below a cut-in wind speed and above cut-out wind speed, there is no power production, and these are not shown in the figure. When the measured wind speed is above the cut-in wind speed, the aim of the control system is to maximize the power production until the rated wind speed of the wind turbine is reached. This can be done by having a optimum tip-speed ratio (TSR). Tip speed ratio is the ratio between the velocity at the tip of the blade and the free wind velocity.

At rated wind speed the power output has reached the rated power output of the wind turbine. In situations where the wind speed is above the rated level, lowering the forces on the wind turbine is required. The aim for the control system for these higher wind speeds, is to keep the power production at the rated power output and minimize the loads on the wind turbine.

On a modern wind turbine there are several control systems. The main

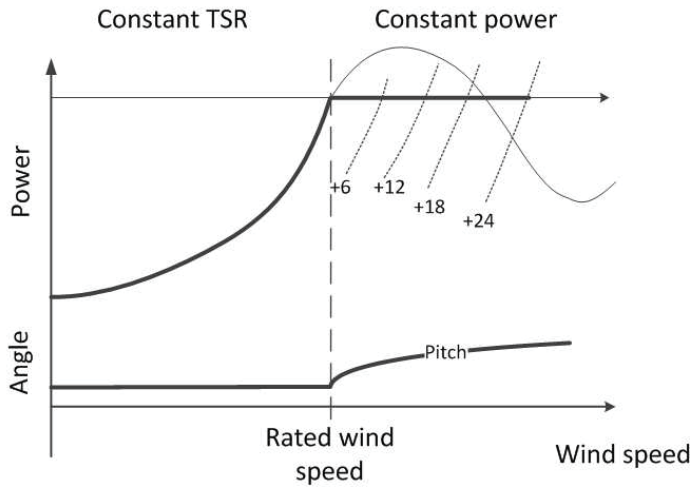

Figure 2.7: A sketched power curve relative to the measured wind speed, which maximizes the power output below rated and reduces the loads on the wind turbine at above rated wind speeds. The effect of the various pitch angles is shown in the region above rated, and the pitch angle is also shown on the lower graph.

control systems are the yaw control, the pitch control and the generator torque control. The yaw control ensures that the rotor plane of the wind turbine is normal to the wind. The speed of the yaw controller is slow compared the the pitch controller. The pitch control changes the pitch of the blades and the generator torque controller regulates the rotor speed. Typical maximum pitch rates for a 5 MW wind turbine is 8 deg/s (0.14 rad/s), which is lower than the first tower bending mode [33].

In Figure 2.2 an overview of the lowest eigenfrequencies of a monopile and a floating wind turbine is shown. Floating wind turbines have frequencies that are lower than the pitch rate, and this needs to be considered when designing the control system.

As mentioned, one can divide the wind turbine control strategy into two main stages for power production, above and below rated wind speed. Below the rated wind speed, the strategy is to maximize the power production. One method to obtain this is to have a constant tip speed ratio (λ_R). The tip speed ratio is defined as the ratio between the rotational speed of the outer tip of the blade and the wind speed:

$$\lambda_R = \frac{\Omega R}{U_\infty} \tag{2.1}$$

where Ω is the rotational speed in rad/s, R is the radius of the wind turbine and U_∞ is the free stream wind speed. The tip speed ratio is kept constant by increasing the rotational speed of the wind turbine as the wind speed increases. The rotational speed is adjusted by the generator torque controller.

Each wind turbine has an optimum tip speed ratio for power production. Figure 2.8 illustrates the power coefficient relative to the tip speed ratio for a wind turbine with optimal power production at $\lambda_R \approx 6$. C_p is the power coefficient and is defined as the relationship between the produced power, P, over the power in the wind:

$$C_p = \frac{P}{1/2\rho A_d U_\infty^3} \tag{2.2}$$

where A_d is the rotor disc area and ρ is the density of the air.

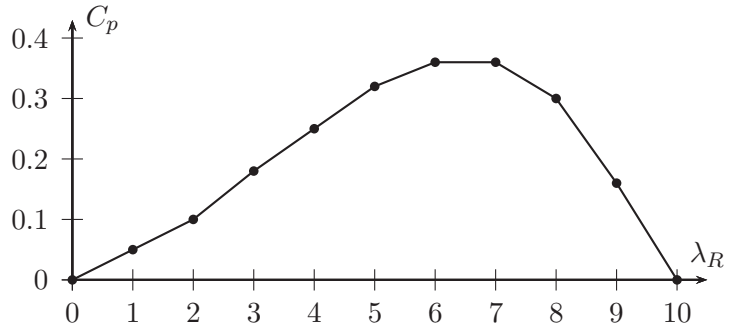

Figure 2.8: The power coefficient as a function of the tip speed ratio, λ_R, for a typical horizontal wind turbine.

Rated wind speed is the wind speed where the power extracted has reached the rated power for the wind turbine design. The aim is to keep the power output at the rated level and alleviate the loads. The rotational speed is kept constant, and the pitch controller is used to alleviate the loads. When the pitch controller changes the angle of the blades, the angle of attack, α is changed to reduce or increase the forces on the blade.

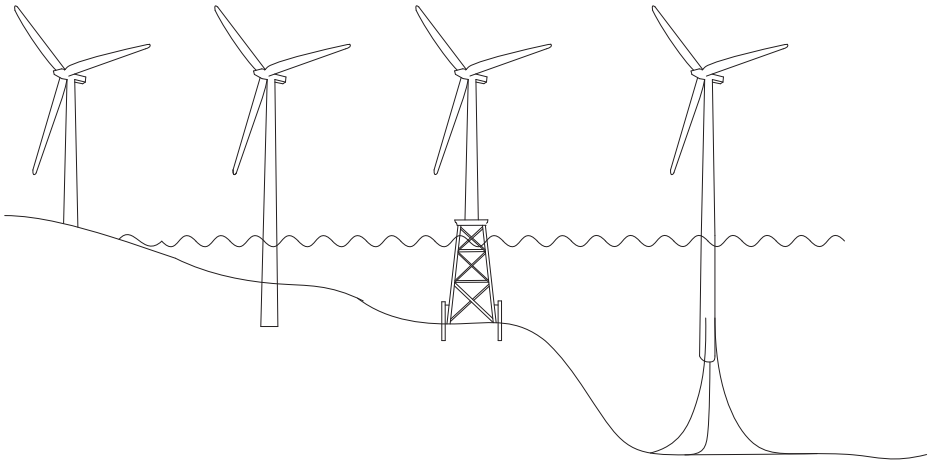

Figure 2.9: Wind turbines with different substructures and at different water depths

2.6 Offshore Wind Turbines

The sub-structures are the area where the offshore wind turbine differs most from the onshore wind turbines. The first offshore wind farm Vindeby in 1991, had concrete foundations, and the remaining part of the wind turbines used were the same as used onshore. These wind turbines were located close to the shore, and in very shallow water [31]. The trend is that the wind turbine are installed in deeper water, and further away from shore. Some of the most common sub-structures and foundations are shown in Figure 2.9.

2.6.1 Fixed Foundations

74 % of the offshore wind turbines today have monopile as foundation [2]. A monopile is basically a steel pipe that is hammered into the sea bed, and the wind turbine is mounted on the top. As the sea depth is increased, the monopile needs to be longer. To maintain the stiffness of the structure, more steel is often added to the structure. There will be a limit where this is economically feaseble. The largest water depth, at which a monopile has been installed is 35 m. Other foundations used for fixed water turbines are gravity based foundations (16 %), jacket (5 %), tripile (3 %) and tripods (2 %). The jacket may provide more stiffness at a lower cost of steel compared to the monopile.

2.6.2 Floating Foundations

Mode	OC3 monopile [Hz]	OC3 Hywind [Hz]
Surge		0.008
Sway		0.008
Heave		0.032
Roll		0.034
Pitch		0.034
Yaw		0.12
1st tower fore-aft	0.25	0.47
2nd tower fore aft	0.25	0.46
1st drivetrain torsion	0.61	0.65
1st blade collective flap	0.70	0.68

Table 2.1: Typical eigenfrequencies of offshore floating wind turbines. The first four elastic modes and the extra rigid degrees of freedom are examplified here using results from the OC3 comparison project [34].

There are very few floating wind turbines in the world. The first floating wind turbine connected to the grid is Hywind. Hywind is a floating wind turbine with a spar buoy type foundation, as illustrated to the right in Figure 2.9. A floating wind turbine will have additional rigid degrees of freedom. For a floating wind turbine similar to Hywind, the additional degrees of freedom will have very low eigenfrequencies. The eigenfrequencies estimated in the code comparison project OC3 are listed in Table 2.1 for a bottom fixed monopile and the floating substructure. Figure 2.2 illustrates the additional floating degrees of freedom for the OC3 Hywind model.

2.7 Mechanics and Dynamics

2.7.1 Introduction

The sources of loads on a wind turbine are several: aerodynamic, gravity, gyroscopic and mechanical control. For an offshore wind turbine, the hydrodynamic loads must also be included. Loads that may arise from these sources are steady, cyclic, transient and stochastic loads. The most important dynamic effect is the resonance response, which is large amplifications of the effects when the the force frequency, ω, is close to the eigenfrequency of the structure, ω_e.

2.7.2 Loads

The wind turbine is subjected to a large variety of loads. It is useful to categorize the forces according to their nature. The variation due to misalignment of the rotor, wind shear and tower interference can be specified as deterministic functions of time, whereas the temporal variation caused by the wind turbulence or wave loadings are introduced in terms of a stochastic model.

2.7.3 Dynamics

The wind turbine can be characterised by stiffness, damping and inertia. The stiffness is from material and soil properties, and the load carrying static system. If it is a floating structure, the buoyancy contributes as a restoring stiffness parameter.

There are several sources of damping; material, soil and aerodynamic damping are together with the control system the most important sources. Viscosity of water, wave radiation and radiation in soil may effect the damping as well. Elements that contributes to the inertia of the wind turbine are the structural mass, the added mass in water and the entrained water mass.

The dynamic effects are important, as it is the structural response to the loading and not the loading itself that drives the design. The natural frequencies of a wind turbine are close to several excitation frequencies, and one must be aware of the danger of resonance response. Resonance happens when the excitation frequency is close to the natural frequency and can give large oscillations. This can lead to fatigue damage, due to the severe cyclic response.

Especially the frequency regions related to the blade rotations, 1P and 3P, should be avoided. 1P is the frequency related to one specific blade passing the tower and 3P is each passing of the tower for one of the three blades. The wind turbines can be classified according to which region relative to 1P and 3P area the eigenfrequency of the first tower bending mode belongs to, this is illustrated in Figure 2.10. If the frequency is lower than 1P it is classified as a soft-soft structure, while a wind turbine with a frequency higher than 3P is stiff-stiff [35].

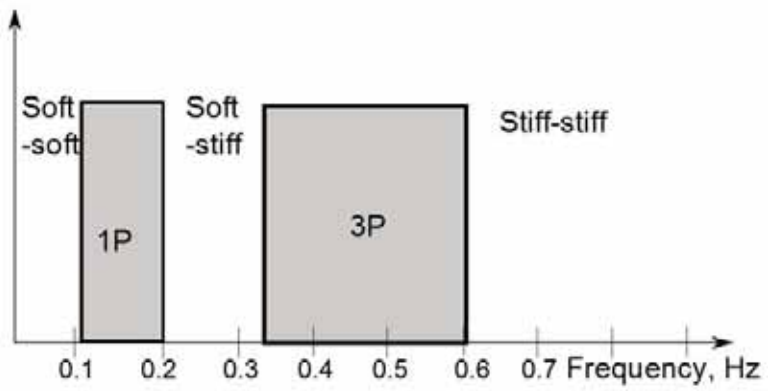

Figure 2.10: Frequency intervals for soft to stiff response of a wind turbine with varying rotational speed. Rotational speed varies from 6.9 to 12.1 rpm and is based on the 5MW reference wind turbine [36].

Others excitation forces that may harm the wind turbine are the wave and wind forces. The turbulent wind has frequencies often lower than the 1P, in the region of the soft-soft structure. The wave spectrum is also mainly in the same region.

2.8 Wind Turbine Analysis Codes

Codes that predict wind turbine structural response and power production need to take a wide variety of elements into consideration. For land-based wind turbines, aero-servo-elastic codes are used, where aero is the part modeling the wind flow and aerodynamics, servo covers the control system and elastic is for the structural-dynamics. As the offshore wind technology is emerging, several of the wind turbine codes includes models

of hydrodynamic forces. If the hydrodynamical models are included, the codes are aero-hydro-servo-elastic. A big effort has been made to compare the newly developed aero-hydro-servo-elastic codes in the Offshore Code Comparison collaborative (OC3) project which was established under IEA (International Energy Agency) Wind Task 23 Subtask 2 [34].

In the final report from the OC3 project, a comparison of the aero-hydro-servo-elastic codes is done, see Table 2.3. In general the results from the load cases run in the OC3 project compared well, but there were some differences. For the aerodynamic loads, it was found that if the wind field was read in polar coordinates, instead of rectangular grid, smoother loads (the peak loads were reduced) were predicted. The discretization of the aerodynamic and hydrodynamic loads gave differences for the calculated loads. Especially the substructure loads were sensitive to the discretization of hydrodynamic loads near the free surface. Another finding was that the shear deflection has a large effect on the distribution of loads for multi-member structures, even for thin and slender structures. This was a finding from the analysis of the structure modelled in Phase III, which is a tripod. Shear deflection is modeled when using Timoschenko beam element, but not with Bernoulli-Euler beam elements.

The OC3 project was divided into four phases, each containing a different support structure for the wind turbine. All phases were run with the 5 MW reference wind turbine developed at NREL [36]. In Phase I and II a monopile in 20 m water was investigated, in Phase I the monopile was modeled as rigid, and in Phase II the monopile was modeled as elastic and soil stiffness was included. The support structure in phase III was a tripod, and the last support structure modeled in Phase IV was a floating wind turbine. The floating structure is similar to the Hywind wind turbine.

As a continuation of the OC3 project the OC4 project is currently ongoing. Phase I with a jacket structure is finished, but there is an ongoing study of another floating wind turbine. The floating wind turbine is similar to Wind Float, and it is expected to have higher contribution of radiation effects (in hydrodynamic loads) relative to the OC3-Hywind wind turbine.

From Table 2.3, it can be seen that the aerodynamic loads are typically predicted by the BEM or Generalized Dynamic Wake (GDW) method by the aero-hydro-servo-elastic codes. Both BEM and GDW will be presented in the following chapter (Chapter 3). The hydrodynamic loads are estimated by the Morison's equation.

	Country	**OC3 participant**
NREL	USA	National Renewable Energy Laboratory
CENER	Spain	National Renewable Energy Centre
DONG	Denmark	Danish Oil and Natural Gas Energy
SWE	Germany	Endowed Chair of Wind Energy of Universität Stuttgart
GH	United Kingdom	Garrard Hassan & Partners Limited
DNV	Denmark	Det Norske Veritas
IWES	Germany	Frauenhofer Institute for Wind Energy and Energy System Technology
Risø	Denmark	Risø national Labratory
Vestas	Denmark	Vestas Wind Systems
Siemens	Denmark	Siemens Windpower

Table 2.2: Full name and country of the OC3 participants

FAST	**FLEX5**	**Bladed**	**Bladed Multi-body**	**ADAMS**	**SIM-PACK**	**HAWC**	**HAWC2**	**BHawC**	**ADCoS-Offshore**
OC3 participant									
NREL + CENER	DONG + SWE + Vestas	CENER + GH	GH	NREL	SWE	DNV + Risø	Risø	Siemens	IWES
Aerodynamics									
(BEM or GDW) + DS	(BEM or GDW) + DS	(BEM or GDW) + DS	(BEM or GDW) + DS	(BEM or GDW) + DS	(BEM or GDW) + DS	(BEM or GDW) + DS	(BEM or GDW) + DS	(BEM or GDW) + DS	(BEM or GDW) + DS
Hydrodynamics									
(Airy$^+$ or UD) + ME	(Airy$^+$, UD or Stream + ME	(Airy$^+$ or Stream) + ME	(Airy$^+$ or Stream) + ME	(Airy$^+$ or UD) + ME	None	(Airy$^+$ or UD) + ME	(Airy$^+$ or UD) + ME	(Airy$^+$ or UD) + ME	(Airy$^+$ or UD) + ME
Control Systems									
DLL, UD, SM	DLL, UD	DLL	DLL	DLL, UD	DLL, UD	DLL, UD	DLL, UD SM	DLL, UD	DLL, UD
Structural Dynamics (elastics)									
FEM^P+ (Modal/ MBS)	FEM^P+ (Modal/ MBS)	FEM^P+ (Modal/ MBS)	MBS	MBS	MBS	FEM	MBS/ FEM	MBS/ FEM	FEM

Table 2.3: An overview of the modelling capabilities for some of the OC4 participants [34]. The full name and country of the participants are given in Table 2.2, and the abbreviations are listed in Table 2.4

ADC	Aero Dynamic Consult Ingenieurgesellschaft mbH
DS	Dynamic Stall
ME	Morison's Equation
GDW	Generalized Dynamic Wake
MSC	MSC Software Corporation
$(Airy^{+}$	Airy wave theory; (+) with free surface connections
FEM^{P}	Finite-Element Method; (P) for mode preprocessing only
SM	interface to Simulink ®with Matlab ®
BEM	blade-element momentum
MBS	Multibody-dynamics formulation
UD	implementation through user-defined subroutine available
DLL	external dynamic link library

Table 2.4: A list of the abbreviations used in Table 2.3

Chapter 3

Rotor Aerodynamics

3.1 Introduction

Aerodynamics is the study of motion of air when interacting with a solid object. The aerodynamic forces acting on the wind turbine blades determine both the power output and the loads on the wind turbine rotor. It is therefore important to have an accurate modelling of the aerodynamic loads. A good model for engineering purposes provides accurate information about expected loads and power output, using a reasonable computational time. Reasonable is a relative term, and it varies according to the application of the program. For fatigue analysis the computational time of the analysis should be far less than the real time period analysed. As an example, a structural analysis of a wind turbine over a simulation time of 10 min, should take less than ten minutes. However, a detailed design analysis is expected to take much more than ten minutes. Reduced accuracy in results is sometimes accepted when the aim is to reduce the computational time.

There are several methods to estimate the aerodynamic forces on the wind turbine rotor. The most common methods used are the Beam Element Momentum (BEM) method and the Generalized Dynamic Wake (GDW) method. Other methods that are important are the vortex method and computational fluid dynamics (CFD). CFD will not be presented in details as this is not a common tool for engineers and is used mainly by blade designers, who need to do more specific studies. The main reason that CFD is not used more extensively is that the computational time is very long.

In this chapter, the main focus is on the BEM method and how it

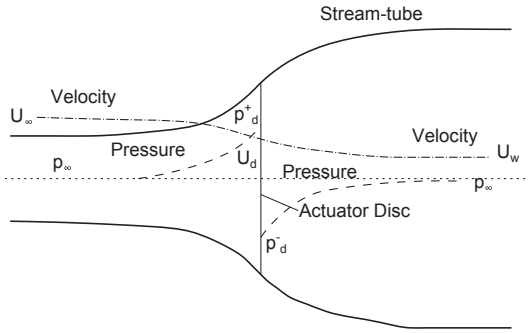

Figure 3.1: One dimensional flow model used for the momentum analysis of a wind turbine rotor.

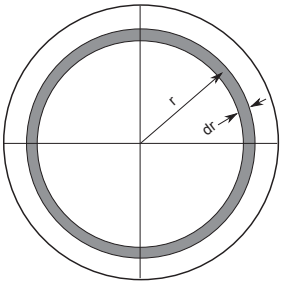

Figure 3.2: Cross sectional view of the annulus of the rotor disc.

is used in wind turbine rotor analysis. First, a linear one dimensional momentum analysis of the wind turbine rotor is presented, thereafter the circulation theory of lift is explained. The basics of the BEM method, with main results such as the Betz limit, are explained. The wind turbine operates in an unsteady environment, while BEM is developed for steady conditions. The unsteadiness is normally included in the BEM code using a semi-empirical function that is based on thin-airfoil theory, and a small discussion of this is included at the end of the cahpter.

3.2 Momentum Analysis

The linear momentum (or translational momentum) is defined as mass times velocity in classical mechanics. The linear momentum is a conserved quantity, and from this it follows that the total linear momentum of a closed system does not change if it is not subjected to any external forces.

A simple flow model that illustrates the momentum analysis of a wind turbine in one dimension is shown in Figure 3.1. The stream tube shown in the figure illustrates the stream line that is tangential to the instantaneous velocity direction. The flow velocity decreases from the start at the inlet and towards the wake while the pressure increases from the inlet towards the disc, where it has a large drop in magnitude. The pressure level at the outlet in the wake and at inlet, is the same atmospheric pressure.

The momentum analysis of a wind turbine rotor is similar to the momentum method used for a helicopter in descent [17]. The main difference

is that for a helicopter the rotor thrust is an input to the analysis. The thrust force is the force normal to the rotor, and for the helicopter in descend it should be equal to the weight of the helicopter. For a wind turbine the thrust load will give a large overturning moment of the tower base.

The thrust force on a wind turbine rotor, can be calculated using a combination of inputs from airfoil data, wind speed, rotor speed (rpm) and the pitch of the blades. One can't estimate the thrust force by only applying the momentum analysis, it needs to be combined with other theories as well. A common approach is to combine the momentum analysis with a blade element theory and predefined aerodynamic airfoil characteristics. This is known as the BEM method, and will be presented later, in section 3.4.

However, using the momentum analysis one can establish relations for mass flow, thrust and power. These are all explained in the following sections, together with the Betz limit for the power and the limitations of the momentum theory.

3.2.1 Mass Flow

By the conservation of mass within the stream tube, the mass flow rate must be the same at the inlet, at the rotor disc and at the outlet;

$$\rho A_{in} U_\infty = \rho A_d U_d = \rho A_w U_w \tag{3.1}$$

At the rotor disc the velocity of the incoming wind is lower than the free stream velocity. The reduction in velocity at the rotor disc is the induced velocity, a. The velocity at the rotor disc, U_d, is written as $U_\infty - a$. If one only considers the shaded area of the cross sectional area, with width dr in Figure 3.2, the mass differential flow rate is:

$$d\dot{m} = \rho U_d dA \tag{3.2}$$

where dA is the shaded area of the cross sectional area, $dA = 2\pi dr$.

3.2.2 Thrust

The thrust is the force normal to the wind turbine rotor. According to the conservation of fluid momentum:

$$\vec{F} = \iint_S p d\vec{S} + \iint_s (\rho \vec{V} \cdot d\vec{S})\vec{V} \tag{3.3}$$

where $d\vec{S}$ is a unit vector normal to the surface surrounding the wind turbine rotor and $\vec{V}$ is the velocity vector of the fluid. The stream tube and the inlet and outlet areas together make a surface surrounding the wind turbine rotor (see Figure 3.1). In an unconstrained flow the net pressure is zero, so the first term of the equation is zero. It is assumed that there is a uniform pressure drop across the rotor disk, which is true for quasi-static one-dimensional flow. As a result the velocity distribution across any vertical cross section within the control surface is uniform, e.g. the velocity across the inlet disc area is uniform. The force in axial direction, the thrust force, can now be calculated based on the change in momentum of the flow across the disc. Assuming that the velocities in the wake and in the free stream are known, the thrust force is:

$$T = \dot{m}U_\infty - \dot{m}U_w = \dot{m}w \tag{3.4}$$

where w is the velocity deficit in the wake.

3.2.3 Power

The main task of a wind turbine rotor is to capture the energy in the wind, and convert it to electrical energy. The total kinetic energy in the wind, with velocity U_∞ is:

$$KE = \frac{1}{2} m U_\infty^2 \tag{3.5}$$

Power is defined as the energy per unit time, and the available power, P_{avail}, in the wind is thus:

$$\begin{aligned} P_{avail} &= \frac{KE}{dt} = \frac{1}{2}\dot{m}U_\infty^2 \\ &= \frac{1}{2}\rho A_d U_\infty^3 \end{aligned} \tag{3.6}$$

The wind turbine will extract less than half of the total energy in the wind. An energy balance of the system in Figure 3.1 shows that the work done on the wind per unit time by the turbine rotor is:

$$\begin{aligned} P &= \frac{1}{2}\dot{m}U_\infty^2 - \frac{1}{2}\dot{m}U_w^2 \\ &= \frac{1}{2}\dot{m}U_\infty^2 - \frac{1}{2}\dot{m}(U_\infty - w)^2 \\ &= \frac{1}{2}\dot{m}w(2U_\infty - w) \end{aligned} \tag{3.7}$$

This approach assumes no viscous or other "non-ideal" losses at this stage, and that all work done on the flow to change the kinetic energy is extracted by the wind turbine.

3.2.4 Betz limit

The power can also be expressed as the thrust multiplied with the velocity of the wind at the rotor disc. As shown in Equation 3.4, the thrust can be expressed as a function of the wake velocity deficit. By combining the equations established for power and thrust, a relation between the wake deficit, w, and the induced velocity at the rotor disc, v_i is found:

$$\begin{aligned} P = TU_d &= \frac{1}{2}\dot{m}w(2U_\infty - w) \\ \dot{m}w(U_\infty - v_i) &= \frac{1}{2}\dot{m}w(2U_\infty - w) \\ U_\infty - v_i &= -\frac{1}{2}w + U_\infty \\ w &= 2v_i \end{aligned} \tag{3.8}$$

The induced velocity of the rotor is thus half the deficit of the wake. Using this relation together with the mass flow definition, the thrust can be written, using the induced velocity at the rotor:

$$T = 2\rho A(U_\infty - v_i)v_i \tag{3.9}$$

and the power:

$$P = 2\rho A(U_\infty - v_i)^2 v_i \tag{3.10}$$

The induction factor, a, is the relationship between the induced velocity and the wind velocity: $a = v_i/U_\infty$. The thrust coefficient, C_t and

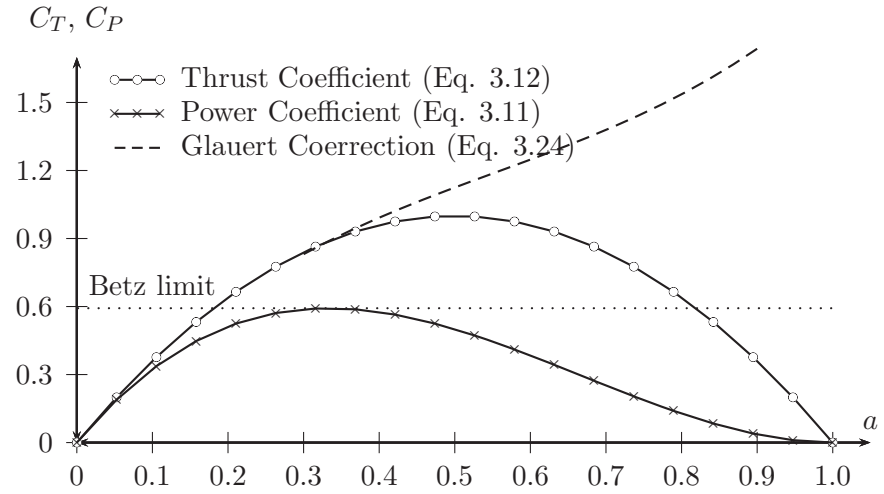

Figure 3.3: The power and thrust coefficient plotted as a function of the induction factor. Glauert correction is used for $a > 0.5$.

the power coefficient C_p, will vary relative to the induction factor. The power coefficient, defined in Eq 2.2, becomes:

$$C_p = \frac{2\rho A_(U_\infty - v_i)^2 v_i}{1/2\rho A_d U_\infty^3} = 4(1-a)^2 a \tag{3.11}$$

The thrust coefficient is similarly defined as:

$$C_t = \frac{2\rho A(U_\infty - v_i)v_i}{1/2\rho A_d U_\infty^2} = 4(1-a)a \tag{3.12}$$

The power coefficient, C_p, and the thrust coefficient, C_t, relative to the induction factor, a, are plotted with circles in Figure 3.3 for illustration. The simple momentum method is not valid for induction factor above 0.5 and Glauert's correction is used for higher values of the induction factor. The dotted line is plotted using Glauert's correction for the thrust force, which is presented in section 3.4.2.

The maximum power is extracted from the wind when the induction factor is one third, $a = 1/3$. This gives a power coefficient of 0.59. This limit for the power coefficient is known as the Betz limit, and is a value based on no viscous or other losses. The values are in practice much lower, and a maximal C_p between 0.4 and 0.5 are typical for a modern wind turbine [17].

3.2.5 Effects of rotation

So far, an ideal rotor with no rotation in the wake has been assumed. In reality the wind turbine rotor will cause the air to rotate in the opposite direction of the rotor. In Figure 3.4, it is illustrated how the tangential velocity grows across the rotor disc. The change in velocity takes place across the rotor disc, and it assumed that the rotation remains constant as the air is moving down in the wake. A tangential component in opposite direction of the rotor motion is shown, where a' is the tangential induction factor. The flow angle, ϕ, is now defined as:

$$\tan(\phi) = \frac{(1-a)U_\infty}{(1+a')\Omega r} \tag{3.13}$$

The aim of the wind turbine is to produce power. It can be shown that the aerodynamic conditions for the maximum power production is:

$$a' = \frac{1-3a}{4a-1} \tag{3.14}$$

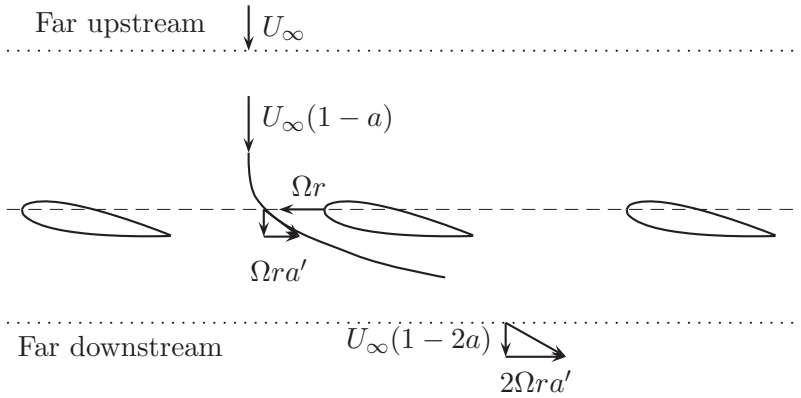

Figure 3.4: An illustration of velocities at a radial distance r from the center of the hub. The tangential velocity at the rotor disc, which is the sum of apparent velocity due to the rotational velocity, Ωr, and the induced tangential velocity, a', will grow across the rotor disc.

3.2.6 Limitations

The momentum analysis is only valid when the induction factor is lower than 0.5. If the induction factor exceeds 0.5, the wake would have negative velocity since $U_w = U_\infty(1-2a)$. For higher induction factors, empirically fitted values must be used, these are not shown here.

The momentum theory assumes that linear momentum is balanced in a plane parallel to the rotor. Large deflections of the plane may lead to errors in the aerodynamic modelling. Such deflections may occur due to misalignment of the wind turbine rotor relative to the wind direction. If the misalignment is in the horizontal plane, it is referred to as yaw error.

3.3 Aerodynamic Forces

The aerodynamic forces on the wind turbine airfoils can either be modeled directly or found in predefined tabulated values. The tabulated values have the obvious advantage of being fast to utilize, the downside is that these are values based on steady aerodynamics and are measured without the three dimensional effects in the spanwise direction that are typical for the wind turbine blades at the tip and the root sections. The tabulated values are therefore considered to be two-dimensional.

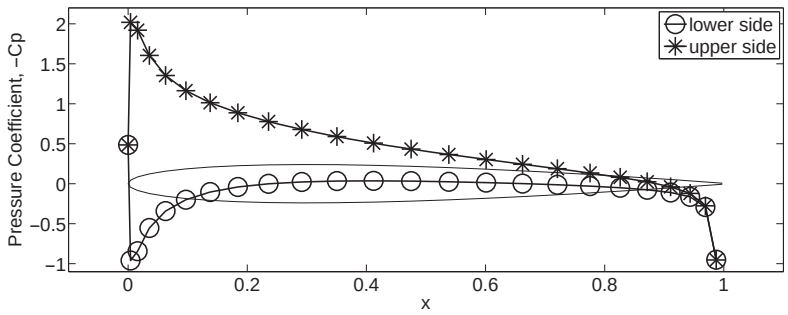

Figure 3.5: Pressure distribution around a NACA 0012 airfoil at 5^o angle of attack.

One method for estimating the aerodynamic loads, without using tabulated values, is the vortex theory, the method will be presented briefly here to illustrate how the lift is generated on the airfoil. The theory of the vortex theory is presented in Chapter 4. The lift can be computed by using other methods such as CFD, but this is not included here. In

Figure 3.5 the pressure distribution around an airfoil is shown. The pressure distribution in Figure 3.5 is calculated for a NACA 0012 airfoil with an angle of attack of 5^o.The difference in the pressure on the lower side relative to the upper side of the airfoil, is creating the lift force on the airfoil.

3.3.1 Blade Element Theory

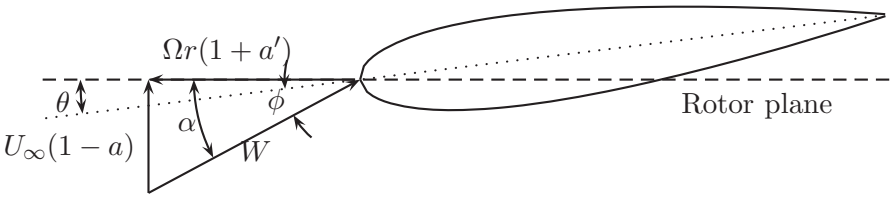

Figure 3.6: An illustration of the velocities at an airfoil. The airfoil is twisted with and angle θ relative to the rotor plane.

The tabulated lift, drag and pitching moment coefficients; C_L, C_D and C_M, can be used to calculate the forces on a blade element. It is assumed that there is no flow in the span-wise direction, and other three dimensional effects are ignored. The lift, drag and pitching moment forces per unit length are associated with the aerodynamic coefficients as:

$$L = 1/2\rho W^2 c C_L \tag{3.15}$$
$$D = 1/2\rho W^2 c C_D \tag{3.16}$$
$$M = 1/2\rho W^2 c^2 C_M \tag{3.17}$$

where c is the chord length, W is the wind speed relative to the blade illustrated in Figure 3.6, and for the wind turbine blade it is combination of the free wind speed, U_∞, and the apparent rotational speed, Ωr, at the blade section. The lift drag and momentum acts is normally defined to act at a point $c/4$ from the leading edge. This is the aerodynamic center for a flat plate, which is defined as the point where the pitch moment coefficient does not vary with the angle of attack.

3.4 Blade Element Momentum Theory

The blade element momentum theory (BEM) is the most common aerodynamic analysis approach. It is based on the assumption that the force of the blades are the only contributor to the change in momentum over the rotor. The thrust on an annulus of the rotor disc can be expressed by the momentum theory, see Figure 3.2 and Equation 3.9. For an incremental section of the rotor, with the area $2\pi r dr$, this is written as:

$$\begin{aligned} dT &= 2\rho 2\pi r dr(U_\infty - v_i)v_i \\ &= 4\pi\rho U_\infty^2 a(1-a)r dr \end{aligned} \tag{3.18}$$

where a is the induction factor defined as the relationship between the induced velocity and the free stream velocity, and is a function of r. The induction factor, a, can be estimated by using the information from the airfoil characteristics and the velocities; wind speed and rotational speed. The force in axial direction due to the aerodynamic loads on the blades is:

$$\begin{aligned} dF_x &= dL\cos\phi + dD\sin\phi \\ &= 1/2\rho W^2 N_b c(C_L\cos\phi + C_D\sin\phi)dr \end{aligned} \tag{3.19}$$

where dL and dD are the aerodynamic forces on the incremental area, using Equations 3.15 and 3.16. The incremental area is here an incremental radial length, dr, multiplied by the number of blades, N_b. ϕ is the flow angle and W is the relative wind velocity, as shown in Figure 2.3.

$$W = \sqrt{(U_\infty \cdot (1-a))^2 + (\Omega r \cdot (1+a))^2} \tag{3.20}$$

As mentioned earlier, the BEM theory assumes that the aerodynamic forces are the only contributors to the change in momentum. The force in the axial direction, dF_x, due to aerodynamic loads (Eq. 3.19), is equivalent to the thrust force, dT (Eq. 3.18). By using this relation one can establish the induction factor along the blade:

$$
\begin{aligned}
4\pi\rho U_\infty^2 a(a-1)r\delta r &= 1/2\rho W^2 N_b c(C_L\cos\phi + C_D\sin\phi)\delta r \\
4a(a-1) &= \frac{N_b c}{2\pi r}\left(\frac{U_\infty^2(1-a)^2 + \Omega^2 r^2}{U_\infty^2}\right) C_x \\
4a(a-1) &= \sigma_r\left((1-a)^2 + \frac{(1-a)^2}{\tan^2\phi}\right) C_x \\
\frac{4a}{(a-1)} &= \frac{\sigma_r C_X}{\sin^2\phi}
\end{aligned} \tag{3.21}
$$

where $C_x = (C_L\cos\phi + C_D\sin\phi)$ and σ_r is the chord solidity defined as $\sigma_r = \frac{N_b c}{2\pi r}$.

In the BEM method shown here, the rotational induction factor a' is not included, and only considered the axial induction factor. In modern version of the BEM methods, both the axial and rotational induction factors are included.

3.4.1 Tip-Loss Factor

At the tip region of the blades, trailing vortices will be present. These are also known as wing-tip vortices. The same trailing vortex can be found at the end of the airplane wings, where winglets are sometimes used to reduce the kinetic energy in the circular airflow leaving the tip of the wing. An illustration of trailing vortices are shown in Figure 3.7, showing the pressure difference which is the driving force of the generation of vortices. The trailing vortices will create high local inflow at the tip region and this is normally referred to as the tip loss. The trailing vortex at the end of a wing with winglets, has a velocity from the lower surface, but will strike the winglet instead of the upper surface of the wing. For an airplane this will give a beneficial increase of thrust force.

The tip loss can be defined as the high local inflow that is produced at the tip region of the blade due to the trailing vortices at the tip. The lifting capacity at the tip region is reduced due to the local inflow from the vortices. One method commonly used in both helicopter and wind turbine analysis to include the tip-loss effect was developed by Prandtl. Prandtl's tip loss function, $F_p(r)$, has a unit value at the inner parts of the blade, and in the tip region it tends to zero. The function is illustrated in Figure 3.8 for a 5 MW reference wind turbine [36].

The tip loss is included in the momentum analysis be multipling the thrust force with the Prandtl function. Equation 3.12 now becomes:

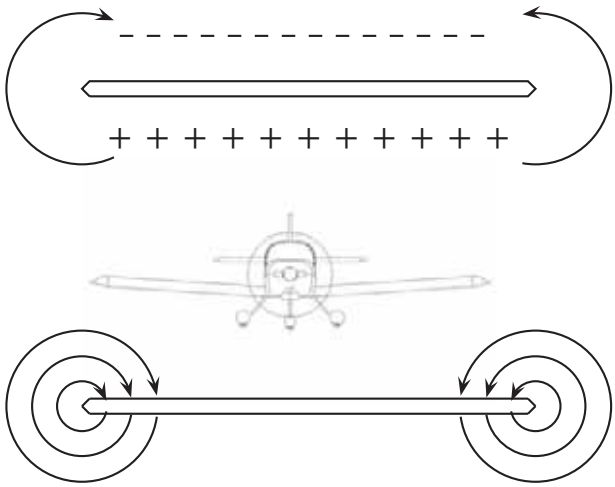

Figure 3.7: The pressure distribution along the full span of a wing (top wing) creates high local inflow at the tip (bottom wing).

$$C_t(r) = 4F_p(r)(1-a)a \tag{3.22}$$

Prandtl's tip loss function, as a function of the distance along the blade is [17]:

$$F_p(r) = \frac{2}{\pi}\cos^{-1} e^{-f_p(r)} \tag{3.23}$$

where $f_p(r) = N_b/2[(1-r)/(r\phi)]$, where N_b is the number of blades and ϕ is the flow angle. The induced velocity over the tip region is reduced when the Prandtl's tip-loss function is implemented. The force in along-wind direction along the blade will be reduced as shown in Figure 3.9 for a 5 MW reference wind turbine blade [36] and 10 m/s wind speed.

The Prandtl's tip-loss correction function, $f_p(r)$, increases with the number of blades. If the number of blades tends to infinity, then the tip

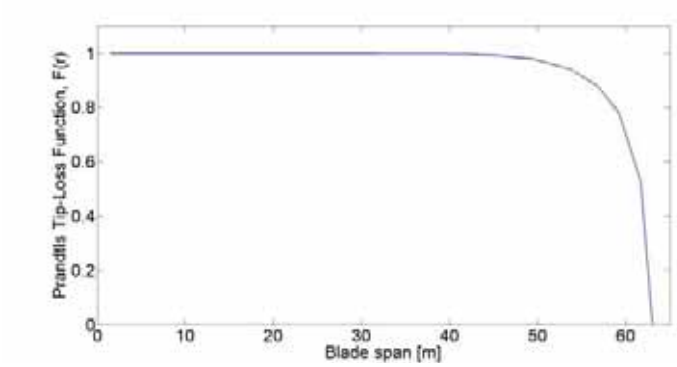

Figure 3.8: The Prandtl's tip loss function (see Eq 3.23) along the span of a wind turbine blade. The wind turbine blade of the 5 MW reference wind turbine [36].

loss correction factor, $F_p(r)$, approaches one at all points along the blade. This corresponds to no tip loss.

3.4.2 Glauert Correction

The simple momentum equation breaks down when the axial induction factor becomes large. This is often a problem at low wind speeds. An empirical relation between the thrust coefficient and the induced velocity is made to fit experimental data.

$$C_t = \begin{cases} 4a\left(1-a\right)F_p & a \leq 1/3 \\ 4a\left(1-0.25(5-3a)a\right)F_p & a \geq 1/3 \end{cases} \tag{3.24}$$

This correction is shown in Figure 3.3.

3.4.3 Unsteady Aerodynamic Models

The BEM method is based on steady aerodynamics, but the wind turbine can be subjected to unsteady aerodynamics. The shear in the incoming wind, the effect of yaw misalignment of the turbine, ambient turbulence, blade flapping, tower shadow are some of the sources that may contribute to unsteady aerodynamic conditions for the wind turbine rotor [8]. Most BEM codes include the unsteady aerodynamics by adding a semi-empirical function to the aerodynamic calculations. Modelling the

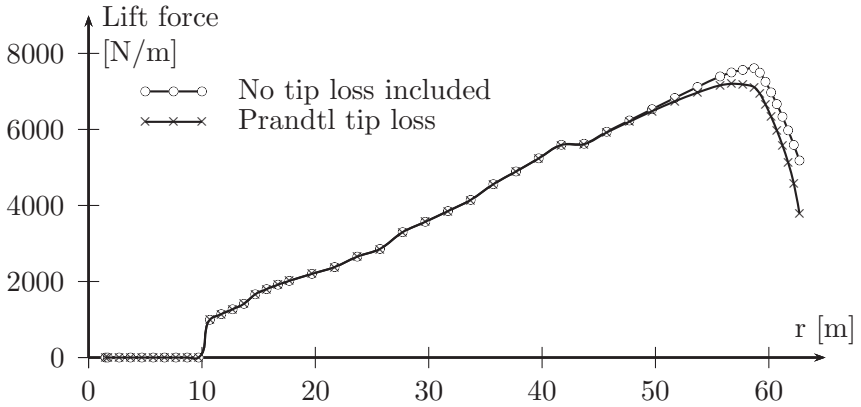

Figure 3.9: The lift force along the blade calculated with Prandtl tip-loss. The wind turbine blade of the 5 MW reference wind turbine [36] is used for illustration and with a wind speed of 11 m/s.

unsteady effects is important due to the presence of turbulence, transient load situations and high effective reduced frequencies that wind turbines may be exposed to. A more detailed description of the theory of unsteady aerodynamics is given in Section 3.6 and in Section 4.4.3.

3.5 Generalized Dynamic Wake

The Generalized Dynamic Wake (GDW) model is often referred to as the acceleration potential method. It is based on the work by Carpenter and Fridoich [37] from 1953. They developed a dynamic inflow model, where the unsteady aerodynamic of the inflow is considered relative to the blade pitch and the change in rotor thrust [8]. The principle of the method can be shown using an appearent mass, m_a [37]:

$$T = m_a \dot{v}_i + \rho A_d v_i \left(v_i - w + \frac{2}{3} \dot{\beta}_f R \right)$$

where T is the thrust force, v_i is the axial induced velocity, w is the tangential induced velocity, A_d is the area of the rotor disc, ρ is the air density, $\dot{\beta}_f$ is the velocity of the blade flapping angle and R is the radius of the rotor. The flap angle, β_f, is the angle between the blade and the rotor plane. The apparent mass analogy assumes that the apparent force on a solid disc is equal to the force on a fluid accelerating through a permeable actuator disc [8].

This method allows a more general distribution of the pressure across the rotor plane compared to the uniform pressure drop of the momentum theory. The method is based on a potential flow solution of the Laplace equation and was developed for lightly loaded rotors and it is assumed that the induced velocity is small compared to the mean flow. Kinner [38] developed an expression for the pressure field in the vicinity of an actuator disc. Peters and others have done much work to develop this method further [39] [40] [41]. The most commonly used GDW model for helicopter and wind turbine aerodynamics is the model by Pitt & Peters [8].

The advantage of the GDW method is the inherent modelling of dynamic wake effect, the tip loss and the skewed wake aerodynamics. The computational time is relatively low, and can be faster than the momentum theory [42]. Similarly to the momentum theory, the GDW is often coupled with the beam element method to estimate the aerodynamic loads of the rotor.

The GDW is limited to lightly loaded rotors, and assumes small induced velocities relative to the mean flow. At low wind speeds the induced velocities are larger relative to the mean flow, and the GDW method should therefore be used with care [42].

3.6 Unsteady Aerodynamics

The wind turbines are subjected to unsteady aerodynamics as mentioned in section 3.4.3. At the blade element level the term unsteady aerodynamics is often considered to be synonymous with dynamic stall. Dynamic stall is an unsteady effect of the aerodynamic stall, which is shown in Figure 2.6. Dynamic stall typically exhibits a higher force than the stall in a stationary flow. In addition to dynamic stall, there are unsteady aerodynamics effects related to the attached flow conditions.

The unsteady aerodynamics, for attached flow, is characterised by the nearby shed wake and the apparent mass. For the steady aerodynamics the nearby shed wake is constant and does not influence the aerodynamic forces. In this section the focus will be on the challenges related to modelling the attached flow conditions in time domain computation.

3.6.1 Thin airfoil theory

A solution to the unsteady aerodynamic force for a thin plate provided by Theodorsen in 1935, and a detailed description to the approach is presented in Section 4.4.3. Theodorsen introduced a transfer function, $C(k)$, between the imposed motion (angle of attack) and the induced forces (lift and pitch moments). The solution was based on an airfoil in harmonic oscillating motion. The unsteady loads were divided into circulatory loads and non-circulatory loads, where only the circulatory loads are dependent on the frequency of the motion.

In this chapter we will concentrate on a solution that can be used in time-domain, which is useful for aeroelasticians investigating phenomena such as rapid maneuvers and gusts. By taking the inverse Fourier transform of the circulatory loads from Theodorsen, one can get a solution in time-domain. The analytical solution is complex, so approximations are often applied. An approximation that can be Laplace transformed, can easily be used in linear time domain analysis.

3.6.2 Time domain

The Duhamel's integral is often used as a tool to describe the circulatory lift contribution of the attached flow unsteady aerodynamics. In the multi-body aeroelastic simulation tool HAWC2, the unsteady lift from attached flow is described as [43]:

$$\begin{aligned} L &= \pi\rho\frac{c^2}{4}\left(U\dot{\alpha} + \dot{U}\alpha + \ddot{h}_{1/2}\right) \\ &\quad +\pi\rho cU\left(w_{3/4}(0)\phi_i(s) + \int_0^s \frac{dw_{3/4}}{d\sigma}\phi_i(s-\sigma)d\sigma\right) \end{aligned} \tag{3.25}$$

where the first term of the equation is related to the non-circulatory loads and the second term is the circulatory loads, U is a time-varying free stream velocity, $\dot{()} \equiv \partial/\partial t$, $w_{3/4}$ is the downwash, which is the induced velocity in vertical direction at 3/4 chord from the leading edge, c is the chord length, $\ddot{h}_{1/2}$ is the plunge acceleration at the mid-chord, ϕ_i is the indicial function, and is presented in more detail in the following section, and s is a dimensionless time-scale:

$$s = \frac{2}{c}\int_0^t U dt \tag{3.26}$$

Equation 3.25 is similar to the Theodorsen's equation (see Eq 4.78), only the acceleration term of the α is different. The acceleration is here replaced with $\dot{U}\alpha$. The acceleration term of both α and h is however regarded as an order lower in magnitude compared to the velocity term, $U\dot{\alpha}$ for moderate frequencies, and is ignored in the HAWC2 computation.

The second term of Equation 3.25 is the circulatory lift. This is expressed using the Duhamel's integral:

$$y(t) = f(0)\phi_i(t) + \int_0^t \frac{df}{dt}\phi_i(t-\sigma)d\sigma \tag{3.27}$$

This approach, with using the Duhamel's integral function to include the unsteady circulatory loads is a common approach both for helicopter rotors and for wind turbine rotors. A detailed description of the approach is given by Leishman [17]. The missing factor is now the indicial function, ϕ_i. To save computational time, these can be approximated by:

$$\phi_i(s) = 1 - A_1 e^{-b_1 s} - A_2 e^{-b_2 s} \tag{3.28}$$

3.6.3 Indicial solutions

The unsteady aerodynamic of a wind turbine is highly complex, and the main sources are the blade motion and the flow field. The blade motion consists of both flapping and pitching. The flapping is due to bending of the blade, and the pitching is mainly due to the control system.

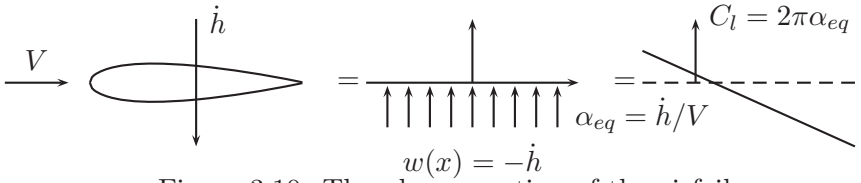

Figure 3.10: The plunge motion of the airfoil

As mentioned previously, the unsteady aerodynamic forces are motion dependent. This can be illustrated by showing the plunging motion in Figure 3.10, the vertical velocity and the lift coefficient, and comparing this to the angular velocity motion in Figure 3.11. Therefore, different indicial functions are developed for different motions. Two of the most commonly used indicial functions will be presented in the following, the Wagner function and the Küssner function.

Wagner's problem is described as:

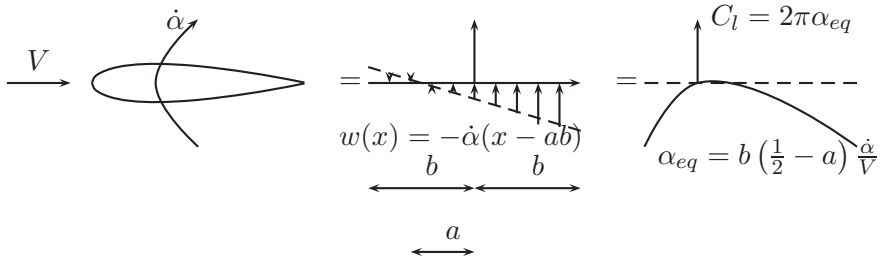

Figure 3.11: Angular pitch velocity of a thin plate

$$w_{3/4} = \begin{cases} 0, & t < 0, \\ -U\alpha, & t > 0. \end{cases} \tag{3.29}$$

This is often referred to as the step change in angle of attack, and can be solved analytically. However, as mentioned before, a solution that can easily be Laplace transformed and included in a linear analysis is normally used. An approximation given by R.T. Jones in 1940 for the Wagner function is [44]:

$$\phi_w(s) \approx 1.0 - 0.165e^{(-0.041s)} - 0.335e^{(-0.32s)} \tag{3.30}$$

The circulatory lift, L_c, due to the step angle of attack is:

$$L_C(s) = 2\pi\rho U^2 b\alpha_0\phi_w(s) \tag{3.31}$$

Using this approach, the Wagner function describes the change in lift as a thin-airfoil undergoes a transient step change in angle of attack in an incompressible flow.

If the airfoil is entering into a sharp-edged vertical gust, the Küssner function should be applied. This is different from the change in angle of attack that was solved by Wagner, which will describe both pitching and plunging motion of a wind turbine blade well. In Küssner problem the quasi-steady angle of attack changes progressively as the airfoil enters the change of the vertical velocity, and this can for example be used to model the blade passing the tower or wind gusts.

Küssner function, $\psi_k(s)$, can be approximated as:

$$\psi_k(s) = 1 - 0.5e^{(-0.13s)} - 0.5e^{(-1.0s)} \tag{3.32}$$

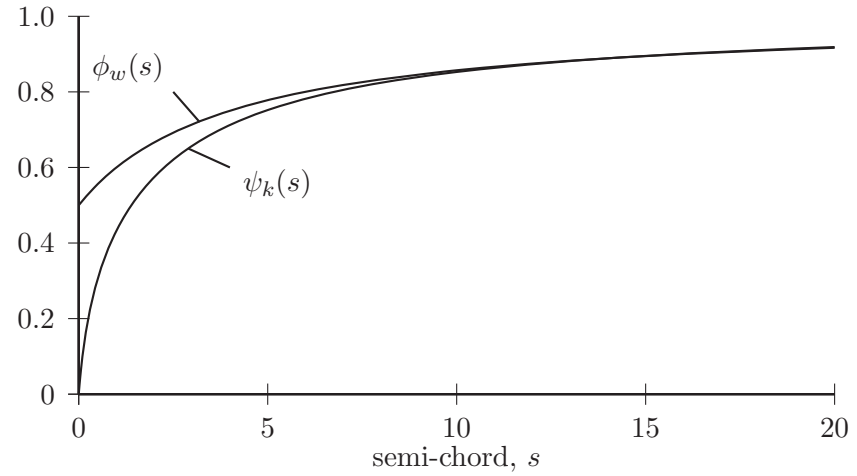

Figure 3.12: Wagner's function, $\phi_w(s)$, for indicial lift due to a step change in angle of attack and Küssner's function $\psi_k(s)$ for lift due to a sharp edged gust, plotted as functions of distance traveled in semichordlengths.

And using a similar approach as above the circulatory lift, L_C, is described:

$$L_C(s) = 2\pi\rho U b v_0 \psi(s) \tag{3.33}$$

Both approximations of the Wagner and the Küssner function are shown in Figure 3.12.

3.6.4 Application to the BEM method

The approached described above, is used in both HAWC2 (developed at DTU) and AeroDyn (developed at NREL). HAWC2 has also other options, i.e. Stig Øye model, which is developed for dynamic stall. The model described above is developed for attached flow and infinitely thin airfoils. It is assumed that the thickness effect can be neglected for the unsteady aerodynamic loads on a wind turbine airfoils. A study, comparing the unsteady aerodynamic lift of a typical wind turbine airfoil, estimated with an inviscid incompressible vortex panel code, to the Wagner function, shows that there is a difference [43]. Results for a 24 % thick airfoil are shown in Figure 3.13 and 3.14.

The response from pitching oscillations in Figure 3.14 shows that both the gradient and the width of the hysteresis loop is influenced by the thickness of the airfoil. The gradient is slightly larger for the flat plate, and

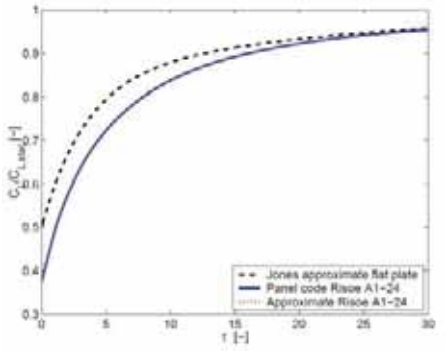

Figure 3.13: Inviscid response of the lift to a step change. The red curve is hidden behind the blue line. Figure from [43]

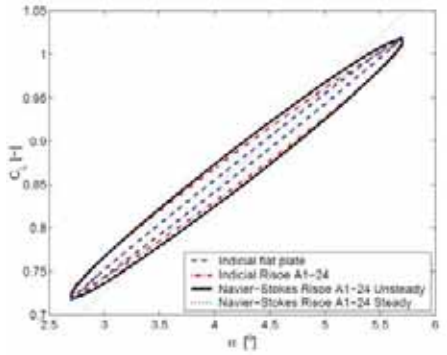

Figure 3.14: Lift coefficient during pitching oscillations $\alpha = 4.2^o \pm 1.5^o$ with k=0.092 for the RISØ A1-24 airfoil. Figure from [43]

the hysteresis loop is slightly narrower. These differences will influence the dynamic response of the airfoil, since there a larger part of the lift is in phase with the pitch velocity. Similar responses are also found using the vortex panel code presented in Chapter 5 and comparing to the aerodynamic code AeroDyn [45].

Chapter 4

Vortex Methods

4.1 Introduction

Vortex methods can be used to evaluate the aerodynamic loads on a wind turbine structure. It is a direct flow simulation approach which dates back to the start of the 20th century. The 4 articles by Joukowsky on *Vortex theory of screw propellors* published between 1912 and 1918 [46, 47, 48, 49] are often regarded as the foundation of the vortex method.

Even though it has been known for more than 100 years, the vortex method has not been a great success in rotor aerodynamics due to:

- its high computational cost.
- the complexity of the underlying theory and the programming.
- the difficulties in including viscosity and compressibility

The severity of these disadvantages are however being reduced by scientific developments. The high computational cost can be reduced by utilizing the parallelization capabilities of the graphical processor unit (GPU). It will be shown later in this chapter (Section 4.5) how the computational cost can be reduced by implementing the vortex calculation on a GPU.

The complexity of the theory is no longer considered a challenge with modern programming tools. There has also been large improvements in how to include the viscosity and the incompressibility over the last years. Viscosity and incompressibility will not be investigated further in this

thesis, and the reader is recommended to read Cottet's book on vortex theory [50] for more information on these topics.

Before looking at the challenges and applications of the vortex method, a short presentation of the underlying potential theory and the elementary flow fields are necessary. Applications to the airfoil, using two dimensional flow, are presented in detail.

4.2 Potential Flow

In this section the potential flow theory is explained. First, a definition of the potential flow, and how the Laplace equation describes the velocity potential, is given. The vortex theory is developed from the potential theory using Green's theorem, and together with the kinematics this rounds off this section about the potential flow. Much of the classical aerodynamic theory, such as Theodorsen theory, is based on potential theory applied to fluid mechanics.

4.2.1 Definitions and Governing Equations

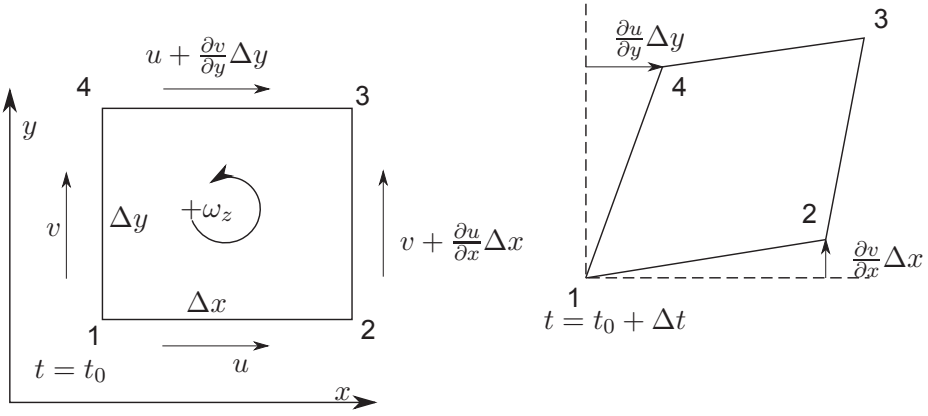

Figure 4.1: The angular velocity of a rectangular fluid element

The vortex method is based on a Langrangian description of the kinematics, this means that the fluid is seen as a group of fluid elements. The motion of a fluid element can be described by its translation, rotation and deformation. A simplified illustration of the motion of a fluid element is shown in Figure 4.1. The element corner number 1 is translated in one

plane ($z = 0$) at a velocity (u, v). Due to velocity variations in within the fluid, the fluid elements may deform and rotate.

The vorticity of the fluid element is two times the angular velocity. The angular velocity can be estimated as the average of the angular velocity for the side segments. For the angular velocity, ω_z, as shown in Figure 4.1:

$$\omega_z = \frac{1}{2}\left(\frac{\partial v}{\partial x} - \frac{\partial u}{\partial y}\right) \tag{4.1}$$

The two other angular velocities, (ω_x and ω_y), can be found in a similar manner. The angular velocity can be written as:

$$\vec{\omega} = \frac{1}{2}\nabla \times \vec{q} \tag{4.2}$$

where $\vec{q}$ is the velocity vector, $\vec{q} = [u, v, w]$. The vorticity, $\vec{\zeta}$ is defined as two times the angular velocity:

$$\vec{\zeta} = \nabla \times \vec{q} \tag{4.3}$$

4.2.2 Helmholtz theorems

The vorticity is closely related to the circulation, Γ. The circulation is defined as the amount of fluid rotation within a closed contour.

$$\Gamma \equiv \oint_C \vec{q} d\vec{l} \tag{4.4}$$

The relation is found by using the Kelvin-Stokes theorem, which relates a surface integral to a line integral. Using Kelvin-Stokes theorem, the relation between vorticity and circulation is:

$$\begin{aligned} \Gamma &= \oint_C \vec{q} \cdot d\vec{l} = \iint_S \nabla \times \vec{q} \cdot \vec{n} dA \\ \Gamma &= \iint_S \vec{\zeta} \cdot \vec{n} dA \end{aligned} \tag{4.5}$$

The rotational motion of the fluid element is shown in Figure 4.2. For a fluid with very large viscous forces the fluid will rotate, but it is common to assume that the shear forces are negligible in air flow. The air flow has zero rotation at the start, it will have zero rotation at all time steps of

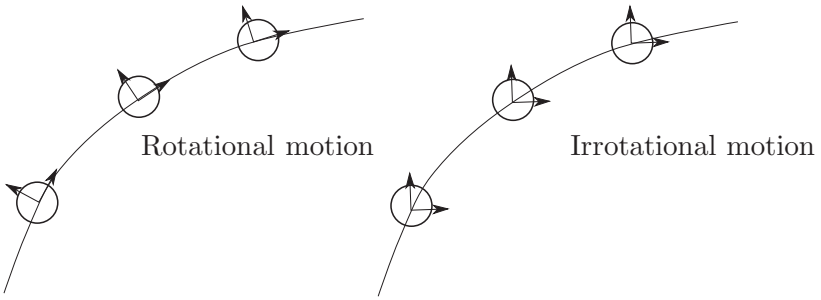

Figure 4.2: Rotational and irrotational motion of a fluid element

the simulation, since shear forces are neglected (i.e. zero viscosity). Since the flow has zero rotational motion at start, and both the vorticity and the circulation will be zero for irrotational fluid elements, only the forces normal to the fluid element will contribute to the changes in velocity.

The velocity is a vector field in three dimensions. The divergence of the curl of any vector field in three dimensions, is equal to zero. The vorticity itself is therefore divergence free:

$$\nabla \cdot \vec{\zeta} = 0 \tag{4.6}$$

From this it follows that the vortex lines can't start or end in the fluid. A vortex line is defined as a line which is tangent to the vorticity vector, and a set of vortex lines forming a vortex tube is shown in Figure 4.3. The vortex lines must therefore form closed paths, end at a boundary, a solid or a free surface, or another alternative is that the vortex line goes to infinity.

Using the divergence theorem, one can show that the circulation around a given vortex line, is constant along its length:

$$\begin{aligned}
\iiint_V \nabla \cdot \vec{\zeta} dV &= \iint_S \vec{\zeta} \cdot \vec{n} dA = 0 \\
\iint_{A_1} \vec{\zeta} \cdot \vec{n_1} dA + \iint_{A_2} \vec{\zeta} \cdot \vec{n_2} dA &= 0 \\
-\Gamma_1 + \Gamma_2 &= 0 \qquad (4.7) \\
\Gamma_1 &= \Gamma_2 \qquad (4.8)
\end{aligned}$$

This can be related to the vortex tube in Figure 4.3, where A_1 is the surface at the bottom end and A_2 is the top surface. The average

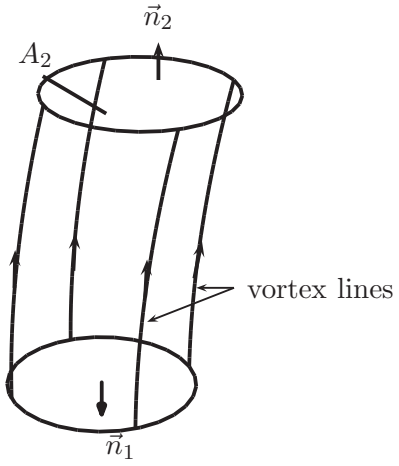

Figure 4.3: A vortex tube with surrounding vortex lines

vorticity at the circular ends are defined as ζ_1 and ζ_2. The cross sectional area changes of the tube can then be related to the vorticity as:

$$\zeta_1 A_1 = \zeta_2 A_2 = \Gamma \tag{4.9}$$

where Γ is the circulation of the vortex tube. It can be shown that the circulation around a material loop of particles changes only if the net viscous force on the particles gives a non-zeros integral. If the fluid is inviscid or irrotational, then:

$$\frac{D\Gamma}{Dt} = 0 \tag{4.10}$$

This is often referred to as Kelvins Circulation Theorem. For an inviscid and incompressible fluid the circulation is constant about any material contour moving with the fluid.

From the above results, several vortex theorems for inviscid incompressible flow follow. These theorems were first developed by Hermann von Helmholtz in 1858[51]. The three Helmholtz's theorems are [52]:

1. The strength of a vortex filament is constant along its length.

2. A vortex filament can't start or end in a fluid. It must form a closed path or extend to infinity.

3. In absence of rotational external forces, a fluid that is initially irrotational remains irrotational.

As a consequence of the third theorem, the fluid that forms a vortex tube and the strength of the vortex tube remains constant. Similarly, vortex elements such as vortex lines, vortex tubes, vortex surfaces, will remain vortex elements with time. The vortex elements are singularities in the flow described by a velocity potential.

4.2.3 Vortex Dynamics

Potential flow is inviscid, irrotational and incompressible. These properties will be applied to the continuity equation (conservation of mass) and the momentum equation. The differential form of the continuity equation in Lagrangian terms is [50]:

$$\frac{D\rho}{Dt} = -\rho \nabla \cdot \vec{q} \tag{4.11}$$

where $D\rho/Dt$ is the rate of change of the density of a fluid element, and the term $\nabla \cdot \vec{q}$ is the particle volume rate.

The Lagrangian description of the conservation of momentum is [50]:

$$\rho \frac{D\vec{q}}{Dt} = -\nabla P + \mu \Delta \vec{q} \tag{4.12}$$

where $\rho \frac{D\vec{q}}{Dt}$ is the acceleration of a fluid particle, ∇P is the net pressure force and $\mu \Delta \vec{q}$ is the net viscous force (μ is the dynamic viscosity). The viscosity of air is relatively low, and this term will be assumed negligible (inviscid and irrotational flow). The momentum equation can be used to relate the velocity to the pressure.

For an incompressible fluid element, the volume is constant. This simplifies the continuity equation (Eq 4.11), since the change in density is zero. Since the density is constant, it can be removed from the equation, and the continuity equation is now:

$$\nabla \cdot \vec{q} = 0 \tag{4.13}$$

$$\vec{q} = \nabla \phi \tag{4.14}$$

By including the velocity potential in the continuity equation, Eq 4.13, the continuity equation is reformulated into Laplace equation:

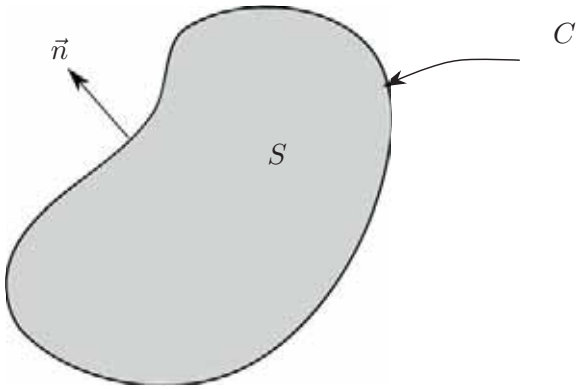

Figure 4.4: The relation between the surface and line integrals

$$\nabla^2\phi = 0 \tag{4.15}$$

4.2.4 Green's theorem

The Laplace equation can be solved by a method of singularity distribution, and the Green's theorem can here be used to find a solution. The theorem is first defined and thereafter applied to the Laplace's equation. Proper solutions of the Green function and the boundary conditions suggested are presented at the end.

The Green's divergence theorem is a special case of the Kelvin-Stokes theorem, and creates a relation between the surface and line integrals. A surface, S, is bounded by the contour line C in Figure 4.4 in 2D. The theory presented here will be limited to 2D. The integral relation is:

$$\int_S (\nabla \cdot \vec{r}) dS = \oint_C \vec{r} \cdot \vec{n} dl \tag{4.16}$$

where $\vec{r}$ is a vector along the contour line C. Thus the divergence of the vector, $\vec{r}$, over a surface is equal to the flux of the normal vector along the contour line C. Let $\vec{r} = \phi\nabla G - G\nabla\phi$, where G is the Green's function and ϕ is the velocity potential. The Green's identity is established as:

$$\int_S \phi\nabla^2 G - G\nabla^2\phi dS = \oint_C (\phi\nabla G - G\nabla\phi) \cdot \vec{n} dl \tag{4.17}$$

The Green's function is chosen such that:

$$\int_S \phi \nabla^2 G dS = \phi \tag{4.18}$$

Combining the above definition, with the Laplace function (Eq 4.15), one gets the following representation of the velocity potential ϕ:

$$\phi = \oint_C (\phi \nabla G \cdot \vec{n} - G \nabla \phi \cdot \vec{n}) dl \tag{4.19}$$

It is a requirement that the Green's function is a solution of Laplace's equation. A good definition of the Green's function for the 2D potential flow is:

$$G(r) = \frac{1}{2\pi} \ln(r) \tag{4.20}$$

where r is the radial distance from the evaluated point, $\vec{x}$, to the singularity, $\vec{x}_0$. The Green's function is singular as r approaches zero, and limits to infinity as r goes to infinity.

Since the Green's function in Equation 4.20 does not exist when the evaluated point, $\vec{x}$, approaches the singularity $\vec{x}_0$, the area around the singularity is extracted from the bounded area considered. By considering a small area, S_ϵ, around the singularity at $\vec{x}_0$, there will be no singularity in the area $S - S_\epsilon$. The curve has the length $C + C_\epsilon$. By doing this, the singularity is extracted from the area considered in the integral. The velocity potential at $\vec{x}$ due to the singularity at $\vec{x}_0$ can now be written as:

$$a(\vec{x})\phi(\vec{x}) = \oint_C \left(\frac{\partial \phi(\vec{x}_0)}{\partial \vec{n}} G(\vec{x} - \vec{x}_0) - \phi(\vec{x}_0) \frac{\partial G}{\partial \vec{n}} (\vec{x} - \vec{x}_0) \right) dl \tag{4.21}$$

where the value of a depends on whether the singularity is on the contour line C and $\nabla \vec{n}$ is exchanged with $\frac{\partial}{\partial \vec{n}}$. If the singularity is on the contour, $a = 1/2$, if the singularity is within the contained surface of the contour, $a = 1$. This relation relates the field values with the boundary data. Depending on the boundary conditions, the solution of $\nabla^2 \phi = 0$ is obtained. Before moving to the boundary conditions, the theory is extended to include unbounded domains.

4.2.5 Unbounded Domains

The theory is extended to unbounded domains to include both an exterior domain, S_e and an interior domain, S_i, see Figure 4.5. The Laplace

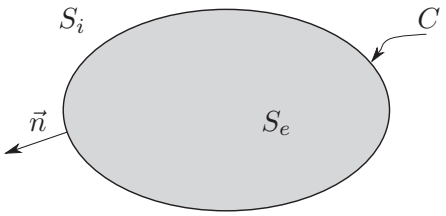

Figure 4.5: Extention of the theory to unbounded domains

equation (Eq 4.15) is valid in both domains S_i and S_e. At the contour line, C, there will be a singularity. This singularity can be described by doublets, μ, and sources, σ:

$$-\mu = \phi_i - \phi_e \tag{4.22}$$

$$\sigma = \frac{\partial \phi_i}{\partial \vec{n}} - \frac{\partial \phi_e}{\partial \vec{n}} \tag{4.23}$$

where ϕ_e is the external velocity potential to the fluid and ϕ_i is the internal velocity potential to the fluid. There are now three different domains; the exterior domain to the fluid (internal to the body), S_e, the interior fluid domain (exterior to the surface), S_i, and the contour line, C. The potential can be calculated for each of these three domains using Eq 4.21. Using the definitions for sources and doublets, the equations can be written as:

$$\left.\begin{array}{ll} \vec{x} \in S_i, & \phi_i(\vec{x}) \\ \vec{x} \in S_e, & \phi_e(\vec{x}) \\ \vec{x} \in C, & 1/2(\phi_{ec} + \phi_{ic})(\vec{x}) \end{array}\right\} = \oint_C \left(\sigma(\vec{x}_0) G(\vec{x} - \vec{x}_0) + \mu(\vec{x}_0) \frac{\partial G}{\partial n}(\vec{x} - \vec{x}_0) \right) dS \tag{4.24}$$

4.2.6 Boundary Equations

So far no boundary conditions are applied. We are interested in investigating the flow around an airfoil, and a condition preventing the fluid from flowing through the airfoil is needed. The vortex singularities can be placed on a boundary, and a no-through flow boundary condition is applied to the integral equation to solve the strength of these singularities.

There are two different approaches to defining the boundary condition; the Neumann condition and the Dirichlet condition.

The Neumann condition is a direct approach to the problem, and the velocity is specified to zero normal to the solid boundary. In this approach the velocity potential is continous across the boundary. The boundary equation is:

$$\nabla\phi_b \cdot \vec{n} = 0 \tag{4.25}$$

where ϕ_b is a velocity potential on the boundary. The Neumann condition is also called the source formulation, since requiring that the potential is continuous across the interface, implies $\mu = 0$. In order to use the Neumann condition, the velocity potential needs to be differentiated.

The Dirichlet approach uses an indirect approach, where the potential is specified on the boundary. The advantage of using this method is its straightforward applicability to numerical methods. In this boundary condition, the stream functions are used. The stream function, Ψ, for an incompressible fluid is defined as:

$$\vec{q} = \nabla \times \Psi \tag{4.26}$$

An enclosed streamline will follow the geometry of the bounded surface, and the potential inside the bounded surface will be constant.

There is also the option of mixing the two boundary conditions, but this will not be the focus here. The Dirichlet boundary condition will be the preferred option in the panel vortex method calculations presented later in chapter 5.

4.2.7 Biot-Savart Law

The Biot-Savart law represents a method to relate the velocity to the vorticity. Using the Helmholtz decomposition of the flow field $\vec{q}$, one has a rotational component, $\vec{q}_\xi$, and a solenoidal component, , $\vec{q}_\phi$:

$$\vec{q} = \vec{q}_\xi + \vec{q}_\phi \tag{4.27}$$

The rotational component contains the vortical part of the flow, and is related to the vorticity as:

$$\vec{\xi} = \nabla \times \vec{q} = \nabla \times \vec{q}_\xi \tag{4.28}$$

As previously stated, the flow is assumed incompressible. Adding the restriction from Eq 4.13, the following relation is found:

$$\nabla^2 \cdot \vec{q}_\xi = -\nabla \times \vec{\xi} \tag{4.29}$$

The solution to the above equation is given by the Biot-Savart law:

$$q_\xi(\vec{x}) = \int_{S_i} K(\vec{x} - \vec{y})\xi(\vec{y})d\vec{y} \tag{4.30}$$

where $K(\vec{x})$ is the Biot-Savart kernel, which is the rotational counterpart to $G(\vec{x})$ (Eq 4.20). In two dimensions K is:

$$K(\vec{x}) = (2\pi|\vec{x}|^2)^{-1}(-x_2, x_1) \tag{4.31}$$

The velocity field can be expressed as:

$$q(\vec{x}) = \int_{S_i} K(\vec{x} - \vec{y})\xi(\vec{y})d\vec{y} + \vec{q}_\phi \tag{4.32}$$

The solendial velocity component, $\vec{q}_\phi$, is given by the free stream potential $\nabla\phi_\infty$.

4.3 Elementary Flows

The Laplace equation is valid for potential flow. The Laplace equation is linear, and a toolbox of elementary flows can therefore be used to describe almost any kind of flow. Two types of elementary flow were identified in Section 4.2.5 as source and doublets. The elementary flows can be due to a point, line, surface or volume singularities. We will only present the 2D elementary flows, points and line. Integration in closed form is only possible in special cases such as straight line segments or planar surfaces due to the singularity of the Green's function.

4.3.1 Principle of Superposition

The Laplace equation is linear, and superposition can be used:

$$\nabla^2\phi = \sum_{k=1}^{n} c_k \nabla^2 \phi_k = 0 \tag{4.33}$$

where c_k is an arbitary constant and ϕ_k is a solution to the Laplace equation. Using the principle of superposition, one can obtain a solution of the flowfield.

4.3.2 Point

The source, doublet and vortex point elements are presented in this section. For the source and doublet elements, the velocity potentials can be found by introducing the Green's function in Eq 4.20 in the velocity potential as given in Eq 4.24. For the source element the velocity potential is:

$$\phi(r,\theta) = \frac{\sigma}{2\pi}\ln(r) \tag{4.34}$$

where σ is the source strength. Similarly for the doublet potential:

$$\phi(r,\theta) = -\frac{\mu}{2\pi r}\cos(\theta) \tag{4.35}$$

where μ is the strength of the doublet.

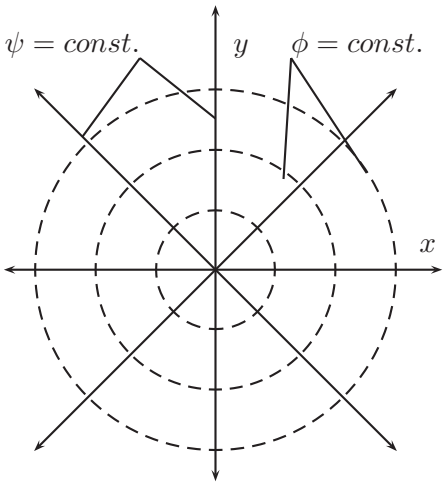

Figure 4.6: Streamlines and equipotential lines due to a source element located at the origin.

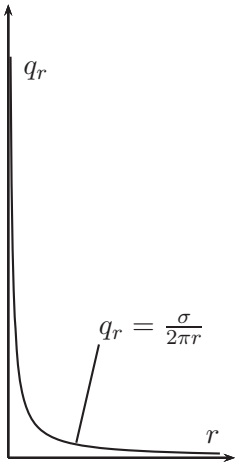

Figure 4.7: Radial velocity due to a source

For the source element the potential is constant at each position, and does not vary with the azimuthal position. The azimuthal velocity will therefore be zero, while the radial velocity for a point source is:

$$q_r = \frac{\sigma}{2\pi r} \tag{4.36}$$

The equipotential lines and streamlines, due to a source element, are illustrated in Figure 4.6. The outgoing surface flux of the point source is equal to its intensity.

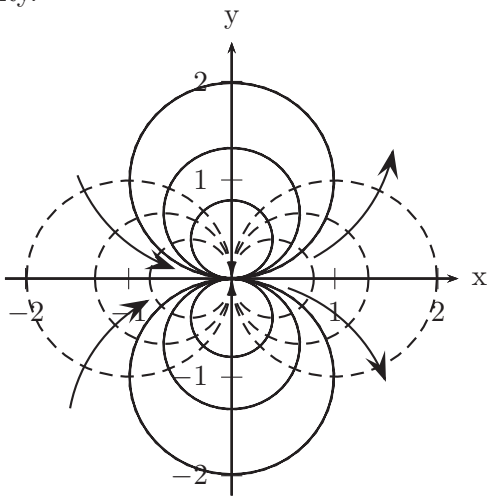

Figure 4.8: Equipotential lines (dotted lines) and stream lines (solid lines) due to a point doublet ($\mu > 0$) at origin pointing in the direction of the x axis

The velocity potential of the doublet element is dependent on both radial and azimuthal position. The velocity components due to a doublet point element, in polar coordinates, are:

$$q_r = \mu \cos(\theta) / \left(2\pi r^2\right), \quad q_\theta = \mu \sin(\theta) / \left(2\pi r^2\right) \tag{4.37}$$

The equipotential lines are plotted together with the streamlines in Figure 4.8. There is no net flux for the point doublet element. The doublet element is associated with the derivative of the Greens function, see Eq 4.22.

The last 2D point element is the point vortex. The general solution to the Laplace solution previously described, consists of doublet and source elements only, but the vortex element represents another possible solution of the Laplace equation that is often used. The velocity potential of the 2D point vortex element is:

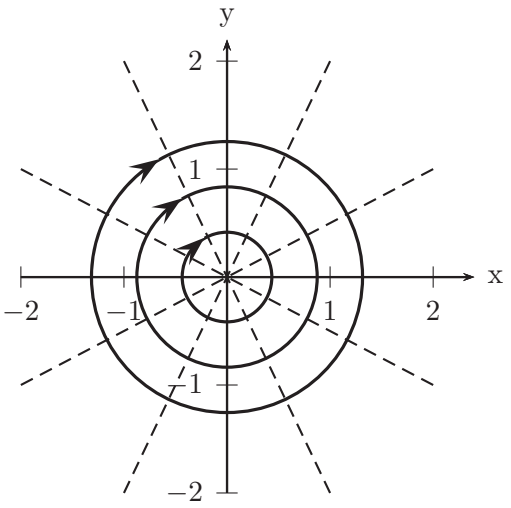

Figure 4.9: The equipotential lines and streamlines for a 2D point vortex element

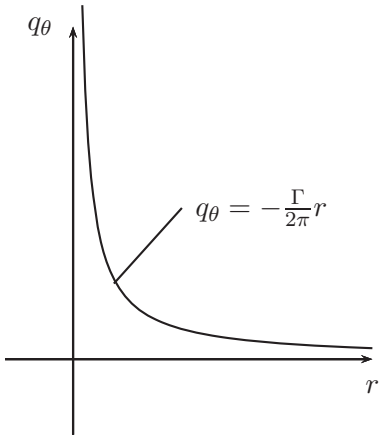

Figure 4.10: Radial variation of the tangential velocity due to a 2D vortex element

$$\phi(r,\theta) = -\frac{\Gamma}{2\pi}\theta \tag{4.38}$$

The equipotential lines and the stream lines are illustrated in Figure 4.9. The radial velocity is zero, and the tangential velocity is:

$$q_\theta = -\frac{\Gamma}{2\pi r} \tag{4.39}$$

4.3.3 Surface Distribution

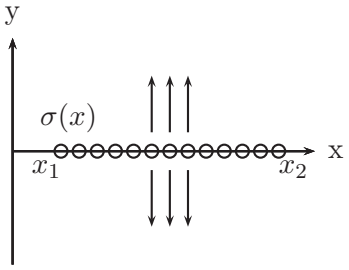

Figure 4.11: Source distribution along the x-axis

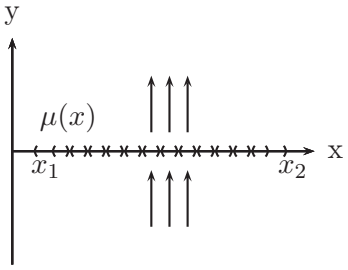

Figure 4.12: Doublet distribution along the x-axis

By distributing the 2D point elements along a line, we can investigate

some of the main features of the elements. The two dimensional elements are located from x_1 to x_2. First we will look at the distribution of source elements, which are shown in Figure 4.11. The source distribution between point x_1 and x_2 will give the following integral for the velocity potential and its derivatives:

$$\begin{aligned}
\phi(x,y) &= \frac{1}{2\pi}\int_{x_1}^{x_2}\sigma(x_0)\ln\sqrt{(x-x_0)^2+y^2}dx_0 && (4.40)\\
\frac{\partial\phi}{\partial x} &= \frac{1}{2\pi}\int_{x_1}^{x_2}\sigma(x_0)\frac{(x-x_0)}{(x-x_0)^2+y^2}dx_0 && (4.41)\\
\frac{\partial\phi}{\partial y} &= \frac{1}{2\pi}\int_{x_1}^{x_2}\sigma(x_0)\frac{y}{(x-x_0)^2+y^2}dx_0 && (4.42)
\end{aligned}$$

It is clear from the illustration in Figure 4.11 that there is a jump in velocity across the surface. The jump in vertical velocity is equal to the source strength:

$$\begin{aligned}
v(x,0\pm) &= \frac{\partial\phi}{\partial y}(x,0\pm) = \pm\frac{\sigma(x)}{2} && (4.43)\\
v^+ - v^- &= \sigma(x)
\end{aligned}$$

The source element is therefore suitable to model flows that are symmetric about y=0 (the x-axis). The next element that is shown is the doublet element. The velocity potential and its derivative due to a doublet distribution, $\mu(x)$, is:

$$\begin{aligned}
\phi(x,y) &= -\frac{1}{2\pi}\int_{x_1}^{x_2}\mu(x_0)\frac{y}{(x-x_0)^2+y^2}dx_0 && (4.44)\\
\frac{\partial\phi}{\partial x} &= \frac{1}{\pi}\int_{x_1}^{x_2}\mu(x_0)\frac{(x-x_0)y}{[(x-x_0)^2+y^2]^2}dx_0 && (4.45)\\
\frac{\partial\phi}{\partial y} &= -\frac{1}{2\pi}\int_{x_1}^{x_2}\mu(x_0)\frac{(x-x_0)^2-y^2}{[(x-x_0)^2+y^2]^2}dx_0 && (4.46)
\end{aligned}$$

The doublet velocity potential is similar to the normal velocity for a source distribution in Eq 4.42. Approaching the surface at $y = \pm 0$, it follows that the velocity potential is:

$$\phi(x,0\pm) = \mp\frac{\mu(x)}{2} \qquad (4.47)$$

The tangential velocity at the surface of the doublet element is therefore discontinuous:

$$u(x,0\pm) = \frac{\partial\phi}{\partial x}(x,0\pm) = \mp\frac{1}{2}\frac{d\mu}{dx} \tag{4.48}$$

The normal velocity is continuous across the doublet element. The strength of the doublet distribution can be related to the jump in velocity potential as:

$$-\mu(x) = \phi_i(x) - \phi_e(x) = \Delta\phi \tag{4.49}$$

where ϕ_i is the velocity potential on the inside and ϕ_e is the exterior velocity potential. It is also important to note the relation between the doublet strength and the circulation:

$$\Gamma(x) = -\mu(x) = \Delta\phi(x) \tag{4.50}$$

The last and third surface distribution is the vortex elements. It can be shown that there are similarities between the doublet and vortex distribution, where the relation is;

$$\gamma(x) = -\frac{d\mu(x)}{dx} \tag{4.51}$$

where $\gamma(x)$ is the distributed vortex elements along the surface. The integral of the strength of the distributed vortex elements, γ, is equal to the circulation strength of elements, Γ. The velocity potential and velocity at a point $P(x,y)$ due to the vortex distribution $\gamma(x_0)$ is;

$$\phi(x,y) = -\frac{1}{2\pi}\int_0^c \gamma(x_0)\tan^{-1}\left(\frac{y}{x-x_0}\right) \tag{4.52}$$

$$u(x,y) = \frac{\partial\phi}{\partial x} = \frac{1}{2\pi}\int_0^c \gamma(x_0)\frac{y}{(x-x_0)^2+y^2}dx_0 \tag{4.53}$$

$$v(x,y) = -\frac{\partial\phi}{\partial y} = \frac{1}{2\pi}\int_0^c \gamma(x_0)\frac{x-x_0}{(x-x_0)^2+y^2}dx_0 \tag{4.54}$$

4.4 Thin Airfoil

Airfoils are shapes with small relative thickness, smooth leading edges and a sharp trailing edge. Wind turbine blades do seldom fit with this

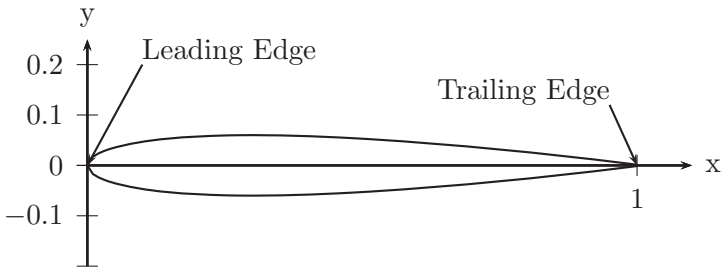

Figure 4.13: A NACA 0012 airfoil with leading edge and trailing edge

description since the trailing edge are normally blunt, and the leading edge may not be completely smooth due to insects and ice accumulations. The NACA 0012 is illustrated in Figure 4.13. However, to simplify the problem it is common to assume that the wind turbine blade have an airfoil shape. Linear theory can be applied for small relative thickness, small angles of attack and high Reynolds number to predict the lift of the airfoil.

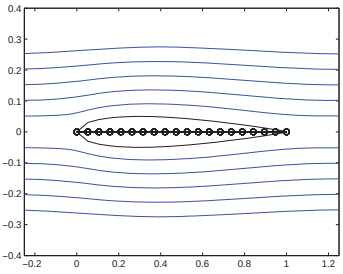

Figure 4.14: Streamlines due to a surface distribution of sources elements

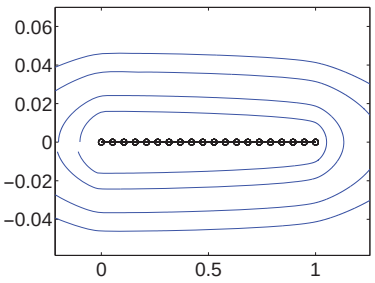

Figure 4.15: Streamlines due to a surface distribution of vortex elements

The effect of thickness of the airfoil on the flowfield can be modeled by using sources as shown in Figure 4.14, and the circulation of the flowfield can be modeled by doublet or vortex elements. The thickness has no effect on the lifting properties in steady potential flow. The singular elements can be placed along the center line of the airfoil, or along the boundary of the airfoil. In the following sections the singularities are placed along the center line. In Chapter 5, the singular elements are placed along the boundary to model the thickness.

In this section the focus is on the thin airfoil (with no thickness) to illustrate some typical aerodynamic behaviour of the airfoil in steady flow. A new boundary condition is needed for airfoil analysis to ensure a smooth flow at the trailing edge of the airfoil, this is provided by the Kutta condition. Using the vortex theory, we can use potential flow modelling to predict the aerodynamic performance of a thin airfoil. A qualitative analysis of a thin airfoil, combined with an analysis of the aerodynamic performance is shown. The next step is to investigate the unsteady case. A few modifications are needed to include the time-varying aerodynamic loads. This is also the basis of the classical unsteady aerodynamic theory by Theodorsen, Küssner and Wagner, which was also presented in Section 3.6.

4.4.1 Vortex Wake

In previous sections, elementary solutions of Laplace equation have been presented together with the zero normal flow boundary condition. In smooth flow, and with the viscous effect of the airfoil confined to a thin layer, the vorticity of the wake is assumed to be shed smoothly from the trailing edge. The Kutta condition (or the Kutta-Joukowski condition) states that the proper circulation of the airfoil is the circulation that causes the flow to leave smoothly, along the centre line, at the trailing edge.

The Kutta condition, together with the Dirichlet or Neumann condition, provides a unique solution to the circulation of the airfoil. Requiring that the flow should leave the sharp trailing edge of the airfoil smoothly is equivalent to stating the velocity at the trailing edge should be finite. The normal component for the velocity at the trailing edge, both at upper surface and the lower surface are zero, and for a continuous velocity this is only possible if there is a stagnation point at the trailing edge. At the stagnation point at the trailing edge, one can assume that the pressure difference is zero. This indicates zero circulation at the trailing edge, see Figure 4.16.

The next step is to include the Helmholtz condition. For steady conditions, the starting vortex of the wake should be located infinitely far downstream the airfoil. The strength of the starting vortex should be equal to the circulation of the airfoil, but the influence tends to zero since it is infinitely far away. For an unsteady analysis any change in the circulation at the blade should be balanced by an equal and opposite change

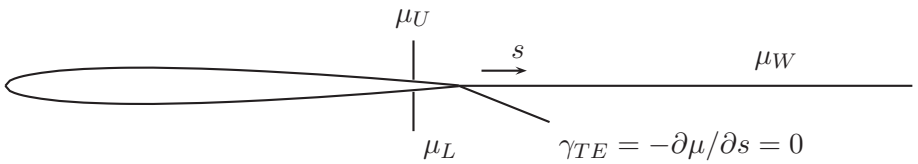

Figure 4.16: Implementation of the Kutta condition when using surface doublet distribution, [52]. The vorticity at trailing edge, γ_{TE}, is zero

in the vorticity of the wake.

The last restriction of the wake is that it should not create loads. By defining the pressure difference across the vortex sheet of the wake as zero, one can get the following relation:

$$\Delta p = \rho \vec{q} \times \vec{\gamma} = 0 \qquad or \quad \vec{q} \times \vec{\gamma} = 0 \tag{4.55}$$

From this it follows that the velocity vector, $\vec{q}$, is parallel to the panel element in the wake.

4.4.2 Steady Flow

The aerodynamic performance of a two dimensional thin plate at a small angle of attack in free flow is investigated. A surface distribution of vortex elements along the thin plate is used to model the circulation. Doublet elements could also have been used, but vortex elements are used here. The first step is to establish the no-through flow boundary condition, where the thin plate surface is described as $y = \eta(x)$. The potential of the flow field, ϕ^*, consists of the free flow potential, ϕ_∞, and a perturbation potential ϕ. This is the Helmholtz decomposition of the velocity potential, as described in Section 4.2.7. The free flow potential is related to the solendial velocity component, $\vec{q}_\phi$ and is defined as:

$$\phi_\infty = U_\infty x + W_\infty y \tag{4.56}$$

The perturbation potential ϕ, represents the velocity induced by the circulation from the airfoil and its wake in a stationary frame of reference. The no flow through the thin plate boundary condition (Eq 4.25) requires:

$$\begin{aligned} \nabla\phi^* \cdot \vec{n} &= \left(\frac{\partial \phi}{\partial x} + U_\infty, \frac{\partial \phi}{\partial y} + W_\infty \right) \cdot \frac{(-d\eta_c/dx, 1)}{\sqrt{(d\eta_c/dx)^2 + 1}} = 0 \\ \frac{\partial \phi}{\partial y} &= -Q_\infty \alpha \qquad on \quad y = \eta_c \end{aligned} \tag{4.57}$$

where Q_{inf} is the total free flow velocity ($Q_\infty = \sqrt{U_\infty^2 + W_\infty^2}$). The free stream velocity in the y-direction is approximated as $W_\infty \approx Q_\infty \alpha$ for small values of α.

The velocity potential at a point $P(x, y)$ due to a vortex element distribution with the strength $\gamma(x_0)$ per unit length at x_0 is given in section 4.3.3, Eq 4.52. The velocities are given in Eqs 4.53 and 4.54. Combining the velocity distribution normal to the plate at the surface($y = 0$), with the boundary condition in Eq 4.57, results in:

$$-\frac{1}{2\pi}\int_0^c \gamma(x_0)\frac{1}{x - x_0}dx_0 = -Q_\infty \alpha, \qquad 0 < x < c \tag{4.58}$$

The Kutta condition provides a second bondary condition. The flow should leave the trailing edge ($x = c$) smoothly, and the velocity should be finite. One approach to fulfill this requirement, is to limit the pressure difference to be zero at the trailing edge. From this it follows that the vortex element at the trailing edge should be zero:

$$\gamma(x = c) = 0 \tag{4.59}$$

The vortex distribution on the flat plate surface can be solved using the above equations. A transformation into trigonometric variables will enable us to use the Glauert integral to solve the problem:

$$\int_0^\pi \frac{\cos n\theta}{\cos\theta_0 - \cos\theta}d\theta_0 = \frac{\pi \sin n\theta}{\sin\theta}, \qquad n = 0, 1, 2, ... \tag{4.60}$$

The transformation from x to θ is:

$$x = \tfrac{c}{2}(1 - \cos\theta) \quad dx = \tfrac{c}{2}\sin\theta d\theta \tag{4.61}$$

The vortex distribution is:

$$\gamma(\theta) = 2Q_\infty \alpha \frac{1 + \cos\theta}{\sin\theta} \tag{4.62}$$

$$\gamma(x) = 2Q_\infty \alpha \sqrt{\frac{c - x}{x}} \tag{4.63}$$

The vortex distribution is established, and the aerodynamic performance of a thin plate at an angle of attack can now be evaluated. The steady-state Bernoulli equation for small-disturbance flow over an airfoil:

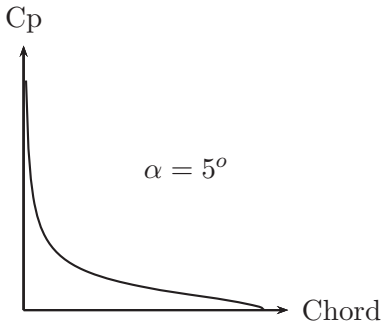

Figure 4.17: Pressure difference on a thin plate

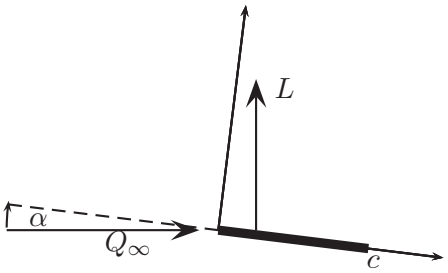

Figure 4.18: Aerodynamic lift force on a flat plate. The lift force is marked at x=0.25 c, where the pitch moment is zero.

$$p - p_\infty = -\rho Q_\infty \frac{\partial \phi}{\partial x} \tag{4.64}$$

where p is the pressure, and p_∞ is the reference pressure in the free flow. It can be shown that the tangential velocity on the surface of the thin airfoil is:

$$u(x, 0\pm) = \frac{\partial \phi}{\partial x}(x, 0\pm) = \pm \frac{\gamma(x)}{2} \tag{4.65}$$

The pressure difference is therefore:

$$\Delta p = \rho Q_\infty \gamma(x) \tag{4.66}$$

In Figure 4.17 the pressure distribution is shown for a flat plate with 5^o angle of attack. The lift force , L, perpendicular to the free stream Q_∞ is:

$$L = \int_0^c \Delta p(x) dx = \int_0^c \rho Q_\infty \gamma(x) dx = \rho Q_\infty \Gamma \tag{4.67}$$

where the circulation of the thin plate, Γ, is connected to the vortex distribution, γ, as:

$$\Gamma = \int_0^c \gamma(x) dx = Q_\infty c \pi \alpha \tag{4.68}$$

The aerodynamic moment relative to the leading edge, M_0, is calculated positive around the y axis in clockwise direction:

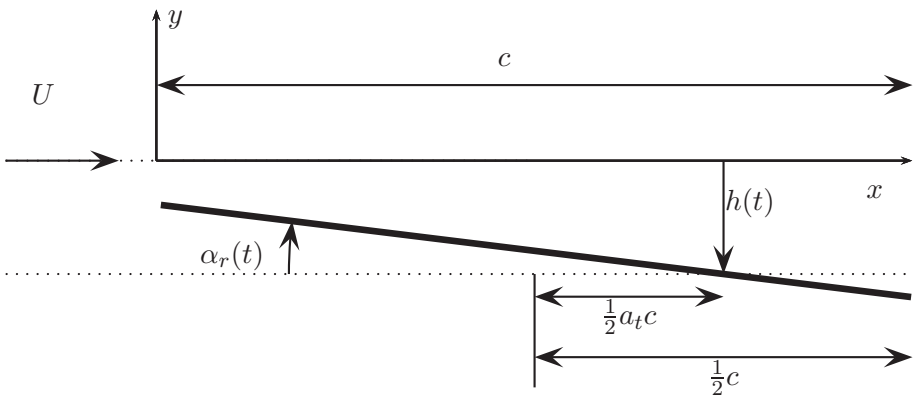

Figure 4.19: A thin plate where h(t) is downward translation of the flat plate, and $\alpha_r(t)$ is the rotation about the axis of rotation at $\frac{1}{2}ac$ relative to the midchord.

$$M_0 = -\int_0^c \Delta p(x) x dx = -\rho Q_\infty^2 \pi \frac{c^2}{4} \alpha \tag{4.69}$$

The aerodynamic coefficients for a flat plate are:

$$C_L = \frac{L}{(1/2)\rho Q_\infty^2 c} = 2\pi\alpha \tag{4.70}$$

$$C_{M_0} = \frac{M_0}{(1/2)\rho Q_\infty^2 c^2} = -\frac{\pi\alpha}{2} \tag{4.71}$$

The aerodynamic pressure center is located at the quarter chord distance from the leading edge, as for a thin plate. The aerodynamic forces acting on the the flat plate are illustrated in Figure 4.18.

4.4.3 Unsteady Flow

The application of unsteady aerodynamics to wind turbines were discussed in the previous chapter, in section 3.4.3. In this section some of the theory is explained.

The problem of unsteady attached flow was first tackled by Glauert [53] and was solved by Theodorsen [26]. The problem was based on a thin airfoil and it was assumed that it had small transversal oscillations. An illustration of the thin plate and the nomenclature used is shown in

Figure 4.19. Both the translational motion of the flat plate, $h(t)$, and the rotation of the flat plate about a point $\frac{1}{2}a_t c$ relative to the mid-chord was studied by Theodorsen. a_t is a coefficient used to define the center of rotation relative to the chord length, where $a_t = 0$ corresponds to rotation about the mid-chord and $a_t = 1$ has rotation about the trailing edge (see Figure 4.19). The motions were restricted to simple harmonic motions. The Laplace equation is still valid, but the boundary conditions need to be re-evaluated relative to the previous section with steady flow. In addition, a model of the wake must be included.

A detailed description of the method applied by Glauert and Theodorsen is given in [54]. The methodology will be presented briefly, before a discussion on the relevance of Theodorsen's results. The result by Theodorsen is given in the frequency domain, and the transformation to time domain is discussed in a previous section (see Sec 3.6).

The no flow boundary condition can be written as:

$$v_a(x,t) = \frac{\partial y_a}{\partial t} + U\frac{\partial y_a}{\partial x}; \qquad for \quad y = 0; \quad 0 \leq x \leq c \tag{4.72}$$

where v_a is the velocity in y-direction at the surface of the thin plate. Kutta's condition with a finite and continuous velocity and pressure at the trailing edge is still valid.

Theodorsen divided the unsteady problem into two parts, a circulatory part and a non-circulatory part. The two different approaches are used separately to solve for the above boundary conditions. The non-circulatory part solves the no-flow boundary equation by applying sources and sinks point elements along the lower and upper surface of the thin plate. The circulatory part of the problem is solved by applying vortices along the thin plate and in the wake. The Kutta condition is fulfilled by locating vortices along the same line and vortices along the wake to infinity. In Theodorsen's analysis it is assumed that the wake does not deform but moves with the speed of the flow, U. The vortices in the wake are counter-vortices to the vortices on the airfoil such that the circulation of the system remains constant:

$$\frac{D\Gamma}{dt} = 0 \tag{4.73}$$

By doing this division of the problem, one can discuss the influence of the solutions separately. The resulting aerodynamic loads based on the

sources and sink elements for the no-flow through boundary condition, are referred to as non-circulatory loads. The circulatory loads are due to the distribution of vortices.

The instantaneous small displacement of the chord line, $y_a(x,t)$, is:

$$y_a(x,t) = -h - \alpha_r \left[x - \tfrac{c}{2}(1+a)\right], \quad for \qquad 0 \le x \le c \tag{4.74}$$

c is the chord length, h is the translation, α_r is the angle of rotation about the point located at $0.5ac$ relative to the mid-chord, as shown in Figure 4.19. Inserting the small displacements, $y_a(x,t)$ into the no flow through the surface condition in Eq 4.72:

$$v_a(x,t) = -\dot{h} - \dot{\alpha_r} \left[x - \tfrac{c}{2}(1+a)\right], \quad for \qquad 0 \le x \le c \tag{4.75}$$

The non-circulatory lift and moment are [54]:

$$L_{NC} = \frac{\pi\rho c^2}{4}\left[\ddot{h} + U\dot{\alpha_r} - \frac{1}{2}ca\ddot{\alpha_r}\right] \tag{4.76}$$

$$M_{yNC} = \frac{\pi\rho c^2}{4}\left[U\dot{h} + \frac{1}{2}ca\ddot{h} + U^2\alpha_r - \frac{1}{4}c^2(1/8+a^2)\ddot{\alpha_r}\right] \tag{4.77}$$

From the estimation of non-circulatory loads, one can see that the motions described by the plunging motion, $h(t)$, and the pitch motion, $U\alpha_r(t)$, are analogous to one another. Both motions have a constant vertical velocity over the airfoil at any point in time, see Figure 3.10. The virtual mass associated with vertical acceleration $\ddot{h}$ is $\frac{\rho\pi}{4}c^2$, which is equal to the mass of a circle of liquid with the same diameter as the chord. The lift due to the angular velocity, $\dot{\alpha_r}$, is of a different nature. The vertical velocity is not constant along the chord as shown in Figure 3.11. The angular velocity contributes if the rotational axis is displaced from the mid-chord. The contribution of the angular velocity to the moment is a virtual moment of inertia, $\rho\left[\frac{\pi}{16}c^4(1/8+a^2)\right]$.

The non-circulatory solution presented above does not fulfill the Kutta condition, for this we need the circulatory part of the solution. Combining the non-circulatory solution with the circulatory solution, the aerodynamic lift and moment from Theodorsen analysis is:

$$L = \frac{\pi\rho c^2}{4}\left[\ddot{h} + U\dot{\alpha_r} - \frac{ca}{2}\ddot{\alpha_r}\right] + \pi\rho U c C(k)\left[\dot{h} + U\alpha_r + \frac{1}{2}c(1/2-a)\dot{\alpha_r}\right] \quad (4.78)$$

$$M_y = \frac{\pi\rho}{4}c^2\left[\frac{1}{2}ca\ddot{h} - U\frac{1}{2}c(1/2-a)\dot{\alpha_r} - \frac{1}{4}c^2(1/8+a^2)\ddot{\alpha_r}\right] + \frac{\pi\rho U c^2}{2}(a+1/2)C(k)\left[\dot{h} + U\alpha_r + \frac{c(1/2-a)}{2}\dot{\alpha_r}\right] \quad (4.79)$$

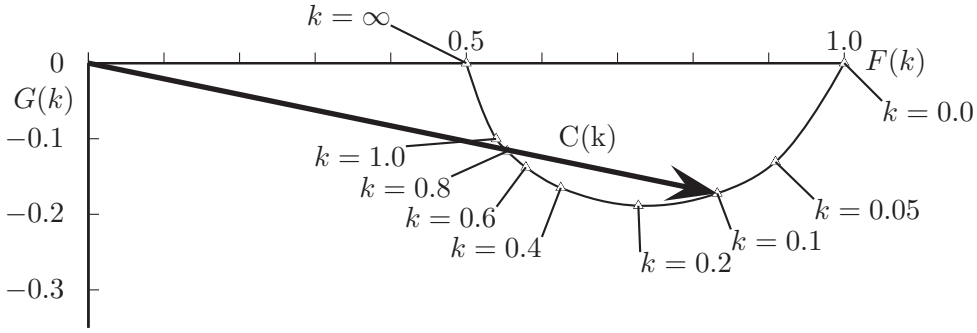

Figure 4.20: The Theodorsen function, $C(k)$, plotted as a complex vector

The reduced frequency is often used as a measure of the unsteadiness of a flow and is a governing variable of the circulatory function, $C(k)$. Theodorsen's function can be expressed in terms of Hankel functions:

$$C(k) = F(k) + iG(k) = \frac{H_1^{(2)}(k)}{H_1^{(2)}(k) + iH_0^{(2)}(k)} \quad (4.80)$$

where $C(k)$ is Theodorsen's function, and k is the reduced frequency, $k = \frac{\omega c}{2U}$. The amplitude, $|C(k)|$, and phase, ϕ_C is defined as:

$$|C(k)| = \sqrt{F^2 + G^2} \quad \phi_C = tan^{-1}(G/F) \quad (4.81)$$

The function is plotted in Figure 4.20. The function the largest phase at $k = 0.2$. For $k = 0$, the flow is steady, and steady-state lift is obtained.

4.4.4 Circulation and non-circulation effect

The first term of the lift and moment equations based on Theodorsen's analysis (Eq 4.78 and Eq 4.79) are the non-circulatory term, which is also called the apparent mass term. The second term, which is related to the Theodorsen function, $C(k)$, is the circulatory term. The non-circulatory term arises from the time-variant term of the unsteady Bernoulli equation, $\partial\phi/\partial t$, where $\phi(t)$ is the velocity potential of the flow [17]. The pressure forces required to accelerate the fluid in the vicinity of the airfoil are accounted for by the non-circulatory term.

The lift coefficient, due to the circulation term, is dependent on the type of oscillating motion. The unsteady lift response, only considering the circulatory lift coefficient for a flat plate in pure pitch oscillations, is shown in Figure 4.21.

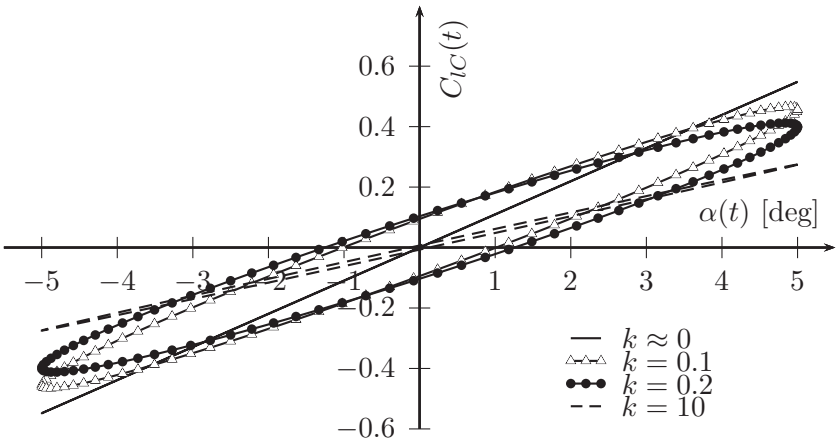

Figure 4.21: The circulatory lift component part of the unsteady lift response, $C_{LC}(t)$, for a harmonic pitch motion, $\alpha(t)$. The direction of the elliptic curves are counterclockwise

The thin plate is oscillating between $\pm 5^o$, and for quasi-static values this corresponds to a quasi-static lift coefficient, C_L, linearly varying between ± 0.55. The quasi-static lift coefficient corresponds to the line plotted with a reduced frequency, k, equal to zero. For higher values of k, the amplitude of the lift coefficient is lower, and the loads are partly out of phase with the oscillating motions. For larger values of the reduced frequency, $k > 0.2$, the phase shift is reduced. It is shown in Figure 4.21

that at $k = 10$, the load and forcing motion are almost in phase, but the amplitude of the load is half the quasi-static values.

The total lift coefficient, for pure angle of attack oscillations, is estimated as [17]:

$$C_L = [2\pi(F(k) + iG(k)) + i\pi k]\,\overline{\alpha}e^{i\omega t} \tag{4.82}$$

where $\alpha(t) = \overline{\alpha}e^{i\omega t}$. The contribution of the non-circulatory load relative to the circulatory load is studied using the normalized lift amplitude shown in Figure 4.22. For reduced frequencies, k, lower than 1, the circulatory part of the lift is dominating. At higher reduced frequencies, the non-circulatory contribution is more important. The circulatory lift coefficient stabilizes at a normalized lift amplitude of 0.5 for high values of k, while the total circulatory lift increases linearly together with the non-circulatory lift.

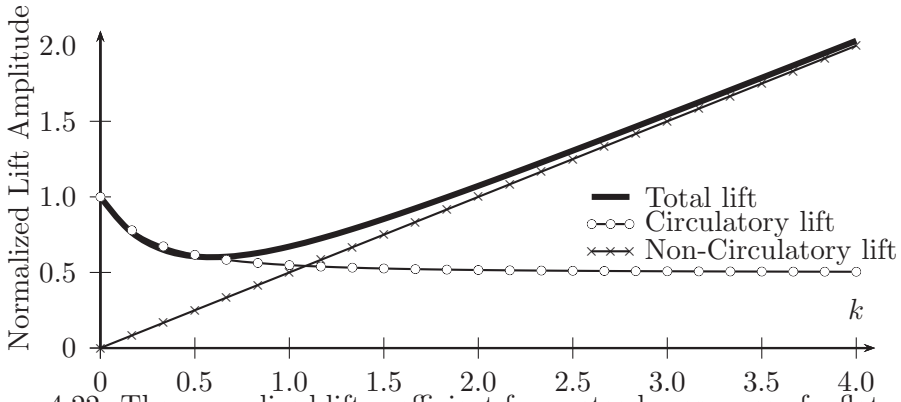

Figure 4.22: The normalized lift coefficient for unsteady response of a flat plate in pure pitching motion

It is also interesting to look at the phase of the unsteady lift, see Figure 4.23. The circulatory lift are most out of phase when $k = 0.2$. The phase is negative at the low frequencies, and this indicate that there will be negative added mass in the dynamic system. However, the total lift is following the phase of the circulatory lift only for very low reduced frequencies. As the reduced frequencies are increased, the total phase lag increases towards the circulatory lead lag of 90^o, and the phase is positive. This indicates a positive added mass.

For a pure plunging motion, the nature of the circulatory lift coefficient for a thin plate, is illustrated in Figure 4.24. The plunging motion

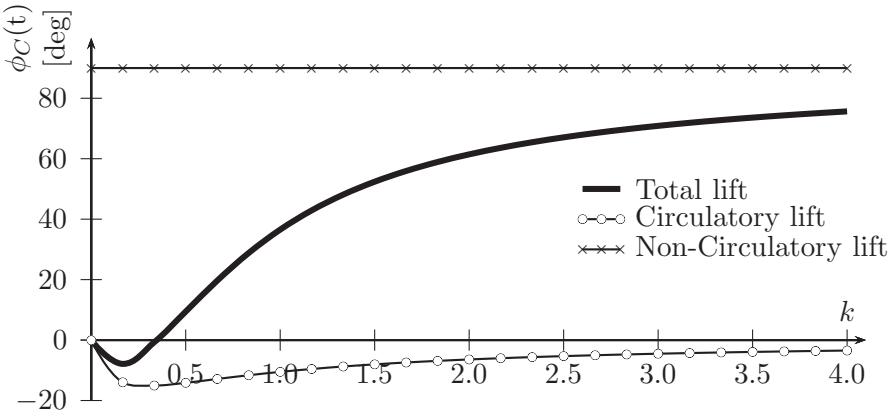

Figure 4.23: The phase angle, ϕ_C(t), for unsteady response of a flat plate in pure angle of attack motion.

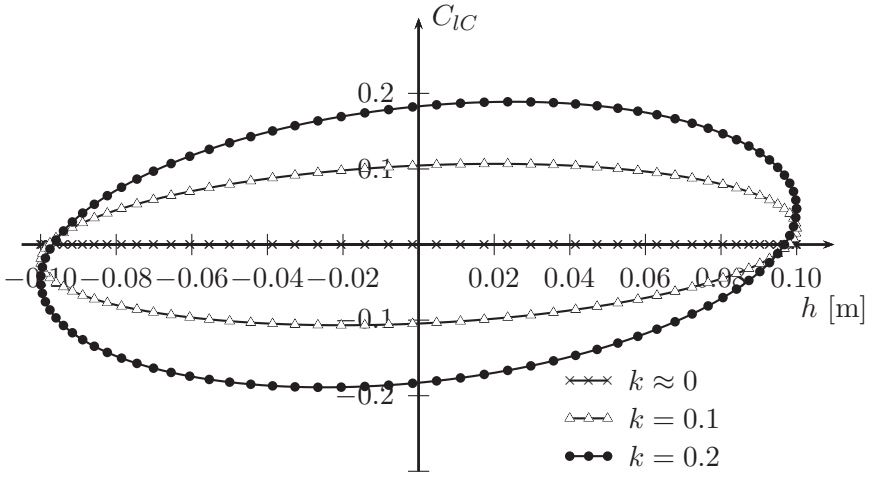

Figure 4.24: The circulatory lift component part, C_{LC}, of the unsteady lift response for a pure plunging oscillation.

is described as $h(t) = \overline{h}e^{i\omega t}$, and combining this with Eq 4.78, the lift coefficient is established:

$$C_l = \left[2\pi k\left(iF(k) - G(k)\right) - k^2\pi\right]\frac{\bar{h}}{0.5c}e^{i\omega t} \tag{4.83}$$

The first term of the lift coefficient is related to the circulatory loads, and it is these unsteady loads that are shown in Figure 4.24. The quasi-static lift coefficient is zero. For increasing values of k, the amplitude

of the lift coefficient is increasing, which differs from the pure oscillating motion, where there was a decrease in lift amplitude with increasing reduced frequencies.

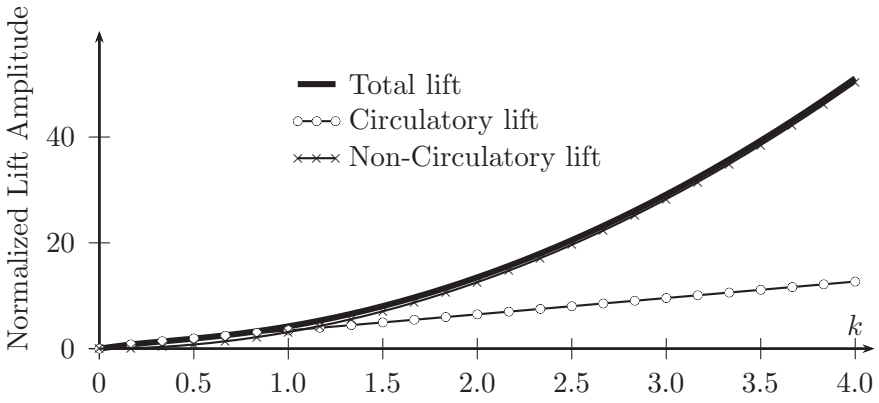

Figure 4.25: The normalized lift coefficient for unsteady response of a flat plate in pure plunging motion

From Figure 4.24, it was seen that the lift amplitude was increasing with increasing k. If the normalized lift amplitude is plotted, see Figure 4.25, it is seen that this trend continues. The lift is normalized by dividing the lift coefficient with $2h/c$. The non-circulatory lift will dominate the total lift for $k > 1$.

The phase of the lift is for lower frequencies governed by the circulatory effects, but the non-circulatory effects are governing as the reduced frequency increases. This is shown in Figure 4.26.

There are similarities between the plunging motion and the pitching motion, that are evident in the plot of the phase angle for the two motions. The plunge oscillating phase has a 90^o lead to the pitch oscillating phase, ref Figure 4.23. This is a reasonable results, since the velocity due to the plunge oscillations will give the same change in angle of attack as the pitch oscillation motion.

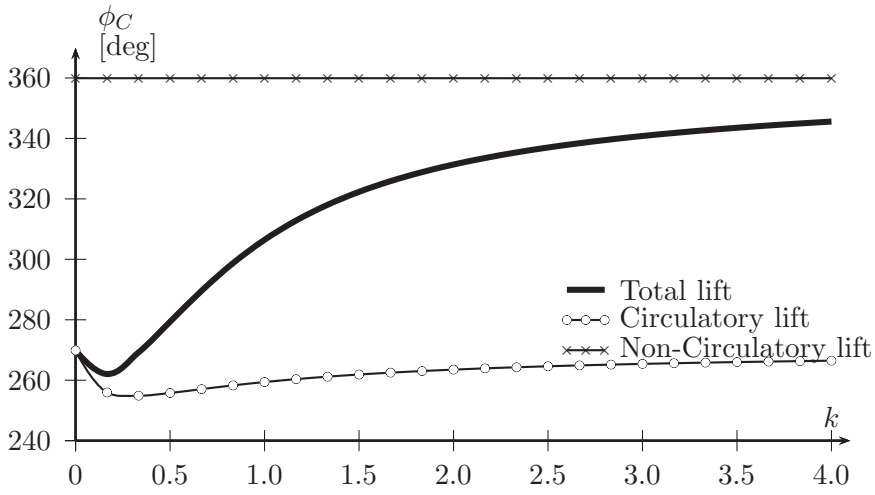

Figure 4.26: The phase angle for unsteady response of a flat plate in plunging motion

4.5 Implementation on a Graphical Processing Unit

One of the main issues with a vortex method is the time-consuming computation. The velocities at points have to be computed, considering all the singular elements in the flow. The influence matrix also needs to be solved with each time step, but this is less computationally demanding compared to the velocity calculation. This is illustrated later, in Figure 5.15. Using a direct sum approach, the order is $O(n^2)$, where n is the number of particles. The cost of computational time can be reduced using a tree-algorithm, and the reduction depends on the type of tree-algorithm. In [55] the order is reduced to $O(n \log n)$. The tree-code algorithm reduces the number of computed interactions by dividing the space into cells, and evaluating the interaction between the vortex elements, depending on if the are far apart or close. Readers interested in more details regarding tree-code algorithm, is referred to [56].

In this section we will investigate how the implementation of the panel vortex method on a graphical processor unit (GPU) will reduce the computational cost. A two dimensional time-stepping vortex code is used to illustrate the reduction in time.

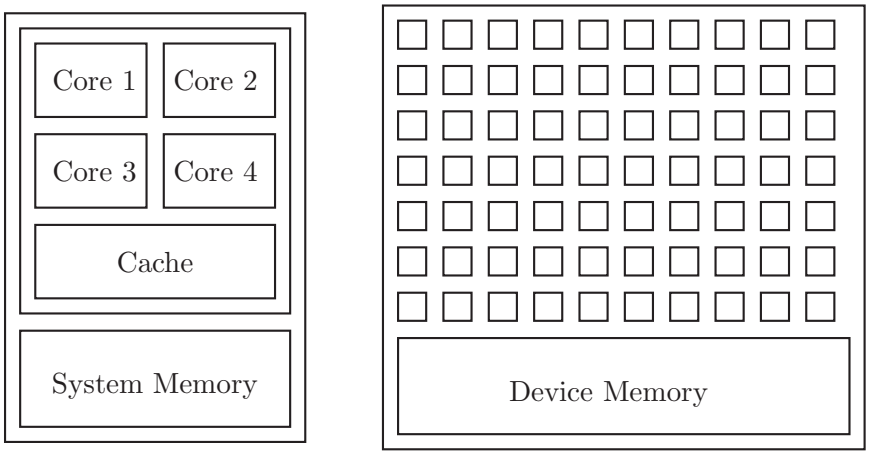

Figure 4.27: Simplified illustrattion of a Central Processing Unit (left) compared to a Graphical Processing Unit (right).

4.5.1 Basics of GPUs

The Graphical Processing Unit (GPU) was originally made for graphics acceleration, but can now also be used in scientific calculations. The GPU consists of a large number of cores, and an illustration of the GPU relative to the CPU is shown in Figure 4.27. A modern CPU has typically 4 or more cores that can run processes in parallel, while a GPU has a massively parallel array of integer and floating point processors. In addition to its processors, the GPU also has a dedicated high-speed memory. The CPU is often referred to as the host, and the GPU is the device.

Due to its many processors, the GPU is ideal for highly parallel problems. The GPU has typically hundreds of processors per card, and GPU cores that compliment the CPU cores. A common used parallel computing technology is CUDA, that is developed by NVIDIA, a company which has specialized in GPUs. This can be used to create kernels, which are codes written for execution on the GPUs processors. Kernels are written as functions that can run on large number of threads. The parallelism is achieved by each thread running independently the same program on different data.

Characteristics that indicate that a program is well suited for a GPU are that they are massively parallel and computationally expensive. One should be able to break down the program into hundreds or thousands of

independent units of work, the GPU shows best performance when the many cores are busy.

The main motivation for using the GPU is to reduce the computational time. The computational time should exceed the time spent on transferring data from, and back to, the CPU. The NVIDIA GPUs have a double precision floating point [57].

4.5.2 A vortex code implemented on the GPU

The step that takes the most time on vortex method computation is the velocity computation of the wake particles. This process can be parallelised since the strength of the singular elements are known prior to the velocity calculation in the wake.

It has become increasingly easier to compute on a GPU, and it is now possible to use matlab for GPU programming. Here, a comparison of the computational time of a vortex method time-stepping simulation on a GPU, relative to a CPU, is performed.

For shorter simulations it is expected that the CPU will run faster than the GPU. This is because of the slow data transfer between the GPU and the CPU, and also due to the fact that the computing in general is slower on a GPU. The advantage is only if the computation can be massively parallelized and this is true for the calculations of the induced velocities of singular elements. This will be illustrated using a simplified two dimensional time stepping simulation for a thin plate at an angle of attack.

A model of the simulation is shown in Figure 4.28. A flat plate is modeled using a single vortex element located at a quarter of the chord length from the leading edge. The boundary condition requiring no-flow through the surface is fulfilled at a quarter chord from the trailing edge. This point is referred to as the collocation point. The wake is modelled as a prescribed wake, where the vortex elements shed from the trailing edge follow the incident wind field (no wake deformation). The velocity at the collocation point due to the vortex element on the airfoil and the vortex elements in the wake, were calculated on the GPU and the CPU in two separate simulations, both using Matlab.

A comparison of the computational time for the time-stepping vortex code using a GPU version and a CPU version is shown in Figure 4.29. The computational time using a CPU relative to the computational time using a GPU is shown along the y-axis, and the number of computational

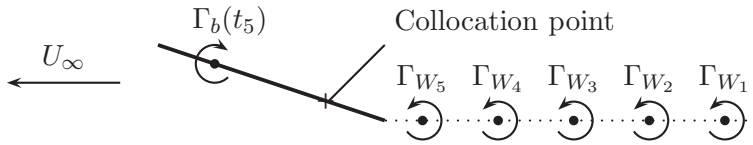

Figure 4.28: A thin plate modeled using a single vortex element Γ_b, and the wake vortex elements shed from the trailing edge, after 5 time-steps

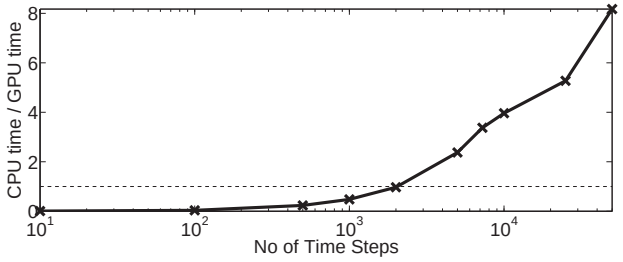

Figure 4.29: The increase in computational time using the CPU relative to the GPU for different number of time-steps.

steps along the x-axis. The dotted line is drawn to illustrate where the GPU and the CPU have equal computational time.

The CPU is an Intel Core i7-3610QM running at 2.3 GHz, and the GPU is a Quadro K1000M which has 192 cores running at 850 MHz. Both are installed on an EliteBook 8570w, which is a regular laptop.

The results indicate that there is a break-even around 2000 number of time-steps. For lower number of time-steps, the CPU will have the lowest computational time. If the number of time-steps is higher than 2000, using the GPU to do the simulations will give the results faster. Similar results for the number of time-steps where concluded in [58], where a panel code was implemented on a GPU.

In a simulation with a time-step of 0.01 seconds, 2000 time-steps are equal to 20 seconds. For a wind turbine, operating with a rotational speed of 12.3 rpm, the rotor will have rotated 4 times within this time period.

4.6 Cascade

So far, only individual blades have been discussed, and we are interested in investigating the aerodynamic loads for the whole rotor. The step from

modeling a single flat plate and calculating the lift force, to modelling a rotor and estimating the thrust force on a rotor, can be done by using a linear cascade. The linear cascade consists of an infinite number of vortex points located along the x-axis resembling an annular section in the rotor plane. The circulation from the neighbouring blades and wakes are now included in the calculation of the aerodynamic forces on the thin foil. The challenge of cascade modeling is to ensure that the method converges.

A stationary version, using conformal mapping, is presented first. This has been widely used in the design of turbo-machines. For the transient analysis, a method using sums is applied. Using the two different approaches, the effect of spacing between the blades and the velocity ratio, are discussed.

It is shown how the distance between the foil influences the resulting thrust force. A discussion with regards to the ratio between axial and tangential velocity influence the thrust force is also presented. This is relevant for wind turbines which will have different 2D spacing and velocity ratio along the blade. The velocity ratio is also wind speed dependent.

4.6.1 Conformal Mapping

Conformal mapping is a mathematical technique that is used to convert a mathematical problem in a particular space into another problem by transforming it via a conformal map to another space. Here we will use the technique to model an infinite sum of vortex points which are located along a line with a constant distance in the z plane, and transform it to the Z plane. Complex notations are applied when using this technique. This is illustrated in Figure 4.30.

In the z plane, a point p is described as $z = x + iy$, and in the Z plane as $\mu_{cm} e^{i\phi_{cm}}$. A straight line $p'p'$ parallel to the y-axis at a distance $\ln \mu_{cm}$ from the y-axis in the z plane is transformed to a circle $P'P'$ of radius μ_{cm} in the Z plane. The following relations can be used:

$$x = \frac{2\pi}{t_{cm}} \ln \mu_{cm} \tag{4.84}$$

$$y = \frac{2\pi}{t_{cm}} \phi_{cm} \tag{4.85}$$

where t_{cm} is the distance in the vortex array in the z plane. The method is illustrated using an array of point vortices in the z plane, and

a vertical uniform stream v_∞. The array of point vortices in the z-plane is a single point vortex in the Z plane.

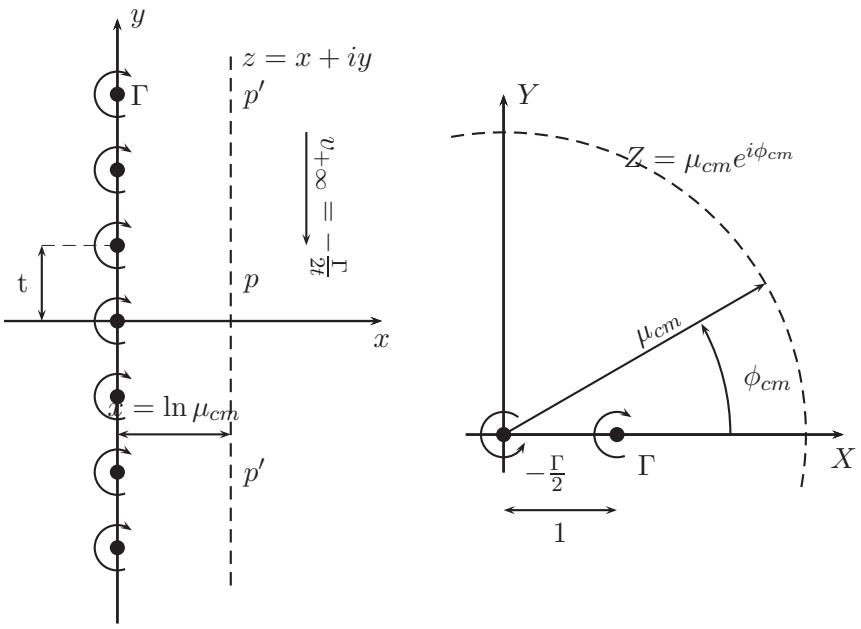

Figure 4.30: Transformation of vortex array in z plane to vortex pair in Z plane, based on figure in [59].

For a wind turbine rotor, t is the separation between the blade sections at a distance r from the hub ($t = 2\pi r/3$). The velocity, v_∞, which for a wind turbine is the combination of both incoming wind speed and rotational speed, is represented by a vortex element of strength $-\Gamma/2$ in the Z plane. The array of vortex elements are represented by a vortex element located at $\mu_{cm} = 1$. The velocity potential for a point vortex is given in Eq 4.38. Using complex notation, the velocity potential is [59]:

$$F(Z) = \frac{i\Gamma}{2\pi}\ln(Z-1) - \frac{i\Gamma}{4\pi}\ln(Z)$$

The velocities in the Z plane are:

$$U - iV = \frac{dF(Z)}{dX} = \frac{i\Gamma}{4\pi Z}\cdot\frac{(Z+1)}{(Z-1)}$$

This result is transformed into the z plane. The velocity due to an infinite array of point vortices located along the y axis is:

$$\begin{aligned} u - iv &= \frac{dF(z)}{dz} = \frac{dF(z)}{dZ}\frac{dZ}{dz} \\ &= \frac{i\Gamma}{4\pi} \cdot \frac{(Z+1)}{(Z-1)} \\ &= \frac{i\Gamma}{4\pi} \cdot \frac{(e^z+1)}{(e^z-1)} \end{aligned} \tag{4.86}$$

Traupel established the relation above for the velocities, using cascade theory in 1945 [60]. The formula can be rewritten into [59]:

$$u - iv = \frac{i\Gamma}{2t_{cm}} \left[\frac{\sinh(2\pi x/t_{cm}) - i\sin(2\pi y/t_{cm})}{\cosh(2\pi x/t_{cm}) - \cos(2\pi y/t_{cm})} \right] \tag{4.87}$$

We will not pursue this method further, but rather concentrate on cascade methods which are based on summing up the neighbouring airfoils.

4.6.2 Linear Cascade

The linear cascade method consists of several foils along a straight line. The induced velocity due to the vortex elements on the foils and in their wakes are considered. The vortices are modelled with equal strength for all foils in the linear cascade. However, in reality, the foils at the edges will have a different vortex strength, but this is assumed to have little influence on the flowfield around the foil in the middle of the cascade.

The advantage with the linear cascade compared to the conformal mapping described above, is that the unsteady aerodynamics will be included. In an ideal cascade, an infinite number of flat foils with chord length c are modeled, but we will have to use a finite amount of blades. A linear cascade with 7 airfoils is illustrated in Figure 4.31.

It is expected that as the distance between the foils, S_c, become larger, the influence of the neighbouring vortex elements is negligible. However, when the distance between the airfoils is small, the influence from neighboring foils may no longer be negligible. A vortex element of strength Γ_b is located at $c/4$ from the leading edge of each element. The normal velocity at the collocation point, x_{cp}, located at $3c/4$ is defined as zero. The induced velocity of the vortex element at the blades, $U_{i,b}$, and in the wake, $U_{i,w}$, is summed up and added to the wind and the rotational velocity. At the collocation point, the sum of these velocities is zero:

$$\sum_{i=-\infty}^{+\infty} u_{bl,i} + \sum_{i=-\infty}^{+\infty} u_{w,i} + U_Y \cdot \cos(\theta) + U_X \sin(\theta) = 0 \qquad at\ x_{cp} \quad (4.88)$$

where U_X is the velocity in the rotational direction, U_Y is the velocity normal to the rotor plane, and θ is the twist of the foil relative to the rotational direction. This is illustrated in Figure 4.31. There are two different coordinate systems in the illustration. A global system, X and Y, and a local coordinate system, x and y. The local velocities are calculated using the local coordinate system, which is tilted with the same angle as the foil, θ. The velocity normal to the foil due to a vortex point element is $v = \Gamma x_g / 2\pi(x_g^2 + y_g^2)$, where x_g and y_g are the distances to the vortex element from the collocation point, x_{cp}, in x and y direction.

An infinite number of airfoils is not feasible to compute, and the number will need to be restricted. If the sum of the influenced velocities from the wake and the blade are converging a limited amount of airfoils can represent an infinite number of airfoils. It is investigated whether the sum of the influenced velocities is converging. There is a large amount of different convergence tests, and we have restricted ourselves to the ratio test and Cauchy's convergence test. The ratio test assumes that for all n, $a_n > 0$, where a_n is the nth element. The series converge if $r < 1$, where r is defined as:

$$r = \lim_{n \to \infty} \left| \frac{a_{n+1}}{a_n} \right| \quad (4.89)$$

However, the ratio test is an inconclusive test for convergence. Another convergence test, the Cauchy condensation test, is a better test. According to Cauchy condensation test, if $\{a_n\}$ is a monotone decreasing sequence then $\sum_{n=1}^{\infty} a_n$ converges if and only if $\sum_{k=1}^{\infty} 2^k a_{2^k}$ converges.

We will start with examining the convergence of the first sum in Eq 4.88. The velocity at the collocation point, x_{cp}, due to the vortex point element located at the blades of the system, is:

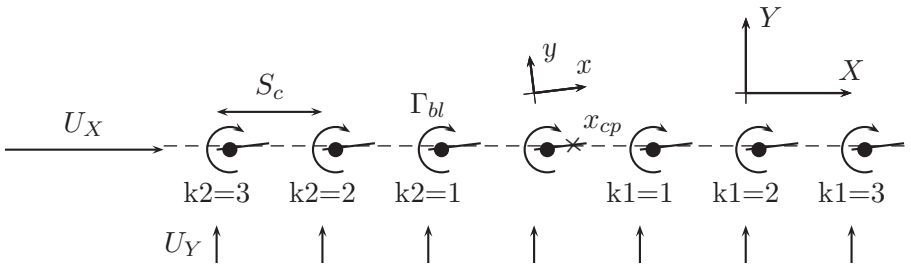

Figure 4.31: A sketch of the linear cascade. The dashed line is the rotor plane.

$$\sum_{i=-\infty}^{+\infty} u_{bl,i} = u_{bl,0} + \sum_{k_c=1}^{\infty} u_{bl,k_c} + \sum_{k_c=-1}^{-\infty} u_{bl,k_c} \tag{4.90}$$

$$= -\frac{\Gamma_{bl}}{2\pi r_{bl}^2} x_{bl} - \sum_{k1=1}^{\infty} \frac{\Gamma_{bl}}{2\pi r_{bl,k1}^2} x_{bl,k1} - \sum_{k2=1}^{\infty} \frac{\Gamma_{bl}}{2\pi r_{bl,k2}^2} x_{bl,k2} \tag{4.91}$$

where the origin of the coordinate system is at the collocation point, the x-axis is along the chord and r is the radial distance. The subscript bl is used for the blade vortex, and k_c for the summation. The element, $a_{bl,k}$, in the series is defined as:

$$a_{bl,k_c} = -\left(\frac{x_{bl,k1}}{2\pi r_{bl,k1}^2} + \frac{x_{bl,k2}}{2\pi r_{bl,k2}^2} \right)$$

$$= -\Bigg(\frac{-c/2 + k_c S_c \cos(\theta)}{2\pi \left[\left(-c/2 + k S_c \cos(\theta)\right)^2 + \left(-k_c S_c \sin(\theta)\right)^2 \right]} + \frac{-c/2 - k_c S_c \cos(\theta)}{2\pi \left[\left(-c/2 - k_c S_c \cos(\theta)\right)^2 + \left(+k_c S_c \sin(\theta)\right)^2 \right]} \Bigg) \tag{4.92}$$

where S_c is the spacing between the airfoils, k_c is the element number, and is equal to $k1$ and $k2$. In Figure 4.32, the normalized values of the sums are plotted for increasing k_c. The sums are normalized by the

influence of the vortex element located on the same foil as the collocation point, x_{cp}:

$$a_{bl,0} = \frac{1}{\pi c} \tag{4.93}$$

Different values of spacing, S_c, are investigated. The spacing is equal to a third of the circumference at the given radii, r. At the inner radii, the spacing between the airfoils is small, and a the sum will need a larger number of sequences to converge relative to the sections at the outer radii.

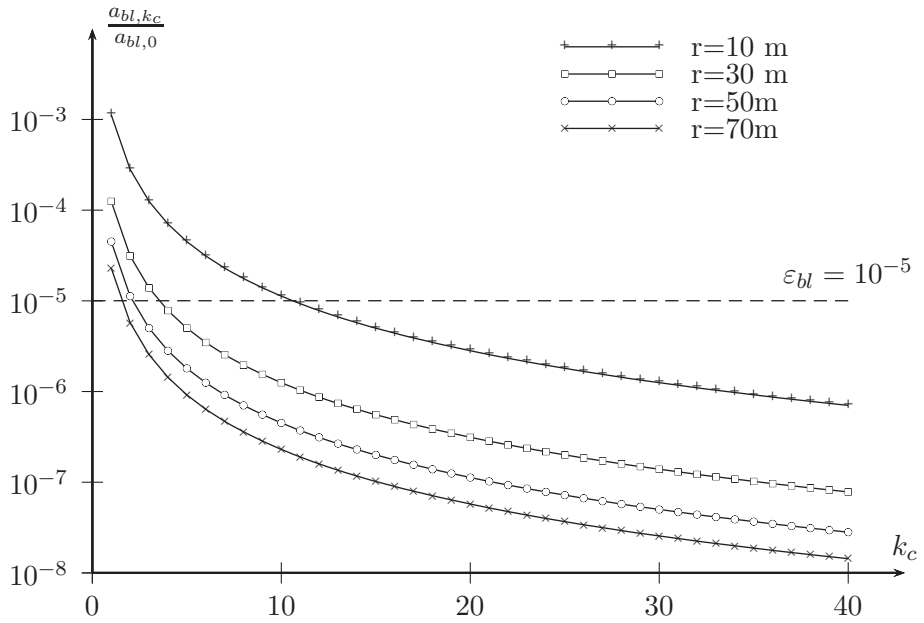

Figure 4.32: The elements of the series in Equation 4.90 for four different radial locations along the blade. The elements are plotted against the number of elements, k_c, in the series. A convergence limit, $\varepsilon = 10^{-5}$ is included in the graph.

The series, $\sum_{k_c}^{\infty} a_{bl,k_c}$, is converging according to the ratio test and the Cauchy condensation test. The convergence is faster for the foils with a large spacing relative to those with a small spacing. A limit, ε_{bl} is included to illustrate this, this will be referred to as the convergence limit. If $\varepsilon_{bl} = 10^{-5}$, the section located at the outer radii, at $r = 70m$, requires only $k = 2$ (5 foils), while the inner most foil at $r = 10$ requires $k = 11$ (23 foils). This is illustrated in Figure 4.32.

For the summation of wake elements, the amount of wake particles will increase with time since each airfoil in the cascade will produce a new wake element at each time step. We define l_w to be the number of wake elements shed from the trailing edge of one blade and l is the counter of wake elements. The induced velocity, due the wake elements in the linear cascade, at the collocation point is:

$$\begin{aligned}
\sum_{i=-\infty}^{+\infty} u_{w,i} &= \sum_{l=0}^{l_w} u_{w,0} + \sum_{l=1}^{l_w}\sum_{k1=1}^{\infty} u_{w,k1,l} + \sum_{l=0}^{l_w}\sum_{k2=1}^{\infty} u_{w,k2,l} \quad (4.94)\\
&= \sum_{l=1}^{l_w} \frac{\Gamma_{w,l}}{2\pi r_{w,l,0}^2} x_{w,l,0} + \sum_{k1=1}^{\infty}\sum_{l=0}^{l_w} \frac{\Gamma_{w,l}}{2\pi r_{w,l,k1}^2} x_{w,l,k1}\\
&+ \sum_{k2=1}^{\infty}\sum_{l=0}^{l_w} \frac{\Gamma_{w,l}}{2\pi r_{w,l,k2}^2} x_{w,l,k2} \quad (4.95)
\end{aligned}$$

where $r_{w,l}$ is the distance to the wake particle with strength $\Gamma_{w,l}$ shed at time-step l. The subscript 0 indicates that it is shed from the airfoil with the collocation point, x_{cp}, and $k1$ and $k2$ is the counter for the remaining foils in the linear cascade, see Figure 4.31. The distances given in Equation 4.95 are calculated as:

$$\begin{aligned}
r_{w,l,0}^2 &= [c/4 + \cos(\theta)\cdot(dxw + l\cdot U_x\cdot dt) - \sin(\theta)\cdot l\cdot U_y\cdot dt]^2\\
&+ [\sin(\theta)\cdot(dxw + l\cdot U_x\cdot dt) + \cos(\theta)\cdot l\cdot U_y\cdot dt]^2 \quad (4.96)\\
r_{w,l,k1}^2 &= [c/4 + \cos(\theta)\cdot(dxw + k_c\cdot S_c + l\cdot U_x\cdot dt) - \sin(\theta)\cdot l\cdot U_y\cdot dt]^2\\
&+ [\sin(\theta)\cdot(dxw + k_c\cdot S_c + l\cdot U_x\cdot dt) + \cos(\theta)\cdot l\cdot U_y\cdot dt]^2 \quad (4.97)\\
r_{w,l,k2}^2 &= [c/4 + \cos(\theta)\cdot(dxw - k_c\cdot S_c + l\cdot U_x\cdot dt) - \sin(\theta)\cdot l\cdot U_y\cdot dt]^2\\
&+ [\sin(\theta)\cdot(dxw - k_c\cdot S_c + l\cdot U_{rot}\cdot dt) + \cos(\theta)\cdot l\cdot U_y\cdot dt]^2 \quad (4.98)
\end{aligned}$$

where dt is the timestep and dxw is the length of the wake element. k_c is replacing $k1$ and $k2$, such that for $k_c = 1$ there is one airfoil in both negative and positive x-direction. The distance to the wake particles, that is shed from the blades in positive x-direction, will have a monotonly increasing distance as the number of particles is increasing. The influence from the wake particles shed from the foils located in negative X-direction, will not have monotone decreasing elements in the series. Neither the simple ratio test, nor the Cauchy's condensation test, is therefore applicable.

The normalized elements in the series are plotted in Figure 4.33 and are defined as:

$$a_{w,k_c} = \sum_{l=1}^{l_w} \frac{x_{w,l,k1}}{2\pi r_{w,l,k1}^2} + \sum_{l=1}^{l_w} \frac{x_{w,l,k2}}{2\pi r_{w,l,k2}^2} \tag{4.99}$$

$$a_{w,0} = \sum_{l=1}^{l_w} \frac{x_{w,l,0}}{2\pi r_{w,l,0}^2} \tag{4.100}$$

To investigate the convergence of the wake particles, the distance to the first wake particle is set to $c/4$ from the trailing edge. The wake particles will be translated in the direction of the wind at each time-step. The wind speed applied in the following example is 14 m/s. The rotational speed is set to 1.1 rad/sec, which corresponds to 10.5 rpm, and the investigated radii is 50 m.

The sum of the series are plotted in Figure 4.33 for four different simulation lengths, using varying number of foils in the linear cascade. It is only the shortest simulation that displays a monotonously decreasing curve. The remaining lines show an increase in value, a sudden drop in value, and then a short increase, prior to a monotonously decreasing curve. The dip is related to the time it takes for the mid-foil ($k_c = 0$) to travel to the initial position of the outer-most foil. The time it takes for the mid-foil to travel to its nearest neighbour is $t = S_c/U_X$. For the shortest simulation, the mid-foil has not yet reached the original position of the neighbouring foil ($k_c = 1$). However, in the three remaining simulations the mid-foil has traveled past the original position of the first 2, 5 and 20 foils in the cascade. As seen in Figure 4.33, the dip in the sums is also found at $k_c = 2$, $k_c = 5$, and $k_c = 20$ for the three simulation lengths.

The number of foils in the cascade must be such that k is past the dip, and where the sum of series in the linear cascade monotonously decreases for increasing number of elements. A limiting number of elements in the series for the sum to converge, k_p, is defined as:

$$k_p \geq \frac{l_w \cdot dt}{S_c} [U_x + U_y] \tag{4.101}$$

This number is referred to as the peak number. In Figure 4.33, the k_p values are 3 (t=390 s), 6 (960 s) and 24 (t=3810 s). The elements after this peak, are monotonously decreasing. This means that it fulfills

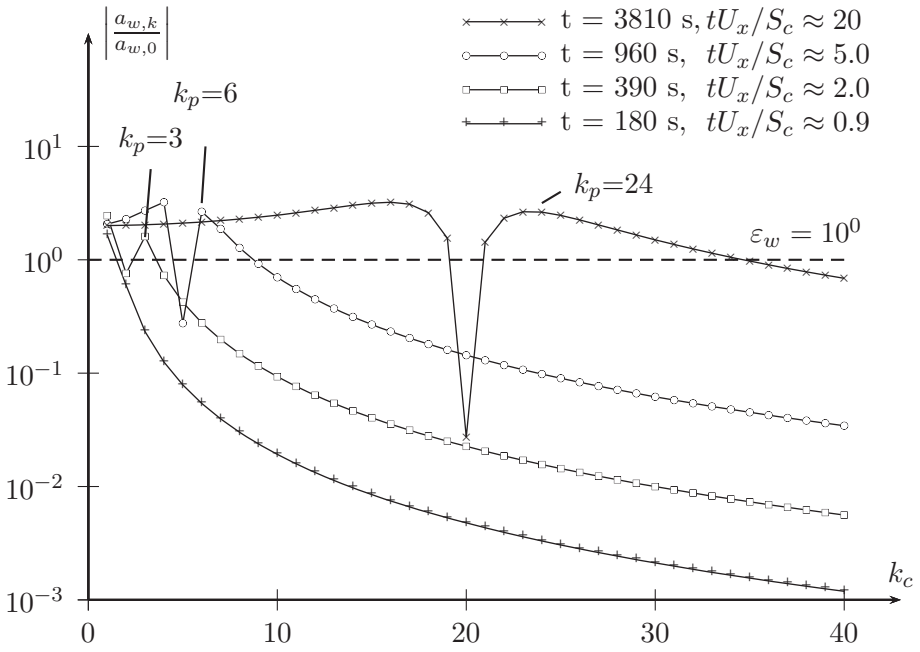

Figure 4.33: The sum of elements in Equation 4.99 considering four different simulation times. The sums are plotted relative to the number of foil elements in the cascade, and is monotonically decreasing for $k < k_p$.

the ratio requirement for convergence. Even though $k_c > k_p$ does not mean that it is sufficient number of foils to represent an infinite series of foils. In this study we suggest the additional requirement of a convergence limit ε_w. We will apply a convergence limit ε_w, for $k_c > k_p$, to limit the number of panels in the linear cascade. This is illustrated in Figure 4.33 with $\varepsilon_w = 10^0$. The shortest simulation does not require many foils, but for the longer simulations the number of foils are increasing fast. For an unsteady linear cascade simulation, the simulation time must therefore be included when choosing the number of foils in the linear cascade.

4.6.3 Application

The linear cascade can be used to evaluate the dynamics of a wind turbine rotor. The motivation is to investigate wether the wake of the neighbouring blades has an influence on the unsteady aerodynamic forces. A

reference case is presented, and the number of elements in the cascade k_c is evaluated. Following this a short discussion with regards to spacing and velocity ratio is presented. At the end, a varying velocity in the y-direction is investigated. This can represent a variation in wind velocity or oscillations of a wind turbine.

4.6.3.1 Reference case

A reference case, which is similar to a typical airfoil section located along a wind turbine blade, is used to study the sensitivity. Typical values for the dimensions and velocities of a section located 45 m from the hub will be applied. The foil has an initial twist of 3.2^o and a chord length of 3 m. The rotational velocity of the rotor is 12.3 rpm, and the wind speed is 12 m/s. Using an axial induction factor, a, of 0.3, the velocity in the y-direction, $U_Y = 8.4$ m/s. For a fully three dimensional vortex method the axial induction factor would be part of the solution, but this is not true for a two dimensional analysis. The velocity in the x-direction is due to rotation, $U_X = 58$ m/s. The flow angle between the two velocity components is 8.2^o, which gives an angle of attack at the section of 5^o. The stationary lift for the flat foil is:

$$L_\infty = \pi\alpha\rho c\left(U_X^2 + U_Y^2\right) \tag{4.102}$$

Using the values for the reference case, the stationary lift is 2.5 kN/m. The velocity of the free stream U_∞, is 58.6 m/s.

4.6.3.2 Number of Airfoils

The total number of airfoils used in the cascade is $n_{bl} = 2 \cdot k_c + 1$, where k_c is the number of elements used in the summations. As shown in the previous section, see Figure 4.33, the number of airfoils needed to achieve convergence of the cascade will vary with the velocities used and the length of the simulation. A cascade simulation is run for a time equal to six rotations of the wind turbine, $t_{max} = 30$ s. The number of blade vortices in the cascade should exceed $n_{bl} \geq 2 \cdot k_p + 1$, where k_p is peak value for the influences from the wake vortices defined in Equation 4.101.

7 different linear cascade analysis, with varying numbers of airfoils in the cascade, are simulated. The number of airfoils in the linear cascade are varied from 1 to 177 airfoils, and the length of the simulation is 30 s. The graph showing the results is in Figure 4.34. The x-axis is normalized

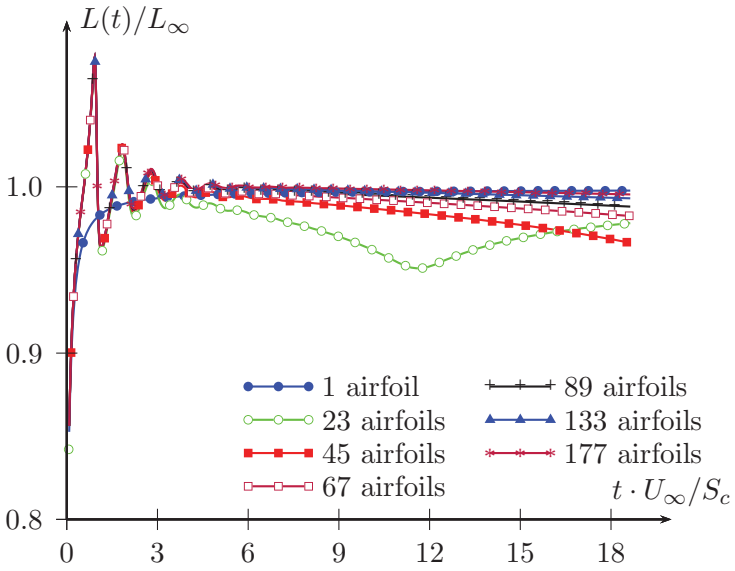

Figure 4.34: The transient loads using different number of airfoils in the cascade. The x-axis is normalized relative to the spacing between the airfoils

with regards to the spacing of the airfoils, and the y-axis is normalized with regards to the infinite reference lift, see Equation 4.102. The peak value, k_p, of the simulation is 22.

The number of airfoils are listed in Table 4.1 together with two convergence parameters, $L(t = t_{max})/L_\infty$ and $|\varepsilon|$. The last parameter, ε, is referred to as the convergence limit in this study, and is defined as the ratio between last element in the series relative to the induced velocity for the mid-foil. The convergence parameter is divided into one for the blade, ε_{bl} and one for the wake, ε_w.

The simulations which has $k_c < k_p$, the simulation with 1 airfoil and 23 airfoils, does not predict the unsteady aerodynamics well. The simulation with one blade has converged to the steady lift, but does not have the oscillating motion at the start of the simulation. The oscillation of the lift is due to the passing of vortices from neighbouring blades. This trend is shown for the simulation with 23 airfoils, but the a decrease in the lift at $U_\infty t/S_c = 11$ is due to the limited number of airfoils in the cascade. It is important to have a number of airfoils above the limit, k_p, if a dynamic

	k_c	n_{bl}	$\frac{L(t=t_{max})}{L_\infty}$	$\lvert\varepsilon_{bl}\rvert$	$\lvert\varepsilon_w\rvert$
single airfoil	0	1	0.998	-	-
$k_c = 0.5 \cdot k_p$	11	23	0.978	$4.21 \cdot 10^{-6}$	$4.50 \cdot 10^{-1}$
$k_c = k_p$	22	45	0.966	$1.05 \cdot 10^{-6}$	$3.31 \cdot 10^{-1}$
$k_c = 1.5 \cdot k_p$	33	67	0.983	$4.68 \cdot 10^{-7}$	$2.69 \cdot 10^{-1}$
$k_c = 2 \cdot k_p$	44	89	0.988	$2.63 \cdot 10^{-7}$	$2.30 \cdot 10^{-1}$
$k_c = 3 \cdot k_p$	66	133	0.993	$1.17 \cdot 10^{-7}$	$1.80 \cdot 10^{-1}$
$k_c = 4 \cdot k_p$	88	177	0.996	$6.58 \cdot 10^{-8}$	$1.51 \cdot 10^{-1}$

Table 4.1: Number of blade vortices in the cascade

solution is sought, in addition to requiring a convergence of the lift. These are values depending on the length of the simulation.

4.6.3.3 Spacing

To investigate the effect of the spacing between the blades, the numbers of blades are well above the limiting k_p. For this simulation, k_p is 24 elements in the series, and the number of blades in the linear cascade is 169 ($k_c = 84$). As specified previously, the foil investigated has a chord of 3 m and is located at a radial distance 45 m from the hub. It is interesting to investigate the effect of the spacing since this will effect the distance that the wake vortices travel between the blades. The spacing investigated is similar to a rotor with 1, 2, 3, 4 or 5 blades. The ratio between the chord length and the spacing between the airfoils, c/S_c, is a better non-dimensional measurement for the spacing than the number of blades. The details are given in Table 4.2, together with the specific solidity values.

In the simulation, the foils were initially at rest. The wind velocity is applied at the first timestep, this is equivalent to instantaneous pitch in angle of attack from 0^o. Here the angle of attack is 5^o. Since the time is non-dimensional, with regards to the spacing, the length of the simulations will differ. The simulation time is listed in Table 4.2 for the different simulations. The simulation with only one blade in the rotor has thus have a simulation time five times the simulation time of the simulation for a five bladed rotor.

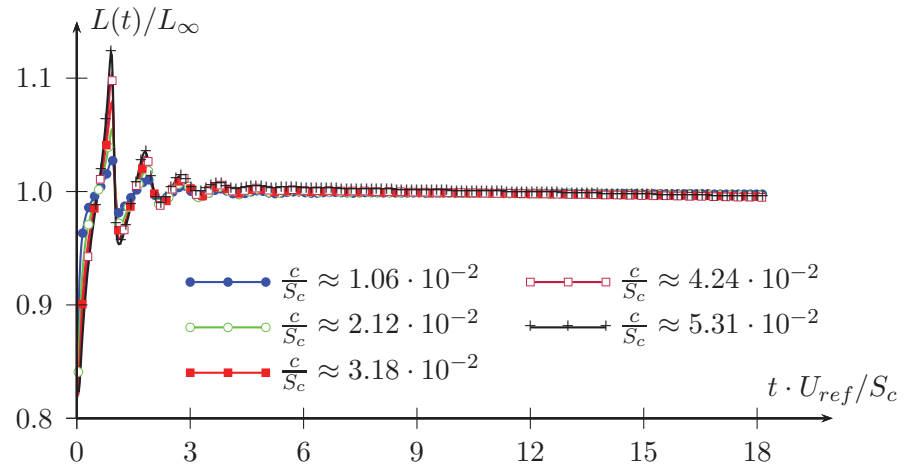

Figure 4.35: The transient loads using different spacing between the airfoils in the cascade. The x-axis is normalized relative to the spacing between the airfoils

no of blades	$\frac{c}{S_c}$	σ	t_{max}	$\lvert\varepsilon_{bl}\rvert$	$\lvert\varepsilon_w\rvert$	$\frac{L}{L_\infty}$	$\frac{L_{max}}{L_\infty}$
1	$\frac{c}{S_c} \approx 0.0106$	0.01	88	$8.02 \cdot 10^{-9}$	0.133	1.00	1.03
2	$\frac{c}{S_c} \approx 0.0212$	0.02	44	$3.21 \cdot 10^{-8}$	0.145	1.00	1.05
3	$\frac{c}{S_c} \approx 0.0318$	0.03	29	$7.22 \cdot 10^{-8}$	0.153	1.00	1.08
4	$\frac{c}{S_c} \approx 0.0424$	0.04	22	$1.28 \cdot 10^{-7}$	0.160	0.99	1.10
5	$\frac{c}{S_c} \approx 0.0513$	0.05	18	$2.00 \cdot 10^{-7}$	0.165	0.99	1.12

Table 4.2: A description of the five simulations with different spacing between the airfoils. The spacing distances are similar to a rotor with 1, 2, 3, 4 and 5 blades.

Figure 4.35 shows that all the resulting lift values are converging to the steady lift, and a sufficient number of foils is used in the simulation. The difference in the simulation is the unsteady behaviour at the start of the simulation. A shorter spacing gives an increase in the dynamic maximum lift.

4.6.3.4 Plunging oscillations of a linear cascade

As a result of the cascade modelling, the lift force will oscillate at a period equal to the time to travel the distance of one spacing, $T_{cas} = U_x S_c$. This will be referred to as the cascade oscillations. If the cascade oscillations have the same frequency as the eigenfrequency of the wind turbine structure, there may be an unsteady aerodynamic effect that is not captured by the unsteady aerodynamics of a single airfoil. An eigenfrequency that may be close to that of the cascade oscillations is the first tower bending mode. This is a mode that will give translations of the blades in the fore-aft direction.

In this study the incoming velocity, U_y, is varied to illustrate the transient load due to an oscillating cascade. Three blades are used in the rotor, and the radial distance from the hub is 45 m. A comparison is made to a single foil to compare the unsteady aerodynamics of a linear cascade and a single airfoil. The results are illustrated in Figure 4.36 for three different oscillation frequencies. The reduced frequency, k, is a common measurement of unsteadiness.

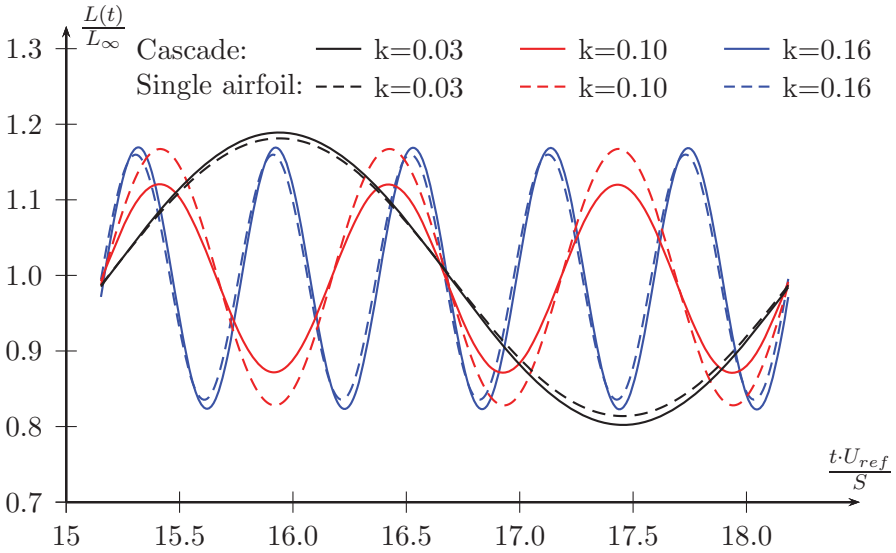

Figure 4.36: Illustration of the normalised lift for a single airfoil relative to a cascade airfoil using different oscillating periods to the wind field.

The single airfoil has a dashed line, while the cascade has a solid line in the graph. The variation seen in the simulation with a single airfoil is related to the unsteady aerodynamics that has been evaluated

by Theodorsen, see Section 4.4.3. The reduced frequency, k, is often used as an indicator of unsteadiness and is defined as $\frac{\omega c}{2U_\infty}$, where ω is the angular frequency, c is the chord length and U_∞ is the relative wind velocity. Here, $\omega = 2\pi/T_{osc}$ is shown in Table 4.3. It is expected that the amplitude of the lift will be reduced at increasing reduced frequencies. This is the trend for the unsteady aerodynamics using a single foil, but not for the linear cascade of airfoil, which is dependent on the oscillating frequency of the cascade in addition to the reduced frequency of the flow.

The linear cascade has the lowest value for the reduced frequency, $k = 0.1$. This is the value at which the period of the oscillations of the velocity, U_y, is the same as the time it takes for the airfoil to travel one spacing, $\frac{T_{cas}}{T_{osc}} = 1$. This will be discussed in more detail in Section 4.6.4.

ω_{osc} $[rad/s]$	$\frac{T_{cas}}{T_{osc}}$	$k = \frac{\omega c}{2U_\infty}$	$\frac{L(t)}{L_\infty}$ single	$\frac{L(t)}{L_\infty}$ cascade
1.29	1/3	0.03	1.18	1.19
2.58	2/3	0.07	1.17	1.18
3.86	1	0.10	1.17	1.12
5.15	4/3	0.13	1.16	1.18
6.44	5/3	0.16	1.16	1.17

Table 4.3: Spacing between the airfoils was 94 m and the cascade oscillation was 3.86 rad/s

Here, the oscillations modelled was a velocity change in the wind, from 7.4 m/s to 9.4 m/s. Another type of oscillation is the motion of a wind turbine. If the wind turbine is moving in the fore-aft direction, the velocity of the translation will induce an oscillating velocity felt by the wind turbine blades similarly to the oscillating velocity modelled here.

The unsteady aerodynamics is important for the dynamic load of the airfoil. For a wind turbine it is normally assumed that this can be modelled using approximation based on a single flat airfoil. In Table 4.3 the amplitudes are listed based on a single airfoil and a cascade of airfoils. The value is the lowest when the oscillation of the wind velocity is coinciding with the cascade oscillations.

4.6.4 Loewy's problem

In the linear cascade, the shed wake elements from neighbouring blades are included in the simulation. This can also be considered as returning wakes, which is a phenomena occurring for helicopters as well as wind turbines. The effect of the returning wake on helicopter rotors has been investigated by Loewy [61]. Loewy developed a function that can replace Theodorsen function, Loewy's function, $C'(k)$, when estimating the unsteady aerodynamic forces on a rotor.

The problem of returning wakes that Loewy solved, is shown in Figure 4.37. The schematic illustrates the problem for a helicopter rotor, where the incoming wind speed is opposite relative to a wind turbine. A series of 2D vortex sheets are modelled with a separation h. h is dependent on both the mean velocity through the rotor disc and on the number of blades, and for a wind turbine rotor the separation distance between the vortex sheets is:

$$h = \frac{2\pi}{N_b \Omega_{rot} U_Y} \tag{4.103}$$

If $h \to \infty$, Loewy function, $C'(k)$, will approach Theodorsen function, $C(k)$.

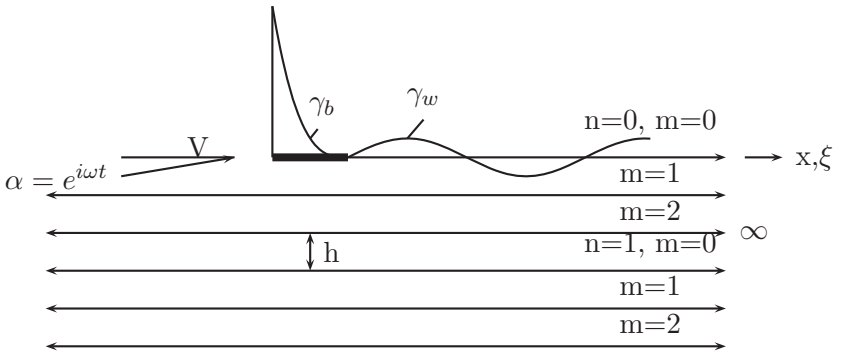

Figure 4.37: Illustration of Loewvys problem and the returning wake in his model. Based on illustration in [17].

Loewy's function is:

$$C'(k) = \frac{H_1^{(2)}(k) + 2J_1(k)W}{H_1^2(k) + iH_0^{(2)} + (J_1(k) + iJ_0(k))\,W}, \tag{4.104}$$

where k is the reduced frequency, H is the Hankel functions ($H_v^{(2)} = J_v - iY_v$), where J_v and Y_v are Bessel functions, and W is a complex function which for a rotor with N_b blades can be written as [17]:

$$W\left(\frac{kh}{b}, \frac{\omega_{osc}}{\Omega_{rot}}, \Delta\psi, N_b\right) = \left(e^{2kh/c} e^{i2\pi(\omega/N_b\Omega_{rot})e^{i(\Delta\psi)\omega_{osc}/\Omega_{rot}}} - 1\right)^{-1} \tag{4.105}$$

where $\Delta\psi$ is the phase shift between the blades. In this study the phase shift between the blades is zero, and the only phase shift in the wake vorticity results from the spacing between the blades.

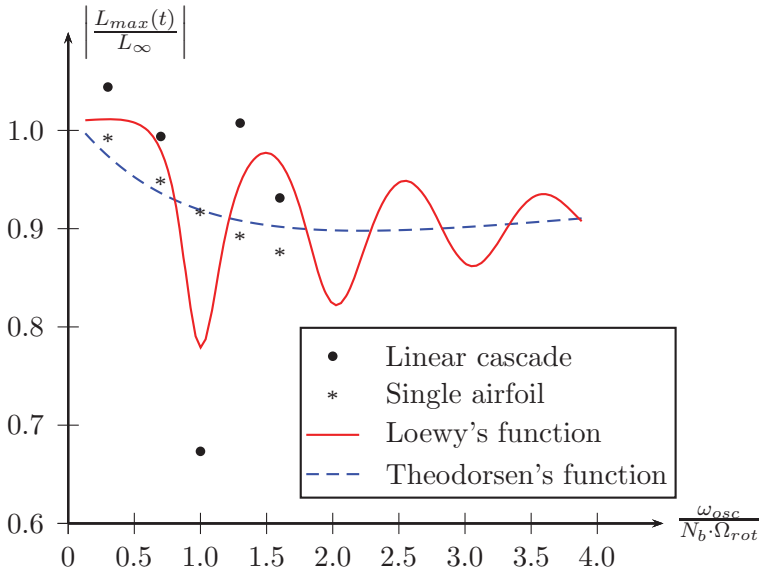

Figure 4.38: The normalized lift amplitude from Loewy's function having no phase shift between the trailing wake and the returning wake compared to Theodorsen's function.

Figure 4.38 shows a comparison between the normalized lift amplitude using Loewy's function and Theodorsen's function. It also includes

5 simulation results with a single point vortex method, and 5 simulation results with the linear cascade point vortex method. The single point vortex simulation results have the same trend as the results estimated using Theodorsen's function. These are both without the effect of the returning wakes. The linear cascade and Loewy's function, both include the effect of returning wake, and have a similar behaviour. It is evident that not including the returning wake when estimating the unsteady aerodynamic lift force for a rotor can give erroneous results.

The rotor speed, Ω, is 1.29 rad/s, which is equivalent to 12.3 rpm. For a three bladed rotor, the reduced frequency, where the rotor oscillations are in phase with the blade frequency is, $N_b\Omega c/2U_{ref} \approx 0.1$. In Figure 4.38, it is seen that Loewy's function, $C'(k)$, has a dip when the ratio between blade frequency, ω_{osc} and the blade passing frequency $N_b\Omega_{rot}$ is an integer. The simulation results are from the simulations presented in Figure 4.36. The real part of the lift is estimated using the lift force moving in phase with the velocity.

For a wind turbine, the blade passing frequency is often referred to as 3P. The eigenfrequencies of modern wind turbines are designed to avoid this frequency, this was discussed in Section 2.7.3. There are large excitation loads at the 3P frequency due to the tower passing and turbulence in the wind field. However, the 3P is not a constant frequency but will vary with the rotor speed and the wind turbine is likely to operate with a 3P frequency close to a structural eigenfrequency of the wind turbine structure.

Both the linear cascade method and Loewy's function predict a low unsteady aerodynamic lift, compared to the single airfoil method and Theodorsen's function, when the blade frequency is coinciding with the blade passing frequency, $\frac{\omega_{osc}}{N_b \cdot \Omega_{rot}} = 1$. For blade frequency not close to the blade passing frequency it is opposite, and Theodorsen's function and the single airfoil method predicts the lower unsteady aerodynamic lift. The difference is largest for the low reduced frequencies, and when there is little spacing between the wakes relative to the chord length [17].

A discussion of Loewy's function and the effect on damping of the blade in flapwise direction for helicopters is found in [17]. In hover, there are similarities between the flow around wind turbines and helicopters. The effect described by Loewy's function has indirectly been studied by Daughaday [62] on helicopter blades. Based on the measurement it was concluded that the damping was reduced for frequencies that were multiples of the rotor rotational frequency. This is similar to what is observed

in Figure 4.38. If these effects are related to the wind turbine, the spacing between the wakes would be lowest for wind speeds at rated or lower. The rotational frequency of the blades, Ω_{rot}, is reduced as the wind turbine rotors are getting larger, the trend is therefore that one are moving towards the lower frequencies. For lower values of reduced frequency, the damping of the blade flapping is reduced and the vibratory response of the blade to the harmonic airloads is increased. The risk may be, that this lead to lower damping of both the blade flapping and the elastic tower bending modes in the fore-aft direction. Several other studies have measured the effect of Loewy's function [63, 64, 65].

The Loewy's function approaches the Theodorsen solution as the relation h/c increases. Since h increases if the wind speed increase, or the rotational speed of the wind turbine decrease, the ratio between these velocities are important for the observed cascade effect. Both the wake geometry and the phasing is important for the unsteady aerodynamics acting on a wind turbine.

4.6.5 Conclusion

Based on a simplified vortex analysis using a single vortex to model the airfoil, an approach using the linear cascade to model a wind turbine rotor is shown. The method must be used with care since too few foils in the cascade may lead to inaccurate estimates of the transient loads. The number of foil elements required is dependent on the length of the simulation. As a minimum, the cascade should consist of $2 \cdot k_p + 1$ foils, where k_p is varying with the simulation length, spacing between foils and the velocities (see Eq 4.101).

The minimum k_p number above does not guarantee a robust simulation of the unsteady aerodynamic lift. In addition a ratio between the velocity influence from the mid-foil wake, relative to induced velocity from the outer cascade foil wake, ε_w, should be evaluated. In Table 4.1, ε_w, of 0.15, gave relatively good results.

The unsteady aerodynamic loads, when considering a cascade of airfoils, will differ from the unsteady aerodynamic loads from a single airfoil. The largest difference was found when the external oscillation frequency was equal, or a multiple, to the cascade oscillation frequency. It was found that the results from the linear cascade simulation were similar to the theoretical results given by Loewy's function, which is an analytic solution for the returning wake problem.

Chapter 5

Numerical Panel Vortex Code

5.1 Introduction

In the previous chapter, the vortex theory is presented together with some basic application of modelling the lift of a simple airfoil. The airfoils are getting increasingly complex in order to get an optimized design of the wind turbine. The potential vortex theory can also be applied to more complex shapes. In 1975, Hess used boundary element techniques to compute the potential flow past airplane hulls. This method, where the governing integral equations of the vortex method are discretized, is commonly known as the panel methods [50].

Even though the panel vortex method is inviscid, which means that the stall limit will not be captured, the method can still provide useful insight when it comes to unsteady aerodynamics for attached flow. The unsteady aerodynamics for attached flow included in most BEM codes is based on thin airfoils. One example is the Küssner function (Section 3.6.3). The vortex panel code presented in this chapter accounts for the thickness of the airfoil.

In this chapter a specific panel vortex code is described. This code is implemented in a cascade analysis and the aerodynamic damping for a floating 5 MW wind turbine is established. The code is also implemented in a GPU to show the reduced computational time that can be achieved. The structure of the code is essential to the case studies performed later, and is presented in detail in this chapter. The panel elements are first in-

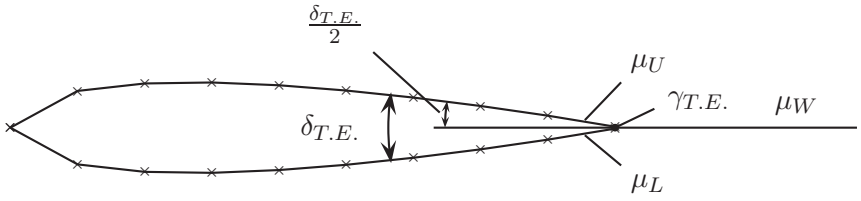

Figure 5.1: A NACA 0012 descretized into 20 linear elements illustrating the implementation of the Kutta condition.

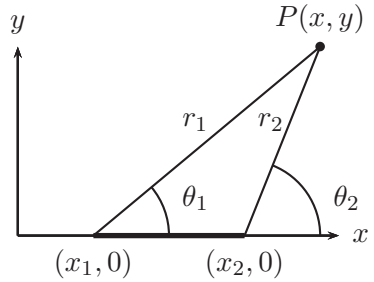

Figure 5.2: A linear panel element, and an influence point, P(x,y)

troduced, followed by the boundary condition applied and the modelling of the wake. This is sufficient information to construct a vortex panel code, and this is the code implemented into Matlab. The difference between the code implemented on a CPU compared to a GPU is outlined. For validation of the code both the pressure distribution at a steady state and the unsteady aerodynamic behaviour is investigated. Finally, the results of implementing the code in a cascade analysis is shown.

5.2 Singular elements

This work uses two dimensional linear panel elements, with constant strength, on the surface of the airfoil. The discretization of the airfoil surface into panels is shown in Figure 5.1. Two different singular elements are used for the airfoil surface; doublet and source. The wake is modeled using the vortex point elements, which is briefly described in Section 4.3.2, and in more details in this section.

The nomenclature in Figure 5.2 will be used in this section. These are easily converted into cartesian coordinates used in the panel vortex

code:

$$\theta_k = \tan^{-1}\frac{y}{x-x_k}, \quad r_k = \sqrt{(x-x_k)^2+y^2}, \quad k = 1,2 \tag{5.1}$$

5.2.1 Constant Source Element

From Section 4.3.3, the velocities and velocity potential due to a surface distribution of source elements is given in Equations 4.40, 4.41 and 4.42. The source distribution over each element is constant. Using the nomenclature shown in Figure 5.2 the velocity potential and its derivatives are:

$$\phi_s(x,y) = \frac{\sigma}{4\pi}\left[(x-x_1)\ln r_1^2 - (x-x_2)\ln r_2^2 + 2y(\theta_2-\theta_1)\right] \tag{5.2}$$

$$u_s(x,y) = \frac{\sigma}{2\pi}\ln\frac{r_1}{r_2} \tag{5.3}$$

$$v_s(x,y) = \frac{\sigma}{2\pi}(\theta_2-\theta_1) \tag{5.4}$$

5.2.2 Constant Doublet Element

The integral of the influence of a two-dimensional doublet distribution at a point in space was presented in Eq 4.44, 4.45 and 4.46. For a constant strength doublet element, with the orientation of the doublet as illustrated in Figure 4.12, the velocity potential and derivatives are:

$$\phi_d(x,y) = -\frac{\mu}{2\pi}\left[\tan^{-1}\frac{y}{x-x_2} - \tan^{-1}\frac{y}{x-x_1}\right] \tag{5.5}$$

$$u_d(x,y) = -\frac{\mu}{2\pi}\left[\frac{y}{(x-x_1)^2+y^2} - \frac{y}{(x-x_2)^2+y^2}\right] \tag{5.6}$$

$$v_d(x,y) = \frac{\mu}{2\pi}\left[\frac{x-x_1}{(x-x_1)^2+y^2} - \frac{x-x_2}{(x-x_2)^2+y^2}\right] \tag{5.7}$$

The potential distribution is not continuous across the surface as commented in Section 4.3.3. If the point, $P(x,y)$, is on the surface element the velocity potential is:

$$\phi(x,0\pm) = \mp\frac{\mu}{2} \tag{5.8}$$

and similarly for the velocity components:

Figure 5.3: The constant doublet element is similar to two point vortices, and will give the same velocities in the far-field.

$$u(x, 0\pm) = 0 \quad v(x, 0) = \frac{\mu}{2\pi}\left[\frac{1}{(x-x_1)} - \frac{1}{(x-x_2)}\right] \tag{5.9}$$

5.2.3 Vortex point element

The vortex point element has a very useful relation to the constant doublet element. A constant doublet element with strength μ, is similar to two vortex point elements with strength μ and $-\mu$ [52]. The relation is illustrated in Figure 5.3. The strength of the wake shed from the trailing edge can thus easily be transformed from a doublet panel element with constant strength to a vortex point element.

The vortex point element is used to model the wake. The velocities in the cartesian coordinate system due to the vortex point element at (x_0, y_0) are:

$$u_v = \frac{\Gamma}{2\pi}\frac{y - y_0}{(x - x_0)^2 + (y - y_0)^2} \tag{5.10}$$

$$v_v = -\frac{\Gamma}{2\pi}\frac{y - y_0}{(x - x_0)^2 + (y - y_0)^2} \tag{5.11}$$

5.3 Boundary Conditions

5.3.1 No flow through surface

Section 4.2.6 gives a general introduction to the two different boundary conditions normally applied to a surface for no flow through the surface. For the numerical panel code developed here, the Dirichlet boundary condition is used, where the potential inside the surface of the airfoil is constant. This potential can be chosen as equal to the free-stream velocity

potential, ϕ_∞. The velocity potential inside the surface of the airfoil, ϕ_i^*, is therefore:

$$\phi_i^* = (\phi + \phi_\infty)_i = \phi_\infty \tag{5.12}$$

The inner potential could be chosen as any constant values, but the advantage of using the free stream velocity potential is that the velocity potential due to the singularities distributed along the boundary is now zero:

$$\phi_i = \phi_i^* - \phi_{\infty_i} = 0 \tag{5.13}$$

It follows from the no-flow requirement that $\frac{\partial \phi^*}{\partial n} = 0$ (where ϕ^* is the total velocity potential) on the outer surface of the airfoil. The drop in velocity potential across the boundary, due to the singularities at the boundary, is thus

$$\begin{aligned} \frac{\partial \phi^*}{\partial n} &= \frac{\partial \phi}{\partial n} + \frac{\partial \phi_\infty}{\partial n} \\ \frac{\partial \phi}{\partial n} &= -\frac{\partial \phi_\infty}{\partial n} = -\vec{n} \cdot \vec{Q}_\infty \end{aligned} \tag{5.14}$$

The sources are associated with the velocity potential normal to the boundary across the boundary, ref Eq 4.23. They are therefore used to model the thickness of the airfoil, and the no-flow through boundary condition.

$$\begin{aligned} \sigma &= \frac{\partial \phi^*}{\partial n} - \frac{\partial \phi_i^*}{\partial n} = \frac{\partial \phi}{\partial n} - \frac{\partial \phi_i}{\partial n} \\ \sigma &= \frac{\partial \phi}{\partial n} = -\vec{n} \cdot \vec{Q}_\infty \end{aligned} \tag{5.15}$$

The potential inside the airfoil due to the singularity distribution was shown to be zero in Eq 5.13, and therefore $\frac{\partial \phi_i}{\partial n}$ is also zero. The distribution of sources on the boundary of the airfoil are now known. This can be used to define the doublet distribution around the airfoil.

Applying only source elements will also provide a solution of the flow field. However, the Kutta condition will not be satisfied when there are only source elements used. By including doublet elements in the solution, the Kutta condition can be satisfied.

5.3.2 Wake Strength

The solution of the doublet strengths using the no-flow boundary condition is not unique. A boundary condition needs to be applied at the trailing edge to ensure that the flow leaves the trailing edge in a smooth manner. This is typically done by applying the two dimensional Kutta condition, which states that the proper circulation is the value that causes the flow to leave smoothly at the trailing edge of the airfoil. The requirement of zero vorticity at the trailing edge gives a smooth flow at the trailing edge, $\gamma_{T.E.} = 0$. The strength of the vortex can be related to the doublet strength as:

$$\frac{\partial \mu(x)}{\partial x} = -\gamma(x) \tag{5.16}$$

From this it follows that there should be no difference in the doublet strength elements at the trailing edge:

$$\mu_U - \mu_L = \mu_W \tag{5.17}$$

where μ_L and μ_U are doublet strength for the lower panel and upper panel element at the trailing edge as shown in Figure 5.1. The wake shape will be discussed in more detail in Section 5.5.1.

5.4 Linear Algebraic Equations

5.4.1 Surface Discretisation

The surface of the airfoil is discretized into linear elements. A NACA 0012 is discretized into 20 panels in Figure 5.1. The number of panels and location of panels have an influence on the solution of the aerodynamic loads. Especially at the trailing edge and at the leading edge the panel elements should be chosen carefully.

The influence of the singular elements were given relative to a local coordinate system. For each element a local coordinate system is therefore needed, and a point $P(x, y)$ is given in the local coordinate system of the panel element.

The first element on the airfoil is the lower panel element on the trailing edge, and the last is the upper element on the trailing edge. If there is a gap between the lower and upper element at the trailing edge, the gap is closed by adding two additional panel elements at the trailing

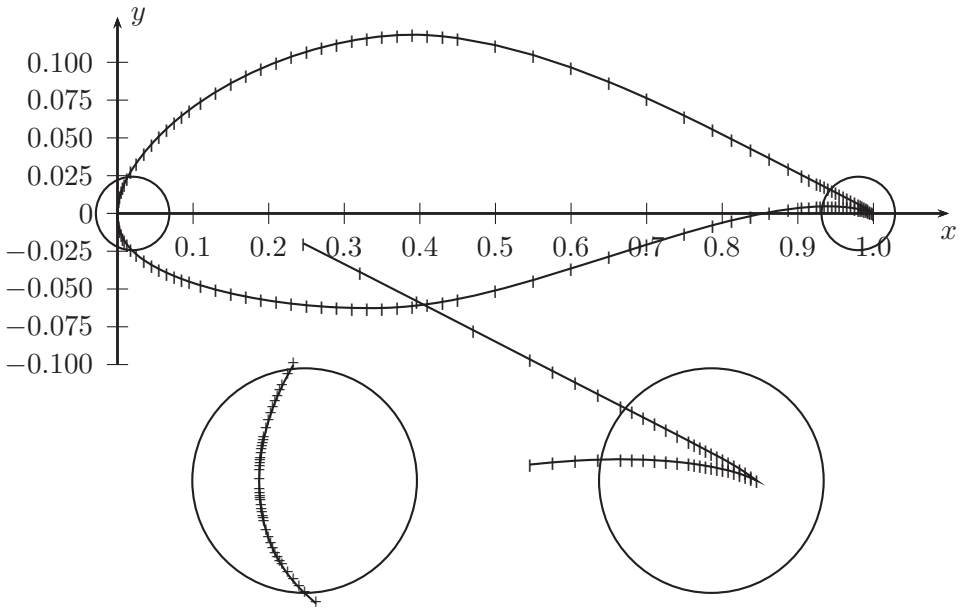

Figure 5.4: The NACA 64 airfoil divided into 228 panel elements. The circled areas around the leading and trailing edge are enlarged three times.

edge. An example of a gap closed by additional panels is given in Figure 5.5.

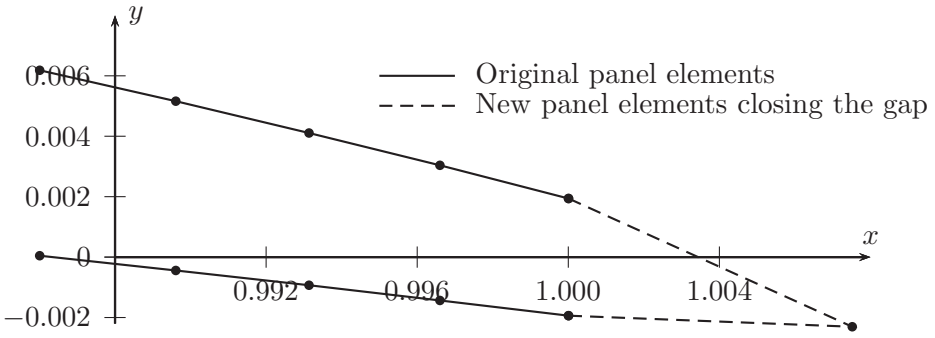

Figure 5.5: A gap between the panels at the trailing edge is closed by additional panels. The airfoil illustrated here is the DU21 profile.

5.4.2 Collocation Point

A collocation point is located at the middle of each panel. For the Dirichlet boundary condition, it is important that the collocation is inside the airfoil boundary. The linear algebraic equation to be solved for at each of the N collocation points is now:

$$\sum_{k=1}^{N} \frac{1}{4\pi} \int_{airfoil} \sigma \left(\frac{1}{r}\right) - \frac{1}{4\pi} \int_{airfoil} \mu \vec{n} \cdot \nabla \left(\frac{1}{r}\right) dS \quad - \\ \sum_{l=1}^{N_W} \frac{1}{4\pi} \int_{wake} \mu \vec{n} \cdot \nabla \left(\frac{1}{r}\right) dS \quad = \quad 0 \quad (5.18)$$

The influence of constant strength source element at panel k at the collocation point (x_j, y_j) is $B_{k,j}$, and the influence from a constant doublet element is $C_{k,j}$. Equation 5.18 can be written as:

$$\sum_{k=1}^{N} C_{k,j}\mu_k + \sum_{l=1}^{N_W} C_{l,j}\mu_l + \sum_{k=1}^{N} B_{k,j}\sigma_k = 0, \qquad at\ (x_j, y_j) \qquad (5.19)$$

where:

$$B_{k,j} = \phi_{s,k}(x_j, y_j) \quad (5.20)$$
$$C_{k,j} = \phi_{d,k}(x_j, y_j) \quad (5.21)$$
$$C_{l,j} = \phi_{d,l}(x_j, y_j) \quad (5.22)$$

where the velocity potentials are defined in Equations 5.2 and 5.5, and the strength of the singular elements are one. These are the difference in velocity potential at a point (x_j, y_j) due to a panel element coefficients for the panel element k at the airfoil or element l in the wake. $B_{k,j}$, $C_{k,j}$ and $C_{l,j}$ are often referred to as the influence coefficients.

5.5 Vortex Panel Code

The vortex panel code is coded in Matlab. An overview of the program is shown in Figure 5.6. For each timestep, there are $N + 1$ unknowns to be solved, where N is the number of panel elements on the airfoil surface.

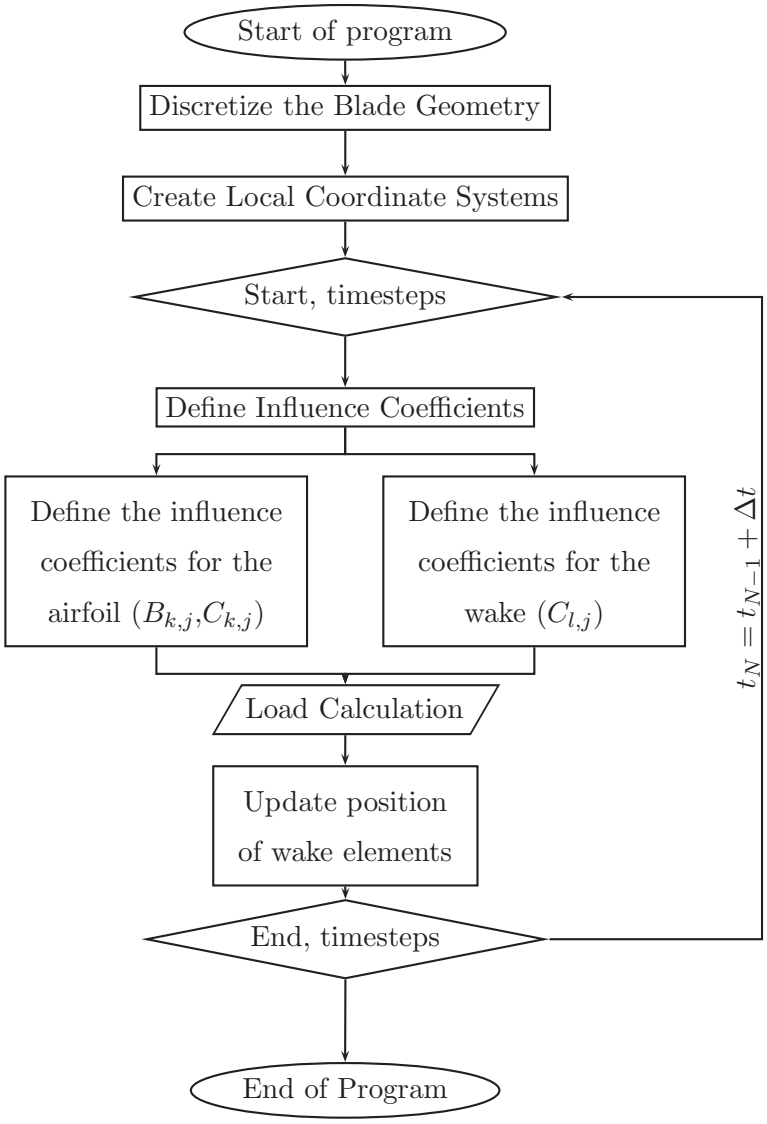

Figure 5.6: A flowchart for the Vortex Panel Code

The Kutta condition (Eq 5.17) reduces the amount of unknowns to N. The doublet influence is rewritten such that:

$$\begin{aligned} A_{k,j} &= C_{k,j}, \qquad j \neq 1, N && (5.23)\\ A_{k,j} &= C_{k,j} - C_{k,N+1}, \qquad j = 1 && (5.24)\\ A_{k,j} &= C_{k,j} + C_{k,N+1}, \qquad j = N && (5.25) \end{aligned}$$

where the wake panel shed at time-step t, is included in the doublet matrix, $A_{k,j}$ at time t. The strength of the wake elements are known, but their position needs to be updated for every time-step.

The source influence coefficients and source strengths are moved to the right hand side of the equation, and solved. This is only needed to be done once, and can be used for all time-steps as long as the shape of the body is constant. This is the RHS_s. For each time-steps a RHS_w vector containing the influence vector of the wake and the doublet strengths needs to be calculated. The RHS vector is established by adding RHS_s and RHS_w together.

$$\begin{aligned} RHS_s &= -\sum_{j=1}^{N} B_{k,j}\sigma_k && (5.26)\\ RHS_w &= -\sum_{l=1}^{N_W} C_{l,j}\mu_l && (5.27)\\ RHS &= RHS_s + RHS_w && (5.28) \end{aligned}$$

Following the steps above, one has the following matrix equation to be solved:

$$\begin{pmatrix} A_{11} & A_{12} & ... & A_{1N} \\ A_{21} & A_{22} & ... & A_{2N} \\ ... & ... & & ... \\ A_{N1} & A_{N2} & ... & A_{NN} \end{pmatrix} \begin{pmatrix} \mu_1 \\ \mu_2 \\ ... \\ \mu_N \end{pmatrix} = \begin{pmatrix} RHS_1 \\ RHS_2 \\ ... \\ RHS_N \end{pmatrix} \qquad (5.29)$$

The strength of the doublets, μ_k can now be calculated. Based on this the circulation can be calculated, which is used when calculating pressure and velocity.

5.5.1 Modelling the wake

The near wake has an influence on the unsteady aerodynamic load. A good model of the wake is not limited to calculating the strength of the panel elements, the positions of the panel elements are also important. The wake will move due to the influence of the wind speed and the panel elements in the wake and along the surface of the airfoil.

The wake panel elements are shed from the trailing edge at an angle that is half the angle between the upper panel and the lower panel. The length of the first panel, d_w, element is given as a relation between the velocity and the time-step of the simulation:

$$d_w = 0.3U_{ref}dt$$

The velocity at the panel elements due to the influence of the source elements is calculated using Equations 5.3 and 5.4. Similarly, Equations 5.6 and 5.7 are used to estimate the velocity due to the influence of the constant strength doublet elements along the airfoil. The velocity due to the wake itself is estimated using the influence from vortex panel element, see Equations 5.10 and 5.11.

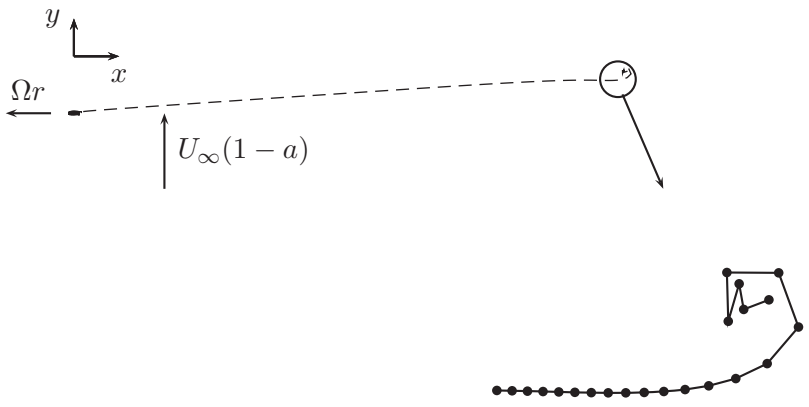

Figure 5.7: Wake roll-up behind an airfoil

The displacement is estimated using the wind speed and the velocity due to the influence of the singular elements at the vortex element in the wake. Figure 5.7 illustrates a typical roll-up behind the blade. This roll-up is a due to the relatively large vortex strength at the start of the simulation.

5.5.2 Load Calculation

The pressure around the airfoil is computed using the strength of the doublet elements. The doublet was defined as the difference in potential between the external and internal fluid potential in Eq 4.22. The potential inside the airfoil surface is constant, and is specified to be equal to the velocity potential of the free stream (see Eq 5.12). Using these limitations, the velocity potential at the outer surface of the airfoil is:

$$\phi_i = \phi_e - \mu \tag{5.30}$$

The tangential velocity of the flow at the airfoil surface is calculated from the derivative of the velocity potential along the surface:

$$q_t = \frac{\partial \phi_i}{\partial l} \tag{5.31}$$

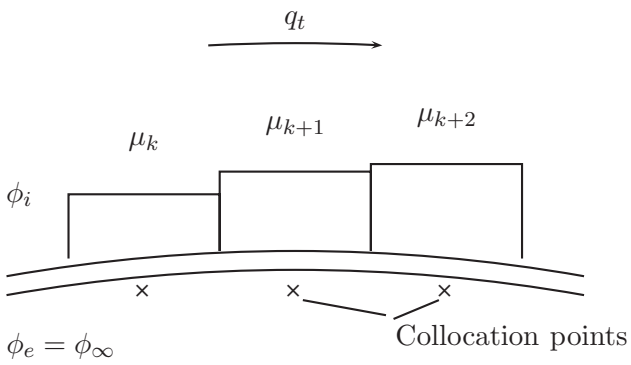

Figure 5.8: Doublet elements along the surface of an airfoil

An illustration of the doublets elements along the airfoil is shown in Figure 5.8. In the vortex code a simple numerical approach to finding the velocity is applied:

$$\phi_i(x_{cp}, y_{cp})_k = U_\infty x_{cp,k} + V_\infty y_{cp,k} - \mu k \tag{5.32}$$

$$q_{t,k} = \frac{\phi_{k+1} - \phi_k}{\Delta l_k} \tag{5.33}$$

where l is the length of the panel elements, and cp specifies that these are values at collocation points. The pressure coefficient between the panel elements, in steady state conditions, are estimated using the above result relative to the free wind speed:

$$C_{p,k} = 1 - \frac{q_{t,k}^2}{Q_\infty^2} \tag{5.34}$$

The pressure field around a NACA 0012 airfoil, using this approach, is shown in Figure 3.5. For a time-stepping approach, the unsteady Bernoulli equation should be used to estimate the pressure distribution. In addition to the tangential velocity, the change in velocity potential with time, is included in the pressure calculation:

$$\frac{p_{ref} - p}{\rho} = \frac{Q^2}{2} - \frac{v_{ref}^2}{2} + \frac{\partial \phi}{\partial t} \tag{5.35}$$

The nature of this unsteady aerodynamic force term is discussed earlier in Section 3.6 and in Section 4.4.3. The lift force of the blade section can be estimated from:

$$L = \rho U(t)\Gamma(t) + \rho \int_0^c \frac{\partial}{\partial t}\Gamma(x,t)dx \tag{5.36}$$

where ρ is the air density and Γ is the circulation. The circulation is calculated from the constant strength doublet panels. The constant doublet distribution is equivalent to two point vortices with opposite sign at the panel edges with opposite sign at the panel edges such that $\Gamma = -\mu$.

5.6 Cascade Approach

The aim of this study is to investigate the wind turbine rotor using the panel vortex code. So far, a solution for the lift on a single two-dimensional airfoil of arbitrary shape is established. The step from airfoil analysis to rotor analysis is done using a cascade approach. The methodology used is similar to what was presented in Section 4.6.

A constant wind speed, U_∞, in the global axial direction, Y, is applied normal to the wind turbine rotor. The rotational velocity at the blade segment at r is Ωr m/s. The dotted lines illustrates the wind turbine tower and the path that the segment is moving along. In the analysis, the airfoil is accelerated from 0 m/s to a rotational velocity of Ωr m/s.

For a wind turbine rotor, the wake shed from the trailing edge of the airfoil is forming a spiral shape, after a full rotation of the rotor, at $t = 2\pi/\Omega$,. The wake that was shed at the initial time-step, has moved

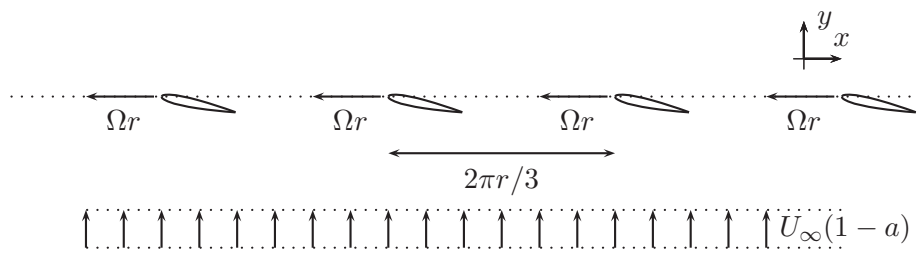

Figure 5.9: Cascade of airfoils

in the axial direction due to the wind speed, U_∞. Since there are three airfoils, there will also be three wakes that are shed.

The linear cascade is an infinite row of airfoils, located at equal intervals parallel to the y-axis, as illustrated in Figure 5.9. Applying the cascade method directly into the panel vortex code would imply that the singularities used to model the aerodynamic forces along the airfoil would be repeated an infinite number of times as well. Limiting the number to 50 airfoil elements may yield adequate representation for the center airfoil, and this would require more computational time.

Before presenting the methodology used in the study, a short presentation of the method using conformal mapping is discussed. This is the method that has typically been used for cascade analysis of turbo-machineries. The conformal mapping technique has been used to analyse the efficiency of turbo-machineries for decades. The approach is however limited to steady flow conditions, and in this study we are focusing on the unsteady flow.

5.6.1 Conformal Mapping

Conformal mapping takes advantage of the periodicity in the y-direction. Each airfoil will have the same singularity distribution along the surface and in the wake. The k^{th} panel element on each airfoil will therefore have the same strength, σ_k and μ_k. The influence on the collocation point located at the m^{th} panel element can be included in coupled influence coefficients. For the singular element panel with a constant doublet strength, which has a velocity potential as given in Equation 5.5, the influence on the element m due to the k^{th} element is:

$$\phi_{d,m}(x,y) = \sum_{k=1}^{\infty} -\frac{\mu_k}{2\pi}\left[\tan^{-1}\frac{y}{x-x_{2,k}} - \tan^{-1}\frac{y}{x-x_{1,k}}\right] \tag{5.37}$$

This can be done similar for the constant source element in Equation 5.2. In the conformal mapping, the cascade of airfoils located in a z-plane is transformed into a Z plane as shown in Figure 4.30. The relation between the z-plane and the Z-plane is $Z = e^{\frac{2\pi}{t}z}$. t is the distance between the vortex elements in the z-plane. In a wind turbine rotor the distance is $t = 2\pi r/3$, where r is the radius where the airfoil is located.

The advantage of using the conformal mapping approach is evident. One can use the same linear equations as used for the single vortex, the only essential change is the modified influence coefficient.

5.6.2 Linear Cascade

The focus in this study is the unsteady aerodynamics. The conformal mapping approach is used for steady aerodynamics, thus another approach is needed to estimate the unsteady aerodynamic forces on the rotor. A method with airfoils located along a straight path, as illustrated in Figure 5.9, is applied. The method was also applied to a cascade of thin airfoils in Section 4.6. The difference between the two cascades is that previously a single vortex point was used to model the airfoil. In this section the vortex panel code will be applied.

A high number of airfoils in the linear cascade will increase the computational time, and a low number is therefore wanted for computational efficiency. However, using too few airfoils in the linear cascade introduces errors in the estimated unsteady aerodynamics. In Section 5.6, the number of airfoils in the linear cascade was discussed. The number of airfoils needed was dependent on the simulation time of the analysis, the velocity applied and the spacing between the airfoils. The airfoils in the cascade was numbered using k_c, so that the number of airfoils, n_{bl} was;

$$n_{bl} = 2 \cdot k_c + 1$$

The critical number that the linear cascade was related to k_p, as defined in Eq 4.101. For the number of blades this is:

$$no_{bl,p} = \frac{2T}{S}\left(U_X + U_Y\right) + 1$$

where T is the simulation time, S is the spacing, U_X is the velocity in global X direction and U_Y is the velocity in the global Y direction. This is not sufficient to ensure that the solution has converged, and a study of the ratio between the influenced velocity from the midfoil, relative to the two foils located at the start and at end of the cascade should be evaluated. The number required for different simulation lengths will be investigated in the following sections.

5.7 Validation

In order to validate the vortex panel code, the validation process is divided into smaller steps. First a convergence test for the number of panel elements on the airfoil surface for a stationary conditions is performed. The next step is to validate the unsteady aerodynamic behaviour of the panel code. The unsteady aerodynamic lift for an airfoil in a straight path will be compared to the Wagner function. This function was developed for the circulatory lift for a flat plate and it is expected that there will be a small difference due to the thickness of the airfoil. The last step is to investigate how the airfoils will behave in the linear cascade.

5.7.1 Stationary values

In this study, the 5 MW reference wind turbine is used to estimate the aerodynamic loads for a wind turbine [36]. The wind turbine wing of this rotor consists of six different different types of airfoils. These are listed in Table 5.1. The cross section of the airfoils are illustrated in Appendix A in Figure A.1. A convergence test to estimate the number of panel elements needed along the airfoil surface is shown in Figure 5.10.

The DU airfoils do not have a sharp trailing edge. The panel vortex code used here is made for sharp trailing edges, and this is therefore manually set for each airfoil. The shape of the trailing edges are shown in Appendix A, in Figures A.2, A.3, A.4, A.5 and A.6.

In the convergence test the angle of attack for all airfoils is 5^o. The final values are compared to lift tabulated coefficients [36]. Unfortunately, these coefficients includes three dimensional correction for the inner airfoils. The tabulated values will also include viscous effects, such as stall. Therefore, it is expected that the lift values will not have an exact match. The comparison between the tabulated lift coefficient and the lift coefficient estimated form the panel vortex code is shown in Table 5.1.

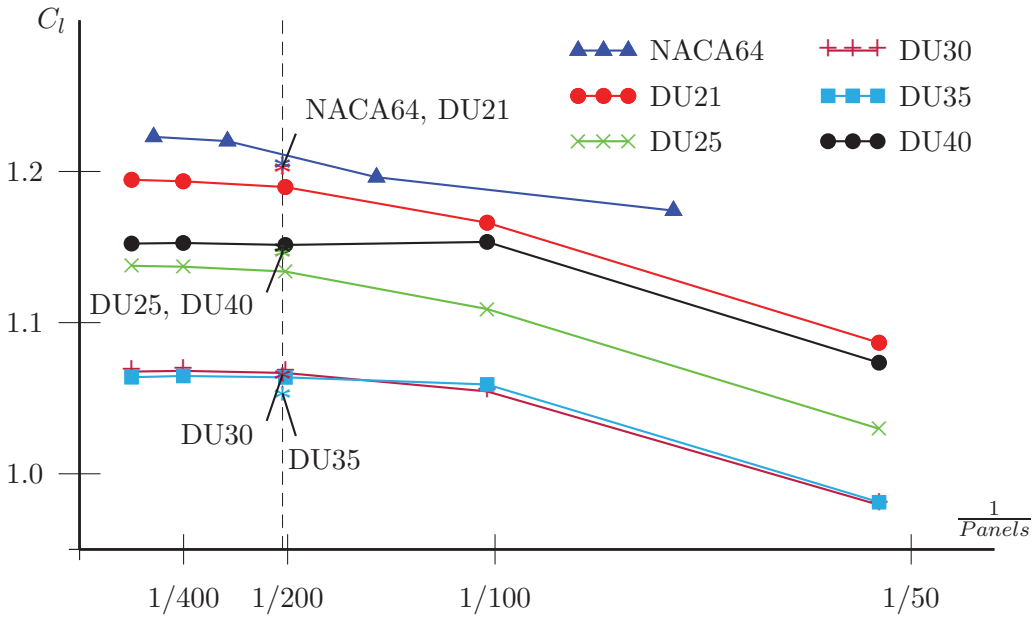

Figure 5.10: A convergence study for the lift coefficient relative to the number of panels. The solid lines are the vortex panel code, and the asterisk dots are the inviscid lift coefficient values from Xfoil using 205 panels.

Airfoil	C_l (200 panels)	C_l (400 panels)	C_l tabulated	C_l XFOIL_i	C_l XFOIL_v
NACA 64	1.196	1.220	1.01	1.2054	1.0762
DU 21	1.190	1.194	1.10	1.2013	1.1316
DU 25	1.134	1.137	1.06	1.1450	1.0798
DU 30	1.067	1.068	0.94	1.0638	0.9602
DU 35	1.064	1.065	0.88	1.0508	0.9011
DU 40	1.151	1.523	0.84	1.1467	0.9185

Table 5.1: Comparison of the calculated lift coefficient with tabulated lift coefficients in [36] and XFOIL (subscript i indicate inviscid and v is viscous).

The results were also compared to estimations of the lift coefficient by XFOIL. XFOIL is a well established panel vortex code, using linearly varying doublet element and constant source elements [21]. The advantage of XFOIL is that it gives the option of computing viscous forces. The computation using inviscid flow is listed in Table 5.1 in column XFOIL_i. The results are similar to the lift coefficient computed by the vortex panel code developed for this study. The lift coefficient using a viscous formulation estimates values similar to the tabulated lift coefficient. This is included in the table in the column listed XFOIL_v. Reynolds number $5.36 \cdot 10^6$ is applied for the lift coefficient listed.

The results indicate that a large number of panel elements are needed to get an accurate estimate of the stationary lift coefficient. As seen in Figure 5.10, the results seem to converge at 200 panel elements. Within this study, the DU airfoils have 200 panels, and the NACA airfoil has 140 panels.

5.7.2 One Blade in a Straight Path

The unsteady aerodynamic lift computed using the panel code is sensitive to the size of both the time step and the wake panel. The Wagner function describes the change in the circulatory part of the lift as a thin-airfoil undergoes a transient step in angle of attack in incompressible flow. The time step, dt, used here is:

$$dt = \frac{s_{dt} \cdot c}{2W} \tag{5.38}$$

where s_{dt} is related to the dimensionless timestep, s. Different values for s_{dt} are tested for the NACA 64 airfoil, and shown in Figure 5.11. The size of the wake panel, dw, is fixed, with $x_{wp} = 0.3$. The size of the wake panel is:

$$dw = x_{wp} W dt$$

The size of the wake panel is dependent on the time-step, dt and the flow velocity W.

In Figure 5.11, different length of the time step is investigated. Based on the sensitivity study with the time step, a time step using $s_{dt} = 0.4$, is chosen. An investigation of the size of the wake panels is also performed, and shown in Figure 5.12. A good wake panel size is $x_{wp} = 0.3$, for the chosen time step. It may look as though a shorter wake panel may give

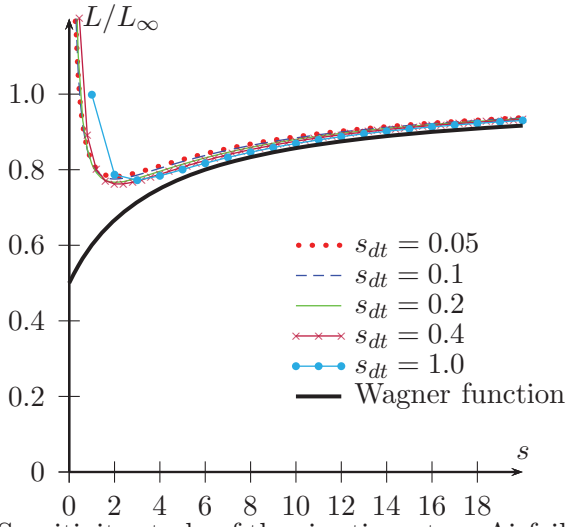

Figure 5.11: Sensitivity study of the size time step. Airfoil section NACA 64 is used and the size of the wake panel, x_{wp} is 0.3.

more accurate solution at lower values of s. However, when plotting the shorter wake panels with different time-steps, one get a wide spread in the results. A wake panel size of $x_{wp} = 0.3$ will give a robust solution.

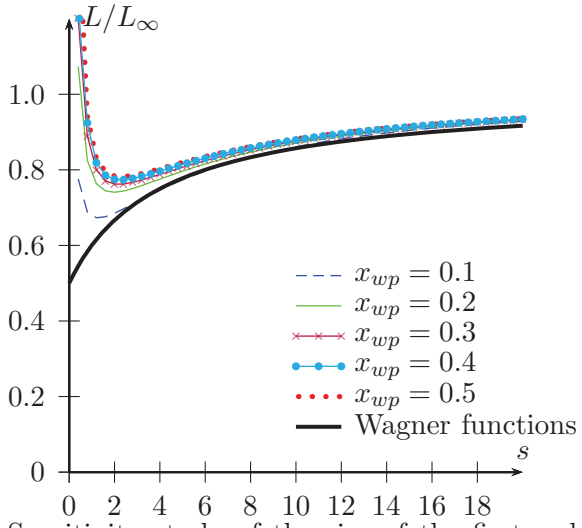

Figure 5.12: Sensitivity study of the size of the first wake panel. The airfoil section NACA 64 is used, and the time step, s_{dt}, is 0.4.

Assuming that Wagner describes the circulatory part of the unsteady

aerodynamic lift of an airfoil that accelerates from zero to W, the panel vortex code is sufficiently accurate in estimating the aerodynamic forces. At the start, the non-circulatory part of the lift will have an influence on the aerodynamic forces. This is an effect that should be added to the circulatory part of lift.

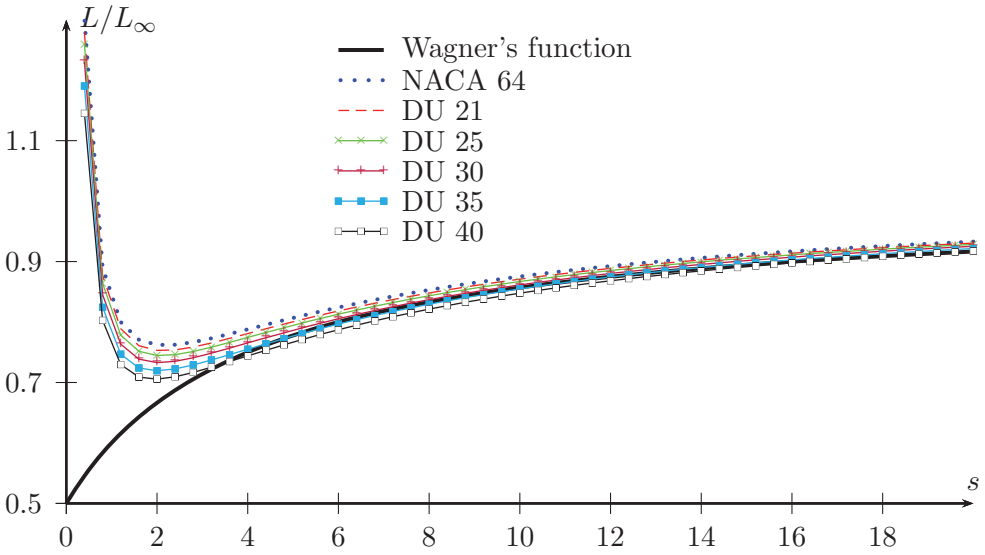

Figure 5.13: Nondimensionalized unsteady lift for airfoil sections in a straight path, starting from still at t=0, accelerated to 10 m/s, all with an angle of attack, $\alpha = 5^o$

For the above simulation the thinnest airfoil section of the 5 MW reference wind turbine was used. Comparing the Wagner function to all the airfoil sections along the blade of the 5 MW reference wind turbine, it is evident that the thickness of the airfoil has an effect on the dynamic response. In Figure 5.13 the unsteady aerodynamic lift for all airfoil sections along the wind turbine blade is shown. An angle of attack of 5 degrees is studied for all airfoils. The trend for the airfoil sections analysed here is that for the thicker airfoils, longer time to build up the lift force will be needed.

5.7.3 Linear Cascade of blades

The single airfoil is now put into a linear cascade of airfoils. The method is described in Section 5.6.2. There is a radial variation along the blade of the flow characterisation that will influence the behaviour of the cascade. A local tip-speed ratio, $\lambda_r = U_x/U_y$, and the spacing of the airfoils relative to the chord length, S_c, is used when discussing the radial variation. The total number of airfoils in the cascade is n_{bl}, which is related to the cascade number, k_c as $n_{bl} = 2 \cdot k_c + 1$. For $k_c = 0$, the results will yield the results for one single airfoil.

The inner airfoil sections show the largest differences when applying the cascade approach. The trend is that there is an increase in aerodynamic thrust force normal to the rotor plane. The thrust force is estimated based on the lift due to circulation and applying the flow angle. The effect of the number of blades on the thrust force is illustrated in Figure 5.14. The wind speed here is 8 m/s, and the node illustrated is node 4.

The linear cascade modeled here, with the panel elements along the airfoil surface, will have a similar behaviour to the linear cascade modeled with point vortex elements in Section 4.6.3. Figure 4.34 shows the effect of having different number of airfoils in the linear cascade, with single vortex elements. This figure has the same decrease in lift as Figure 5.14, however it also illustrates the increase in lift for a number of airfoils in the cascade lower than the cascade number, k_c.

In both figures there is an increase in lift force, which is higher than the stationary value at the start of the simulation. The peak occur after a time equal to the time it takes for a an airfoil to travel S_c, which is the spacing between the airfoils. The spacing in Figure 5.14 is 24.6 m, and it takes 2.2 s for the airfoil to travel this length. The chord length is 4.6 m, and the ratio c/S_c is 0.19. The local velocity ratio, λ_r, is relatively low due to the low rotational velocity at the inner section of the blade. An increase in the local velocity ratio would increase the cascade effect since the wake would travel slower in the direction of the wind.

By increasing the number of airfoils in the cascade, the negative slope of the thrust force in Figure 5.14 is decreasing. For an infinite number of airfoils, the thrust force will be an horizontal line for steady flow. Thus, it is evident that the number of airfoils in the cascade is of importance for the unsteady aerodynamics. The number of airfoils applied in the cascade should be evaluated with regards to simulation length and fre-

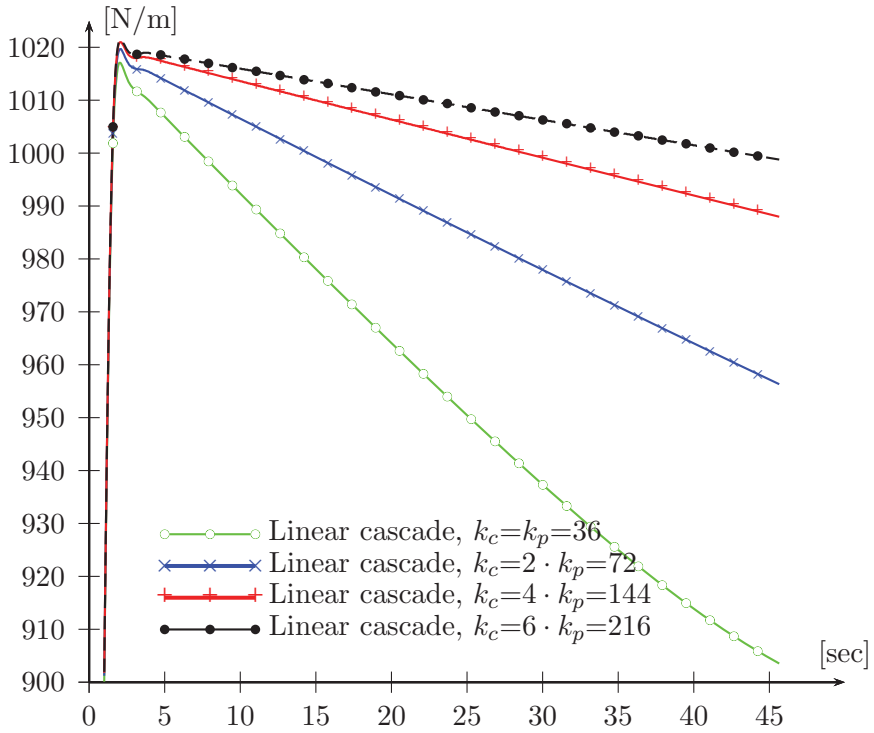

Figure 5.14: The normal force on an airfoil (DU 40) is computed with different number of airfoils in the cascade. The wind speed here is 8 m/s, the rotational speed is 9.16 rpm and the airfoil is located 11.75 m from the hub.

quency studied. Comparing the period of an oscillation to the time it takes an airfoil to travel to the initial position of the neighbouring blade, will give an indication whether it is necessary with a cascade analysis. If the oscillation period of the blade is the same as the time to travel a blade length, or it is an integer of the time, the linear cascade effects the unsteady aerodynamic loads. But if the oscillating period is not close to the time it takes to travel to the initial position of the neighbouring blade, a single airfoil simulation is sufficient. The number of airfoils needed in the linear cascade, is again depending on spacing, but now also the local velocity ratio. It should be able to model the unsteadiness of the frequency studied.

In this specific situation, $k_c = 144$, is a sufficient number to model

frequencies up to 1/8 Hz. However, it is also seen that above this frequency it is mostly steady aerodynamics. The linear cascade requires a significant increase in computational power, and it is therefore important to evaluate this before the simulations.

5.8 Implementation in a Graphical Processor Unit

The code described above was implemented on a GPU. This was presented in ref [58]. The CPU is faster for few time-steps, and the break-even is at around 1500 time-steps. At 2000 time-steps the GPU is already two times as fast.

The GPU-simulation in [58] are implemented on a NVIDIA Tesla C2050 GPU (448 processor elements running at 1.15 Hz). A single workstation was used, with an Intel Xeon quad-core CPU (running at 2.39 GHz) for comparison. From these simulations it was concluded that it is the calculation of the velocities that are time consuming. Solving the linear equation takes almost no-time, but setting up the linear equation seems to increase in computational time for the CPU with increasing number of time-steps. The computational speed can be increased even further using a tree-algorithm.

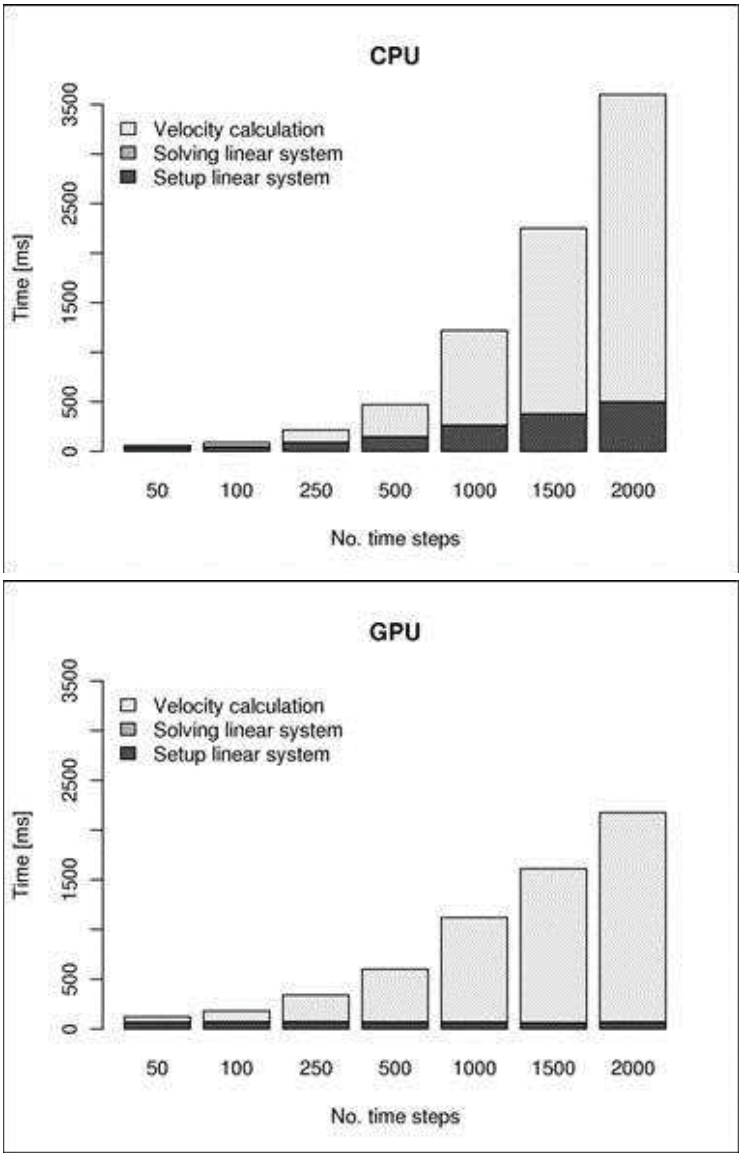

Figure 5.15: The computational time running the vortex panel code on a CPU and on a GPU for different timesteps [58].

Chapter 6

Wind Structure Interaction

6.1 Introduction

The unsteady aerodynamic forces on a wind turbine are dependent on both the wind, the rotational speed of the rotor and the relative motion of the rotor. In this chapter the unsteady aerodynamics using different simulation tools will be investigated. A wind field with constant velocity across the rotor is applied, and the unsteady aerodynamic loads due to an oscillating motion of the rotor are estimated. Two frequencies, similar to the eigenfrequencies of the first fore-aft elastic bending mode and the platform pitch mode, will be investigated. First, we will investigate the motion-induced aerodynamic loads using a quasi-static approach, before using two approaches defined in frequency domain; Theodorsen's function and Loewy's function. The results are then compared to those obtained running AeroDyn, which is a part of the wind turbine simulation code FAST. Finally, the vortex code is applied to the problem, both a single airfoil and a linear cascade.

Computational speed is always important when discussing simulation tools. Among the unsteady methods used here, the frequency domain methods, Theodorsen's function and Loewy's function, are by far the fastest methods. The AeroDyn tool features both the Dynamic Inflow and BEM and is relatively fast. The Dynamic Inflow is based on the Generalized Dynamic Wake method (GDW) and will be slightly faster than BEM since it does not require the iterations to find the influence coefficients, which is required in BEM. The panel vortex method has the longest computational time.

Both frequency methods, and the unsteady aerodynamics in AeroDyn

are based on the assumption that the unsteady response of the airfoil is independent of the thickness of the airfoil. Loewy's function will include the effect of the returning wake, while the Theodorsen function and the BEM method will assume this effect to be negligible. Comparing these methods to the vortex panel method, one can study the effects of thickness of the airfoil on unsteady aerodynamics. The comparison is done for both a single airfoil, and also looking at a cascade of airfoils, which includes the effect of a returning wake in the simulation. Since the panel vortex code is based on potential theory, the effect of flow separation (stall) is not included.

In this study, the fluid structure interaction of a floating wind turbine is investigated. The focus is on the first fore-aft elastic bending motion of the tower and the pitch motion of the rigid platform. The aim of the study is to investigate the aerodynamic damping and the added mass effects.

6.2 Properties investigated

The dynamic equilibrium of the rotor in axial oscillations can be expressed by the following equation of motion:

$$M_i\ddot{x} + C_i\dot{x} + K_i x = F_{aero}(t) \tag{6.1}$$

where M_i is the modal mass, C_i is the damping, K_i is the modal stiffness of the structure and $x(t)$ is the modal displacement. The modal displacement is a function of time, and together with the mode shape, $\phi_m(z)$, it can describe the resultant displacement, $r(t, z)$:

$$r(t, z) = x(t)\phi_m(z) \tag{6.2}$$

The mode shape, $\phi_m(z)$, gives the deformation along the span. In case of smooth uniform flow, the time-varying aerodynamic force, $F_{aero}(t)$, is due to the motion of the structure. In general the harmonic oscillation may generate aerodynamic forces in phase with acceleration, velocity or displacement. Similarly to the structural dynamic properties, the parameters linking the aerodynamic loads to the underlying acceleration, velocity and displacement are termed aerodynamic added mass, aerodynamic damping and aerodynamic stiffness. The loading can then all be grouped at the left hand side of Eq 6.1.

Here, a harmonic axial motion of a rigid rotor, $\eta_x(t)$, is studied. The motion is defined positive in the down wind direction. This is equivalent to the nacelle motion of the tower top, in the along wind direction. The equation of motion, using the axial motion and axial force is:

$$(M_i + M_a)\ddot{\eta_x} + (C_i + C_a)\dot{\eta_x} + (K_i + K_a)\eta_x = 0 \tag{6.3}$$

where $\ddot{\eta_x}$ is the acceleration, $\dot{\eta_x}$ is the velocity and η_x is the translation of the wind turbine tower top. The subscript a indicates that it is an aerodynamic property. The motion of the rotor η_x, can be related to the plunging motion, $h(t)$, in the Theodorsen function as $\eta_x = -h(t)$.

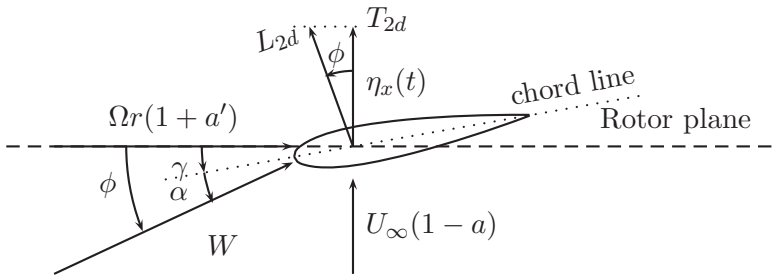

Figure 6.1: Illustration of the velocities due to wind speed, U_∞, and a plunging motion, η_x, of the airfoil relative to the axial motion of the wind turbine rotor.

For the time-domain simulation, it is difficult to separate the aerodynamic stiffness and the added mass. Instead a virtual aerodynamic added mass, M_{va}, can be used as a common term for the aerodynamic stiffness and the aerodynamic mass. This term is related to the aerodynamic stiffness and added mass as:

$$M_{va} = M_a - K_a/\omega_n^2 \tag{6.4}$$

where n is the angular eigenfrequency. The dynamic aerodynamic force, $F_{aero}(t)$, investigated in this study is the the force normal to the rotor plane. At the two dimensional blade section, this is equivalent to the thrust force, T, which is related to the lift force, L, as:

$$T_{2D} \approx L_{2D} \cdot \cos(\phi) \tag{6.5}$$

where ϕ is the flow angle between the flow and the rotor plane. This relation is illustrated in Figure 6.1. The drag force is assumed much smaller than the lift force on the blade, and only the lift force is therefore considered in these calculations. The local two dimensional unsteady aerodynamic forces are investigated, and separated into inertia force, damping force and elastic restoring force. The inertia force is in phase with the acceleration, the damping force will be in phase with the velocity and the elastic restoring force will be in phase with the displacement. In the present case the aerodynamic added mass, damping and stiffness, due to a harmonic rotor motion, will be estimated based on the two-dimensional unsteady aerodynamic force. By integrating the two dimensional aerodynamic forces from the hub to the tip, the aerodynamic added mass, damping and stiffness for the wind turbine rotor can be obtained.

For the platform pitch, the structural properties are related to the angular displacement, ω_x, angular velocity, $\dot{\omega}_x$, and angular acceleration, $\ddot{\omega}_x$, calculated in Section 6.3.2. The angular motion, ω_x, is related to the translational motion, η_x, as:

$$\eta_x = \omega_x \cdot z_{nac} \tag{6.6}$$

where z_{nac} is the distance from the nacelle to the pitch rotational center. The two-dimensional aerodynamic response is estimated relative to the translational motion. The rotational center is located 74.6 m below Still Water Level (SWL), as calculated in Appendix D.

The wind-structure interaction is studied in terms of the overturning moment about the mass center. In Eq 6.7 to 6.9 the distance from the rotational center to the nacelle, z_{nac}, appears squared. The distance is multiplied once when relating the angular pitch motion to the displacement at the nacelle height, and once for translating the thrust modal force into the moment about the center:

$$M_{p,a} \approx N_b \cdot \int_0^R M_{a,2D} dr \cdot z_{nac}^2 \tag{6.7}$$

$$C_{p,a} \approx N_b \cdot \int_0^R C_{a,2D} dr \cdot z_{nac}^2 \tag{6.8}$$

$$K_{p,a} \approx N_b \cdot \int_0^R K_{a,2D} dr \cdot z_{nac}^2 \tag{6.9}$$

where N_b is the number of blades, R is the length of the blade, z_{nac} is the distance from the rotational center to the nacelle and subscript p

indicates pitch motion. Using the above equation, it is assumed that the rotor radius is much less than the distance between the nacelle and the rotational center.

When considering the dynamic equilibrium in relation to the first tower bending mode, the aerodynamic forces are multiplied with the mode shape at the nacelle:

$$M_{t,a} = N_b \cdot \int_0^R M_{a2D} dr \cdot \phi_m^2(z = z_{nac}) \tag{6.10}$$

$$C_{t,a} = N_b \cdot \int_0^R C_{a2D} dr \cdot \phi_m^2(z = z_{nac}) \tag{6.11}$$

$$K_{t,a} = N_b \cdot \int_0^R K_{a2D} dr \cdot \phi_m^2(z = z_{nac}) \tag{6.12}$$

where $\phi_m(z)$ is the mode shape and z is the distance from the tower bottom. For the first tower mode the mode shape is normalized to value 1 at the nacelle. Comparing the dynamic aerodynamic properties to the pure structural dynamic properties of the structure, will show the relative significance of the aerodynamic forces. Here, the motion-dependent forces will be quantified in term of the aerodynamic damping ratio and the change in the natural frequency. The aerodynamic damping ratio for the wind turbine is calculated as;

$$\xi_a = \frac{C_a}{C_{cr}} = \frac{C_a}{2\omega_n M_i} \tag{6.13}$$

where M_i is the mass moment of inertia or the modal mass, and C_{cr} is the critical damping, which is defined as:

$$C_{cr} = 2\omega_n M_i \tag{6.14}$$

The change in mass and stiffness will influence the eigenfrequency, ω_n, of the wind turbine. An increase in the mass will give a decrease in the eigenfrequency. The virtual aerodynamic added mass is defined in Equation 6.4, and includes both the change in aerodynamic stiffness and in aerodynamic added mass. Taking the virtual mass into account, the eigenfrequency, ω_n, of the mode can be computed. The ratio between the eigenfrequency, which includes the aerodynamic effects, and the undamped natural eigenfrequency of the structure, is defined as:

$$\frac{\omega_n}{\omega} = \sqrt{\frac{1}{1 + M_{va}/M_i}} \tag{6.15}$$

From the relation above, it is seen that the relationship between the modal mass and the virtual aerodynamic mass and the damping ratio can therefore tell us the importance of the aerodynamic mass and stiffness on the structural response.

6.3 5 MW reference wind turbine

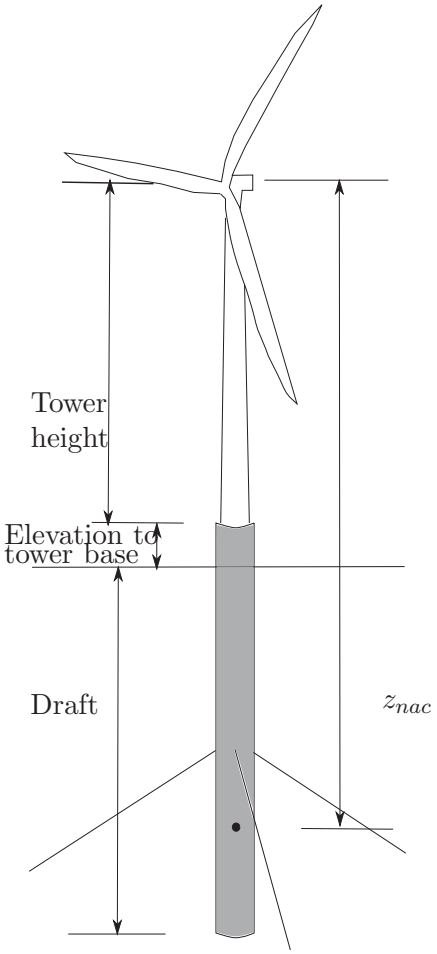

Figure 6.2: Sketch of the OC3 Hywind.

The wind-structure interaction for the 5 MW reference wind turbine rotor used in the OC3 and OC4 code comparison project is investigated. The presentation here is limited the floating Hywind structure used in the OC3 project. This will be referred to the as the OC3 Hywind wind turbine and is sketched in Figure 6.2. The rotor is modeled as a stiff structure, with no elasticity in the blades, in the aerodynamic analysis. The calculated dynamic aerodynamic forces are compared to a structural properties of the OC3 Hywind. The rotor section properties and the structural configuration used in the analysis, are presented in the following sections.

6.3.1 Rotor Properties

The rotor blade is divided into 17 blade sections, from the hub to the root. Close to the root, the blade sections have circular cross sections, which are not included in the study. The main properties of the blade section distributed along the rotor blade are given in Table 6.1.

The tabulated two dimensional airfoil coefficients used in this study were intended for a code comparison study. To reduce the amount of scatter among the participants in the code comparison, the three dimensional correction of the two dimensional aerodynamic coefficients were integrated into the aerodynamic coefficients distributed to the code comparison participants [36]. Some of the tables of aerodynamic lift coefficients distributed for the comparison project have an inclination of the lift curve that is larger than the theoretical maximum of 2π, and this is due to the implemented three dimensional correction. The lift coefficient curves are shown in Appendix B.

6.3.2 Structural Properties

The 5 MW reference wind turbine is a three bladed upwind wind turbine, with a variable speed and collective pitch controller. The rated wind speed is 12 m/s, and below this wind speed the power output is maximized by varying the rotor speed. At wind speeds above rated wind speed, the blades are pitched to reduce the aerodynamic loading, and the power output is constant. In this study, the rotational speed and blade pitch angle is kept constant for each simulation, but varying for the different wind speeds. The applied rotor speed and pitch angle for three different wind speeds are listed in Table 6.2. These are estimated using a simple steady BEM code, as described in Chapter 3.

Table 6.1: Aerodynamic properties for the 17 airfoil sections along the 5 MW reference wind turbine

Section	Radius [m]	Twist [deg]	Chord [m]	Airfoil
1	2.87	13.308	3.542	Cylinder1
2	5.6000	13.308	3.854	Cylinder1
3	8.33	13.308	4.167	Cylinder2
4	11.75	13.308	4.557	DU40
5	15.85	11.480	4.652	DU35
6	19.95	10.162	4.458	DU35
7	24.05	9.011	4.249	DU30
8	28.15	7.795	4.007	DU25
9	32.25	6.544	3.748	DU25
10	36.35	5.361	3.502	DU21
11	40.45	4.188	3.256	DU21
12	44.55	3.125	3.010	NACA64
13	48.65	2.319	2.764	NACA64
14	52.75	1.526	2.518	NACA64
15	56.17	0.863	2.313	NACA64
16	58.90	0.370	2.086	NACA64
17	61.63	0.106	1.419	NACA64

In this study, the blade pitch angle and rotational speed is assumed constant, for each wind speed. This is however a simplification of a real controller, since the controller will pitch the blades for low frequency oscillations of the wind. Motions in the fore-aft direction will be interpreted by the controller as a change in the wind. The controller pitches the blades to maintain a constant thrust at wind speeds above rated wind speed. When the wind turbine moves towards the wind, the controller registers an increase in wind speed, and pitches the blades to reduce the

Table 6.2: The rotor speed and blade pitch angle at three different wind speeds.

Wind speed U_∞	Pitch angle γ	Rotor speed Ω_{rot}
8 m/s	0^o	9.16 rpm
14 m/s	8.4^o	12.3 rpm
20 m/s	16.5^o	12.3 rpm

torque on the rotor. Consequently, the thrust force is reduced when the wind turbine moves forward toward the wind. This may give a negative aerodynamic damping of the fore-aft motion of the wind turbine.

The tower is 77.6 m high, and is connected to the foundation 10 m above SWL. The main properties of the wind turbine structure, needed for the estimation of the mass moment of inertia, are listed in Table 6.3. More details with regards to the rotor and control system can be found in [36], and the substructure is described in detail in [66].

Table 6.3: The mass distribution and center of gravity for the wind turbine structural parts relative to the SWL [66] [36] [67].

	Mass [Te]	L_{cog} [m]
Tower	250	43.4
Nacelle	240	90
Rotor	110	90
Platform	7 466	-88.46

The hydrodynamic damping is less than 10^7 kgm/s for the pitch motion [66], which is 0.04 % of the critical damping of the platform pitch motion. Since the hydrodynamic damping is very low for the platform pitch it is assumed negligible.

6.3.3 Wind-structure Interaction Properties

A simple modal analysis of the pitch and the first tower bending mode is defined here, specific for the OC3 Hywind wind turbine. The modal analysis is used to relate the dynamic aerodynamic forces to the response of the wind turbine structure. In this study the focus is on the aerodynamic damping and the aerodynamic added mass. The relative importance of these two properties with regards to the specific structure is discussed in terms of aerodynamic damping ratio, ξ_a, and the natural frequency, ω_n.

The mass moment of inertia for the platform pitch motion and the modal mass for the first tower mode, together with the eigenfrequency, are needed to estimate these properties. The general formula for the mass moment of inertia of a slender structure is:

$$M_1 = \int m(z) \cdot z^2 dz \tag{6.16}$$

where $m(z)$ is the for the mass distribution at a distance z. For the platform pitch, M_1 is estimated as:

$$\begin{aligned} M_1 &= \int m_{tow}(z) \cdot z^2 dz + \int m_{sub}(z) \cdot z^2 dz \\ &\quad + (m_{rot} + m_{nac}) \cdot z_{nac}^2 + I_{rot} \end{aligned} \tag{6.17}$$

where the subscript, 1 indicates the pitch mode, *tow* tower, *sub* is the supportstructure (here: floating platform), *nac* is the nacelle and *rot* is the rotor (blade and hub). z_{nac} is the distance from the nacelle to the rotational center. The inertia of the rotor, I_{rot}, the hydrodynamic added mass for the pitch component, A_p, and the mass distributions, $m(z)$, for each structural part are listed in Appendix C. The location of the platform pitch rotational center is calculated in Appendix D, and is located 69.3 m below SWL.

The modal mass of the first tower bending mode is:

$$M_2 = \int_0^{h_{tow}} m_{tow}(z)\phi_m^2(z)dz + (m_{rot} + m_{nac}) \cdot \phi_m^2(h_t) \tag{6.18}$$

where $\phi_m(z)$ is the mode shape and h_{tow} is the height of the tower. The mode shape, illustrated in Figure 6.3, is estimated using the software Modes [68].

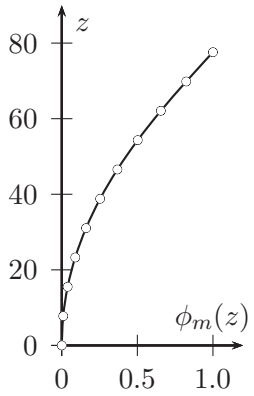

Figure 6.3: The mode shape of the first elastic tower bending mode

The modal mass and mass moment of inertia for the OC3 Hywind structure are listed in Table 6.4 together with the angular eigenfrequencies and the critical damping.

Mode	**Angular frequency**	**Period**	**Mass moment of intertia**	**Critical Damping**
Platform pitch	0.21 rad/s	30 s	$5.6 \cdot 10^{10}$ kg m ^{2}	$2.38 \cdot 10^{10} kgm^2/s$
1^{st} **elastic tower bending mode**	2.95 rad/s	2.14 s	$3.9 \cdot 10^5$ kg	$2.31 \cdot 10^6 kg/s$

Table 6.4: The structural properties for the two analysed eigenmodes of the OC3 Hywind

6.4 Method

The aim of this study is to investigate the wind-structure interaction using different methods. These methods include a quasi-static approach, Theodorsen's function, AeroDyn (a commercial aerodynamic code, with BEM and dynamic inflow implemented), a vortex panel code and Loewy's

Method	Unsteady aerodynamics		Neighbouring wakes
	Thin foil	Thickness and curvature	
Quasi-Static flat	-	-	-
Time-domain engineering tool, AeroDyn:			
BEM Steady	-	-	-
BEM Unsteady	√	-	-
GDW Unsteady	√	-	-
Time-domain vortex panel code:			
Single airfoil	-	√	-
Cascade of airfoils	-	√	√
Frequency-domain method:			
Theodorsen's theory	√	-	-
Loewry's theory	√	-	√

Table 6.5: An overview of the different aerodynamic methods discussed in this chapter, and their main unsteady aerodynamic properties.

function, which are listed in Table 6.5. As shown in the table, the quasi-static approach does not account for any unsteady aerodynamics, which the other methods do. Theodorsen's function and Loewy's function are both analytical frequency domain methods, but the Loewy's function takes the returning wake into the consideration. The returning wake problem in Loewy's function was presented in Section 4.6.4. The computational efficiency of these three methods are high.

The aerodynamic force on the blade sections along the 5 MW wind turbine blade is estimated. The local two dimensional forces at the blade sections are related to the acceleration and velocity of the axial plunge motion of the wind turbine rotor. The variation along the radial length of the blade is investigated, as well as the full rotor properties. The wind structure interaction of the two frequencies, first tower bending and platform pitch, at three different wind speeds, 8 m/s, 14 m/s and 20 m/s, are studied. The corresponding rotational speed and blade pitch angle

are listed in Table 6.2.

6.4.1 Wind Velocities

The wind speed relative to the blade, W, is a combination of the axial wind flow at the rotor disc, U_∞, the apparent wind speed due to the rotation, Ωr, and the tangential and axial induction factors, a and a' (see Eq 3.20 and Figure 6.1). A simple BEM analysis (see Section 3.4), is used to estimate the axial and tangential induced velocities. The relative wind speed varying along the blade is shown in Figure 6.4.

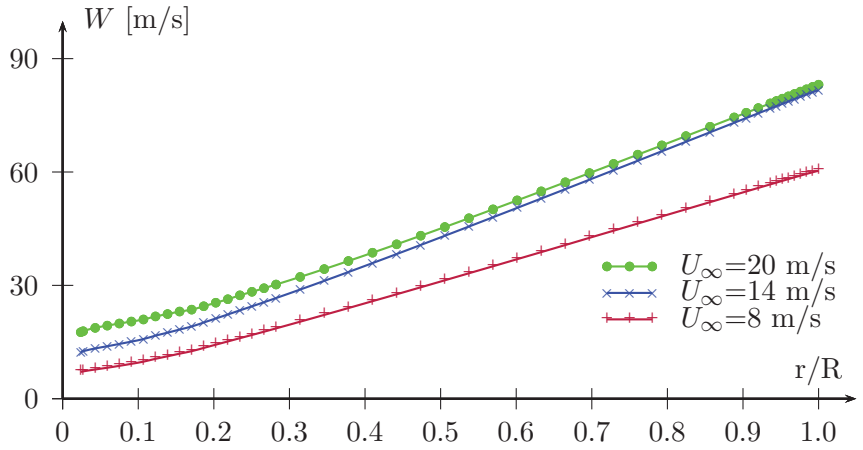

Figure 6.4: The relative wind speed, W, relative to the radial position along the blade of the 5 MW reference wind turbine. 0 is at the root of the blade and 1 is at the tip of the blade.

The wind speed, U_∞, is assumed to be constant with height, and no turbulence is accounted for. In reality, the free wind velocity, U_∞, is varying across the rotor disc due to the shear profile of the mean wind speed and turbulence in the wind field.

6.5 Quasi steady wind-structure interaction

6.5.1 Method

The quasi-steady wind structure interaction is investigated using wind turbine aerodynamics as presented in Chapter 3. The thrust force is approximated using the lift force and the flow angle, see Equation 6.5.

Both the lift force and the flow angle are dependent on the oscillating motion. The time varying aerodynamic lift force can be expressed as:

$$L(t) = \frac{1}{2}\rho C_L(t) W^2(t) c \tag{6.19}$$

where ρ is the air density, $C_L(t)$ is the two dimensional lift coefficient, $W(t)$ is the relative velocity and c is the chord length. Both the relative wind speed and the lift coefficient will vary with time. The relative velocity, $W(t)$, is expressed as:

$$\begin{aligned} W^2(t) &= (U_\infty(1-a) - \dot{\eta}_x)^2 + \left(U_{rot}(1+a')\right)^2 \\ &= U_\infty^2(1-a)^2 - 2U_\infty(1-a)\dot{\eta}_x + \dot{\eta}_x^2 + \left(U_{rot}(1+a')\right)^2 \end{aligned} \tag{6.20}$$

where the translation of the rotor in the along wind direction is defined as η_x, and $\dot{\eta}_x$ is the velocity in the axial direction. The axial and tangential induction factors are assumed constant. It is also assumed that all motion is in the same plane, i.e. the platform pitch motion is studied using translation in the axial direction, and no rotation about the center of mass. The flow angle, $\phi(t)$, is:

$$\phi(t) = \tan^{-1}\left(\frac{U_\infty(1-a) - \dot{\eta}_x}{U_{rot}(1+a')}\right) \tag{6.21}$$

If the flow angle is small, the expression can be simplified to:

$$\phi(t) \approx \frac{U_\infty(1-a) - \dot{\eta}_x}{U_{rot}(1+a')} \tag{6.22}$$

Using the above expression, the angle of attack is:

$$\alpha(t) \approx \frac{U_\infty(1-a) - \dot{\eta}_x}{U_{rot}(1+a')} - (\gamma + \theta) \tag{6.23}$$

where γ is the twist of the blade section and θ is the pitch of the blade. In order to find a time varying lift coefficient, the angle of attack is linearized about its mean value, α_0:

$$\alpha(t) = \alpha_0 - \frac{\dot{\eta}_x}{U_{rot}(1+a')} \tag{6.24}$$

Using the above linearized α, the time varying lift coefficient, $C_L(t)$, can be expressed as:

$$C_L(t) = C_{L0} - \left(\frac{\partial C_L}{\partial \alpha}\right)_{\alpha_0} \frac{\dot{\eta}_x}{U_{rot}(1+a')} \tag{6.25}$$

where C_{L0} is the lift coefficient for the mean angle of attack, α_0, and $\left(\frac{\partial C_L}{\partial \alpha}\right)_{\alpha_0}$ is the derivative of the lift at α_0. Inserting Equations 6.20 and 6.25 in the relation for the time varying lift force in Equation 6.19, the time varying lift is expressed using 8 terms:

$$\begin{aligned} L(t) &= \underbrace{\frac{1}{2}\rho C_{L0} U_\infty^2 (1-a)^2 c}_{1} + \underbrace{\frac{1}{2}\rho C_{L0} U_{rot}^2 (1+a')^2 c}_{2} \\ &- \underbrace{\frac{1}{2}\rho \left(\frac{\partial C_L}{\partial \alpha}\right)_{\alpha_0} \frac{\dot{\eta}_x U_\infty^2 (1-a)^2 c}{U_{rot}(1+a')}}_{3} - \underbrace{\frac{1}{2}\rho \left(\frac{\partial C_L}{\partial \alpha}\right)_{\alpha_0} \frac{\dot{\eta}_x U_{rot}^2 (1+a')^2 c}{U_{rot}(1+a')}}_{4} \\ &+ \underbrace{\rho C_{L0} U_\infty (1-a)\dot{\eta}_x c}_{5} + \underbrace{\rho \left(\frac{\partial C_L}{\partial \alpha}\right)_{\alpha_0} \frac{\dot{\eta}_x}{U_{rot}} U_\infty (1-a)\dot{\eta}_x c}_{6} + \underbrace{\frac{1}{2}\rho C_{L0} \dot{\eta}_x^2 c}_{7} \\ &+ \underbrace{\frac{1}{2}\rho \left(\frac{\partial C_L}{\partial \alpha}\right)_{\alpha_0} \frac{\dot{\eta}_x}{U_{rot}(1+a')} \dot{\eta}_x^2 c}_{8} \end{aligned} \tag{6.26}$$

The two first terms are mean forces, and do not contribute to the dynamic wind-structure interaction. These two terms are equivalent to the mean value of the lift force, L_0. The velocity of the structure $\dot{\eta}_x$ is assumed to be small compared to the rotational velocity. The three last terms, (6), (7) and (8), contain the term $\dot{\eta}_x^2$, and are therefore assumed negligible compared to the other terms. The remaining three terms, (3), (4) and (5), are used in evaluating the quasi steady aerodynamic damping:

$$\begin{aligned} L(t) &\approx L_0 + \left(\rho C_{L0} U_\infty (1-a)c - \frac{1}{2}\rho \left(\frac{\partial C_L}{\partial \alpha}\right)_{\alpha_0} \frac{W_0^2}{U_{rot}(1+a')} c\right) \dot{\eta}_x \\ &= L_0 + \frac{C_{a,2D} \cdot \dot{\eta}_x}{\cos(\phi)} \end{aligned} \tag{6.27}$$

where W_0 is the mean relative wind;

$$W_0 = \sqrt{U_\infty^2 (1-a)^2 + U_{rot}^2 (1+a')^2} \tag{6.28}$$

The aerodynamic damping is divided by $\cos(\phi)$, since it is related to the thrust force, and not the lift force. The thrust force is out of phase with the structural velocity corresponds to an aerodynamic damping force; with the aerodynamic coefficient, $C_{a,2D}$, as a connecting parameter:

$$C_{a,2D} \approx -\left(\rho C_{L0} U_\infty (1-a)c - \frac{1}{2}\rho \left(\frac{\partial C_L}{\partial \alpha}\right)_{\alpha_0} \frac{W_0^2}{U_{rot}(1+a')}c\right) \cdot \cos(\phi) \tag{6.29}$$

The quasi-steady aerodynamic damping is positive if:

$$\frac{1}{2}\left(\frac{\partial C_L}{\partial \alpha}\right)_{\alpha_0} \frac{W_0^2}{U_{rot}(1+a')} > C_{L0} U_\infty (1-a) \tag{6.30}$$

This is generally true, since the wind speed relative to the blade, W_0, is much larger than the free wind speed, U_∞. The fore-aft damping is therefore normally assumed positive. This is illustrated in Figure 6.6.

6.5.2 Results

The aerodynamic damping coefficient for the rotor is estimated by integrating the two dimensional blade section coefficients along the blade. The lift coefficient is found using tabulated values for each airfoil. A simplified estimate of the steady aerodynamic damping, using the properties flat plate with $\frac{\partial C_L}{\partial \alpha} = 2\pi$, is compared to the results based on the data for the blades. The aerodynamic damping coefficient and damping ratio are shown in Table 6.6 and 6.7.

Figure 6.5 shows the aerodynamic damping coefficient along the blade, using both a flat plate assumption and tabulated lift coefficients. The difference between assuming a flat plate, and using the tabulated values for the aerodynamic lift coefficient is relative small. The trend, for both methods, is that the aerodynamic damping increases with the wind speed.

The quasi-steady aerodynamic damping $C_{a,2D}$, Equation 6.29, consists of two terms, and the contribution from these two terms are investigated in Figure 6.6 for the wind speed of 20 m/s. It is obvious that the dominating term of the aerodynamic damping is the second term. It is therefore the slope of the lift curve, and not the mean load, which is important for the quasi-static aerodynamic damping.

	Aerodynamic damping coefficient		
Wind Speed, U_∞	8 m/s	14 m/s	20 m/s
Flat plate	$6.0 \cdot 10^4$	$8.2 \cdot 10^4$	$8.7 \cdot 10^4$
Airfoil	$6.0 \cdot 10^4$	$8.6 \cdot 10^4$	$8.8 \cdot 10^4$
	Aerodynamic damping ratio [%]		
Flat plate	2.6	3.6	3.7
Airfoil	2.6	3.7	3.8

Table 6.6: Aerodynamic damping properties for the elastic tower bending motion using the quasi-static approach in Equation 6.29.

	Aerodynamic damping coefficient		
Wind Speed, U_∞	8 m/s	14 m/s	20 m/s
Flat plate	$1.9 \cdot 10^9$	$2.7 \cdot 10^9$	$2.8 \cdot 10^9$
Airfoil	$2.0 \cdot 10^9$	$2.8 \cdot 10^9$	$2.8 \cdot 10^9$
	Aerodynamic damping ratio [%]		
Flat plate	6.17	8.51	8.95
Airfoil	6.25	8.88	9.10

Table 6.7: Aerodynamic damping properties for the platform pitch motion using the quasi-static approach in Equation 6.29.

A similar expression for aerodynamic damping coefficient was derived by Garrad [69]:

$$C_{a,G} = \frac{1}{2}\rho U_{rot} c \left(\frac{\partial C_L}{\partial \alpha}\right)_{\alpha_0} \tag{6.31}$$

Garrad's expression assumes a small flow angle ($\cos\phi \approx 1$) and a high tip speed ratio. Using the flat plate approximation, Garrad's aerodynamic damping expression is included in Figure 6.6. This expression gives results similar to the 2^{nd} term in Equation 6.29. Garrard's expression gives a reasonable estimation of the steady aerodynamic damping.

In the following chapter, the importance of unsteadiness in the esti-

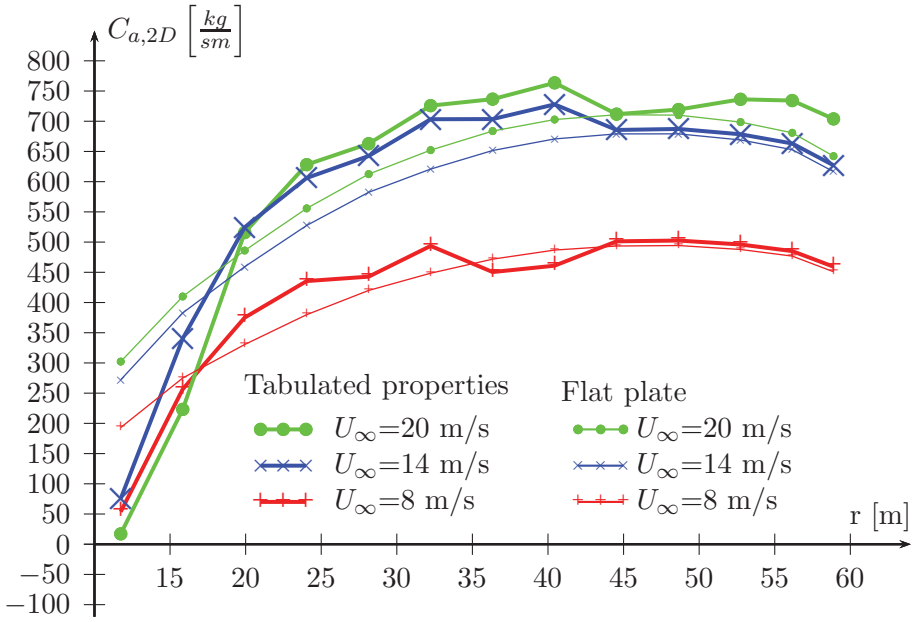

Figure 6.5: The two-dimensional aerodynamic damping coefficient, $C_{a,2D}$, estimated using Equation 6.29. The assumption of flat plate is compared to using tabulated aerodynamic properties for the 5 MW reference wind turbine.

mation of aerodynamic damping will be investigated. The methods are based on various assumptions; some are using the thin plate aerodynamics, some uses tabulated values and the panel method uses sources to model the thickness.

6.6 Theodorsen's Theory

Theodorsen's solution for unsteady lift force due to harmonic variations in the plunging and pitching motion was presented and discussed in Section 4.4.3. In this study we will use the theory presented previously to study the unsteady aerodynamic response of a wind turbine rotor.

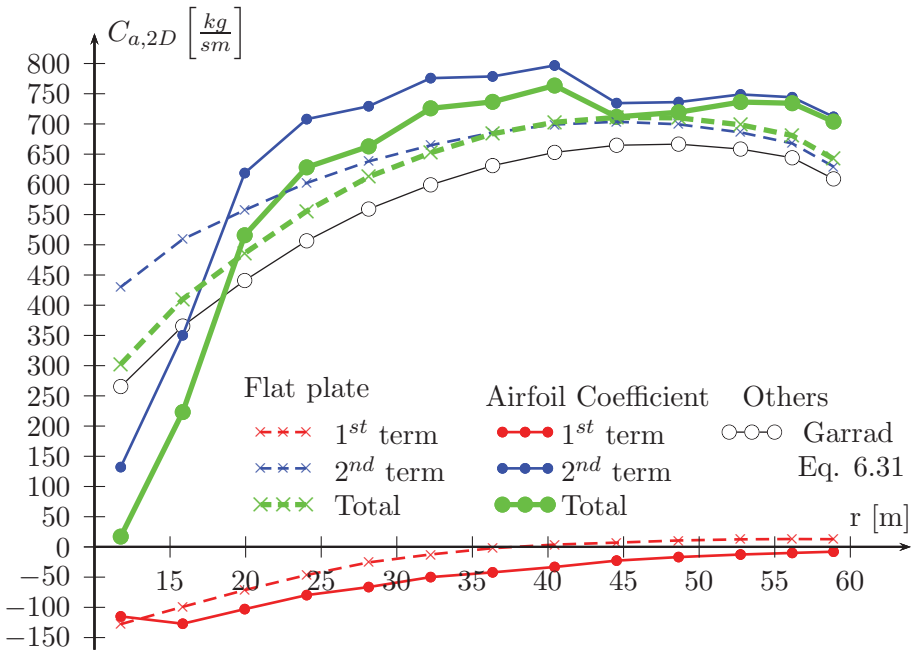

Figure 6.6: The two-dimensional aerodynamic damping coefficient at the wind speed of 20 m/s, split in the two terms in Equation 6.29.

6.6.1 Method

The aerodynamic lift coefficient, using Theodorsen's theory, for a thin foil in oscillating plunge motion is given in Equation 4.83. The thrust force for a 2D section is then:

$$\begin{aligned} T_{2D} &= 0.5\rho c W^2 \left[2\pi k(iF(k) - G(k)) - \pi k^2\right] \frac{\bar{h}}{0.5c} e^{i\omega t} \cos(\phi) \\ &= -\left[2\rho W^2 \pi k i F(k) - 2\rho W^2 \pi k G(k) - \rho W^2 \pi k^2\right] \bar{\eta_x} e^{i\omega t} \cos\phi \\ &= -\left[\rho c W \pi \omega i F(k) - \rho c W \pi \omega G(k) + \rho c^2 \pi (\frac{i\omega}{2})^2\right] \bar{\eta_x} e^{i\omega t} \cos\phi \\ &= -\rho c \pi \left[\frac{c}{4}(i\omega)^2 + W F(k)(i\omega) - W\omega G(k)\right] \bar{\eta_x} e^{i\omega t} \cos\phi \quad (6.32) \end{aligned}$$

where k is the reduced frequency along the blade, $k = \frac{\omega c}{2W}$. The reduced frequencies along the span of the blade for a high frequency oscillation (ω=0.21 rad/s) and a high frequency oscillation (ω=2.95 rad/s), for the three wind speeds studied here, are shown in Figure 6.7.

The motion dependent part of the Theodorsen's theory may be split into aerodynamic added mass, M_a, damping, C_a, and stiffness, K_a, see Equation 6.3. This is done by defining the aerodynamic added mass as a parameter defining the force in phase with the acceleration, the

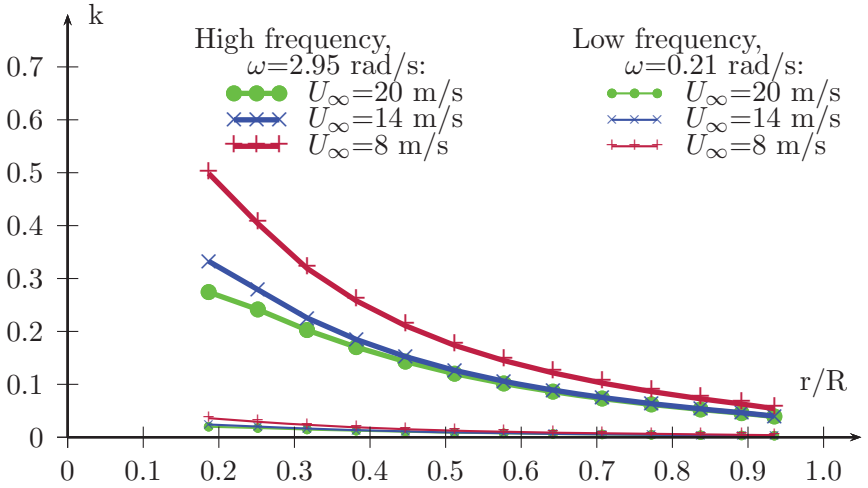

Figure 6.7: The reduced frequency, k, for a low and a high frequency oscillating motion of the rotor at positions along the blade, where 0 is at the root of the blade and 1 is at the tip of the blade.

aerodynamic damping for the force in phase with the velocity and the aerodynamic stiffness for the force in phase with the translation. Relating this to the thrust force, T, and the axial motion of the rotor, $h(t)$:

$$\begin{aligned} T &= -\left[M_a(i\omega)^2 + C_a i\omega + K_a\right] \\ T &= N_b \cdot \int_{r_i}^{R} [\frac{\pi\rho c^2}{4}(i\omega^2) + \pi\rho W c F(k) i\omega \\ &\quad -2kW^2\pi\rho G(k)]\bar{\eta}_x e^{i\omega t}\cos(\phi)dr \end{aligned} \tag{6.33}$$

This leads to the following relationships for the dynamic aerodynamic properties for a wind turbine moving in and out of the wind:

$$M_{a,2D} = \frac{\rho c^2 \pi}{4}\cos\phi \tag{6.34}$$

$$C_{a,2D} = \rho c W \pi F(k)\cos\phi \tag{6.35}$$

$$K_{a,2D} = -2kW^2\pi\rho G(k)\cos\phi \tag{6.36}$$

6.6.2 Results

The aerodynamic added mass is shown in Figure 6.8. This property is not dependent on the frequency of the motion. The variation in added mass at different wind speeds is due to the change in flow angle, ϕ. As the wind speed increases, the flow angle will increase if the rotor speed is constant. Since the added mass is linearly dependent on the cosine of the flow angle, an increase in wind speed will give a decrease in the added mass. The lowest wind speed, $U_\infty = 8m/s$, will therefore give the largest added mass contribution.

The aerodynamic damping is related to the real part of the Theodorsen function, $F(k)$, and is therefore dependent on the reduced frequency. For the low frequency oscillation, the aerodynamic loading can be considered quasi steady, while the high frequency oscillation will include unsteady aerodynamics. For quasi-steady loads, $F(k) = 1$, and for unsteady loads, $0.5 < F(k) < 1$. It is therefore expected that the aerodynamic damping of the low frequency oscillation is larger than for the high frequency oscillation. This is shown in Figure 6.9, where the damping of the low frequency oscillation is plotted with thin lines and high frequency oscillation is plotted with thick lines.

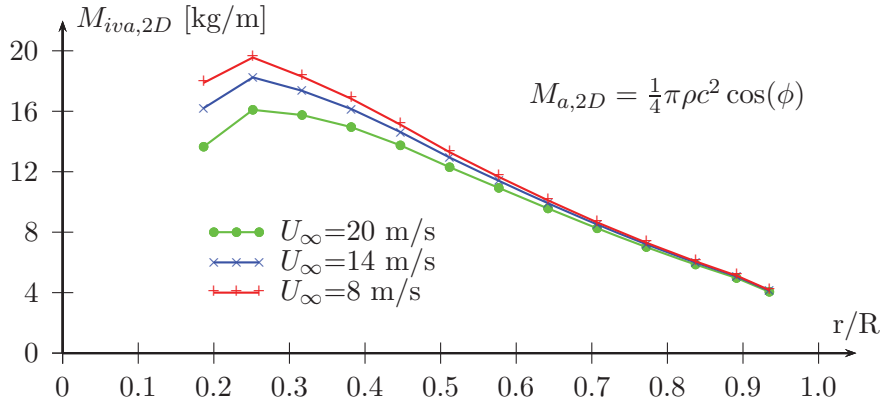

Figure 6.8: Aerodynamic virtual mass or added mass along the blade of a 5 MW turbine at three different wind speeds.

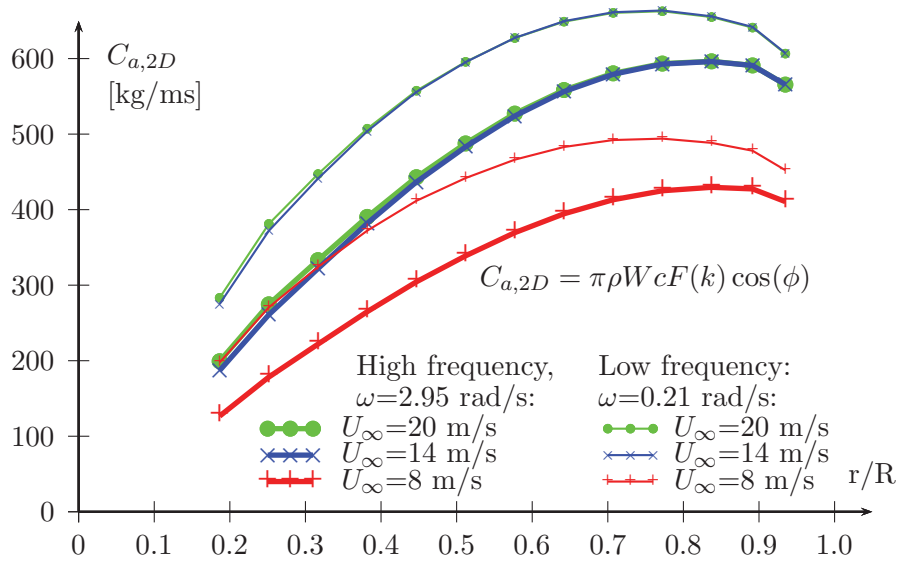

Figure 6.9: Aerodynamic damping along the blade of a 5 MW turbine for a low frequency oscillation and a high frequency oscillation at three different wind speeds.

The wind speed is another important factor. The aerodynamic damping is proportional to the relative wind speed, W, and the cosine to the flow angle. As with the added mass, the cosine of the flow angle gives a decrease with increasing wind speeds, but there is a linear relation with

the relative wind speed. The aerodynamic damping is therefore expected to increase with the rotational velocity of the rotor. Figure 6.9 shows that the rotor motion at wind speeds above rated wind speed, $U_\infty = 14$ m/s and $U_\infty = 20$ m/s, has the highest damping.

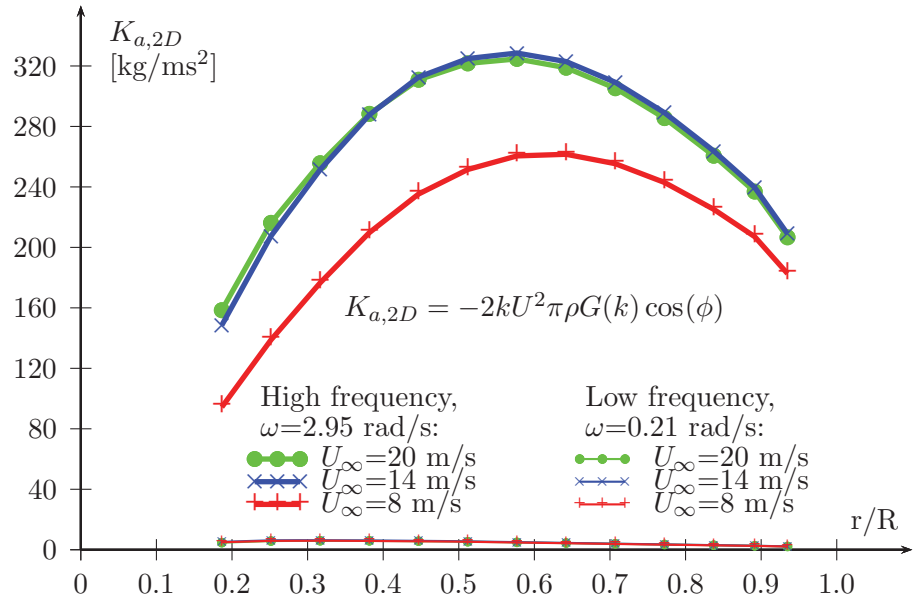

Figure 6.10: Aerodynamic stiffness along the blade of a 5 MW turbine for a low and a high frequency oscillating motion at three different wind speeds.

The aerodynamic stiffness is dependent on the imaginary part of Theodorsen function, $G(k)$. For quasi-steady loads, $G(k) \approx 0$, and the low frequency oscillation has therefore very little aerodynamic stiffness. The high frequency oscillation is subjected to more unsteady aerodynamic load, which include have an aerodynamic stiffness effect. The lowest value for $G(k)$ is at $k = 0.2$, where it is approximately -0.2. Similarly to the aerodynamic damping, the aerodynamic stiffness has the highest value at wind speeds above rated wind speed, $U_\infty = 14$ m/s and $U_\infty = 20$ m/s. This is shown in Figure 6.10.

Using Eq 6.7-6.12, the results in Figure 6.8, 6.9 and 6.10 are translated into modal parameters for the platform pitch and the first tower elastic bending mode. The results are presented in Table 6.8. Comparing these

	Platform Pitch		
U_∞ [m/s]	8	14	20
M_{ia} [kg m^2]	$4.26 \cdot 10^7$	$4.09 \cdot 10^7$	$3.81 \cdot 10^7$
C_{ia} [kg m^2/s]	$1.46 \cdot 10^9$	$1.97 \cdot 10^9$	$1.97 \cdot 10^9$
K_{ia} [kg m^2/s^2]	$1.60 \cdot 10^7$	$1.69 \cdot 10^7$	$1.61 \cdot 10^7$
ξ_{ia}	6.12 %	8.25 %	8.28 %
M_{iva} [kg m^2]	$-3.08 \cdot 10^8$	$-3.29 \cdot 10^8$	$-3.15 \cdot 10^8$
M_{iva}/M_i	-0.55 %	-0.59%	-0.56%
	1^{st} tower bending mode		
U_∞ [m/s]	8	14	20
M_{ia} [kg]	$1.73 \cdot 10^3$	$1.66 \cdot 10^3$	$1.55 \cdot 10^3$
C_{ia} [kg/s]	$4.71 \cdot 10^4$	$6.65 \cdot 10^4$	$6.72 \cdot 10^4$
K_{ia} [kg/s^2]	$3.08 \cdot 10^4$	$3.94 \cdot 10^4$	$3.93 \cdot 10^4$
ξ_{ia}	2.04 %	2.88 %	2.91 %
M_{iva} [kg]	$-1.80 \cdot 10^3$	$-2.85 \cdot 10^3$	$-2.95 \cdot 10^3$
M_{iva}/M_i	-0.46 %	-0.73%	-0.76 %

Table 6.8: The integrated aerodynamic virtual mass, damping and stiffness for the platform pitch mode and the first elastic tower bending using Theodorsen's function.

values to the structural mass, damping and stiffness characteristics of the wind turbine, the significance of the unsteady aerodynamic contribution can be discussed.

The platform pitch motion has, for all wind speeds, a higher aerodynamic damping than the first tower bending mode. The highest damping ratio, $\xi = 8.08\%$, occurs at $U_\infty = 14$ m/s. The frequency for the first tower bending mode is increasing due to the decrease in virtual aerodynamic mass. The increase in natural frequency is approximately 0.4% from stand still to rated wind speed and is illustrated in Figure 6.39.

6.7 Loewy's theory

The method using Loewy's theory to estimate the wind-structure interaction is very similar to the method from Theodorsen's theory. They are both frequency domain theories, and can be used to find the unsteady aerodynamic lift of a thin airfoil with an harmonic plunging motion. Loewy's theory is presented in more detail in Section 4.6.4, and includes the returning wake as shown in Figure 4.37.

6.7.1 Method

The returning shed wake may influence the dynamic aerodynamic properties investigated, and the wind-structure interaction properties is estimated using Loewy's theory. Replacing Theodorsen's function, $C(k)$, with Loewy's function to estimate the thrust in Equation 6.33, will give the aerodynamic added mass, damping and stiffness. The Loewy's function, $C'(k)$, is shown in Equation 4.104, and can be divided into a real part, $F'(k)$, and imaginary part, $G'(k)$.

$$M_{a,2D} = \frac{\rho c^2 \pi}{4} \cos\phi \tag{6.37}$$

$$C_{a,2D} = \rho c W \pi F'(k) \cos\phi \tag{6.38}$$

$$K_{a,2D} = -2kW^2 \pi \rho G'(k) \cos\phi \tag{6.39}$$

The aerodynamic added mass is the same, since this does not include the circulatory function. The difference between the two methods will be in the aerodynamic damping or the aerodynamic stiffness.

6.7.2 Results

The two-dimensional local aerodynamic stiffness along the blade is plotted in Figure 6.11 for the low frequency oscillation. The estimates using both Theodorsen's function and Loewy's function are included in the graph. Theodorsen's function predicts a negative aerodynamic stiffness, while Loewy's function predicts a positive aerodynamic stiffness.

The damping of the high frequency oscillation is significantly changed compared to the results using Theodorsen's funcion, especially for the low wind speed. This is because the $\omega_t/N_b\Omega$ is close to an integer for this simulation. The rotational velocity of the wind turbine at 8 m/s is 9.16

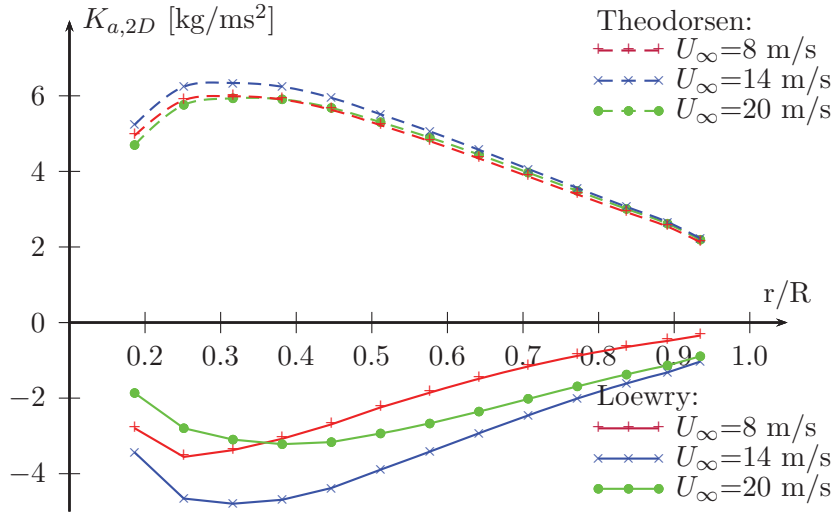

Figure 6.11: Aerodynamic stiffness for the two-dimensional airfoils along the blade oscillating at a low frequency (ω=0.21 rad/s). The values calculated using both Loewry's function and Theodorsen's function are shown.

rpm, or 0.96 rad/s. As seen in Figure 4.38, the value of Loewy's function

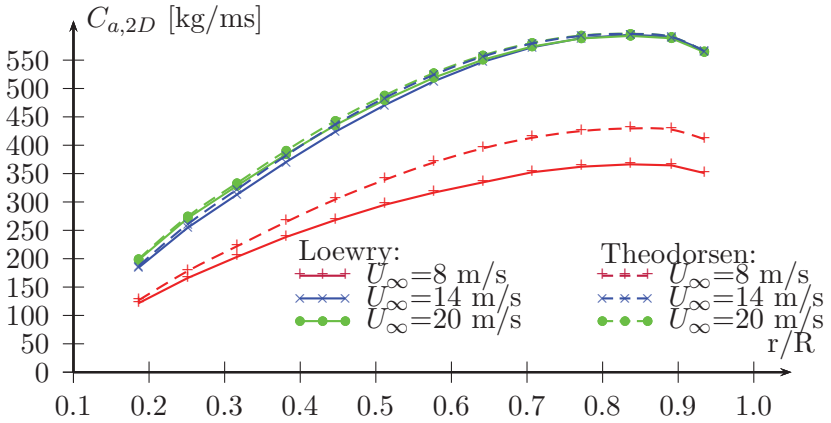

Figure 6.12: Aerodynamic damping for the two-dimensional airfoils along the blade oscillating at a high frequency (ω=2.95 rad/s). The values calculated using both Loewry's function and Theodorsen's function are shown.

drops when $\omega_t/N_b\Omega$ is an integer.

	Platform pitch mode		
V_∞ [m/s]	8	14	20
M_{ia} [kg m^2]	$4.26 \cdot 10^7$	$4.09 \cdot 10^7$	$3.81 \cdot 10^7$
C_{ia} [kg m^2/s]	$1.46 \cdot 10^9$	$1.95 \cdot 10^9$	$1.95 \cdot 10^9$
K_{ia} [kg m^2/s^2]	$-0.69 \cdot 10^7$	$-1.14 \cdot 10^7$	$-0.83 \cdot 10^7$
ξ_{ia}	6.14 %	8.18 %	8.17 %
M_{iva} [kg m^2/s]	$1.94 \cdot 10^8$	$2.91 \cdot 10^8$	$2.19 \cdot 10^8$
M_{iva}/M_i	0.35 %	0.52%	0.39%
	1^{st} tower bending mode		
V_∞ [m/s]	8	14	20
M_{ia} [kg]	$1.73 \cdot 10^3$	$1.66 \cdot 10^3$	$1.55 \cdot 10^3$
C_{ia} [kg/s]	$4.09 \cdot 10^4$	$6.55 \cdot 10^4$	$6.65 \cdot 10^4$
K_{ia} [kg/s^2]	$1.87 \cdot 10^4$	$5.22 \cdot 10^4$	$4.65 \cdot 10^4$
ξ_{ia}	1.77 %	2.83 %	2.88 %
M_{iva} [kg]	$-0.41 \cdot 10^3$	$-4.33 \cdot 10^3$	$-3.78 \cdot 10^3$
M_{iva}/M_i	-0.10 %	-1.11%	-0.97%

Table 6.9: The integrated aerodynamic virtual mass, damping and stiffness for the platform pitch mode and the first elastic tower bending using Loewy's function.

Relating the two-dimensional aerodynamic results for the two oscillation frequencies, one can get the modal aerodynamic properties. These are presented in Table 6.9. The wind structure interaction properties are Comparing the result for the wind structure interaction properties for the platform pitch mode to the results presented in Table 6.8 for Theodorsen, the difference is small. The difference is mainly in the damping of the first elastic tower bending mode. Using Theodorsen's function, the estimated aerodynamic damping was 2.04 %. This has been reduced to 1.77 % when using Loewy's function, which is a 13 % decrease in damping.

6.8 AeroDyn

AeroDyn is an aerodynamic simulation tool developed at the National Renewable Energy Laboratory, NREL. It is an inherent part of the servo-hydro-aero-elastic analysis tool FAST [70]. For the aerodynamic analysis, one can choose either the BEM method or the Dynamic Inflow method, which is based on Generalized Dynamic Wake theory (see Section 3.5). Both methods will be used in this study. There is also an option to do the simulation where the unsteady aerodynamics is not taken into account.

6.8.1 Method

The 5 MW reference wind turbine is modeled in FAST, with no tilt of the nacelle and no cone angle of the blades. The structural components of the wind turbine are modeled as stiff, only the rotor is free to rotate. The rotational speed and the pitch angle is set as fixed values as listed in Table 6.2. This is to ensure that the simulations have the same input as the results presented in previous sections.

Instead of moving the structure in and out of the wind, the velocity of the wind is varied. The applied wind field is constant across the rotor, and is only varying in time. The applied velocity, $U_{\eta,x}$, across the rotor is described as:

$$U_{\eta,x}(t) = U_\infty - \dot{\eta}_{xp}(t) \tag{6.40}$$

where $\dot{\eta}_{xp}(t)$ is an predefined oscillation of the axial rotor velocity. This is illustrated in Figure 6.13 for a wind speed of 8 m/s. The oscillating velocity for both the low frequency and the high frequency oscillation are drawn in the graph. The low frequency oscillation has the same frequency as the platform pitch motion, and the velocity change is equal to a displacement with amplitude of 3 m. Similarly, the eigenfrequency first elastic bending mode for the tower is equal to the high frequency motion and the velocity corresponds to an amplitude of 0.25 m for the motion.

The velocity change felt at each blade section will not be the same as the predefined velocity, shown in Figure 6.13, since there will be a calculation of the induced velocity at each time step. Previously, the induced velocities were set as fixed throughout the simulation. Therefore the velocity of the rotor is estimated as:

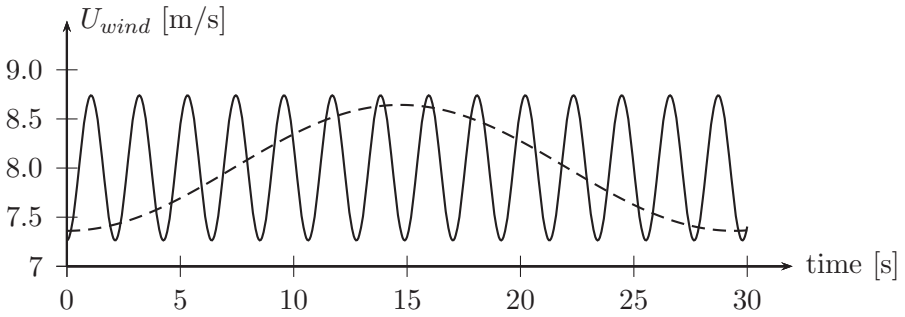

Figure 6.13: The applied wind field for low and high frequency oscillations for a wind speed of 8 m/s. The solid line illustrates high frequency motion (ω=2.95 rad/s), and the dashed line is low frequency motion (ω=0.21 rad/s).

$$\dot{\eta}_x(t) = U_\infty(1-\bar{a}) - U_{\eta,x}(t)\cdot(1-a(t)) \tag{6.41}$$

where $\bar{a}$ is the mean value of the axial induction factor, $a(t)$. The first term is the mean value of the axial velocity felt at the rotor disc, while the second term is the time dependent axial velocity.

The difference between the velocity at the rotor, $\dot{\eta}_x$, and the predefined values for the velocity, $\dot{\eta}_{xp}$, is shown in Appendix C in Figure C.3 for a wind speed of 8 m/s and an applied tower bending frequency. The same is shown acceleration is shown in Figure C.4 for four blade sections, relative to the preliminary defined acceleration. The acceleration curve is not smooth, but experiences a discontinuity close to its maximum and minimum acceleration values.

Similarly to the other methods, the thrust force is evaluated using only the lift at each blade section, using Equation 6.5. A graph with the thrust force at a blade section plotted relative to the axial motion of the rotor, η_x, is shown in Figure 6.15. The slope of the linear trendline is used to compute the damping coefficient for the blade section. This is similarly done for the acceleration.

The reduced frequency, k, is used as a measure of the unsteadiness in the simulations. In Figure 6.7, the reduced frequencies along the span for all simulations are shown. It is seen that it is the blade sections close to the root have the most unsteadiness. The most unsteady simulation is the one with lowest wind speed, 8 m/s, and the highest frequency, the

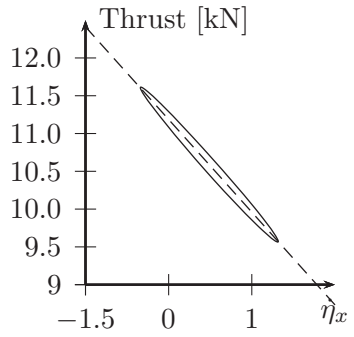

Figure 6.14: The slope of the linear trendline is used to estimate the damping coefficient. This is the high frequency motion with, U_∞=8 m/s, ω=2.95 rad/s.

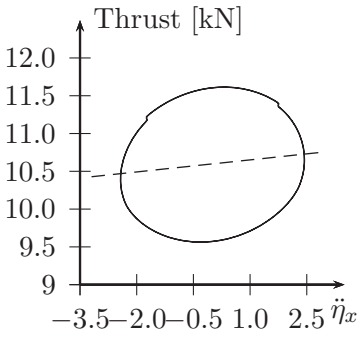

Figure 6.15: The slope of the linear trendline is used to estimate the aerodynamic added mass coefficient, U_∞=8 m/s, ω=2.95 rad/s.

tower bending frequency. Since we are now doing time domain analysis, it is important to have time steps that capture the unsteadiness of these situations correctly.

A convergence test of the time steps in AeroDyn was performed to check that the time steps were small enough to get the correct aerodynamic loads. The convergence test, investigating different timesteps, is shown in Appendix C, Figure C.5. A timestep of dt = 0.05 s, i.e. 600 points for the high frequency oscillation cycle (ω = 2.95 rad/s), shows a very good convergence.

6.8.2 Results

The wind structure interaction using two different inflow conditions is evaluated. The aim of the study shown here is to investigate the wind structure interaction locally at an airfoil, and the effect of the time-varying induced velocity is therefore removed from the main results, see Equation 6.41. This is to be able to compare the motion-induced aerodynamic loads estimated by AeroDyn relative to the other methods, where the induced velocity is kept constant.

The aerodynamic damping for the BEM simulation, including the unsteady aerodynamic, is shown in Figure 6.16. Both results for the low frequency and the high frequency oscillations of the airfoil are included in the graph. The dynamic inflow method produced similar results, and

are included in Appendix C, Figure C.8.

For the low frequency oscillations, the aerodynamic damping is almost equal to the one calculated with steady aerodynamic simulation. The radial distribution of the steady results, using BEM inflow, are included in Appendix C, Figure C.9. The results show that the damping is reduced for high frequency oscillations, where the aerodynamics is more unsteady.

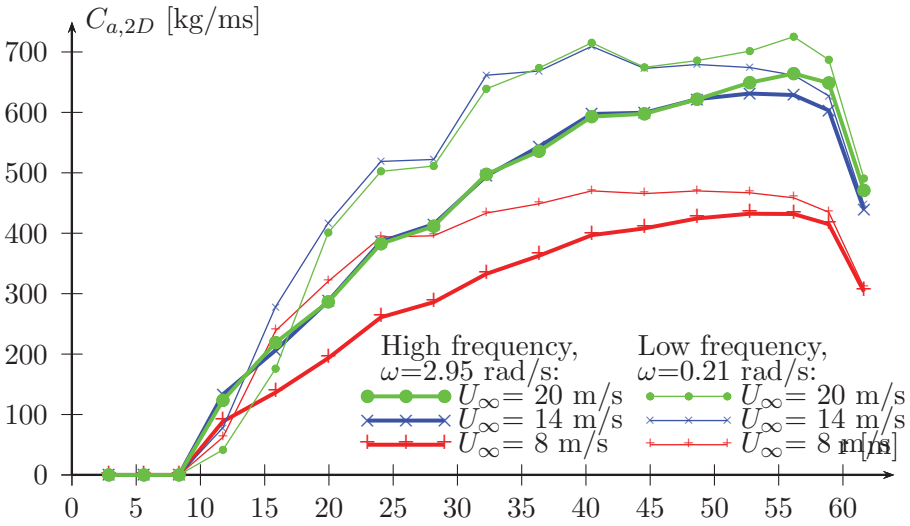

Figure 6.16: The local aerodynamic damping at each blade section along the radial distance of the blade for three different wind speeds. BEM method is applied here.

Even though the study here is on local two dimensional unsteady aerodynamic, a comment should be made on the difference between the two different inflow models, BEM and DYNIN in AeroDyn. DYNIN is the dynamic inflow model based on a Generalized Dynamic Wake model. This dynamic inflow model includes tip losses and skewed wake dynamics. However it is only valid for lightly loaded rotors and assumes that the induced velocities are small relative the the mean flow, i.e. the GDW model is not valid at low wind speeds.

A comparison between the results based on the BEM inflow model and the Dynamic Inflow model, where the time-varying influence coefficient is included, is shown in Figure 6.17. The aerodynamic damping coefficients are estimated for the high frequency oscillations, using the applied wind field as shown in Figure 6.13 for U_∞ = 8 m/s, and assuming constant

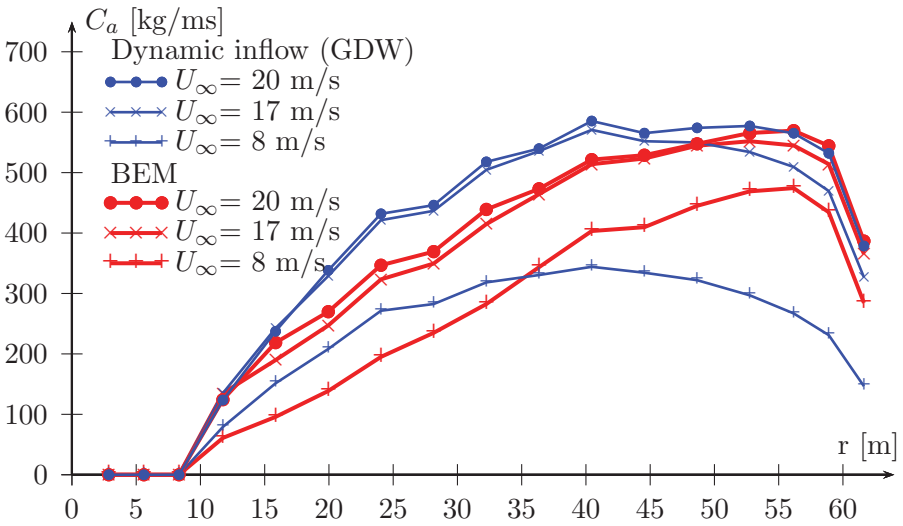

Figure 6.17: Comparing the dynamic aerodynamic damping using the predetermined velocity change, $\dot{\eta}_{xp}$ for the high frequency motion (ω=2.95 rad/s).

induction coefficients. The results indicate that the damping in general is slightly higher when applying the dynamic inflow model compared to the BEM method, except for the low wind speed. For this specific condition with a wind speed of 8 m/s, the damping is reduced when applying the dynamic inflow condition. This is due to the low wind speed, and the GDW model is not valid for this low wind speed.

The estimated virtual aerodynamic mass is included in Appendix C, Figure C.7. The aerodynamic added mass here includes the aerodynamic stiffness component, which is defined as the virtual aerodynamic mass, see Eq 6.4.

6.8.3 Discussion

The integrated modal properties for the virtual aerodynamic mass and the aerodynamic damping are shown in Table 6.11 for the first tower bending mode (ω=2.95 rad/s) and in Table 6.10 for the platform pitch mode (ω=0.21 rad/s). An overview of the what is the differences between the three methods are listed in Table 6.5. Even though the aerodynamic damping coefficient is the same for both frequencies using steady aerodynamics, the integrated aerodynamic properties will differ since it is

		8m/s	14 m/s	20 m/s
C_a [kg m^2/s]	Unsteady	$1.39 \cdot 10^9$	$1.97 \cdot 10^9$	$1.94 \cdot 10^9$
	GDW	$1.36 \cdot 10^9$	$1.96 \cdot 10^9$	$1.93 \cdot 10^9$
	Steady	$1.36 \cdot 10^9$	$1.92 \cdot 10^9$	$1.90 \cdot 10^9$
ξ [%]	Unsteady	5.83	8.25	8.15
	GDW	5.70	8.21	8.09
	Steady	5.70	8.08	7.97
M_{va} [kg m^2]	Unsteady	$-1.78 \cdot 10^8$	$-1.99 \cdot 10^8$	$-1.76 \cdot 10^8$
	GDW	$-7.74 \cdot 10^7$	$-7.03 \cdot 10^7$	$-4.11 \cdot 10^7$
	Steady	$-1.75 \cdot 10^5$	$-1.43 \cdot 10^5$	$-1.50 \cdot 10^5$
$\frac{M_{va}}{M_i}$ [%]	Unsteady	-0.32	-0.36	-0.32
	GDW	-0.14	-0.13	-0.07
	Steady	-0.00	-0.00	-0.00

Table 6.10: Integrated aerodynamic properties for the platform pitch mode, estimated using AeroDyn. Three different options are used for the aerodynamics; BEM with unsteady aerodynamics , General Dynamic Wake and BEM with steady aerodynamics.

related to different modes of the wind turbine structure. For the higher wind speeds, the BEM and GDW method both give similar results.

The low aerodynamic damping result for the low wind speed (U_∞= 8 m/s), using the GDW model, is not due to returning wake effects. The GDW model was developed assuming that the induced velocities are small relative to the mean flow, and this is not true for the low wind speed. The GDW model should therefore not be used at this wind speed.

In the results from AeroDyn, the induced velocities are removed. This is the reason why the results from GDW and BEM method are similar for most simulations, since they use the same unsteady aerodynamic calculations, the Beddoes-Leishman function. The difference between these approaches are how they compute the induced velocities of the inflow, and not the local two dimensional unsteady aerodynamics. In order to show this effect, the damping calculated using the targeted velocity, $\dot{\eta}_{xp}$,

		8m/s	14 m/s	20 m/s
C_a [kg/s]	Unsteady	$4.56 \cdot 10^4$	$6.73 \cdot 10^4$	$6.73 \cdot 10^4$
	GDW	$4.56 \cdot 10^4$	$6.89 \cdot 10^4$	$7.00 \cdot 10^4$
	Steady	$5.49 \cdot 10^4$	$7.82 \cdot 10^4$	$7.71 \cdot 10^4$
ξ [%]	Unsteady	1.97	2.91	2.94
	GDW	1.97	2.98	3.03
	Steady	2.38	3.38	3.34
M_{va} [kg]	Unsteady	$-3.02 \cdot 10^3$	$-5.06 \cdot 10^3$	$-5.31 \cdot 10^3$
	GDW	$-2.83 \cdot 10^3$	$-5.07 \cdot 10^3$	$-5.18 \cdot 10^3$
	Steady	$8.98 \cdot 10^{-2}$	$-5.66 \cdot 10^{-2}$	$-6.06 \cdot 10^{-2}$
$\frac{M_{va}}{M_i}$ [%]	Unsteady	-0.77	-1.30	-1.36
	GDW	-0.72	-1.30	-1.33
	Steady	0.00	-0.00	-0.00

Table 6.11: Integrated aerodynamic properties for the first elastic bending mode, estimated using AeroDyn. Three different options are used for the aerodynamics; BEM with unsteady aerodynamics, General Dynamic Wake and BEM with steady aerodynamics.

is shown in Figure 6.17.

There are some small differences between the AeroDyn calculations and the estimates using Theodorsen's theory. This can be related to that the unsteady aerodynamics computed by AeroDyn is not limited to only attached flow and potential flow. The unsteady aerodynamics corrections also includes the dynamic stall. In the unsteady results presented earlier, the effect of dynamic stall is expected to be small. If the velocity of the axial motion is increased, the angle of attack will increase, and there will be stall effects at the blade sections. The largest and smallest angles of attack along the blade are shown for two wind speeds, U_∞=8 m/s and U_∞=20 m/s in Figure 6.18.

The stall angle will be dependent on the aerodynamic characteristics of the airfoil. The airfoil sections used close to the root of the blade will have a larger stall angle, then the airfoils section located towards the tip

		8m/s	14 m/s	20 m/s
C_a [kg/s]	BEM	$4.32 \cdot 10^4$	$5.81 \cdot 10^4$	$6.03 \cdot 10^4$
	GDW	$3.88 \cdot 10^4$	$6.44 \cdot 10^4$	$6.68 \cdot 10^4$
ξ [%]	BEM	1.87	2.52	2.61
	GDW	1.68	2.79	2.89
M_{va} [kg]	BEM	$-2.94 \cdot 10^3$	$-4.31 \cdot 10^3$	$-4.65 \cdot 10^3$
	GDW	$-9.34 \cdot 10^2$	$-4.57 \cdot 10^3$	$-4.18 \cdot 10^3$
$\frac{M_{va}}{M_i}$ [%]	BEM	-0.75	-1.11	-1.19
	GDW	-0.24	-1.17	-1.07

Table 6.12: Integrated aerodynamic properties for the first elastic bending mode, estimated using AeroDyn. These values include the outer unsteady aerodynamics effects.

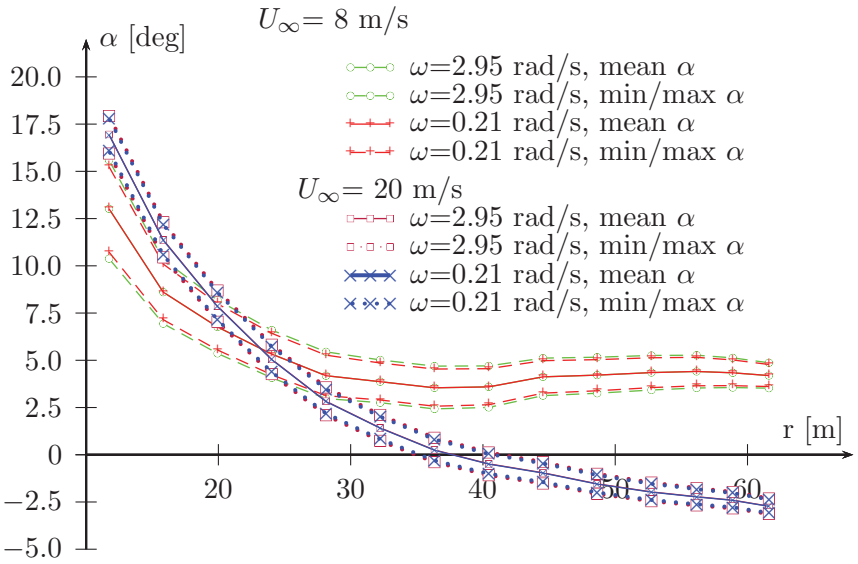

Figure 6.18: Variation of angle of attack, α, along the blade

of the blade. In Appendix A, the lift curve of each of the airfoil sections used are plotted. The maximum angle of attack occurring in the AeroDyn simulations are also plotted. All angle of attack within this simulation

have a value lower than the static stall value.

6.9 Vortex Panel Code

A momentum analysis, as described in Section 3.4 will be used to estimate the induced velocity at the rotor disc for the single airfoil. This is the same approach as used when estimating the induced velocity used as input to the Theodorsen's function (Section 6.6) and Loewy's function (Section 6.7). The comparison is made for 13 airfoil sections along the wind turbine blade. The effect of using a linear cascade approach, as described in Section 5.6, compared to a single airfoil is also investigated.

The airfoils have 200 panel elements to ensure a good quality of the results. Using the single airfoil vortex code is more time consuming than applying the Theodorsen function. Adding more airfoils in the cascade simulation increases the computational time further. However, it is expected that these results will yield more accurate unsteady aerodynamic forces, relative to the previous methods.

6.9.1 Single airfoil

As shown in Figure 5.13 the dynamic lift of an airfoil depends on the shape of the airfoil and will not behave exactly as for a thin airfoil. It is therefore expected that the dynamic response of a wind turbine will be dependent on the airfoil shape. In this section an analysis using the vortex panel code will be compared to results using Theodorsen's function, which is using a flat foil with no thickness.

In the analysis a single airfoil is moved along a path, as shown in Figure 6.19. The velocity which the airfoil moves at in the x direction is equal to the velocity of an airfoil located at radii, r, rotating with speed Ω. The motion in the axial direction, η_x, is due to the platform pitch motion or the elastic tower bending, depending on the mode that is studied. The airfoil oscillates with a period $2\pi/\omega$ and an amplitude of 0.2 m. As before, two different frequencies of the oscillations are investigated, one high frequency (ω = 2.95 rad/s) and one low frequency (ω=0.21 rad/s). These are corresponding to the first elastic bending tower eigenfrequency and the platform pitch eigenfrequency respectively.

To avoid start-up effects, the simulation is run for $120s$, where s is a non-dimensional timestep, $s = 2Wt/c$. W is the resulting flow velocity, which is a combination of the velocity of the wind and the velocity of the

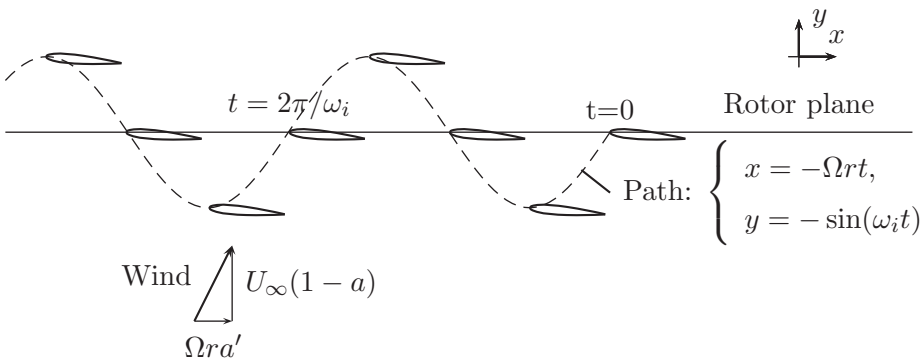

Figure 6.19: An airfoil is illustrated at different time steps as it moves along a path illustrated by a dashed line. The velocity along the rotor plane is equal to the rotational speed (Ωr). An incoming wind speed, U_∞, and the normal and tangential induced velocities, a and a', are also included in the method.

airfoil. The resulting velocity, W, at each airfoil are illustrated in Figure 6.1. The time used for start-up effects is therefor dependent on chord length and resulting velocity. The lowest velocity and largest chord is at the root of the blade, and we will apply the simulation time estimated for the inner airfoil to all airfoils along the blade.

The aerodynamic damping is estimated by finding a linear trend between the thrust and the velocity of airfoil in the axial direction. When the airfoil moves in the direction of the free wind, it reduces the relative fluid velocity in axial direction. The relative fluid velocity is increased when the airfoil moves towards the wind direction.

To estimate the aerodynamic damping, the thrust force is plotted against the velocity of the airfoil in the y-direction (see Figure 6.19). This is illustrated for the first elastic tower motion in Figure 6.20 for the airfoil segment located at node 11. The solid line illustrates the aerodynamic load due to the load at the high frequency oscillation, and the dashed line is the trendline. There is a strong correlation between the thrust force and the velocity. Similar result is presented done for the low frequency oscillation in Figure 6.22. The slope of the trend-lines are used to compute the damping coefficients of the airfoil section at the two different frequencies.

The damping coefficients for all 13 nodes along the blade are shown in Figure 6.25 for the high frequency oscillation. The results from the vortex panel code is shown with a solid line, while the Theodorsen results

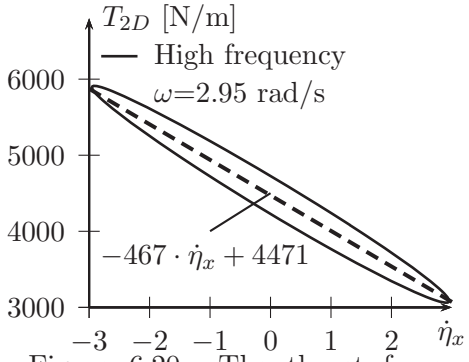

Figure 6.20: The thrust force plotted against the velocity of the wind turbine rotor for the airfoil at node 11 with a wind speed $U_\infty = 8$ m/s.

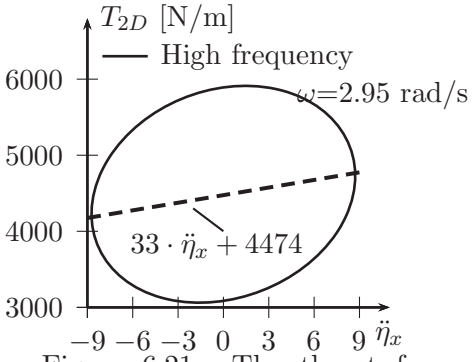

Figure 6.21: The thrust force plotted against the acceleration of the wind turbine rotor for the airfoil at node 11 with a wind speed $U_\infty = 8m/s$.

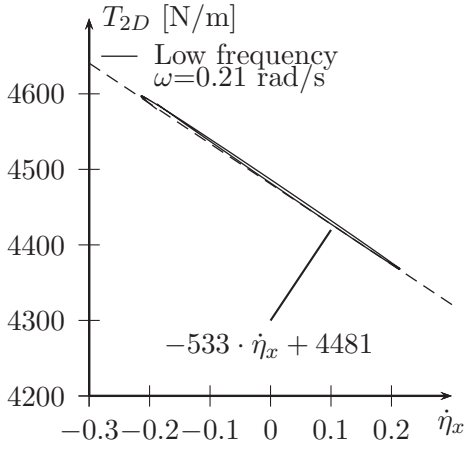

Figure 6.22: The thrust force plotted against the velocity of the wind turbine rotor for the airfoil at node 11 with a wind speed $U_\infty = 8m/s$.

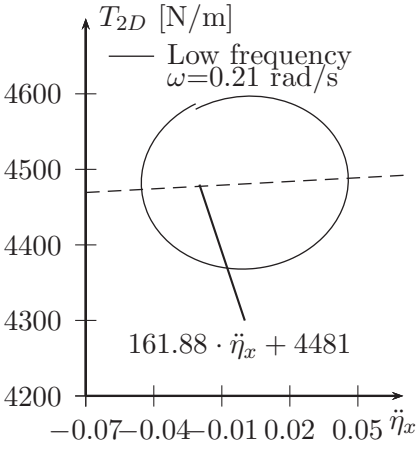

Figure 6.23: The thrust force plotted against the acceleration of the wind turbine rotor for the airfoil at node 11 with a wind speed $U_\infty = 8m/s$.

are plotted with dashed lines. The trend is that the damping is generally higher when evaluated with the vortex panel code.

A similar approach is used to investigate the aerodynamic virtual added mass. The thrust force is plotted against the acceleration of the airfoil in y-direction. Figure 6.21 and Figure 6.23 illustrate this for the airfoil segment at node 11 for high frequency oscillation and the low frequency oscillation respectively. The linear trend-line is the dashed line. It is evident that the correlation between the thrust force and the acceleration is weak. Since it is a weak correlation, this is an effect that is not easily measured.

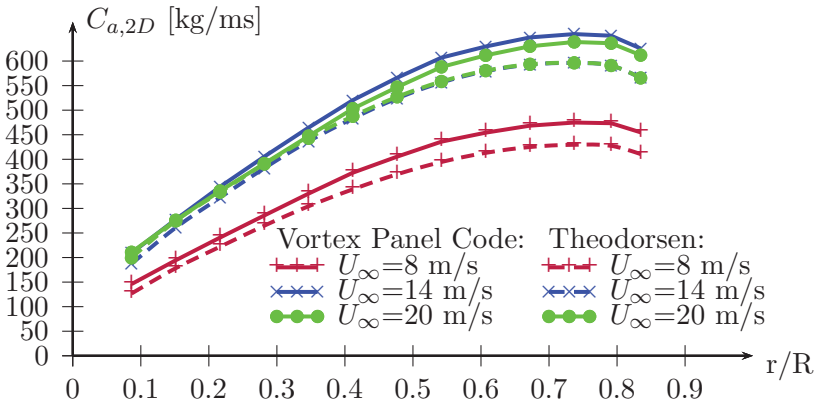

Figure 6.24: The estimated aerodynamic damping along the blade for high frequency oscillation. The solid lines are based on the vortex panel code, and the dashed line is based on Theodorsen theory.

Similarly to the aerodynamic damping, the virtual added mass is calculated using the inclination of the linear trendline for thrust force and the acceleration. The results are presented in Figures 6.26 and 6.27 together with results from Theodorsen.

The results from the first tower bending moment are similar to the results estimated using Theodorsen's theory. They are generally lower, which means a negative added mass. This implies that there is a higher aerodynamic stiffness than predicted by Theodorsen.

The first elastic bending tower mode has an eigenfrequency of 2.95 rad/s similar to the high frequency oscillation studied, and similarly for the platform pitch mode and the low frequency studied. The integrated values of the aerodynamic added mass and damping coefficients can therefore be used to estimate modal quantities for the two modes, as shown in

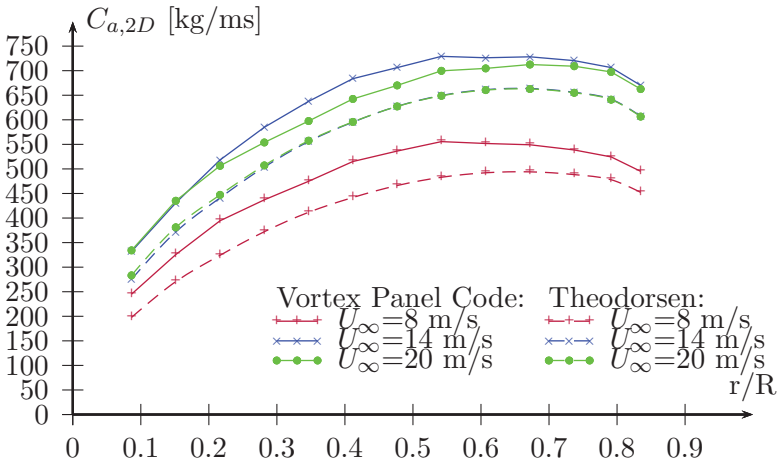

Figure 6.25: The estimated aerodynamic damping for the low frequency oscillation, along the blade. The solid lines are based on the vortex panel code, and the dashed line is based on Theodorsen theory.

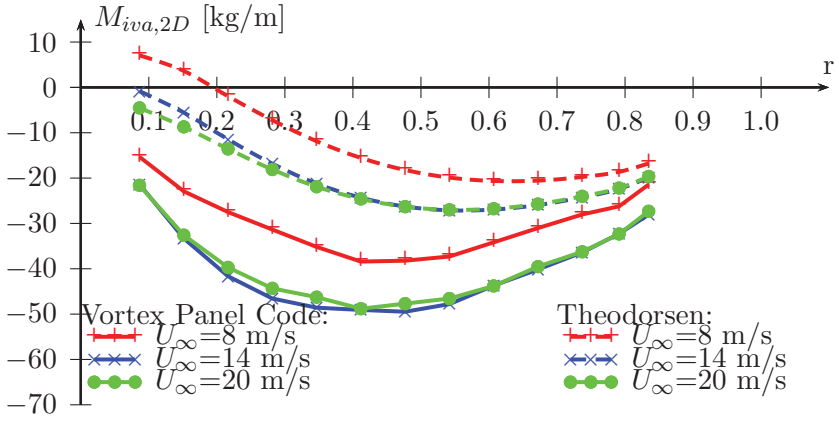

Figure 6.26: The aerodynamic added mass calculated for high frequency motion using the vortex panel code, compared to estimation based on Theodorsen theory

Table 6.14 and Table 6.13 for all wind speeds.

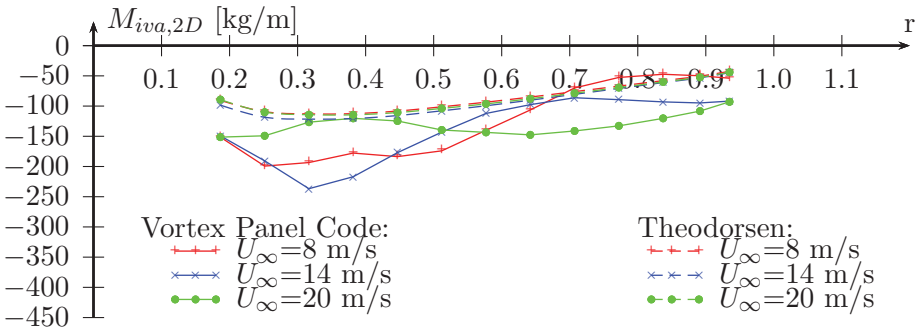

Figure 6.27: The aerodynamic added mass calculated for the low frequency motion using the vortex panel code, compared to estimation based on Theodorsen theory

	8m/s	14 m/s	20 m/s
C_a [kg m^2/s]	$1.67 \cdot 10^9$	$2.22 \cdot 10^9$	$2.14 \cdot 10^9$
ξ [%]	7.01	9.31	9.00
M_{va} [kg m^2]	$-4.46 \cdot 10^8$	$-4.88 \cdot 10^8$	$-4.61 \cdot 10^8$
$\frac{M_{va}}{M_i}$ [%]	−0.80	−0.88	−0.83

Table 6.13: Integrated aerodynamic properties for the platform pitch mode, estimated using panel vortex code

	8m/s	14 m/s	20 m/s
C_a [kg/s]	$5.17 \cdot 10^4$	$7.21 \cdot 10^4$	$7.01 \cdot 10^4$
ξ [%]	2.24	3.12	3.04
M_{va} [kg]	$-4.38 \cdot 10^3$	$-5.88 \cdot 10^3$	$-5.74 \cdot 10^3$
$\frac{M_{va}}{M_i}$ [%]	−1.12	−1.51	−1.47

Table 6.14: Integrated aerodynamic properties for the first elastic bending mode for the tower, estimated using panel vortex code

6.9.2 Linear Cascade

Previous investigation of the linear cascade using a thin plate model indicates that the behaviour of the linear cascade is dependent on the local

velocity ratio, $\lambda_r = \Omega r(1+a')/U_\infty(1-a)$, the spacing between the airfoils, S_c, and the frequency of the oscillation. These properties are all listed in Table 6.15 for the simulation cases. The spacing between the airfoils will be constant for all wind speeds, while the velocity ratio will vary.

wind	R	S_c	8 m/s	14 m/s	20 m/s
node	[m]	[m]	λ_r	λ_r	λ_r
4	11.9	24.61	3.9	2.5	1.7
5	14.7	33.20	4.7	2.9	1.9
6	18.0	41.78	5.4	3.3	2.2
7	21.7	50.37	6.4	3.7	2.4
8	26.0	58.96	7.3	4.1	2.7
9	31.0	67.54	7.8	4.5	3.0
10	36.9	76.13	8.7	4.9	3.2
11	43.9	84.72	9.6	5.3	3.5
12	50.9	93.31	10.6	5.7	3.7
13	59.1	101.89	11.8	6.1	3.9

Table 6.15: The local velocity ratio, λ_r, and spacing between the airfoils, S_c, for three different wind speeds.

The unsteady aerodynamics for a section with reduced spacing value, S_c, will have more influence of the neighbouring wake. Similarly, an increase in the λ_r would also increase the influence from the neighbouring wakes. Based on these observations, it is the simulation with $U_\infty = 8$ m/s which will have most influence from the wakes, and the simulation with $U_\infty = 20$ m/s which will have the lowest.

Using the limiting number of airfoils as defined in Equation 4.101, one can estimate the number of airfoils needed in the cascade to compute the unsteady loads. This limiting number is not sufficient for convergence, but a too high number of airfoils will also reduce the computational speed severely. In this study, the number of airfoils required has been multiplied by four. For the high frequency oscillation, this give good convergence with a reasonable computational time, but for the low frequency oscillation the computational time is too large. The reason is that the simulation

node	High frequency, ω=2.95 rad/s $k_c = 4 \cdot k_p$			Low frequency, ω=0.21 rad/s $k_c = 4 \cdot k_p$		
U_∞	8 m/s	14 m/s	20 m/s	8 m/s	14 m/s	20 m/s
Time	*17.8 s*	*13 s*	*12.7 s*	*45.7 s*	*40.9 s*	*40.6 s*
4	56	64	76	144	196	232
5	52	56	64	128	172	200
6	48	52	56	120	156	180
7	44	48	52	116	148	168
8	44	48	52	112	140	156
9	44	44	48	108	136	148
10	44	44	48	104	132	144
11	40	44	44	104	128	140
12	40	40	44	100	128	136
13	40	40	44	100	124	132
14	40	40	44	100	124	132
15	40	40	40	100	124	128
16	40	40	40	96	120	128

Table 6.16: The applied number of panels is estimated for each simulation. k_p is the limiting number, and the number of airfoils is $no_{bl} = 2 \cdot k_c + 1$.

length needs to be longer since the eigenperiod is longer.

The cascade number, k_c, and the length of the simulations are listed in Table 6.16 both for the high frequency oscillation and the low frequency oscillation. The number of airfoils in the cascade is multiplied four times the critical number k_p, but there is still an effect due to the limited number of airfoils. For an ideal case this number should be infinite. In Figure 6.28, the unsteady aerodynamic lift for the low wind speed, $U_\infty = 8$ m/s, is investigated for node 4, close to the root of the blade. When investigating the aerodynamic damping of the wind turbine structure, this decreasing slope will give an artificial increase the estimated damping. However, the lift force have a linear decreasing trend for $t > 5$.

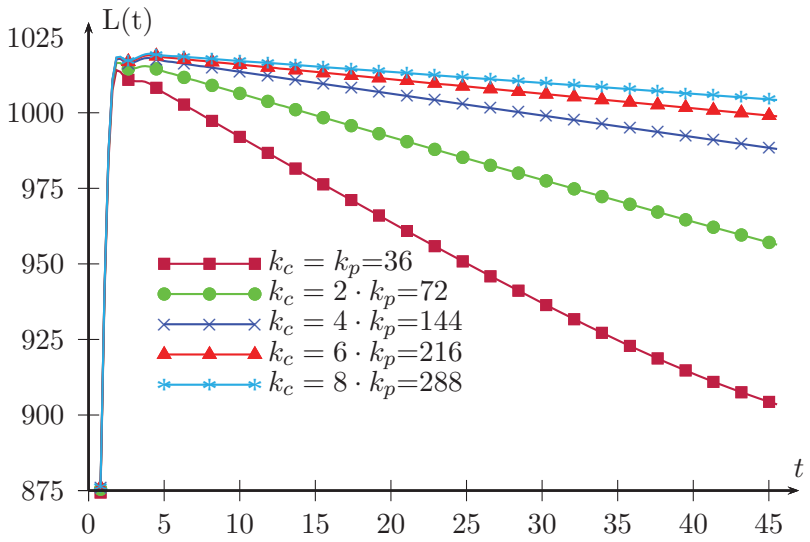

Figure 6.28: The unsteady aerodynamic lift force using different number of airfoils in the linear cascade for a wind speed 8 m/s for the first 45 seconds. The cascade number, k_c, is related to the number of airfoils in the cascade as: $no_{bl} = 2 \cdot k_c + 1$

The low frequency oscillation has a period of 30 sec. The results using a cascade number four times the limiting is shown with a dashed line in Figure 6.29. The aerodynamic damping estimated based on this simulation would be wrong. In order to correct for this, the analysis with no amplitude shown in Figure 6.28 can be used. The thrust force from the analysis with no oscillating amplitude is subtracted from the thrust force with the low frequency oscillations. This is the corrected line in Figure 6.29.

For the short period of the high frequency oscillation, the decreasing slope due to the cascade is not as dominating. Figure 6.30 illustrates both the original and the corrected solution. The motion-dependent forces estimated using the corrected and the original values are approximately the same. The correction is therefore only performed for the low frequency oscillations.

The linear cascade results will be compared to Loewy's function, which is a frequency domain solution which includes the returning wake,

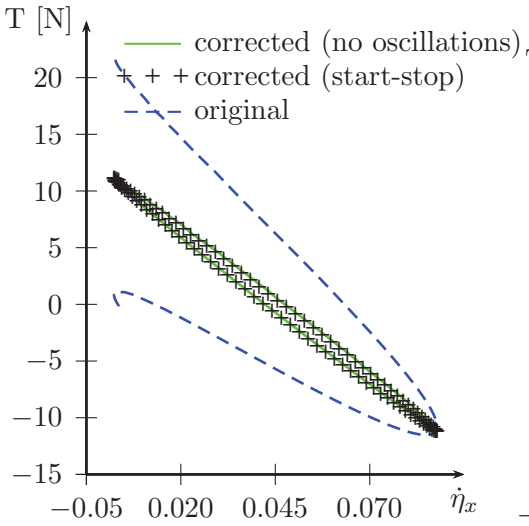

Figure 6.29: The aerodynamic thrust force estimated for the low frequency motion, and corrected for the limited number of airfoils, relative to the velocity of the rotor.

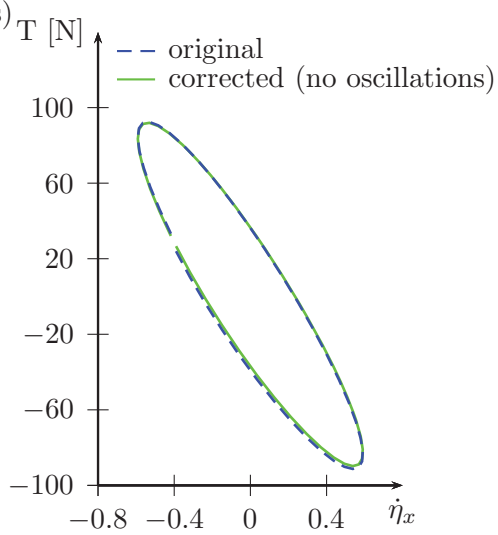

Figure 6.30: The unsteady aerodynamic thrust force during the high frequency motion.

see Chapter 4.6.4 for more details.

At the lowest wind speed the linear cascade shows a significant reduction in the aerodynamic damping for the high frequency oscillations. This effect is not seen for the two higher wind speeds. The reason is a low rotational velocity, which has a cascade frequency close to the high frequency (ω=2.95 rad/s). The rotational speed is 9.16 rpm at the low wind speed, which gives rotational frequency of 0.96 rad/s. Since it is a three bladed rotor, the blade passing frequency is 2.88 rad/s, which is relatively close to the high frequency oscillation used in these studies.

The two higher wind speeds have a lower velocity ratio and a rotational frequency that is higher than eigenfrequency of the tower mode investigated. The rotational frequency due to the rotational speed of 12.3 RPM is 1.29 rad/s, which gives a blade passing frequency of 3.86 rad/s. The effect of the returning wake is therefore not dominant at the other wind speeds.

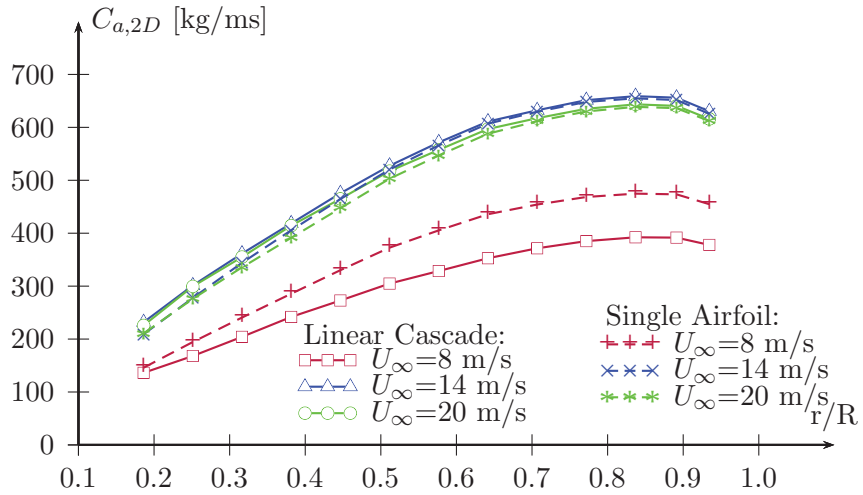

Figure 6.31: Aerodynamic damping along the blade for the high frequency oscillation estimated with the linear cascade method compared to a single airfoil method. Both methods uses the panel vortex code to estimate the loads.

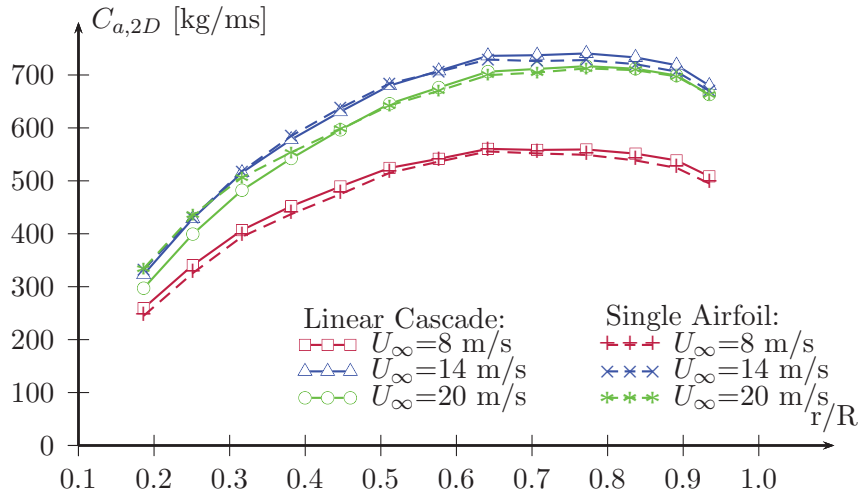

Figure 6.32: Aerodynamic damping along the blade for the low frequency oscillation estimated with the linear cascade method compared to a single airfoil method. Both methods uses the panel vortex code to estimate the loads.

6.10 Discussion

Three approaches has been used to estimate the aerodynamic added mass and the aerodynamic damping. These are the engineering tool AeroDyn,a

vortex panel code and two frequency-domain approaches. An overview of the different aerodynamic methods are shown in Table 6.5. Using these methods, the motion-induced aerodynamic loads on a wind turbine rotor has been investigated, focusing on the platform pitch mode (ω_n=0.21 rad/s) and the first elastic tower bending mode (ω_n=2.95 rad/s).

6.10.1 Aerodynamic damping

An overview of the estimated aerodynamic damping for first tower bending moment is given in Table 6.17. The quasi-static approach, which does not include any unsteady aerodynamics, is estimating a higher aerodynamic damping relative to the unsteady aerodynamic approaches.

	$U_\infty = 8$ m/s	$U_\infty = 14$ m/s	$U_\infty = 20$ m/s
Quasi-Static flat	2.62 %	3.72 %	3.81 %
Garrad	2.58 %	3.47 %	3.47 %
BEM U	1.97 %	2.91 %	2.94 %
BEM inflow	1.87 %	2.52 %	2.61 %
GDW inflow	1.68 %	2.79 %	2.89 %
Theodorsen	2.04 %	2.88 %	2.91 %
Loewy	1.77 %	2.83 %	2.88 %
Vortex - Single	2.24 %	3.12 %	3.04 %
Vortex - Cascade	1.85 %	3.18 %	3.11 %

Table 6.17: Aerodynamic damping ratio estimated using the 1^{st} tower bending eigenfrequency.

The quasi-static approach and the frequency domain methods are both very fast. The aerodynamic damping for all wind speeds are estimated for the first elastic tower bending mode. The results are shown in Figure 6.33. The results of the other methods discussed in this chapter is included at the wind speeds 8 m/s, 14 m/s and 20 m/s. The steady aerodynamic method of Garrad is overestimating the aerodynamic damping for all the wind speeds considered.

The quasi-steady estimate of the aerodynamic damping based on Garrad's equation are the simplest. This is only based on the rotational speed

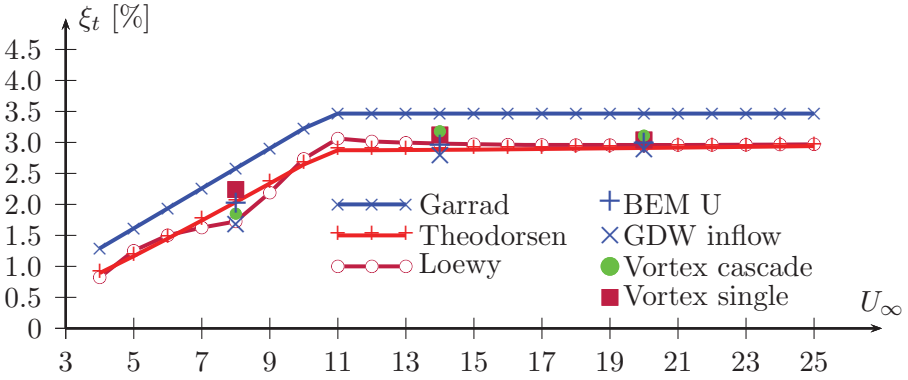

Figure 6.33: The quasi-static aerodynamic damping of first elastic bending mode for the tower for all wind speed. Point values for other simulations.

of the wind turbine. The method overpredicts the aerodynamic damping, but gives a good indication of the aerodynamic damping. Using Theodorsen's theory gives a much better prediction of the aerodynamic damping.

The largest difference in aerodynamic damping between the methods applied is found for the low wind speed, $U_\infty = 8$ m/s. The two dimensional aerodynamic damping coefficient along the blade is shown in Figure 6.34 for this low wind speed. The reason for the large spread in results at this wind speed is that high frequency oscillation (ω=2.95 rad/s) is close to the blade-passing frequency (ω=2.88 rad/s). When the blade-passing frequency is an integer of the frequency that the blades are oscillating at, the aerodynamic damping is reduced. This effect is due to the neighbouring blades, and are modelled by Loewy's theory and the linear cascade of airfoils.

The trend is that the lowest values of aerodynamic damping are estimated by the methods which include the returning wake effect. It is evident that this effect is most profound towards the tip of the blade. This is where the spacing between the blade is largest, and we would expect that this would reduce the effect. But the local velocity ratio, λ_r, is high at the tip and low at the root. It is therefore assumed that the velocity ratio is more important than the blade spacing when discussing the neighbouring wake effects in this simulation.

However, GDW also predicted reduced aerodynamic damping for the low wind speed and the high frequency oscillation. This is because the

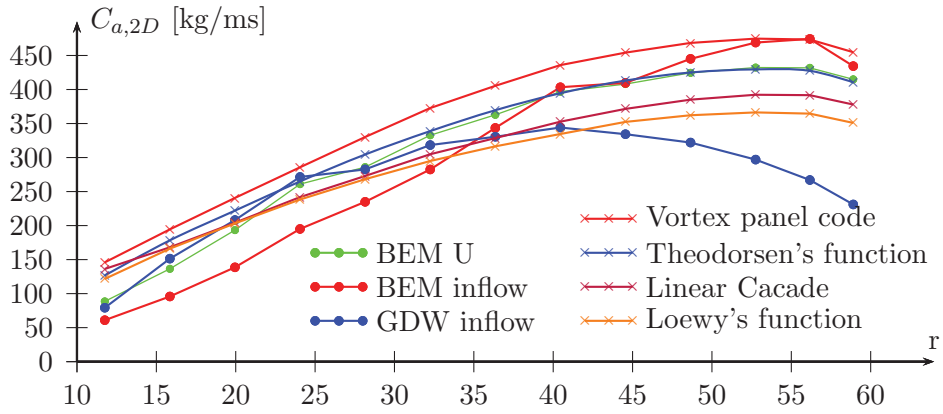

Figure 6.34: The estimated aerodynamic damping for the high frequency oscillation (ω=2.95 rad/s) and wind speed 8 m/s

assumption of small induced velocities relative to the mean wind flow is validated. The GDW results are therefore erroneous. GDW is the only method which includes tip-loss in the comparison, and this explains the differences in the aerodynamic damping towards the tip of the blade.

The two wind speeds above rated have less spread in the results. The radial distribution of the aerodynamic damping coefficient is shown in Figure 6.35 for U_∞ = 14 m/s and in Figure 6.36 for U_∞ = 20 m/s for the high frequency oscillations. Both graphs show similar trends with the frequency domain methods Theodorsen's theory and Loewy's theory giving similar estimates of the coefficient. There is a relatively small difference between the aerodynamic coefficient estimated using a single airfoil relative to a cascade of airfoils when applying the vortex panel code.

The aerodynamic damping ratio of the platform pitch motion is larger than the aerodynamic damping of the first elastic tower bending in the fore-aft direction. The results are listed in Table 6.18. The lowest aerodynamic damping is predicted at 8 m/s, and the highest at 14 m/s.

The platform pitch mode has a very low eigenfrequency, and should be well described by the steady aerodynamic tools. Surprisingly, the aerodynamic damping estimated by the panel vortex code is higher than the other methods for all wind speeds. Both the simulation using a single airfoil, and the simulation using a cascade of airfoils are estimating up to 20% higher damping relative to the other methods.

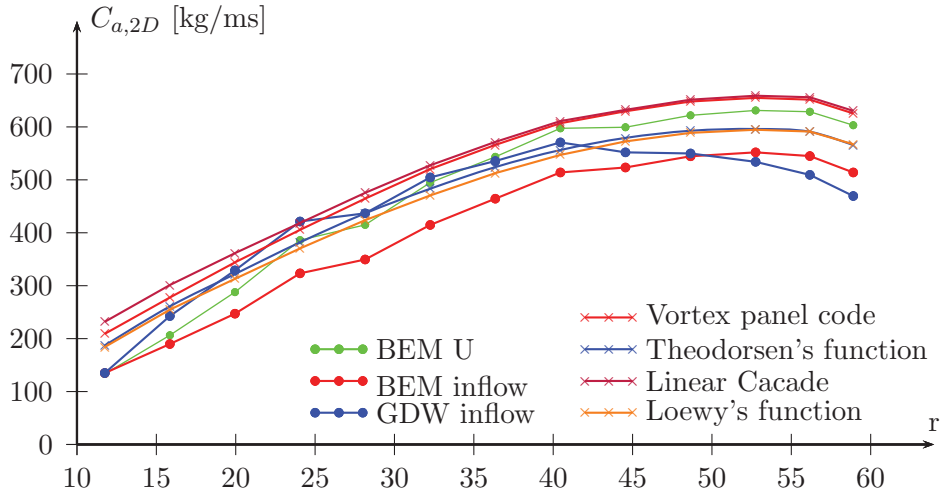

Figure 6.35: The estimated aerodynamic damping for the high frequency motion (ω=2.95 rad/s) and wind speed 14 m/s

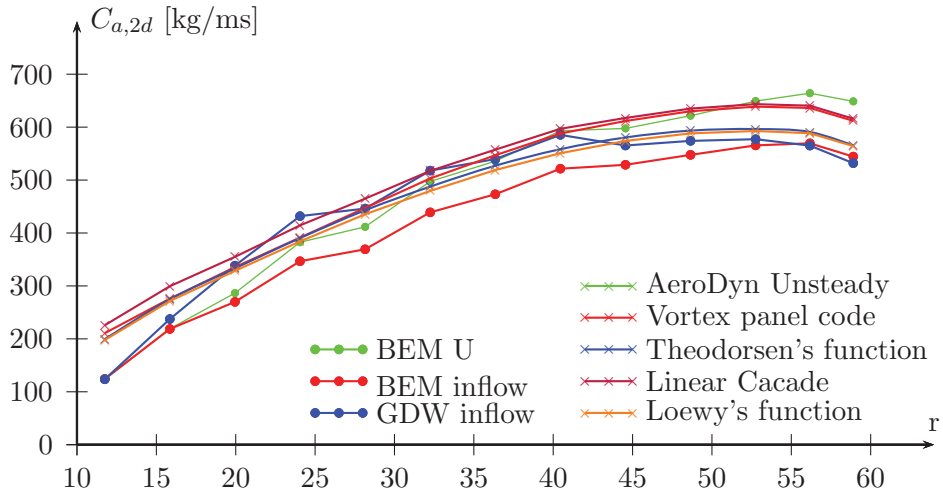

Figure 6.36: The estimated aerodynamic damping for the high frequency motion (ω=2.95 rad/s) and wind speed 20 m/s

The two dimensional local damping estimated, using the different aerodynamic methods, at the radial position of the blade is shown in

	$U_\infty = 8$	$U_\infty = 14$	$U_\infty = 20$
Quasi-Static flat	6.25 %	8.88 %	9.10 %
Garrad	6.16 %	8.27 %	8.27 %
BEM U	5.83 %	8.25 %	8.15 %
Theodorsen	6.12 %	8.25 %	8.28 %
Loewy	6.14 %	8.18 %	8.17 %
Vortex - Single	7.01 %	9.31 %	9.00 %
Vortex - Cascade	7.17 %	9.35 %	8.93 %

Table 6.18: Aerodynamic damping ratio estimated using the platform pitch eigenfrequency.

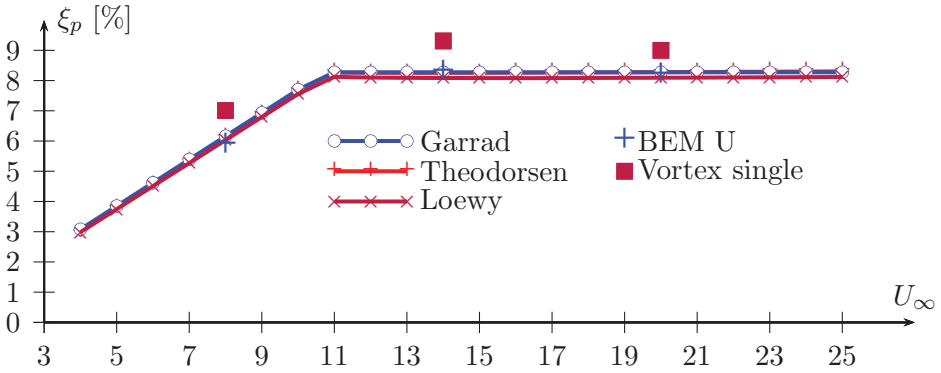

Figure 6.37: The quasi-static aerodynamic damping of the platform pitch mode for the tower for all wind speed. Point values for other simulations.

Figure 6.38 for the low frequency oscillation. The wind speed is here 20 m/s. The results based on the vortex panel code has a similar shape to the results based on Theodorsen's function, Loewy's function and Garrad, but it has a higher value compared to the others.

6.10.2 Aerodynamic added mass

The virtual aerodynamic added mass does not have a large impact on the dynamic properties of the modes investigated, and the change in the eigenfrequency of the structure is very small. This is illustrated in Figure

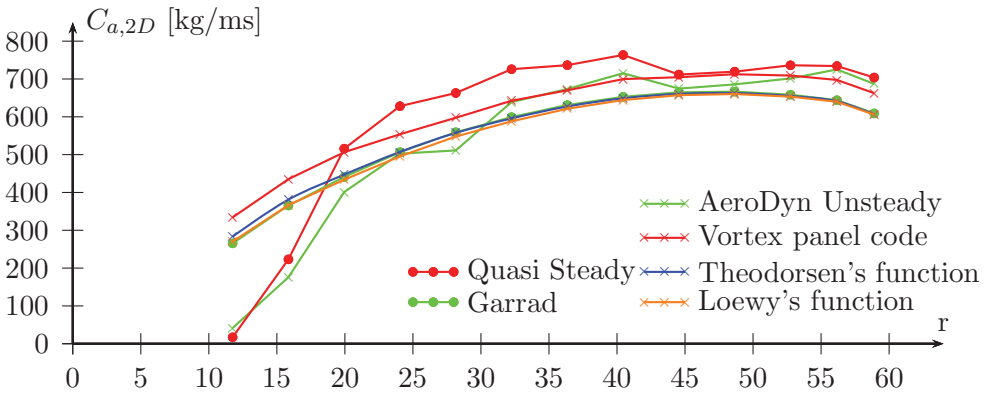

Figure 6.38: The estimated aerodynamic damping for the low frequency (ω=0.21 rad/s) oscillation and wind speed 20 m/s

6.39 where eigenfrequency is estimated considering the change in added mass as shown in Equation 6.15. The results from the simulations have also shown that it is not an easy property to estimate correctly, since the dependency is weak.

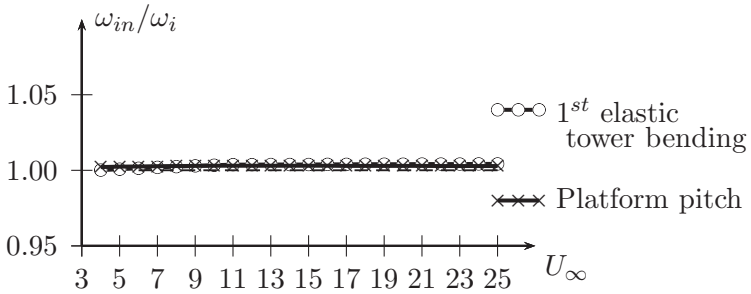

Figure 6.39: The natural frequencies for the platform pitch and the first tower bending mode for a floating wind turbine estimated using Theodorsen's theory.

6.10.3 Fatigue

One consequence of applying the wrong unsteady aerodynamic models in fatigue analysis is an overestimate, or underestimate, of the damage to the structure. An underestimate of fatigue damage may lead to an earlier

failure than predicted of the wind turbine structure. A too high estimate of fatigue damage will give a design requiring higher material cost than necessary, and thus an increase in the cost of energy.

In this section the aim is to discuss the aerodynamic properties from the different unsteady aerodynamic models and their effect on the estimated wind turbine fatigue damage. For simplicity, it is assumed that the damage is due to a single narrow-banded response, and that the loading is Gaussian white noise. This is not true for an offshore wind turbine, which will have a much more complex excitation and response spectra.

Examples of some excitation spectra are shown in Figure 6.40, which illustrates Kaimal wind spectra, S_u, at three different wind speeds; 8 m/s, 14 m/s and 20 m/s, and a JONSWAP wave spectra S_j for T_p =4 s and H_s= 1 m. The excitation spectra from the wind is shown as it would be seen by a fixed observer, e.g. a meteorologic measurement mast. Since the wind turbine is rotating, the wind spectra seen by the rotating observer on the blade will be dependent on the rotational speed. The frequency of one rotation of the blade is 1P, and the blade passing frequency is 3P for a three bladed rotor. The 3P excitation is included in Figure 6.41, which illustrates the tower top response spectra, in the horizontal fore-aft direction, for three wind speeds at one sea state.

The tower top response is modeled using the OC3 Hywind aero-elastic structure in FAST [70]. The wind turbine is set to operate at a fixed speed, and with a fixed blade pitch angle. For all three wind speeds there are two main regions where the tower top response is excited, and these two fall in to the regions around the platform pitch and the first elastic tower bending mode. The wave spectra is the same for all three simulations, and a small peak in response is seen around the peak period, at 4 seconds. This is a rigid body wave induced response.

The excitation of the tower top around the eigenfrequency of the platform pitch, which is at 0.034 Hz, is largest for the highest wind speeds. The dynamic response of the first tower mode is concentrated at 0.47 Hz, and is largest for the low wind speed, U_∞ = 8 m/s. This is due to the blade passing frequency at 3P, which in this case is close to the first tower bending mode, and the response is amplified. At above rated, the blade passing frequency is higher than the eigenfrequency, and the response at the first tower bending mode is mainly due to the wave loading.

In the following discussion, the focus will be on the response of the first elastic tower bending mode, which is narrow banded. For simplicity, no other modal responses of the wind turbine structure are considered

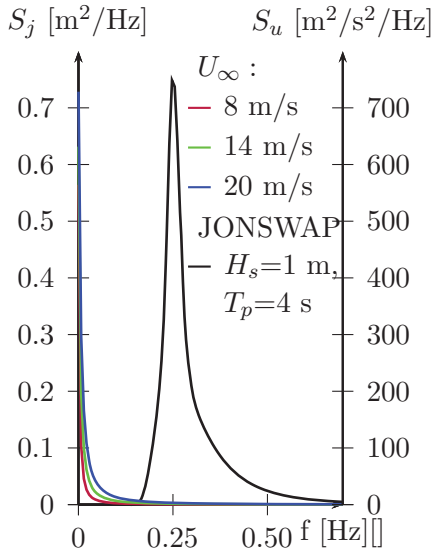

Figure 6.40: A JONSWAP wave spectra S_j (H_s=1 m, T_p=4 s) and the Kaimal wind spectra, S_u for three wind speeds.

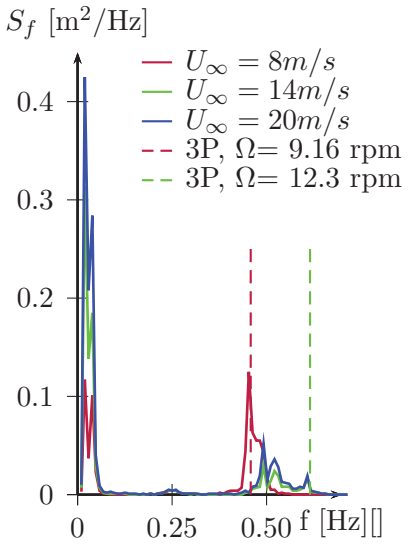

Figure 6.41: The tower top response spectra for Hywind OC3 with three different wind speeds.

in the following fatigue damage calculation. The excitation force is assumed broad banded. The fatigue damage discussed here is therefore not applicable to the total damage of a realistic offshore wind turbine, but it illustrates the effect that the unsteady aerodynamics has on the fatigue damage due to the resonant part of the first tower bending mode. The model assumed here is a single-degree-of-freedom (SDOF) system with a mass M_{sdof}, a damping coefficient, C_{sdof}, and a stiffness K_{sdof}. The system properties consists of the structural, hydrodynamic and aerodynamic properties.

Let $x(t)$ be the input variable, which has a Gaussian white spectra with intensity S_0. The response, $y(t)$, will have a spectra $S_y(\omega)$:

$$S_y = |H(\omega)|^2 S_0 \tag{6.42}$$

where $H(\omega)$ is the complex frequency response function:

$$H(\omega) = \frac{1}{-M_{sdof}\omega^2 + iC_{sdof}\omega + K_{sdof}} \tag{6.43}$$

The squared complex response function is shown in Figure 6.42. Here, the motion-induced aerodynamic loads, with a wind speed of 8 m/s and estimated using Theodorsen's theory is shown. The frequency investigated is that of the first tower bending mode.

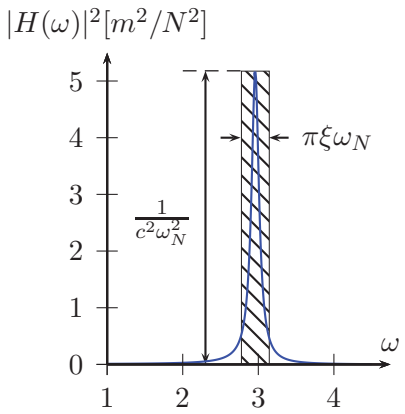

Figure 6.42: The squared complex response function, $|H(\omega)|^2$

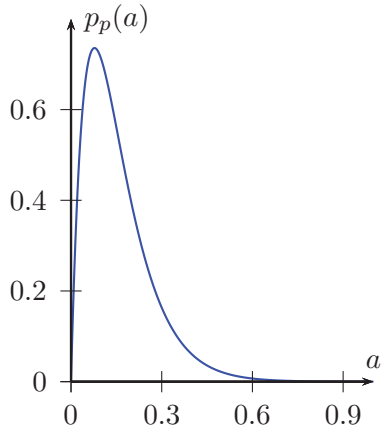

Figure 6.43: The probability that any peak of y(t), chosen at random, lays in the range a to $a + da$.

The area of the squared response function, $|H(\omega)|^2$, can be approximated by the squared box shown in Figure 6.42. The width of the box is $\pi\xi\omega_N$ and is often referred to as mean square bandwidth. The height of the box is $1/C_{sdof}^2\omega_N^2$. An increased damping ratio will therefore give a wider bandwidth and a reduced peak of the response function. This simplification is useful when estimating the standard deviation of the response which is defined as [71]:

$$\begin{aligned} \sigma_y^2 &= 2 \cdot S_0 \int_{-\infty}^{+\infty} |H(\omega)|^2 \, d\omega \\ &\approx S_0 \cdot \pi / \left(K_{sdof} C_{sdof}\right) \end{aligned} \tag{6.44}$$

The variance of the response is inversely proportional to the damping and stiffness of the model. Since the variance in the response is reduced with increasing damping and stiffness, it follows that the fatigue damage will be reduced. The fatigue damage is a result of a weakening of the material due to repeatedly applied loads.

To quantify the effect, it is necessary to estimate the distribution of peaks of the response. The distribution of peaks in the response spectra can be described as Rayleigh distribution for a narrow banded single response with a Gaussian white noise excitation [71]:

$$p_p(a) = \frac{a}{\sigma_y^2} e^{-a^2/2\sigma_y^2}, \qquad 0 \leq a \leq \infty \tag{6.45}$$

where $p_p(a)da$ is the probability that any peak of $y(t)$ lays in the range a to $a + da$, and σ_y^2 is the variance of the response, $y(t)$. The response here is the displacement of the tower top. The probability distribution of the peaks of a narrow banded process, in this case the tower bending, is shown in Figure 6.43 using the wind-structure interaction properties estimated based on Theodorsen's theory.

The distribution of the response can thus be found, and in order to calculate the fatigue damage, one also needs information about the material behaviour. A Wöhler curve, or S-N curve, is used to describe the fatigue properties of a material in high-cycle fatigue situations, such as an offshore wind turbine. The Wöhler curve gives the number of cycles that a material can sustain at different stress ranges [72]:

$$\log N_i = \log \bar{a} - m \log \Delta\sigma_i \tag{6.46}$$

where n_i is the number of stress cycles with stress range $\Delta\sigma_i$ and N_i is the allowable number of cycles at this level of stress range. For offshore steel structures, the DNV-RP-C203 Fatigue Design of Offshore Steel Structures [72], gives guidance on which Wöhler curve to use.

The fatigue damage in a stochastic, narrow banded loading is estimated using Palmgren-Miner summation:

$$D = \sum_{i=1}^{j} \frac{n_i}{N_i} \tag{6.47}$$

The failure is expected when the accumulated damage, D is 1.

The average damage resulting from the load spectra, using the probability function $p_p(a)$ in Eq 6.45, can now be estimated as:

$$D = \left(v_o^+ T\right) \int_0^\infty \frac{1}{N(\Delta\sigma)} p_p(\Delta\sigma/2) d\Delta\sigma \tag{6.48}$$

where $N(\Delta\sigma)$ is the number of stress cycles until failure at the given stress range $\Delta\sigma$, $p_p(\Delta\sigma/2)$ is the probability distribution of peaks (see

Eq 6.45) and v_o^+ is the frequency of zero crossings with positive slope. For a Gaussian white noise excitation, this is given by:

$$v_o^+ = \frac{\omega_N}{2\pi} \tag{6.49}$$

The damage associated with aerodynamic loads estimated by the different methods are shown in Table 6.19 for the first elastic tower bending, using m=3. The numbers are relative to the fatigue damage estimated using the results from Theodorsen's theory and are illustrated in Figure 6.44.

Table 6.19: The fatigue damage relative to fatigue damage estimated using Theodorsen's theory.

Method	$U_\infty = 8$ m/s	$U_\infty = 14$ m/s	$U_\infty = 20$ m/s
Garrad	0.70	0.76	0.77
BEM U	1.05	0.98	0.99
BEM inflow	1.14	1.22	1.18
GDW inflow	1.34	1.05	1.01
Theodorsen	1.00	1.00	1.00
Loewy	1.23	1.02	1.02
Vortex - single	0.87	0.89	0.94
Vortex - cascade	1.15	0.86	0.90

The fatigue damage is sensitive to the slope of the Wöhler curve, which is represented by m in Equation 6.46. Here, we have used m=3 and in Appendix E we have applied m=5. It is found that an increased value of m will increase the relative difference in fatigue damage.

Garrad's method, which contains no unsteady aerodynamics, overestimates the aerodynamic damping of the first elastic tower bending. Consequently, the fatigue damage is underestimated at all the three wind speeds. The predicted fatigue is around 30% less compared to the fatigue damage predicted using the Theodorsen's theory. This is for the dynamic response of the first tower bending mode.

The other methods align reasonably well at wind speeds above rated wind speeds. The largest spread in fatigue damage is for the low wind

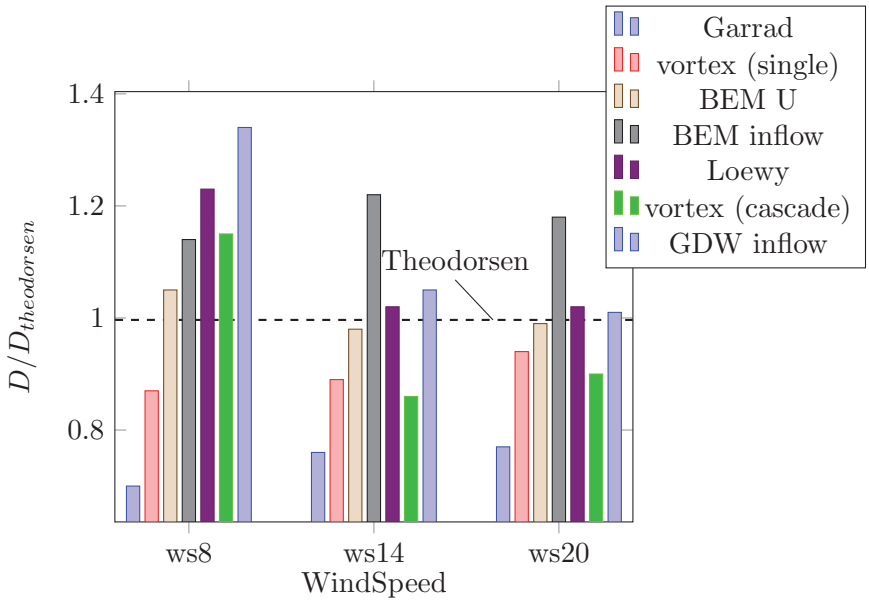

Figure 6.44: The fatigue damage listed in Table 6.19. All values are relative to the fatigue damage estimated using Theodorsen's theory.

speed, where the blade passing frequency is close to the eigenfrequency of the first tower bending mode. The models which include the returning wake, i.e. Loewy's theory and cascade vortex, all predict a fatigue damage relative to Theodorsen's theory. The three methods predict a 15-34 % increase in fatigue damage relative to the fatigue damage predicted by Theodorsen's theory.

The erroneous results of the GDW method is also included in the calculation of the fatigue damage in Figure 6.44. The fatigue damage estimated with the modal characteristics of the GDW model is the highest of all simulation models for the low wind speed.

Van der Tempel [73] studied the aerodynamic damping ratio using Garrads method and comparing it to aerodynamic damping estimated based on a simulation using aero-hydro-servo-elastic analysis tool. The results are shown in Figure 6.45. All the wind turbines were bottom-fixed wind turbines and it is the first elastic bending mode of the substructure which is shown. Similar to the results presented in Figure 6.33, Garrad's theory overestimates the aerodynamic damping, compared to unsteady aerodynamic simulation. In Figure 6.45 unsteady aerodynamics is in-

cluded in the non-linear simulation. However, the aerodynamic damping in van der Tempel's results have a significant dip at above rated. This may be related to the control system of the wind turbine.

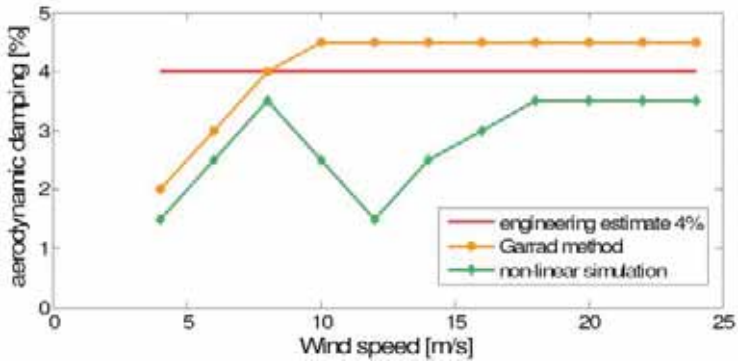

Figure 6.45: Aerodynamic Damping of a NEG-Micon 92 NM92 turbine estimated by van der Tempel [73]. A fixed engineering estimate, results based on Garrad's theory and the aerodynamic damping from non-linear simulations are shown.

Van der Tempel [73] compared a frequency domain approach to a time-domain approach and compared the fatigue damage using different aerodynamic damping estimates as shown in Figure 6.46. The advantage of a frequency domain simulation is that it has lower computational time compared to a time domain simulation, however it is not easy to include non-linearities in the frequency domain simulation. The biggest differences in the damage calculated are not due to the unsteady aerodynamics, but are related to the control system operating the wind turbine.

6.11 Summary and Conclusions

The aim of the wind-structure investigation was to study the effect of the unsteady aerodynamics and the effect of thick airfoils. It is seen that the effect of thick airfoils seems to be negligible. However, the importance of including the returning wake, i.e. the wake due to neighbouring airfoils and the wake returning due to rotation of the rotor, is large, especially if the wind turbine operate with a blade passing frequency that can be a multiple of the eigenfrequency. The unsteady aerodynamics of returning wakes has been modeled using the Loewy's theory and a linear cascade

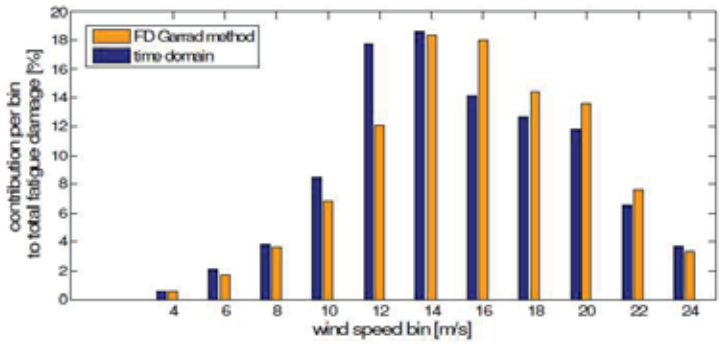

Figure 6.46: Fatigue damage estimated using Garrad's theory compared to fatigue damage of a time-domain simulation [73].

of airfoils modeled with the panel method.

These methods all predicted a reduced aerodynamic damping when the oscillation period was equal to the time it takes for an airfoil to travel the spacing distance between the airfoils, compared to the methods not including the effect of neighbouring wakes. Comparing the aerodynamic damping estimated using Theodorsen's theory and Loewy's theory, the difference is 13 % for the high frequency oscillation and the wind speed, U_∞, is 8 m/s. In this simulation the oscillation period is close to the time to travel one airfoil spacing. For the other simulations, the difference between the aerodynamic damping estimated using Theodorsen's theory and Loewy's theory is less than 2 %. Both Theodorsen's theory and Loewy's theory are frequency domain theories, using thin airfoil assumption. The only difference between the two methods is that Loewy's theory includes the effect of returning wake.

Similarly, the single airfoil and cascade method using the panel vortex code, also have the largest difference in aerodynamic damping for the low wind speed ($U_\infty = 8$ m/s) and high frequency oscillation (ω=2.95 rad/s). The difference between the aerodynamic damping estimated using the two panel vortex methods is 17 %, while for the other wind speeds it is 2% or less. Since the panel vortex code includes a free wake and thickness of the airfoil, the aerodynamic damping estimated will differ from the results using Theodorsen's and Loewy's theory.

Both the frequency domain methods and the panel vortex methods are not commonly used by engineers when doing structural analysis. The most commonly used method is the BEM method. However, retrieving

the local unsteady aerodynamic loads from a wind turbine simulation program is not an easy task, since they also include dynamic inflow and other corrections to the aerodynamic model. Two different aerodynamic methods have been compared, the BEM method and the GDW method, in the wind turbine simulation tool FAST. The BEM method, which is often used by engineers for fatigue load analysis, often uses an unsteady aerodynamic model where the wake from neighbouring airfoils and the returning wake due to rotation are not included.

The motion-induced aerodynamic loads estimated using the panel vortex code in a linear cascade configuration, is the method that probably is giving the most accurate two dimensional loads in this comparison. The panel vortex code includes both the thickness and the curvature of the airfoil, as well as the wake, and in a cascade configuration the wake of neighbouring airfoils is included. However, this is also the most time-consuming simulation method, and the advantage over using the cascade configuration relative to a single airfoil, is only present for simulations where the oscillation period is close to the time it takes to travel an airfoil spacing.

Comparing the fatigue damage results based on the panel vortex code, the single airfoil simulation estimates 24 % lower fatigue damage compared to the linear cascade simulation. Similarly, the aerodynamic loads using Theodorsen's theory estimates 19 % lower fatigue compared to Loewy's theory.

Using a wind turbine simulation tool, which estimates a too high aerodynamic damping, will result in a calculated fatigue damage which is too low. Since most engineers are using a BEM methods with an unsteady aerodynamic model, which does not include neighbouring wake, the estimated aerodynamic damping is too high for certain conditions. Comparing the difference in fatigue damage due to the dynamic response of the first bending mode of the tower, estimated using GDW and BEM model in FAST, the BEM model predicts 15 % lower fatigue damage compared to the GDW model. This result is based on the low wind speed, $U_\infty = 8$ m/s. The difference is most likely due to the low wind speed, in which the GDW model is not valid.

Another unsteady aerodynamic effect not discussed here is dynamic stall, which is not included in neither the frequency domain methods nor in the panel vortex code. This is included in the wind turbine simulation tool, AeroDyn. None of the methods have included the dynamics of the control system. A static pitch and rotational speed is chosen in all analy-

sis. Further work is recommended to include the control system into the models as this would greatly improve the quality of the estimated aerodynamic damping. The control system could be implemented in AeroDyn and the vortex panel code, both for the single airfoil and the cascade method.

Chapter 7

Conclusion and Further Work

There is pressure on the wind turbine industry to improve cost effectiveness of offshore wind turbines. One method to reduce the cost is to optimize the wind turbine structure, but this requires an accurate analysis tool which is computationally efficient. An offshore wind turbine is subjected various types of time-varying loads, e.g. aerodynamics, hydrodynamics, soil-mechanisms, gravitation, which the analysis program needs to consider. The scope of the present study is limited to the analysis of the aerodynamic loads, with focus on the motion-induced aerodynamic loads.

7.1 Summary

A vortex panel code was developed and validated as a part of this study. Even though there exist many validated vortex codes, a new code needed to be developed, in order to reduce the computational time by implementing it on a GPU. The aim of this thesis was to investigate the unsteady aerodynamics and the wind structure interaction of an offshore wind turbine. Using the vortex code, a set of numerical tools was developed and used to study the motion dependent aerodynamic loads of a floating wind turbine. The result showed that the traditional approach using BEM has its limitations if the unsteady aerodynamics is based upon a single wake approximation, i.e. that the wake from the neighbouring airfoils, and the wake returning after a rotation, are not considered. In this summary an

overview of the developed panel vortex code is given, followed with some details on the cascade method used in the panel vortex code and a short summary of the characteristics of the wind-structure interaction.

7.1.1 Vortex code

A detailed presentation of a two-dimensional vortex panel code is given in this thesis. The code is based on constant source and doublet elements located on linear elements. The unsteady version of the code has a free vortex wake and has been implemented both on a CPU and a GPU. It has been demonstrated how a parallelized version can reduce the computational time. The reason for the speed-up is that the time consuming part of the calculation which consists of estimating the velocities at all the points, can be parallelized. Since the strength of all the vortex elements is known a-priori to the velocity calculations, the velocities at each point can be computed simultaneously, independent of the other velocities in the analysis domain.

A GPU has thousands of threads, and the more threads used, the more the computational time is reduced. For a low number of vortex elements, computation may be faster on a CPU. It was shown in Section 4.5 that for a single vortex element, shedding one wake particle for each time-step, the GPU is faster only after around 2000 time-steps. Similar results was found for using a panel vortex code [58].

Both the CPU and the GPU code presented here is not fully optimized and can be further developed for speed-ups. Applying a tree-code algorithm to the vortex panel code and including a far-wake model will lower the computational time even more. It should also be noted that the time for the transfer of data back and forth to the GPU can be reduced.

The panel vortex code itself is based on a potential flow theory. This is the same theory as Wagner, Küssner and several other analytical functions for unsteady aerodynamic loads are based upon. The advantage of the panel vortex code is however that it can consider any general motions, e.g. pitch and plunge, while Wagner and Küssner are limited to a specific motion. Two further limitations of the vortex panel code is that it is not three dimensional, and does not include stall.

7.1.2 Cascade effects

The developed panel vortex code is two dimensional, and will therefore not include any flow along the span of the wind turbine blade, or induced

velocities due to the tip and hub vortices. However, one can include the effect of the wakes from the other blades on the wind turbine and the returning wakes due to rotation of the rotor using a linear cascade of airfoils. It is found that if the oscillating frequency has an integer relation to the blade passing frequency, it is important to consider the wake from neighbouring airfoils and the returning wake after each rotation of the rotor. A linear cascade simulation, with several airfoils, is much more time-consuming than a simulation with a single airfoil, and it is therefore not recommended to use this approach. However, it is an effect that should be taken into consideration.

The Loewy's function includes the effect of the neighbouring wake in frequency domain. Another method is the GDW approach for modelling the aerodynamic loads. These two methods will use much less computational time than the panel vortex code. The GDW method is already implemented in some wind turbine simulation codes, e.g. FAST.

7.1.3 Aerodynamic damping

The panel vortex code is valuable because it is a more direct method of modelling the unsteady aerodynamics compared to other methods such as the BEM method where unsteadiness is included from semi-emprical functions, e.g. Beddoes-Leishman function. To illustrate the importance, the oscillating aerodynamic forces have been studied on a floating wind turbine structure. The aerodynamic damping associated with the fore-aft motion, both for the platform pitch mode and the first elastic tower bending mode, is an important part of the dynamics for this structure.

There was no significant difference found when comparing the results using different numerical tools to estimate the aerodynamic damping for the platform pitch mode. The aerodynamic damping ratio of the platform pitch mode is 8-9 % for situations above rated wind speeds. For the first tower bending mode the results are very similar for wind speeds above rated, with an aerodynamic damping ratio around 3 %. At wind speed of 8 m/s, where the blade passing frequency is the same as the eigenfrequency of the tower, the aerodynamic damping drops when the neighbouring wake is considered. In the wind-structure interaction study presented in Chapter 6, the aerodynamic damping ratio is reduced by 17 %, comparing the results based on a single airfoil analysis to the results based on a linear cascade analysis with multiple wakes using the panel vortex code.

The largest limitation of this study was that the control system was neglected. This plays an important role, especially for the simulations where the wind speed is at rated or above, and the frequency of the oscillation is low, such as for the platform pitch motion. If the oscillations have a high frequency (e.g. the eigenfrequency of the first bending mode of the tower), the control system may not respond to the change in aerodynamic load, and the control system will not have a large influence on the motion induced aerodynamic load.

7.2 Conclusion

In this study a vortex panel code is developed, and is verified using XFoil and the analytical unsteady aerodynamic solutions. The panel vortex code is useful for analysis of dynamic loads, and has been implemented in a wind-structure analysis of a floating offshore wind turbine. The main advantage of the vortex panel code is that the airfoil wake, both vorticity strength and position, is included in the estimation of the unsteady aerodynamic loads.

However, the panel vortex code has a relatively long computational time, but the code can be speeded up. Implementing the code on a GPU, reduces the computational time, relative to a CPU implemented version, if there is a large number of vortex particles in the simulation.

Comparisons of the panel vortex code with analytical solutions of the unsteady aerodynamics, such as the Wagner function, show that the unsteady aerodynamics of a single airfoil is accurately modeled. Using a linear cascade of multiple airfoils will include the effect of neighbouring airfoils and their wakes, as well as the effect of the returning wake, due to rotation of the wind turbine blades around the rotor axis. The unsteady aerodynamic analysis using a linear cascade has been compared to results using Loewy's theory, which is an analytical solution that includes returning wake effects. Similarly to results using Loewy's theory, the unsteady aerodynamic force was sensitive to situations where the oscillation period of the airfoil was close to the time for an airfoil traveling the distance between neighbouring airfoils.

In the wind-structure analysis a low frequency and a high frequency oscillating motion were investigated. The frequencies were chosen to correspond with the eigenfrequencies of a platform pitch mode (low frequency) and the first elastic bending mode (high frequency) of a 5 MW floating wind turbine. Several methods of estimating the unsteady aero-

dynamics were used, and for the low-oscillating frequency they all gave similar results. The motion induced loads due to the high-frequency oscillation have a larger variation and the largest variation occurred when the blade passing frequency was equal to the high-frequency oscillation of the blades. For this specific situation, Loewy's theory and the linear cascade with panel vortex code, all predicted a lower aerodynamic damping of the first elastic tower mode. These methods both include wakes from neighbouring airfoils and the returning wakes after a rotation of the rotor. The remaining methods; Theodorsen's theory, single airfoil with panel vortex code and the unsteady BEM model in AeroDyn, all predicted a too high aerodynamic damping. As a consequence, the methods with a single airfoil approximation, will underestimate the fatigue damage in this specific situation.

A recommendation based on the study is to consider the unsteady aerodynamics for attached flow included in a BEM model with care. This is often based on an unsteady aerodynamic model with a single wake. If the wind turbine blades have an oscillating frequency close to the blade passing frequency, it should be investigated whether the motion-induced aerodynamic forces are correct. This can be done using the tools such as a vortex code or CFD.

7.3 Further Work

Much work has been put into verification of the two dimensional vortex panel code. The limited time available for a PhD has also limited the work that has been performed using the code. It is a very versatile code that can be used in many applications.

7.3.1 Aerodynamics of a blade passing the tower

The change in flow around a wind turbine blade as it passes the tower has not been considered in this work and is expected to have a different unsteady behaviour compared to the results for the studied plunge motions in the present work. Including this in a cascade model, and comparing to the current model in BEM programs can give information whether or not this is modelled correctly in the present codes.

7.3.2 Flow control

To improve flow control, deformable blades are suggested. This means that the shape of the airfoil will change during the operation. Since the shape will change, the aerodynamic coefficients such as lift coefficient and drag coefficients will change as well. The vortex code is a very interesting option to study these kinds of situations since the method is fast relative to CFD. Using a panel code the surface of the airfoil is included as a part of the solution, and this gives a very flexible option for the deformable blades.

7.3.3 Three dimensional vortex panel code

The developed vortex panel code should be extended to a three dimensional vortex panel code with a free wake. This would decouple it from the BEM totally, which is currently used for the inflow conditions.

The panel vortex code developed has not been optimized to reduce the computational time of the simulation. One major issue is the large number of vortex particle in the wake. A variety of methods have been developed to reduce the computational time, and one common method is to use a tree algorithm. This is demonstrated by Willis et al for a 3D unsteady panel method with vortex particle wakes [55].

7.3.4 Aerodynamic damping

In this study it is shown how the aerodynamic damping, of the rotor fore-aft motion, can be estimated. However, the method is restricted to rigid translational motion. The platform pitch mode will have a rotational motion, and this may influence the estimated aerodynamic damping. With a three-dimensional vortex code, the aerodynamic damping of all modes, including elasticity, can be investigated.

Van der Tempel [73] also investigated the aerodynamic damping of offshore wind turbines, these were however bottom fixed wind turbines. He compared the simple quasi-steady aerodynamic damping model (see Eq 6.31) with results from a nonlinear time-domain simulation, which includes the control system in its calculations. The results show that the aerodynamic damping is overestimated around rated wind speed using the simple quasi-steady method, as illustrated in Figure 6.45. Since the large dip is at around rated wind speed of the controller, the reason for

the dip is likely the control system of the wind turbine. This should be investigated further.

References

[1] "Vindeby — SEAS-NVE." http://www.seas-nve.dk/AboutSeasNve/Wind/References/Offshore/Vindeby.aspx. Accessed: 29-06-2014.

[2] EWEA, "The european offshore wind industry - key trends and statistics 2013," tech. rep., European Wind Energy Association, Jan 2013.

[3] "London Array - harnessing the power of offshore wind." http://www.londonarray.com. Accessed: 29-06-2014.

[4] EWEA, "Deep Water - the next step for offshore wind energy," tech. rep., European Wind Energy Association.

[5] T. C. Estate, "Offshore wind cost reduction pathways study," tech. rep., The Crown Estate, 2012.

[6] "Offshore Wind Accelerator (OWA) - Carbon Trust." http://www.carbontrust.com/our-clients/o/offshore-wind-accelerator. Accessed: 29-03-2014.

[7] Statoil, "Hywind demo." http://www.statoil.com/no/technologyinnovation/newenergy/renewablepowerproduction/offshore/hywind/pages/hywindputtingwindpowertothetest.aspx, Oct. 2009. accessed 09.07.2014.

[8] J. G. Leishman, "Challenges in modeling the unsteady aerodynamics of wind turbines," *Wind Energy*, vol. 5, pp. 85–132, 2002. doi:10.1002/we.62.

[9] A. C. Hansen and C. P. Butterfield, "Aerodynamics of horizontal-axis wind turbines," *Annual Review of Fluid Mechanics*, vol. 25, pp. 115–149, 1993.

[10] D. Simms, S. Schreck, M. Hand, and L. J. Fingersh, "NREL unsteady aerodynamics experiment in the NASA-Ames wind tunnel: A comparison of predictions to measurements," Technical Report NREL/TP-500-29494, National Renewable Energy Laboratory, June 2001.

[11] J. G. Scherpers, K. Boorsma, T. Cho, S. Gomez-Iradi, P. Schaffarczyk, A. Jeromin, W. Z. Shen, T. Lutz, K. Meister, B. Stoevesandt, S. Schreck, D. Micallef, R. Pereira, T. Sant, H. A. Madsen, and N. Sørensen, "Final report of IEA task 29, Mexnext (phase1): Analysis of mexico wind tunnel measurement," Tech. Rep. ECN-E-12-004, February 2012.

[12] K. Boorsma, J. G. Schepers, S. Gomez-Iradi, H. A. Madsen, N. Sørensen, W. Z. Shen, C. Schulz, and S. Schreck, "Mexnext-II: the latest results on experimental wind turbine aerodynamics," in *EWEA 2014, Barcelona, Spain*.

[13] P.-Å. Krogstad and P. E. Eriksen, "Blind test calculations of the performance and wake developement for a model wind turbine," *Renewable Energy*, vol. 50, pp. 325–333, 2013.

[14] DNV, "Design of offshore wind turbines, DNV-OS-J101," tech. rep., september 2011.

[15] IEC, "Wind turbines: Part 1: Design requirements, IEC 61400-1," tech. rep., IEC, 2005-08.

[16] F. Vorpahl, M. Strobel, J. Jonkman, T. J. Larsen, and P. Passon, "Verification of aero-elastic offshore wind turbine design codes under IEA wind tast XXII," *Wind Energy*, vol. 17, 2014.

[17] J. G. Leishman, *Principles of Helicopter Aerodynamics*. Cambridge University Press, 2nd ed., 2006.

[18] "NTUA/FS. wind/GENUVP/detailed rotor aerodynamics using free wake modelling." `http://www.fluid.mech.ntua.gr/wind/G/genuvp.html`. Accessed: 24-10-2014.

[19] "AWSM - b-09-013." `https://www.ecn.nl/fileadmin/ecn/units/wind/docs/Aerodynamics/AWSM_B-09-013.pdf`. Accessed: 24-10-2014.

[20] "RotorFlow - b-09-004." https://www.ecn.nl/fileadmin/ecn/units/wind/docs/Aerodynamics/Rotorflow_B-09-004.pdf. Accessed: 24-10-2014.

[21] "XFOIL - subsonic airfoil development system." http://web.mit.edu/drela/Public/web/xfoil/. Accessed: 01-05-2014.

[22] "AVL - aerodynamic analysis, trim calculation, dynamic stability analysis and aircraft configuration development." http://web.mit.edu/drela/Public/web/avl/. Accessed: 24-10-2014.

[23] S. Øye, "Dynamic stall, simulated as a time lag of seperation," in *Proceedings of the 4th IEA Symposium on the Aerodynamics of Wind Turbines*, 1991.

[24] J. G. Leishman and T. S. Beddoes, "A semi-empirical model for dynamic stall," *Journal of the American Helicopter Society*, vol. 34, no. 3, pp. 3–17, 1989.

[25] M. O. L. Hansen, *Aerodynamics of Wind Turbines*. Earthscan, 2nd ed., 2008.

[26] T. Theodorsen, "General theory of aerodynamic instability and the machanism of flutter," *NACA Report No. 496*, 1935.

[27] H. Wagner, "Über die entstehung des dynamischen auftriebes von tragflügeln," *Zeitschrift für Angewandte Mathematik und MEchanick*, vol. 5, no. 1, 1925.

[28] H. G. Küssner, *DVL-Jahrbuch*, ch. Scwingungen von Flugseugflügeln, pp. 313–334. 1929.

[29] M. O. L. Hansen and N. S. H. A. M. J. N. Sørensen, S. Voutsinas, "State of the art in wind turbine aerodynamics and aeroelasticity," *Progress in Aerospace Sciences*, vol. 42, pp. 285–330, 2006.

[30] E. Hau, *Wind Turbines, Fundamentals, Technologies, Application, Economics*. Springer, 2nd ed., 2006.

[31] EWEA, "Wind directions article: EWEA at 30 - from humble beginnings to mainstream power player." http://www.ewea.org/press-releases/detail////wind-directions-article-ewea-at-30-from-humble-beginnings-to-mainstream-power-player/, Nov. 2007. accessed 19.03.2011.

[32] GL, "Guidelines for the certification of offshore wind turbines," tech. rep., 2005.

[33] L. Y. Pao and K. Johnson, "A tutorial on the dynamics and control of wind turbines and wind farms," in *American Control Conference, 2009. ACC '09.*, pp. 2076–2089, 2009.

[34] J. Jonkman and W. Musial, "IEA wind task 23 offshore wind technology and deployment," final technical report, National Renewable Energy Laboratory, 2010.

[35] J. V. der Temple, *Offshore Wind Power*, ch. 8, pp. 151–188. Multi-Science Publishing, 2009.

[36] J. Jonkman, S. Butterfield, W. Musial, and G. Scott, "Definition of a 5-MW reference wind turbine for offshore system developement," Final Technical Report NREL/TP-50038060, National Renewable Energy Laboratory, 2009.

[37] P. J. Carpenter and B. Fridovich, "Effect of a rapid-pitch increase on the thrust and induced-velocity response of a full-scale helicopter rotor," tech. rep., NASA, 1953.

[38] W. Kinner, "Die kreisförmige tragfläche auf potentialtheoretischer grundlage," *Ingenieur-Archiv*, vol. 8, no. 1, pp. 47–80, 1937.

[39] D. M. Pitt and D. A. Peters, "Theoretical prediction of dynamic-inflow derivatives," *Vertica*, vol. 5, no. 1, 1981.

[40] D. A. Peters, D. D. Boyd, and C. J. He, "Finite state induced flow model for rotors in hover and forward flight," *Journal of American Helicopter Society*, vol. 34, no. 4, pp. 5–17, 1989.

[41] G. Goanker and D. A. Peters, "Review of dynamic inflow modelling for rotorcraft flight dynamics," *Vertica*, vol. 2, no. 3, pp. 213–242, 1988.

[42] P. J. Moriarty and A. C. Hansen, *AeroDyn Theory Manual*. NREL, December 2004. NREL/EL-500-36881.

[43] M. H. Hansen, M. Gaunaa, and H. A. Madsen, "A Beddoes-Leishman type dynamic stall model in state-space and indicial formulations," Tech. Rep. Risø-R-1354(EN), Risø National Laboratory, 2004.

[44] R. T. Jones, "The unsteady lift of a wing of finite aspect ratio," Technical Report 681, NASA, 1940.

[45] L. Eliassen, J. B. Jakobsen, and F. G. Nielsen, "Wind-structure interaction for a floating wind turbine," in *6th European-African Conference on Wind Engineering*, 2013.

[46] N. E. Joukowsky, "Vortex theory of screw propellers, I," *Trudy Otdeleniya Fizicheskikh Nauk Obshchestva Lubitelei Estestvoznaniy (in Russian)*, vol. 16, no. 1, 1912.

[47] N. E. Joukowsky, "Vortex theory of screw propellers, II," *Trudy Otdeleniya Fizicheskikh Nauk Obshchestva Lubitelei Estestvoznaniy (in Russian)*, vol. 17, no. 1, 1914.

[48] N. E. Joukowsky, "Vortex theory of screw propellers, III," *Trudy Otdeleniya Fizicheskikh Nauk Obshchestva Lubitelei Estestvoznaniy (in Russian)*, vol. 17, no. 2, 1915.

[49] N. E. Joukowsky, "Vortex theory of screw propellers, I-IV," *Trudy Avia Raschetno-Ispytatelnogo Byuro (in Russian).*, 1918.

[50] G.-H. Cottet and P. D. Koumoutsakos, *Vortex Methods, Theory and Practice*. Cambridge University Press, 2000.

[51] H. Helmholtz, "Über integrale der hydrodynamichen gleichungen, welche den wirvelbewegungen entsprechen," *Journal für die reine und angewandte Mathematik*, vol. 55, 1858.

[52] J. Katz and A. Plotkin, *Low-Speed Aerodynamics*. Cambridge University Press, 2000.

[53] H. Glauert, "M. a. fellow of trinity college cambridge. die grundlagen der tragflügel-und luftschraubentheorie. uebersetzt von dipl.-ing. h. holl. mit 115 textabbildungen. verlag springer, berlin 1929. 202 s. preis 12,75 m, geb. 13,75 m .," *ZAMM - Journal of Applied Mathematics and Mechanics / Zeitschrift für Angewandte Mathematik und Mechanik*, vol. 9, no. 4, pp. 346–346, 1929.

[54] R. L. Bisplinghoff, H. Ashley, and R. L. Halfman, *Aeroealsticity*. Mineola, New York: Dover Publications Inc, 1996.

[55] D. J. Willis, J. Peraire, and J. K. White, "A combined pFFT-multipole tree code, unsteady panel method with vortex particle wakes," in *43rd AIAA Aerospace Sciences Meeting and Exhibit*, January 2005. Reno. N.V.

[56] S. Pfalzner and P. Gibbon, *Many-body tree methods in physics*. Cambridge University Press, 1996.

[57] NVIDIA, *CUDA C Programming Guide*, pg-02829-001 v06 ed., February 2014.

[58] L. Eliassen and M. Muskulus, "A study of the NACA 0012 blade using a parallel vortex method," in *7th PhD Seminar on Wind Energy in Europe*, 2011.

[59] R. Lewis, *Vortex Element Methods for Fluid Dynamic Analysis of Engineering Systems*. Cambridge Engine Technology Series, Cambridge University Press, 2005.

[60] W. Traupel, "Calculation of potential flow through blade grids," *Sulzer Review*, no. No 1, 1945.

[61] R. G. Loewy, "A two-dimensional approximation to the unsteady aerodynamics of rotary wings," *Journal of the American Helicopter Society*, vol. 24, no. 2, pp. 81–92, 1957.

[62] H. Daughaday, F. DuWaldt, and C. Gates, "Investigation of helicopter blade flutter and load amplification problems," *Journal of the American Halicopter Society*, vol. 2, pp. 27–45, July 1957.

[63] N. Ham, E. Brunelle, and H. Ashley, *Investigation of Rotor Response to Vibratory Aerodynamic Inputs*. Technical report (Massachusetts Institute of Technology. Aeroelastic and Structures Research Laboratory), Wright Air Development Center, Air Research and Development Command, United States Air Force, 1958.

[64] W. Anderson and G. A. Watts, "Rotor blade wake flutter - a comparison of theory and experiment," *Journal of the American Helicopter Society*, vol. 21, pp. 32–43, April 1976.

[65] M. Silveira, G. Brooks, and L. R. Center, *Dynamic-model Investigation of the Damping of Flapwise Bending Modes of Two-blade Rotors*

in Hovering and a Comparison with Quasi-static and Unsteady Aerodynamic Theories. NASA technical note, National Aeronautics and Space Administration, 1959.

[66] J. Jonkman, "Definition of the floating system for phase IV of OC3," Tech. Rep. NREL/TP-500-47535, National Renewable Energy Laboratory, May 2010.

[67] A. Myhr, K. J. Maus, and T. A. Nygaard, "Experimental and computational comparisons of the oc3-hywind and tension-leg-buoy (tlb) floating wind turbine cenceptual ideas," *Proceedings of the Twenty-first International Offshore and Polar Engineering Conference*, 2011.

[68] "NWTC design codes (Modes)." `http://wind.nrel.gov/designcodes/preprocessors/modes/`. Accessed: 07-07-2014.

[69] A. Garrad, "Forces and dynamics of horizontal axes wind turbines," in *Wind Energy Conversion Systems* (L. Freris, ed.), Prentice-Hall, 1990.

[70] J. M. Jonkman and M. L. Buhl, *FAST User's Guide*. National Renewable Enery Laboratory, NREL.

[71] D. E. Newland, *An introduction to random vibrations, spectral & wavelet analysis*. Longman, 3rd ed., 1993.

[72] DNV, "Fatigue design of offshore steel structures," tech. rep., April 2010. DNV-RP-C203.

[73] J. V. D. Tempel, *Design of Support Tructures for Offshore Wind Turbines*. Phd thesis, Technische Universiteit Delft, 2006.

Appendices

Appendix A

Airfoil Sections

This appendix illustrates the different airfoil sections of the NREL 5 MW reference wind as they are modeled in the thesis and Figure A.1 shows a comparison of all the airfoil sections. Figure A.2 illustrates the discretization of the DU 21 airfoil into panel elements. Similarly, Figure A.3, Figure A.4, Figure A.5 and Figure A.6 shows the panel elements of the DU 25, DU 30, DU 35 ans DU 40. The last airfoil, NACA 64, is shown in Figure 5.4 in Chapter 5.

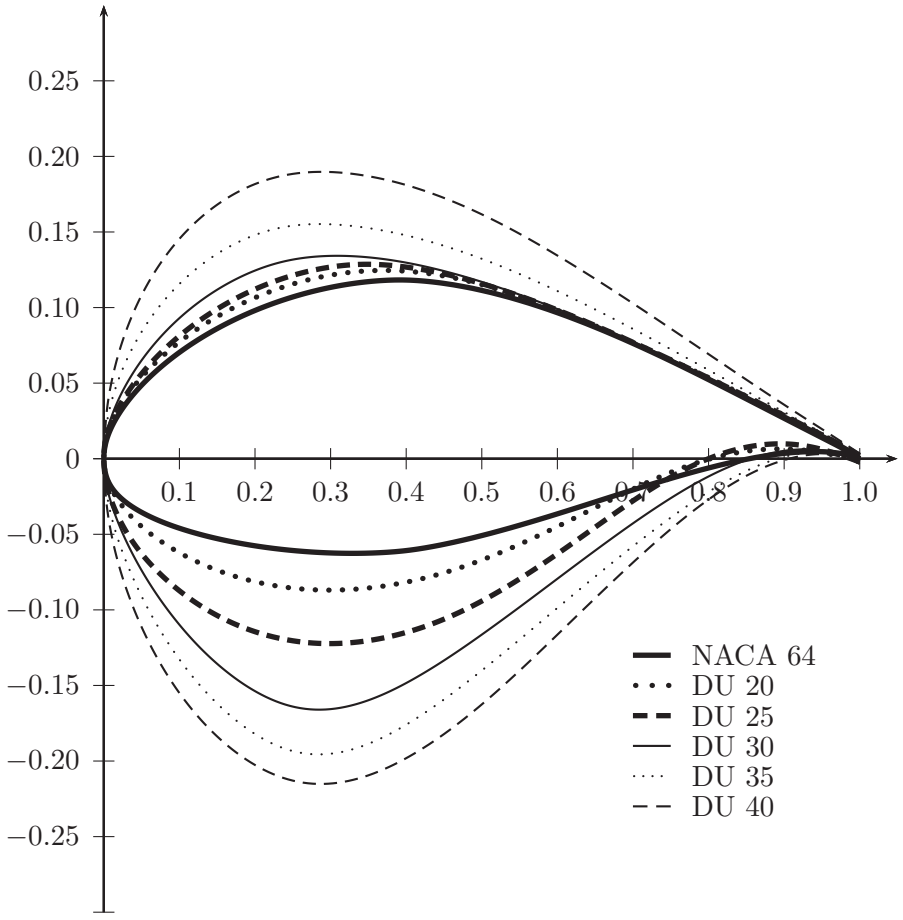

Figure A.1: The airfoil sections used for the 5 MW reference wind turbine

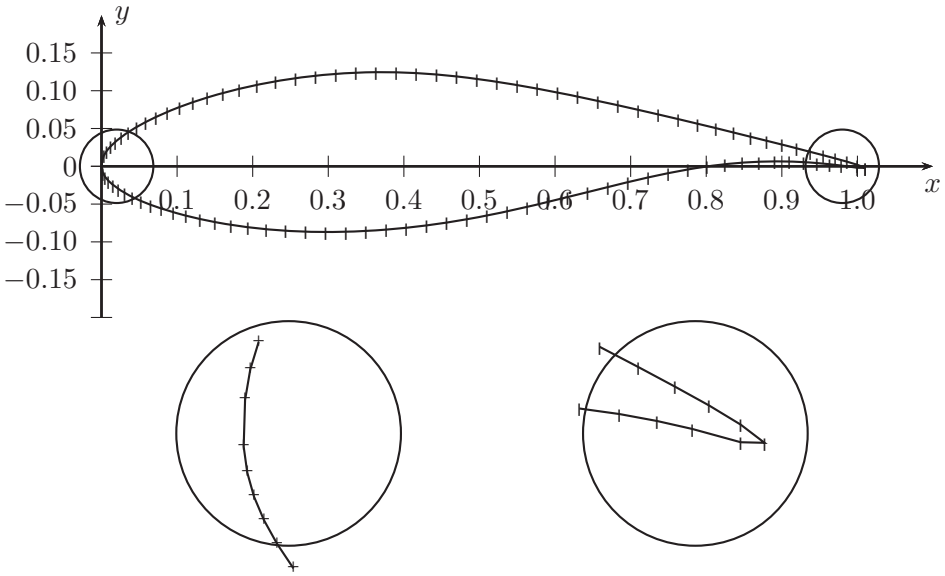

Figure A.2: The DU 21 airfoil divided into 101 panel elements. The circled areas around the leading and trailing edge are enlarged three times.

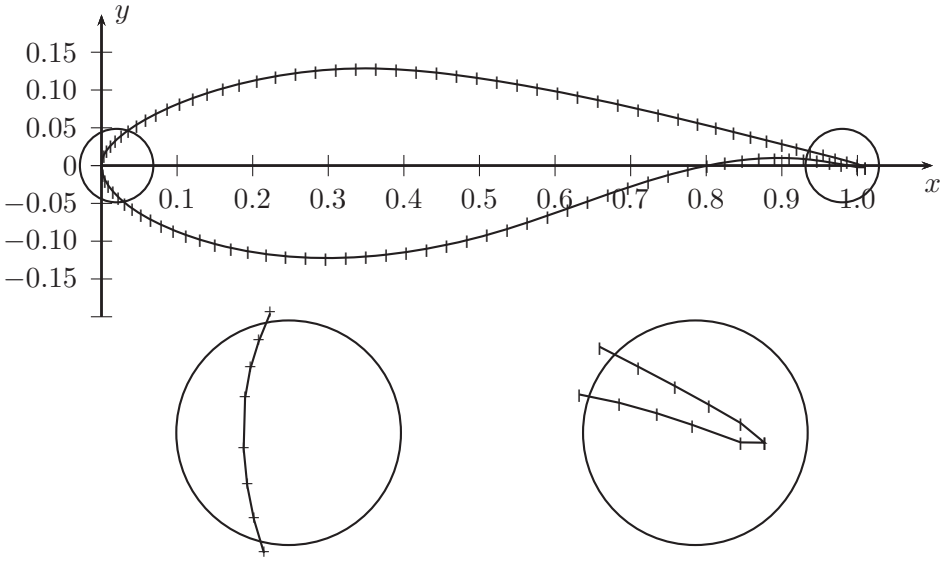

Figure A.3: The DU 25 airfoil divided into 101 panel elements. The circled areas around the leading and trailing edge are enlarged three times.

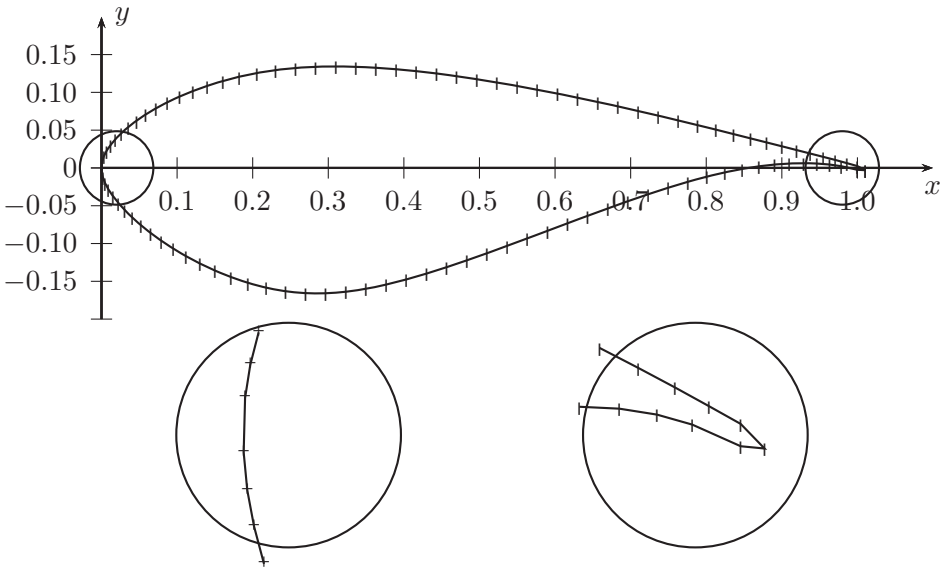

Figure A.4: The DU 30 airfoil divided into 101 panel elements. The circled areas around the leading and trailing edge are enlarged three times.

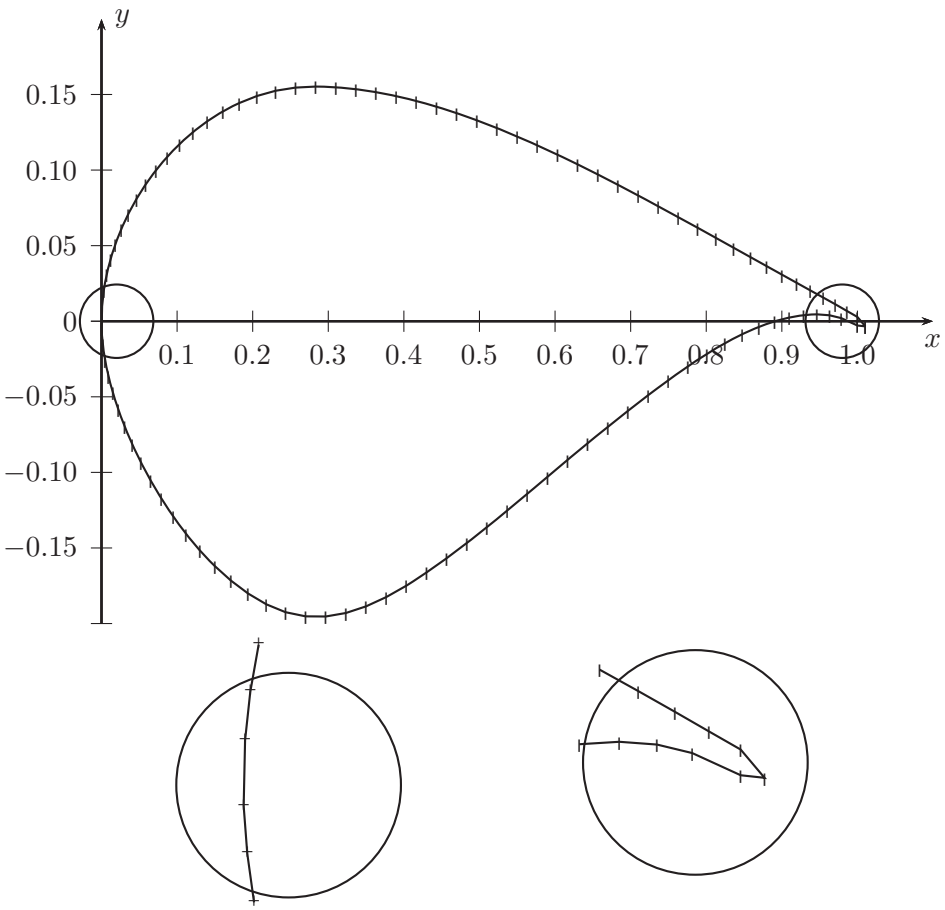

Figure A.5: The DU 35 airfoil divided into 101 panel elements. The circled areas around the leading and trailing edge are enlarged three times.

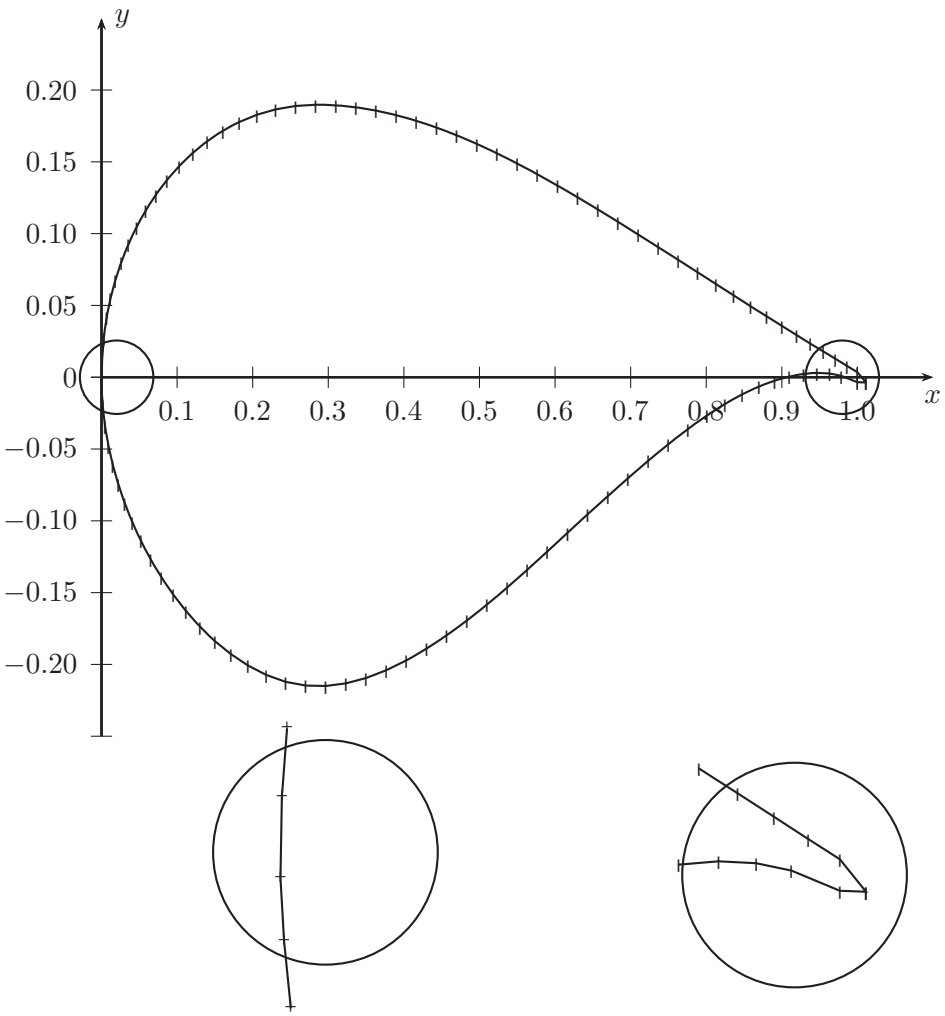

Figure A.6: The DU 40 airfoil divided into 101 panel elements. The circled areas around the leading and trailing edge are enlarged three times.

Appendix B

Lift Coefficients

The lift coefficient for the different airfoils as provided in the reference document [36] for the NREL 5 MW reference wind turbine are illustrated in the appendix.

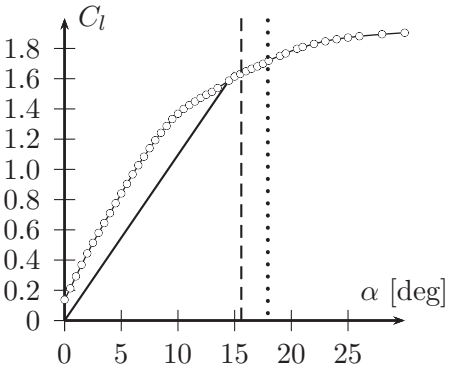

Figure B.1: Aerodynamic lift coefficient for DU40, used at airfoil section no 4.

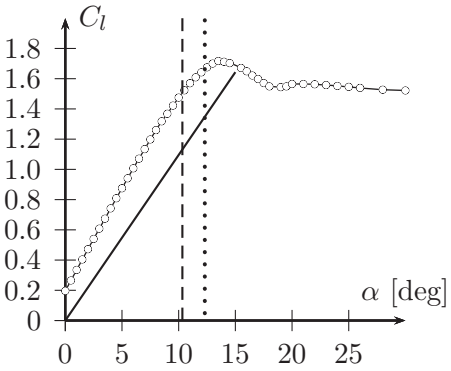

Figure B.2: Aerodynamic lift coefficient for DU35, used at airfoil sections no 5 and 6.

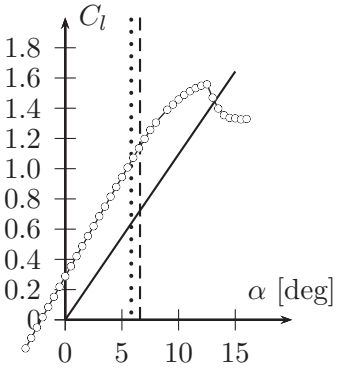

Figure B.3: Aerodynamic lift coefficient for DU30, used at airfoil section no 7.

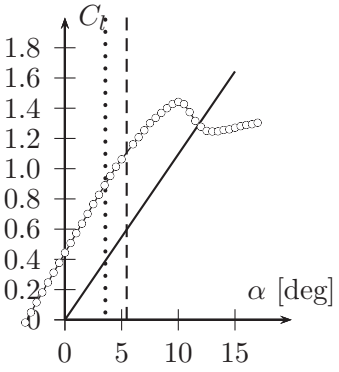

Figure B.4: Aerodynamic lift coefficient for DU25, used at airfoil sections no 8 and 9.

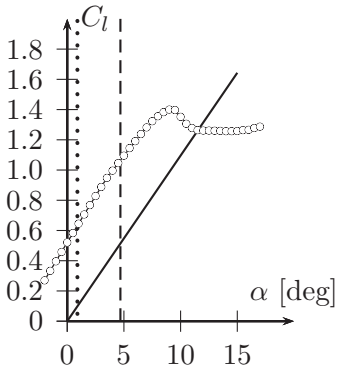

Figure B.5: Aerodynamic lift coefficient for DU21, used at airfoil section no 10.

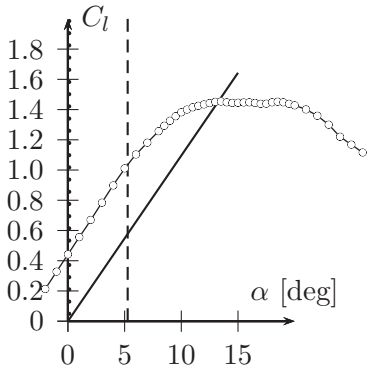

Figure B.6: Aerodynamic lift coefficient for DU25, used at airfoil sections no 11 to 17.

Appendix C

Wind-Structure Interaction

This appendix contains some of the results not presented in Chapter 6. This was done to reduce the amount of results presented. In this way it is hopefully more clear to the which results are important.

C.1 Loewy's theory

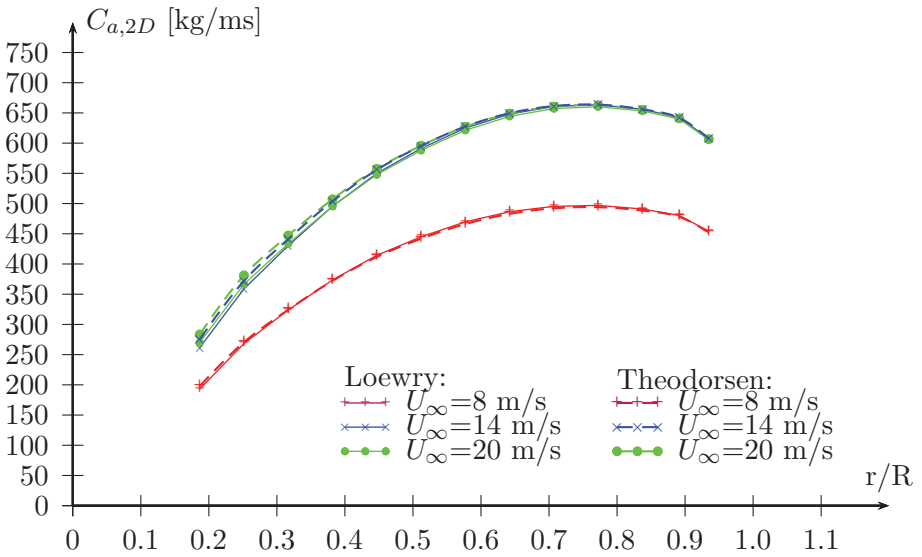

Figure C.1: Aerodynamic damping along the blade estimated Loewry function and compared to Theodorsen function for the platform pitch motion.

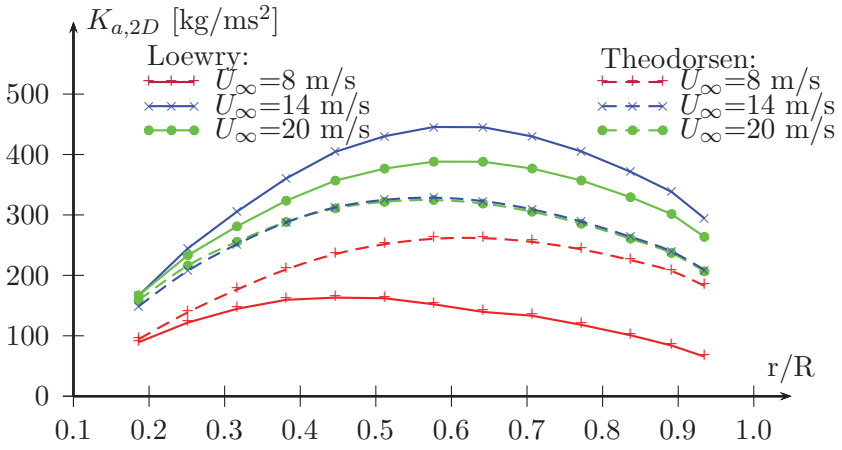

Figure C.2: Aerodynamic damping along the blade estimated Loewry function and compared to Theodorsen function for the first tower bending frequency.

C.2 Aerodyn

The velocities and accelerations used to estimate the damping and added mass coefficients from AeroDyn is $\dot{\eta}_x$ and $e\ddot{t}a_x$.

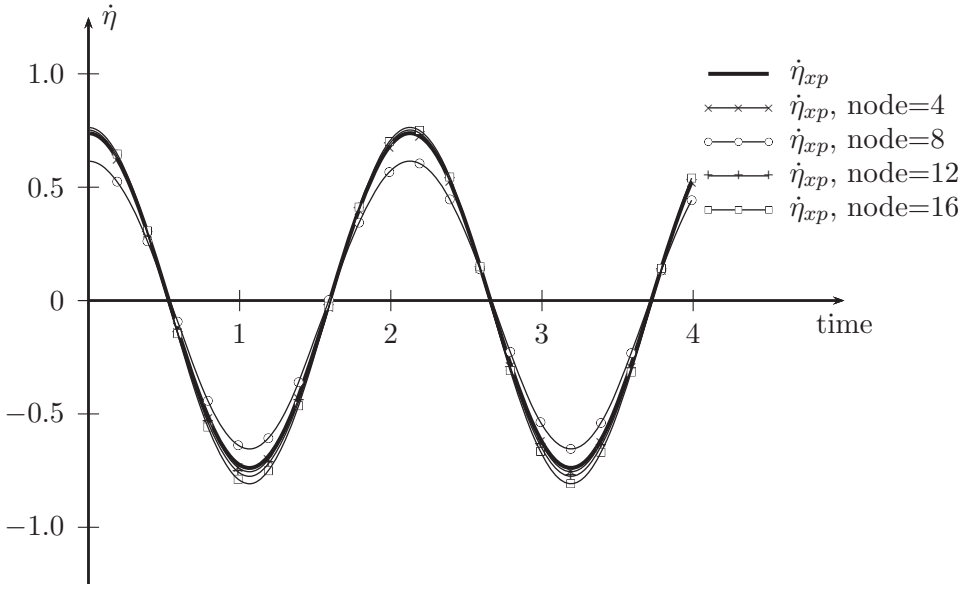

Figure C.3: The velocity of the blade section, $\dot{\eta}_x$, for different blade sections compared to the preliminary velocity, $\dot{\eta}_{xp}$, for a wind speed of 8 m/s and the tower bending frequency.

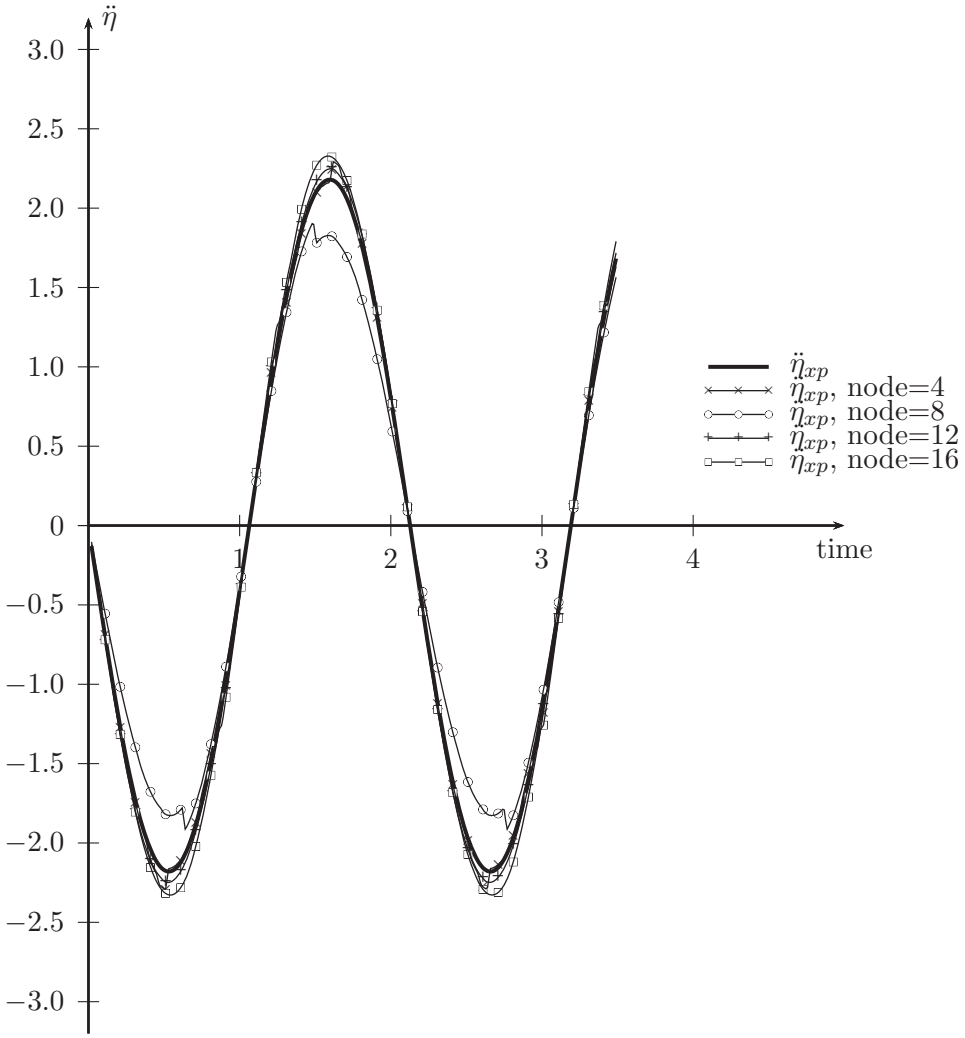

Figure C.4: The acceleration of the blade section, $\ddot{\eta}_x$, at different blade sections compared to the preliminary acceleration, $\ddot{\eta}_{xp}$, for a wind speed of 8 m/s and the tower bending frequency.

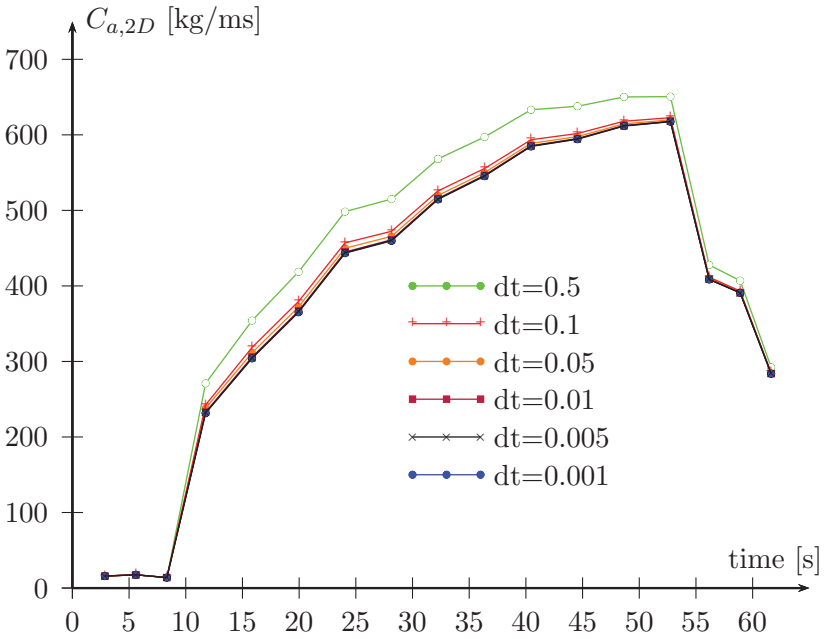

Figure C.5: Different timesteps for the computation of aerodynamic damping in AeroDyn for a wind speed of 8 m/s.

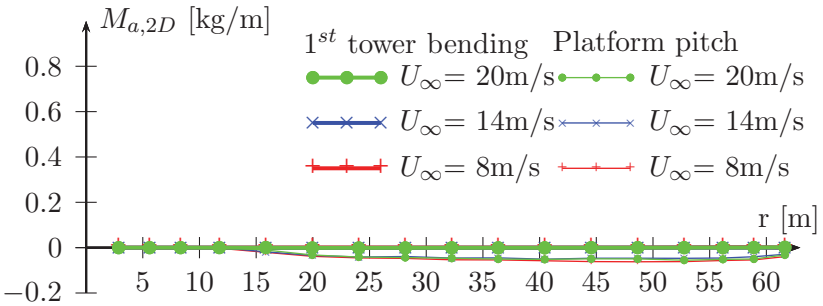

Figure C.6: The linear relation between the thrust force and the acceleration of the rotor for steady aerodynamic conditions.

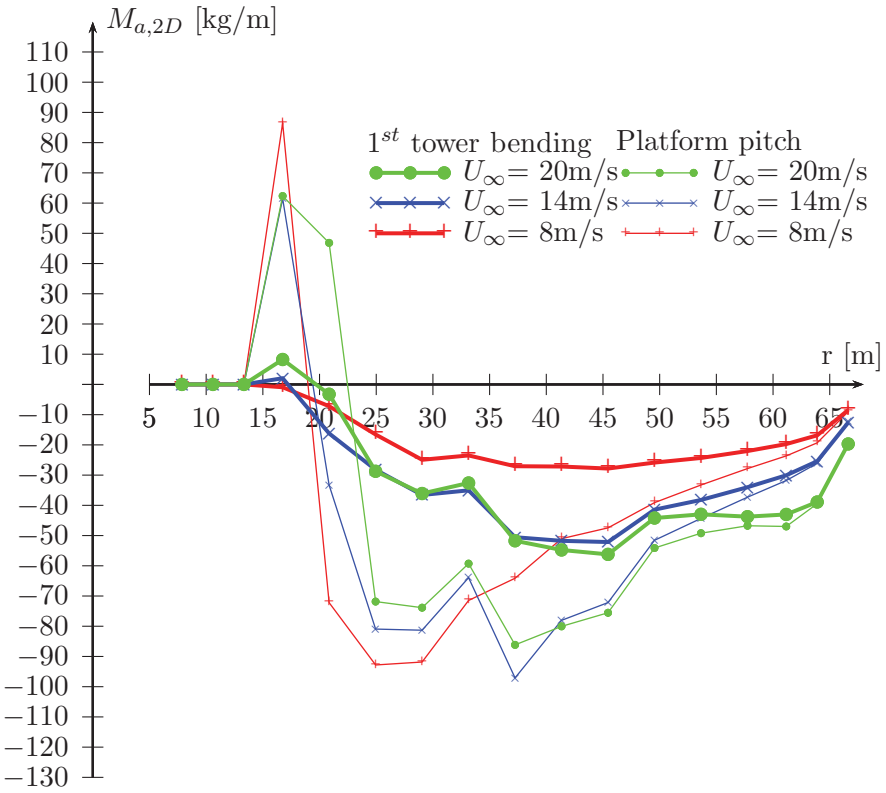

Figure C.7: The linear relation between the thrust force and the acceleration of the rotor for steady aerodynamic conditions.

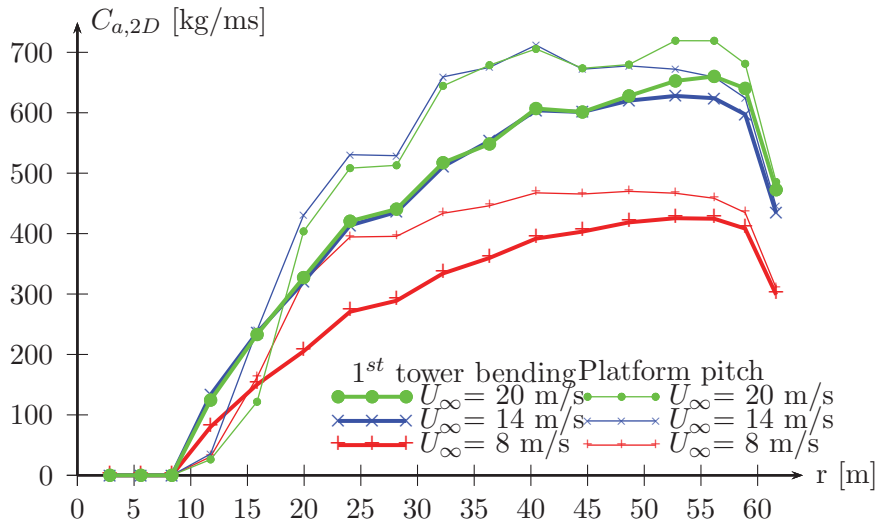

Figure C.8: The local aerodynamic damping at each blade section along the radial distance of the blade for three different wind speeds. GDW method is applied here.

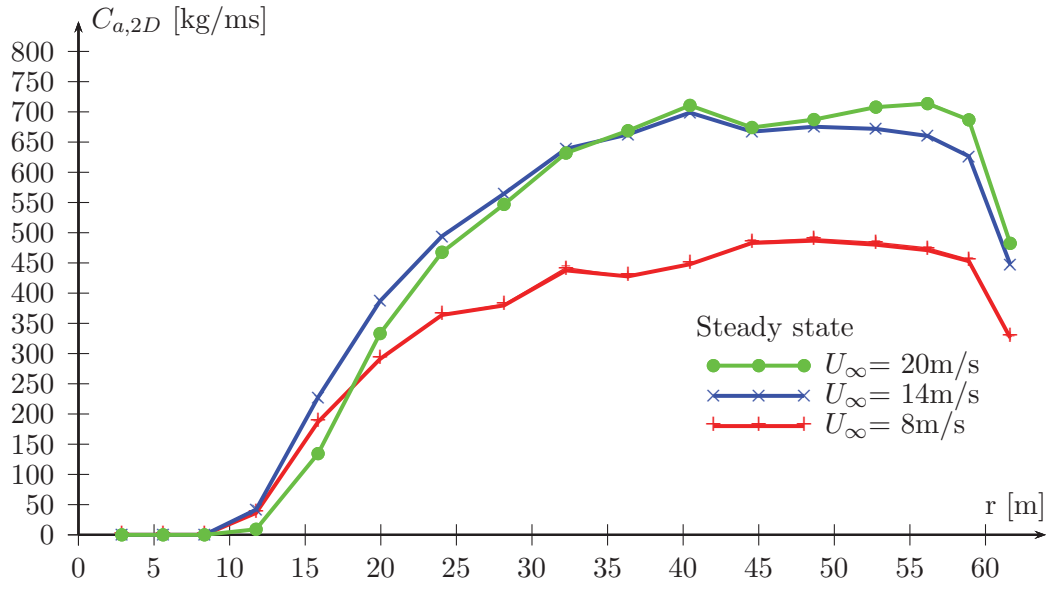

Figure C.9: The linear relation between the thrust force and the velocity of the rotor for steady aerodynamic conditions.

Table C.1: Integrated Aerodynamic Properties

Platform pitch	**8 m/s**	**14 m/s**	**20 m/s**
BEM: Ca	1.30e+09	1.69e+09	1.72e+09
GDW: Ca	1.34e+09	1.71e+09	1.69e+09
BEM: ξ	5.47	7.10	7.22
GDW: ξ	5.64	7.18	7.09
BEM: Mva	-1.56e+08	-1.64e+08	-1.48e+08
GDW: Mva	4.65e+06	3.45e+08	2.06e+08
BEM: M%	-0.28	-0.29	-0.27
GDW: M%	0.01	0.62	0.37

Appendix D

Platform pitch motion

The aim of this appendix is to estimate the rotational center of the platform pitch motion that is used in Chapter 6. We will consider a 2 DOF system with surge and pitch. This is a simplified calculation of a very complex system. The calculations in this chapter will be performed using the OC3 Hywind structure as described in [66] and the 5 MW rotor as described in [36].

$$[\mathbf{M} + \mathbf{A}]\,\vec{\ddot{x}} + \mathbf{C}\vec{x} = \vec{f} \tag{D.1}$$

where $\mathbf{M}$ is the mass matrix, $\mathbf{A}$ is the added mass matrix, $\mathbf{C}$ is the restoring matrix and $\vec{f}$ is the excitation forces.

First we will present the model, then estimate the mass matrix and the hydrodynamic matrices, finally we will estimate the platform pitch eigenfrequency and rotational center.

D.1 Model description

D.1.1 Tower

The mass distribution along the tower is shown in Table D.1. This gives a center of gravity 43.4 m above SWL. The total mass of the tower is 250 Te.

D.1.2 Rotor and nacelle

The nacelle weighs 240 Te and the rotor weighs 110 Te [36]. The hub height is 90 m above SWL, and this is used as the distance for the center

Length fraction	Elevation [m]	Mass density [kg/m]
0	10	4667.00
0.1	17.76	4345.28
0.2	25.52	4034.76
0.3	33.28	3735.44
0.4	41.04	3447.32
0.5	48.80	3170.40
0.6	56.56	2904.69
0.7	64.32	2650.18
0.8	72.08	2406.88
0.9	79.84	2174.77
1	87.60	1953.87

Table D.1: Distributed tower properties [66]

of mass for both rotor and nacelle.

D.1.3 Floating platform

The floating platform has a cylindrical shape and a draft of 120 m, and is connected to the tower at 10 m above SWL. Thus, the total length of the platform is 130 m and the total mass is 7466 Te, which consists of steel, wet ballast and dry ballast. The specific weights of these components are not given in the reference documentation [66], but they were later estimated by Myhr et al [67]. Table D.2 shows the estimated weights, and also typical densities for concrete as dry ballast, and water as wet ballast. Using these parameters the length of each section is calculated, with the dry ballast at the bottom and the wet ballast on top. The steel part of the platform encapsulates the ballast, and the weight of the steel is assumed uniformly distributed along the platform.

The cylindrical platform has not a constant diameter, but has a small diameter (6.5 m) at the top and a larger diameter at the bottom (9.4 m). The two sections are connected by a tapered section, which starts at 4 m

	Mass [Te]	Length [m]	Density [kg/m^3]
Steel	1 666.3	130	7 850
Wet ballast	2 700	38.0	1 025
Dry ballast	3 100	17.9	2 500

Table D.2: Mass and lengths of the ballast in the OC3 Hywind platform

below SWL and ends at 12 m below SWL.

D.2 Mass matrix

The mass matrix, **M**, is:

$$\mathbf{M} = \begin{pmatrix} M & M \cdot z_{cog} \\ M \cdot z_{cog} & I_{swl} \end{pmatrix} \tag{D.2}$$

where M is the mass, z_g is the location of the Center of Gravity (COG) and I_p is inertia about COG. The mass, distance to COG and inertia about SWL are shown in Table D.3.

Component	Mass Te	z_{cog} [m]	I_{swl} [kg m^2]
Tower	250	43.4	$5.89 \cdot 10^8$
Nacelle & Rotor	350	90	$2.84 \cdot 10^9$
Platform, steel	1 666	-55	$7.39 \cdot 10^9$
Platform, wet ballast	2.7	-83.2	$1.90 \cdot 10^{10}$
Platform, dry ballast	3.1	-111.1	$3.83 \cdot 10^{10}$

Table D.3: The parameters used to estimate the mass matrix for the OC3 Hywind

The mass matrix for the OC3 Hywind:

$$\mathbf{M} = \begin{pmatrix} 8.07 \cdot 10^6 & -6.18 \cdot 10^8 \\ -6.18 \cdot 10^8 & 6.81 \cdot 10^{10} \end{pmatrix} \tag{D.3}$$

D.3 Hydrodynamic properties

D.3.0.1 Added mass matrix

The added mass matrix, **A** consist of the following elements:

$$\mathbf{A} = \begin{pmatrix} A_{11} & A_{15} \\ A_{51} & A_{55} \end{pmatrix} \tag{D.4}$$

which is estimated as:

$$A_{11} \simeq \sum A_{2Di}(z_{ti} - ztb) \tag{D.5}$$

$$A_{55} \simeq \sum A_{2Di} \left[\frac{1}{3}(z_{ti}^3 + z_{tb}^3) \right] \tag{D.6}$$

$$A_{15} = A_{51} \simeq \frac{1}{2} \sum A_{2Di}(z_{ti}^2 - z_{tb}^2) \tag{D.7}$$

where subscript i is the section number, L_i is the section length, z_{ti} is the section top and z_{bi} is the section bottom. The two dimensional added mass for section i, A_{2Di}, for a cylinder is:

$$A_{2Di} = \pi\rho(D_i/2)^2 \tag{D.8}$$

where ρ is the sea water density and D_i is the diameter of the section.
The added mass matrix for the OC3 Hywind platform is:

$$\mathbf{A} = \begin{pmatrix} 8.22 \cdot 10^6 & -5.11 \cdot 10^8 \\ -5.11 \cdot 10^8 & 4.10 \cdot 10^{10} \end{pmatrix} \tag{D.9}$$

D.3.0.2 Restoring matrix

It is only the pitch motion that has a hydrostatic part in this case:

$$\mathbf{C} = \begin{pmatrix} 0 & 0 \\ 0 & C_{55} \end{pmatrix} \tag{D.10}$$

where

$$C_{55} = \rho g I_{wl} + \rho g V_b z_B - M g z_g$$

where g is the gravitation, V_b is the displaced volume (8 352 m^3), z_B is the distance to the center of buoyancy (-54.2 m), I_{wl} is the inertia at the water line area given by $I_{wl} = \pi(D/2)^4/4 = 87.6$ m^4. The hydrostatic stiffness for the OC3 Hywind is $C_{55} = 1.51$ kg m^2/s^2

D.4 Eigen-values

It is assumed that there is no damping of the system in this simplified calculation.

$$\mathbf{K} = [\mathbf{M} + \mathbf{A}]^{-1}[\mathbf{C}] \tag{D.11}$$

$$\left[\vec{Vm}\vec{Dm}\right] = eig\left(\mathbf{K}\right) \tag{D.12}$$

$$\omega_n = \sqrt{Dm} \tag{D.13}$$

$$z_{rot} = -\frac{Vm(1,:)}{Vm(2,:)} \tag{D.14}$$

D.5 Results

The resulting eigenfrequency for the pitch is estimated as 0.22 rad/s, which is an eigenperiod of 28.4 s. This is similar to the platform pitch eigenfrequency used in Chapter 6, which is 0.21 rad/s.

The rotational center is located at -69.3 m from the SWL. The global cog of the structure is at -76.6 m below SWL.

Appendix E

Sensitivity of fatigue

The fatigue calculation in Section 6.10.3 is based on m=3 for the Wöhler curve. In this appendix the results are shown for m=5, to illustrate the sensitivity to the material used.

Table E.1: The fatigue damage relative to fatigue damage estimated using Theodorsen's theory.

Method	$U_\infty = 8$ m/s	$U_\infty = 14$ m/s	$U_\infty = 20$ m/s
Garrad	0.55	0.63	0.64
BEM U	1.08	0.97	0.98
BEM inflow	1.24	1.40	1.31
GDW inflow	1.62	1.08	1.02
Theodorsen	1.00	1.00	1.00
Loewy	1.42	1.04	1.03
Vortex - single	0.79	0.82	0.90
Vortex - cascade	1.27	0.78	0.85

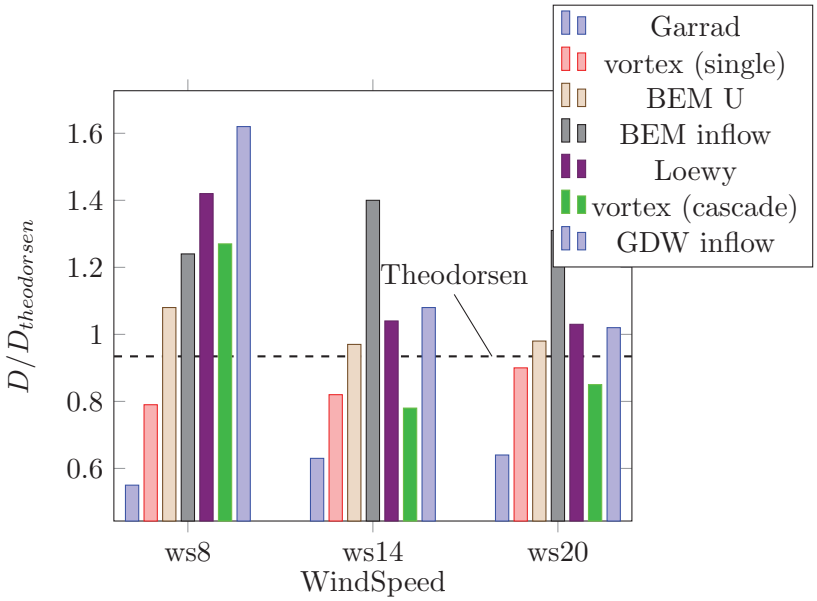

Figure E.1: The fatigue damage listed in Table E.1. All values are relative to the fatigue damage estimated using Theodorsen's theory.